The composition of salt-rich ice grains emitted by Enceladus' cryo-volcanic plume and implications for the subsurface ocean

A dissertation presented

by

Zenghui Zou

to

The Department of Earth Sciences

in partial fulfillment of the requirements

for the degree of

Doctor rerum naturalium (Dr. rer. nat.)

Freie Universität Berlin

Berlin, Germany

May 2021

First reviewer:

Prof. Frank Postberg

Institute of Geological Sciences

Freie Universität Berlin

Malteserstr. 74-100

12249 Berlin

Germany

Second reviewer:

Prof. Mario Trieloff

Institute of Earth Sciences

Heidelberg University

Im Neuenheimer Feld 234-236

D-69120 Heidelberg

Germany

Date of defence: July 13, 2021

"The universe is a pretty big place. If it's just us, seems like an awful waste of space."

— Carl Sagan, Contact

Kurzfassung

Es wird angenommen, dass die salzhaltigen Eispartikel im E-Ring des Saturns von gefrorenen aerosolisierten Tröpfchen des salzigen unterirdischen Ozeanwassers von Enceladus stammen. Sie werden in einem Plume aus Gas und Eispartikeln durch Spalten in der südlichen Polarregion des Mondes in den Weltraum geschleudert. Aufgrund ihrer Geschwindigkeit können einige dieser eisigen Partikel Enceladus‘ Schwerkraft entkommen und werden zu E-Ring-Teilchen, die typischerweise ein relativ junges Alter (nicht mehr als 200 Jahre) haben. Daher wird angenommen, dass die salzreichen Teilchen die Zusammensetzung des unterirdischen Ozeans Wasser widerspiegeln. Die in-situ-Massenspektren von E-Ring- und Plume-Eispartikeln, die mit dem Cosmic Dust Analyzer (CDA), einem Einschlagsionisations-Massenspektrometer an Bord der Cassini-Raumsonde erstellt wurden, zeigen eine erhebliche Vielfalt in der Zusammensetzung der salzhaltigen Partikel. Das Verständnis der Zusammensetzungen der in den Eisteilchen (und damit im Ozean) gelösten Substanzen, einschließlich Salze, Siliziumdioxid und organische Komponenten, kann entscheidende Hinweise für geochemische Ozeanmodelle für Enceladus liefern. Diese Arbeit untersucht die Vielfältigkeit der in situ Massenspektren der salzreichen Eispartikel und versucht, die Variationen in der Zusammensetzung der Eispartikel mit Hilfe von Analogexperimenten im Labor zu quantifizieren. Die in situ Massenspektren und damit die salzreichen Eispartikel werden anhand ihrer Zusammensetzung in verschiedene Gruppen und Subtypen eingeteilt. Die Verteilung der wichtigsten Subtypen der E-Ring-Spektren/Partikel hinsichtlich deren Abstand zu Saturn, Einschlagsgeschwindigkeit und Größe wurden untersucht. Außerdem wurde der Unterschied zwischen der E-Ring- und der Plume-Population untersucht. Die wichtigsten Ergebnisse sind: Die „natriumreichen und kaliumarmen“ Spektren (und damit Eisteilchen) machen den größten Teil sowohl der E-Ring- als auch der Plume-Population aus, während sowohl die „kaliumreichen und natriumarmen“ Spektren als auch die „natriumreichen und kaliumreichen“ Spektren selten sind. Carbonat- und chloridhaltige Spektren schließen sich in den meisten Fällen gegenseitig aus. Die „natriumreichen und kaliumarmen“ Spektren (und damit Eisteilchen) werden basierend auf den relativen Amplituden von carbonat- und chloridbezogenen Peaks weiter in die Untertypen A, B, H, C, D, E und L unterteilt. Von diesen Untertypen sind A, B, C, D und L die häufigstens im E-Ring. Ein Teil der Eispartikel, die Subtyp A und Subtyp L Spektren bei niedrigen Einschlagsgeschwindigkeiten erzeugt, könnte bei höheren Einschlagsgeschwindigkeiten Spektren des Subtyps B erzeugen. Die Häufigkeiten der wichtigsten Natrium-Subtypen innerhalb der salzreichen E-Ring-Populationen sind vergleichbar. Die Spektren des ultrakarbonatreichen Subtyps A sind viel häufiger als die Spektren der anderen Subtypen in der salzreichen Population des Plumes

zu finden, was bedeutet, dass die Energie der Mehrheit der ultrakarbonatreichen reichen (Subtyp A) Eispartikel nicht ausreicht, um der Schwerkraft von Enceladus zu entkommen, sodass sie den E-Ring erreichen könnten. Möglich ist auch, dass die E-Ring-Teilchen älter sind und rasch ihre karbonatsignatur verlieren. Die räumliche Verteilung der Subtypen und der relativen Peakamplituden legt nahe, dass die Karbonat- und Labor nachgestellt wurden. Danach rekonstruierte ich die Massenspektren von chloridreichen und karbonatreichen Enceladus-Ozean-Analoga, in denen Chlorid-Komponenten in den Eispartikeln mit der Zeit verloren gehen. Sowohl die Verteilung der Einschlagsgeschwindigkeiten der Subtypen als auch die der relativen Peakamplituden in den Spektren der salzreichen E-Ring Eispartikel implizieren, dass höhere Einschlagsgeschwindigkeiten tendenziell die Karbonatmoleküle aufbrechen und somit die Amplituden der karbonatbezogenen Peaks verringern. Um die Zusammensetzung der Eisteilchen zu quantifizieren, wurde eine laserinduzierte Flüssigstrahl-Desorptions (LILBID) Methode verwendet, um ein breites Spektrum von Enceladusozean-ähnlichen Lösungen zu desorbieren und zu ionisieren. Die enstandenen Ionen wurden mit einem Reflektron-Flugzeit-Massenspektrometer gemessen. Da der Laser-Desorptionsmechanismus den Einschlag der Eispartikel auf das CDA-Instrument simuliert, können im Labor erzeugte Massenspektren von einer großen Anzahl gut charakterisierter Salzlösungen verwendet werden, um deren spektrales Erscheinungsbild in CDA-Massenspektren zu bestimmen. Zunächst wurde der Parameterraum (NaOH, NaCl und Na_2CO_3 als Endglieder) für die vier bedeutendsten Untertypen von salzreichen Eispartikeln untersucht, indem die Massenspektren dieser Untertypen im Spurenkonzentrationen von einer Vielzahl von geochemisch relevanten Salzen, Siliziumdioxid und organischen Substanzen gelöst wurden, um deren Nachweisgrenzen für die CDA-Einschlagsionisationsmassenspektren der gefrorenen Ozeantröpfchen zu bestimmen.

Abstract

Salt-rich icy particles within Saturn's E-ring are thought to originate from frozen aerosolized droplets of the salty seawater of Enceladus' subsurface ocean. They are ejected into space, through fractures in the moon's south polar region, within a plume of gas and ice particles. Some of these icy particles can escape the gravity of Enceladus thanks to their high velocities, and become E-ring particles, which typically have relatively young (no more than 200 years) ages. Therefore, it is believed that the salt-rich grains reflect the composition of the subsurface ocean water.

The in situ mass spectra of E-ring and plume icy particles, produced by the Cosmic Dust Analyzer (CDA) impact ionization mass spectrometer onboard the Cassini spacecraft, reveal significant compositional diversity within the salt-rich population. Understanding the compositions of dissolved substance, including salt, silica, and organics, within the grains, and thus in the ocean, can provide crucial constraints for geochemical models of Enceladus' subsurface ocean environment.

The research presented in this thesis investigates the compositional diversity of the in situ mass spectra and hence the salt-rich icy particles and attempts to quantify the variations in grain composition with the aid of analogue mass spectra generated in the laboratory.

In this work, the in situ mass spectra and thus the salt-rich icy particles are classified into various compositional groups and subtypes. The major subtype distributions of E-ring spectra/particles with respect to distance to Saturn, impact speed and size have been studied and the contrast between the E-ring population and plume population examined. The major findings are: The 'sodium-rich and potassium-poor' spectra (and hence icy particles) are the majority among both E-ring and plume salt-rich populations, while 'potassium-rich and sodium-poor' spectra and 'both sodium and potassium-rich' spectra are rare. Carbonate and chloride-containing spectra are mutually exclusive in most cases. The 'sodium-rich and potassium-poor' spectra (and hence icy particles) are further classified into Subtypes A, B, H, C, D, E and L according to the presence and relative amplitudes of carbonate and chloride related peaks. Among them Subtypes A, B, C, D and L are the majorities in E-ring spectra. A part of ice particles producing Subtype A and Subtype L spectra at lower impact speed could produce Subtype B spectra at higher impact speed. While abundances of the major sodium subtypes are comparable in the E-ring salt-rich populations, the ultra carbonate-rich subtype, which is named as Subtype A, spectra are much more frequent than the spectra of other subtypes in the plume salt-rich population, which implies that the majority of the ultra carbonate

rich (Subtype A) ice particles do not have enough energy to escape from the gravity of Enceladus and reach the E-ring or that the E-ring grains are older and rapidly lose their carbonate signature. The spatial distribution of the subtypes and relative peak amplitudes implies the carbonate and chloride compounds in the ice particles are lost slowly with time. The impact speed distributions of the subtypes and relative peak amplitudes for the spectra of E-ring salt-rich ice particles imply higher impact speeds tend to break up carbonate molecules and thus lower the amplitudes of carbonate related peaks.

To quantify the grains' compositions, a Laser Induced Liquid Beam Ion Desorption (LILBID) technique was used to desorb and ionize a wide range of Enceladean ocean-like solutions containing dissolved salts. The resulting ions were then measured by a reflectron-type time of flight mass spectrometer. Since the laser desorption mechanism simulates the ice grain impact process occurring on the CDA target, spectra produced in the laboratory from a large range of well-characterized salt solutions can be used to determine the CDA-applicable spectral appearances of substances within the ice grains emitted from Enceladus' ocean.

Firstly, the composition parameter space, with NaOH, NaCl, and Na_2CO_3 as endmembers, for the four major subtypes of salt-rich ice particle were explored via spectra mimicking. After this, I reconstructed the mass spectra from chloride-rich and carbonate-rich Enceladus ocean analogues, into which trace concentrations of a wide range of geochemically-relevant salts, silica and organics were been dissolved, to evaluate their detection limits for CDA impact ionization mass spectra of the frozen ocean droplets.

Contents

Kurzfassung i

Abstract iii

Acknowledgements xi

1 Introduction 1

1.1 Dust in outer space - cosmic dust 2

1.1.1 Interstellar dust 3

1.1.2 Interplanetary dust 10

1.1.3 Planetary dust 12

1.2 The Cassini-Huygens mission 14

1.3 The Saturnian system 18

1.4 Saturn's E-ring, Enceladus and its subsurface ocean 23

1.4.1 E-ring 23

1.4.2 Enceladus and its subsurface ocean 29

2 Instruments and Methodology 35

2.1 The Cosmic Dust Analyzer 35

2.1.1 The structure of Cosmic Dust Analyzer 35

2.1.2 The working principle of the Chemical Analyzer 37

2.1.3 The principle of impact ionization 40

2.1.4 CDA Impact Event Data 41

2.2 Analogue spectra by Infrared Laser Induced Liquid Beam Ion Desorption Time of Fight Mass Spectrometer (IR-LILBID-TOF-MS) 44

2.2.1 Techniques for simulating impacts of ice grains onto the CAT in CDA and mimicking analogue spectra 44

2.2.2 Impact speed simulation 46

2.3 Comparison of the principles and spectra of impact ionization in CDA and laser ionization in IR-LILBID-TOF-MS 47

2.4 Main compositional types of ice grains in the E-ring and Enceladus' plume 49

2.5 The formation mechanism of water clusters and salt clusters 52

3 The motivation and goals of this work 57

3.1 The motivation and goals of this work 57

4 Compositional variation in Type-3 salt-rich ice grains, as revealed by their spectra 59

4.1 Introduction 59

4.1.1 Ice grain formation processes 59

4.1.2 Research objectives 61

4.2 The properties of the datasets 62

4.3 Methodology 63

4.3.1 Peak threshold for CDA spectra 63

4.3.2 Classification of the potential preliminary classified salt-rich spectra 63

4.3.3 Sub-classification of the Type-3 spectra into several subtypes . 64

4.3.4 Co-adding the spectra of subtypes 65

4.3.5 Statistics and plotting: 65

4.3.6 The relation between impact speeds and important peak amplitude ratios in co-added spectra 67

4.4 Results . . . 67
4.4.1 Preliminary results of peaks analysis . . . 68
4.4.2 Preliminary classification of spectra of E-ring salt-rich ice grains 68
4.4.3 Further classification of the spectra of E-ring Na-rich ice grains 73
4.4.4 The impact speed of different spectral subtypes . . . 89
4.4.5 Distribution of spectral subtypes with Saturnian distance . . . 94
4.4.6 Distribution of spectral subtypes with calculated grain size . . 104
4.4.7 The relation between impact speeds and important peak amplitude ratios derived via spectra co-adding . . . 106
4.5 Discussion . . . 107
4.5.1 The identification of peak at 81 u . . . 107
4.5.2 The popularly mutual exclusion between carbonate and chloride 109
4.5.3 The potential revolution trend of carbonate-rich Subtypes (A and B with peak Na(Na_2CO_3) (129 u)) . . . 110
4.5.4 The revolution of chloride-rich Subtypes (C and D) . . . 110
4.5.5 The potential relation between Subtype B and Subtype L . . . 111
4.5.6 The possible impact speed dependent conversion between Subtype A spectra and Subtype B spectra of carbonate-rich ice particles . . . 111
4.5.7 The possible physical mechanism for the different behaviors of carbonate and chloride related ions in high speed impact . . . 112

5 Enceladus Plume Grain Compositions 115

5.1 Introduction . . . 115
5.2 Dataset . . . 116
5.3 Plume particle salt-rich subtype distribution . . . 116
5.4 Discussion . . . 120

6 Laboratory mass spectra mimicking and concentration parameter

space determination **123**

6.1 Introduction . . . 123

6.2 Methodology . . . 123

6.2.1 Settings of the experimental setup . . . 124

6.2.2 The major salts forming the major subtypes *typical* CDA spectra of the Na-rich ice particles . . . 125

6.2.3 Understanding the relative ionization efficiencies of salts . . . 125

6.2.4 Spectra mimicking . . . 126

6.2.5 Exploring the concentration parameter space for major subtypes 127

6.3 Results and discussion . . . 127

6.3.1 The range of the total concentration of Na^+ . . . 127

6.3.2 Relative ionization efficiencies of Salts . . . 128

6.3.3 Spectra Mimicking . . . 131

6.3.4 Mimicking archetypal spectra for individual subtypes . . . 132

6.3.5 Concentration parameter space for subtypes . . . 134

7 Approximate CDA detection limit predictions for relevant geochemical and organic compounds **141**

7.1 Introduction . . . 141

7.2 Methods . . . 143

7.2.1 Mimicking co-added spectra of different subtypes of Type-3 spectra as template spectra to explore the detection limits of trace substances . . . 143

7.2.2 Measured substances . . . 145

7.2.3 Evaluating approximate CDA detection limits . . . 146

7.2.4 Comparison of the two CDA detection limit evaluation methods 150

7.2.5 Error Analysis . . . 156

7.3 Results . . . 159

7.3.1 The composition of analogue solutions and the resulting laboratory template spectra . . . 159
7.3.2 Identification of suitable mass lines (peaks) for detection limits evaluation . . . 163
7.3.3 Approximate CDA detection limits prediction using Method 1 (Peak threshold conversion) . . . 165
7.3.4 Approximate CDA detection limits prediction using Method 2 (correlation between concentration and peak amplitude ratios) 172
7.4 Discussion . . . 181
7.4.1 Reaction between compounds of interest and the two analogue solutions . . . 181
7.4.2 Differences between CDA spectra and the laboratory analogue spectra . . . 182
7.4.3 Detection limits variation with different settings . . . 183
7.4.4 Data used for linear regression in Method 2 . . . 183
7.4.5 Negative intercept problem during linear regression in Method 2 183
7.4.6 Detection limit differences between Mixes 1 and 2 . . . 184
7.4.7 Comparison of the results of CDA detection limit evaluation methods . . . 186

8 Summary **189**

References **195**

Appendix **209**

A Data Tables **211**

A.1 Basic information about the original dataset of the CDA spectra used in this thesis . . . 212
A.2 The subtype distribution of the spectra of salt-rich plume particles measured during flybys E17, E18, and E19 . . . 213

B CDA spectra **215**

C Determining the 129 u/63 u peak amplitude ratio boundary between Subtypes A and B **225**

D Laboratory analogue spectra **229**

D.1 About peak at 81 u 229

D.2 A spectrum of solution of 0.1 M NaCl and 0.01 M NaOH 230

E The distribution of Type-3 spectral subtypes with high certainty **233**

F Analyzing the 129 u/63 u peak amplitude ratios in CDA Subtypes A and B spectra separately. **237**

G Upper limits **241**

G.1 Mimicked Subtype A spectrum and Subtype B spectrum 242

G.2 Criteria for spectra calibration for CDA detection limits 243

G.3 The reactions for compounds of interest 243

G.4 Spectra of pure Mix 1 solution and saturated solution of $MgCl_2$ in Mix 1 at setting 1 247

H Approximate detection limit predictions using Method 1 **249**

I Approximate detection limit predictions using Method 2 **253**

J Comparison of detection limits determined using the different methods via bar charts **277**

Eidesstattliche Erklärung **291**

Acknowledgements

I would like to express my sincere gratitude to my supervisor Professor Frank Postberg for his enlightening guidance to my research and enduring trust and patience. I would like to thank my co-supervisor Nozair Khawaja for his conscientious training and guidance on my research. I also would like to thank my another co-supervisor Jon Hillier for his conscientious guidance on my research and thesis. I also thank Fabian Klenner for teaching me the operation of laboratory setup and the skills for experimental performance.

I would like to thank Lenz Nölle for the discussion on my research. He often gave me smart suggestions. I thank René Reviol for helping me to fix the malfunction of the laboratory setup.

I also thank the free study and research atmosphere and system in Heidelberg University and Freie Universität Berlin, thanks to which I can take very useful courses or practices on physics and astronomy from Heidelberg University, Max Planck Institute for Astronomy, and Berlin University Alliance. I would like to thank all the professors and teachers who trained me with the knowledge and skills and thus broadened my horizons on astronomy, planetary sciences and physics.

Thank Heidelberg University and the Berlin University Alliance for offering so many fantastic sport courses, such as kayak, Stand Up Paddling, windsurfing, dances, rowing, sailing, archery and beach volleyball, so that I can have a balance between work and life.

Finally, I thank China Scholarship Council and Professor Frank Postberg for offering me the funding for my study and research. I also thank Institute of Deep-sea Science and Engineering, Chinese Academy of Sciences, especially Professor Xiaotong Peng, for granting me to go abroad to pursue my PhD.

Chapter 1

Introduction

Icy moons harboring subsurface oceans are some of the most promising objects for extraterrestrial life, and therefore an important focus of current astrobiology research.

However, with current technologies direct analysis of subsurface oceans by drilling is impossible, thus indirect detection methods are required to study the habitability of these environments. Fortunately some icy moons, such as the sixth-largest moon of Saturn, Enceladus, 'leak' into outer space via plume. Hubble space telescope imaging (Roth et al. 2013; Sparks et al. 2016, 2017) and Galileo spacecraft in situ observations (Jia et al. 2018) also show evidence of water plume erupting from Europa, one of Jupiter's icy moons. For these icy objects, one important and promising method to study their inner oceans is to analyze the dust particles which originate from them. These dust particles are emitted in the cryovolcanic plume, with some of them remaining bound by the gravity of a planet or a moon, and potentially forming rings, as in the case of Enceladus and Saturn's E-ring. The compositions of these dust particles provide constraints on the physical and chemical environment of the subsurface ocean and dust formation regions.

Unfortunately, remote sensing observations only provide very limited compositional and dynamical information about dust particles in the Solar System due to the tenuousness and small sizes of the dust. Therefore, in situ measurements with spacecraft are necessary to study these dust particles. Since the late 1960s, cosmic dust detectors onboard spacecraft have been used for measurements of interplanetary space dust particles in the solar system: In 1967, the first interplanetary spacecraft with an in situ cosmic dust detector, Pioneer 8 (Barnett 2019; Berg & Richardson 1969), was launched, and Pioneer 9 followed in 1968 (Barnett 2019). In the 1970s, Helios 1 (launched in 1974) and Helios 2 (launched

in 1976) were employed for the in situ detection of dust particles in the inner solar system (Grün et al. 1980). In the 1980s, Vega 1, Vega 2 and Giotto were launched to investigate the chemical and physical nature of cometary dust particles from comet Halley (Kissel et al. 1986a,b). Since the end of 1980s, more advanced spacecraft with dust detectors combining large sensitive areas (1000 cm^2) with high sensitivities (a lower mass threshold, i.e. $\leqslant 2 \times 10^{-18}$ kg) were launched, such as Galileo launched in 1989 (O'Neil 1990); Ulysses launched in 1990 (Smith et al. 1991) and Cassini launched in 1997 (Goodson et al. 1998).

The Cosmic Dust Analyzer (CDA) (Srama et al. 2004) on Cassini provided the in situ dust data for this thesis. Equipped with a time of flight mass spectrometer, Cassini's dust detector not only investigated the dust's dynamical properties but also its composition, providing further information about its sources. Combining flight data with laboratory analogue experiments, the composition of the subsurface ocean in Enceladus can be investigated in detail.

This thesis focuses on two main subjects:

1) The chemical analysis of mass spectra, produced by the Cosmic Dust Analyzer (CDA) onboard the Cassini spacecraft, of salt-rich ice grains in Saturn's E-ring and Enceladus' plume;

2) Based on the results of the analysis of this in situ data, the CDA spectra were simulated with laser desorption mass spectrometry to verify the results and obtain quantitative physical and chemical information about Enceladus' subsurface ocean.

This thesis consists of six chapters and is organized as follows: the first chapter provides an introduction to cosmic dust, the Saturnian system, the E-Ring, Enceladus, its subsurface ocean and the Cassini-Huygens mission; the second chapter gives a detailed description of the methods and instrumentation used in the research; chapter three focuses on variations between mass spectra of Enceladus' subsurface ocean-originated salt-rich icy particles in the E-ring; the fourth chapter concerns the laboratory analogue spectra of salt-rich icy particles; in the fifth chapter the inferred CDA detection limits of potential dissolved substances in Enceladus' ocean are determined; and finally the last chapter is the summary and discussion.

1.1 Dust in outer space - cosmic dust

Dust is ubiquitous in the universe. Dust in outer space is known as cosmic dust, consisting of small solid particles varying in composition and size (Flynn et al. 2016;

Greenberg 2002; Brownlee 1985).

Cosmic dust in our Galaxy, the Milk Way, can be further distinguished by its origin: **interstellar dust**, **interplanetary dust** and **planetary dust (or circumplanetary dust)**(Grün et al. 2001, 2019; Badescu & Zacny 2018; Inoue 2012).

With current techniques, only a tiny fraction of cosmic dust in the solar system can be detected in situ. The remainder is usually investigated via remote sensing observations, i.e. the cosmic dust's interaction with electromagnetic radiation.

1.1.1 Interstellar dust

Interstellar dust is an important component of the Interstellar Medium (ISM).

Most elements composing cosmic dust, such as C, O, Mg, Si, Fe, etc. except H, the most of He, Li and Be, and elements heavier than ^{56}Fe, are originally mostly formed during nuclear fusion processes within stars (Nomoto et al. 2013). These elements are dredged up to the stellar surface and then shed off with expanding shells (AGB stars and planetary nebulae) or blown off with the stellar winds (mainly for post-main-sequence massive stars, such as Wolf-Rayet stars) or blown off in massive star explosions (novae/supernovae), and then condense from gaseous form into solid form, when their temperatures drop, to form interstellar dust (Nomoto et al. 2013; Arnett & Bazan 1997). These dust particles can be complex in shape and grow by sticking together (Dominik et al. 2006; Birnstiel et al. 2016).

Evidence of interstellar dust:

As with the intergalactic dust, the observational evidence and information about interstellar dust mostly arise from the interaction of dust with electromagnetic radiation:

- Infrared thermal emission: Heated by starlight, dust emits continuum thermal emission, usually with a maximum at wavelengths in the mid- or far-infrared range. See Fig. 1.2a.
- Reflection nebulae: clouds of interstellar dust reflecting the light of a nearby star or stars. See Fig. 1.2b.
- Wavelength-dependent extinction of starlight: Absorption and scattering

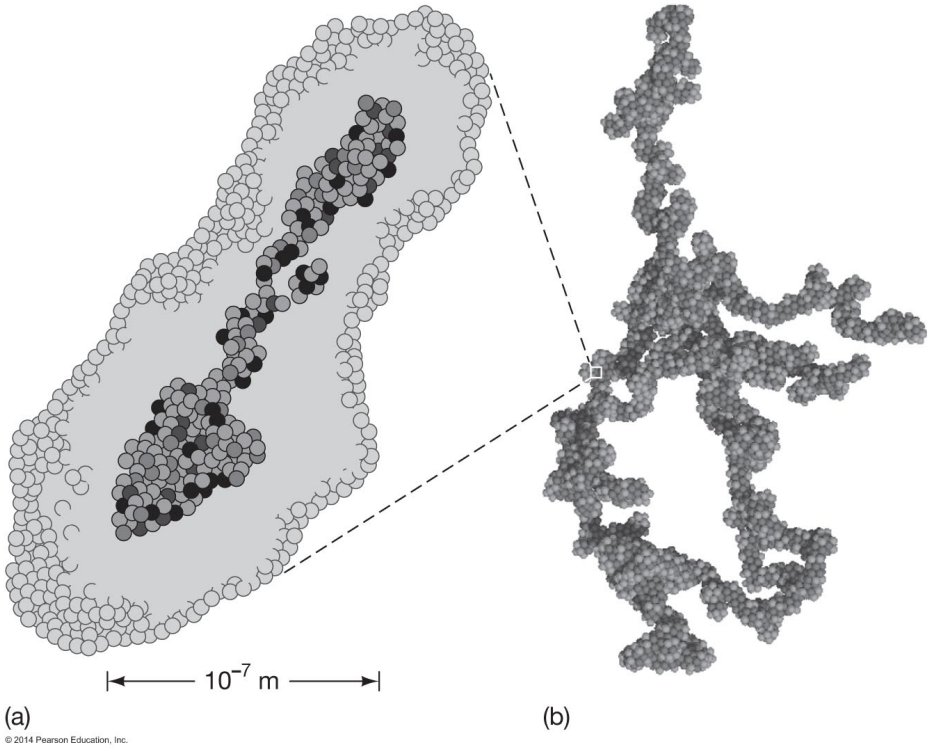

Figure 1.1: Left (a): A dust particle. It is non-spherical but elongated in shape. Right (b): Dust particles can grow by sticking together. Image credit: 2014 Pearson Education, Inc

(a) Infrared image of the shock wave created by the runaway star Zeta Ophiuchi in an interstellar dust cloud. Green and red represent light with wavelengths of 12 and 22 microns, respectively, which is mostly emitted by dust at the shock front. Image taken by NASA's Wide-field Infrared Survey Explorer, WISE. Image credit: NASA/JPL-Caltech/UCLA

(b) The Witch Head reflection nebula (IC2118), about 900 light years from Earth, is illuminated by the bright star Rigel (Spectral type B8) in the constellation Orion. The fine dust in the nebula reflects the light from Rigel, located just outside the top right corner of the image. The blue color is caused not only by Rigel's blue color but also because the dust grains reflect blue light more efficiently than red. Image Credit and Copyright: Gary Stevens

Figure 1.2: Infrared emission from interstellar dust (a) and reflection of starlight by interstellar dust (b)

.

of electromagnetic waves with shorter wavelengths (such as optical and ultraviolet) by dust grains. This produces the following observational effects:

1. Interstellar dimming: Making astronomical objects appear fainter than they should be or even be completely obscured to form dark nebulae at certain wavelengths (mainly in the ultraviolet and visible). See Fig. 1.3.

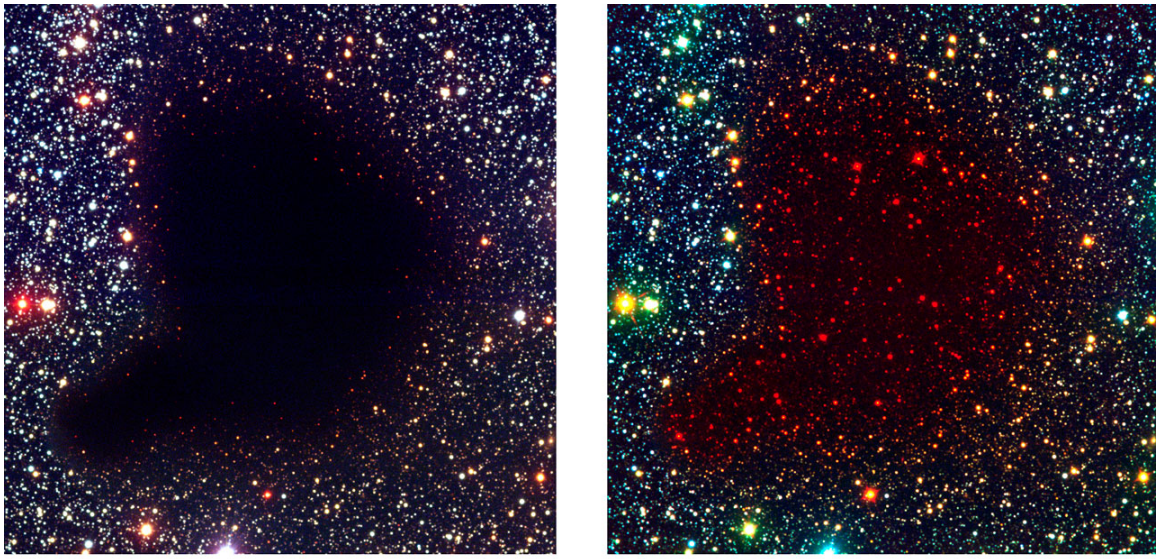

B, V, I B, I, K

Figure 1.3: Barnard 68: A high concentration of dust and molecular gas absorbing practically all the visible light and the near-infrared emitted from background stars but with the longer wavelengths (infrared) light passing. The left image is a colour composite of visible and near-infrared; the right image is a false-colour composite based on a visible (here rendered as blue), a near-infrared (green) and an infrared (red). The light from stars behind the dust cloud is only visible at the infrared wavelengths, which indicates that the extinction of starlight is wavelength-dependent. Image Credit: FORS Team, 8.2-meter VLT Antu, ESO.

2. Interstellar reddening: It is another effect contributed by the Wavelength-dependent extinction of light, making astronomical objects look redder than their real colors. See Fig. 1.4.

- Polarization of starlight: After passing through interstellar dust, the starlight becomes polarized due to absorption and scattering by elongated dust grains (Fig. 1.1 on Page 4) aligning along the magnetic fields present in interstellar space (Hadley 2019). See Fig. 1.5.

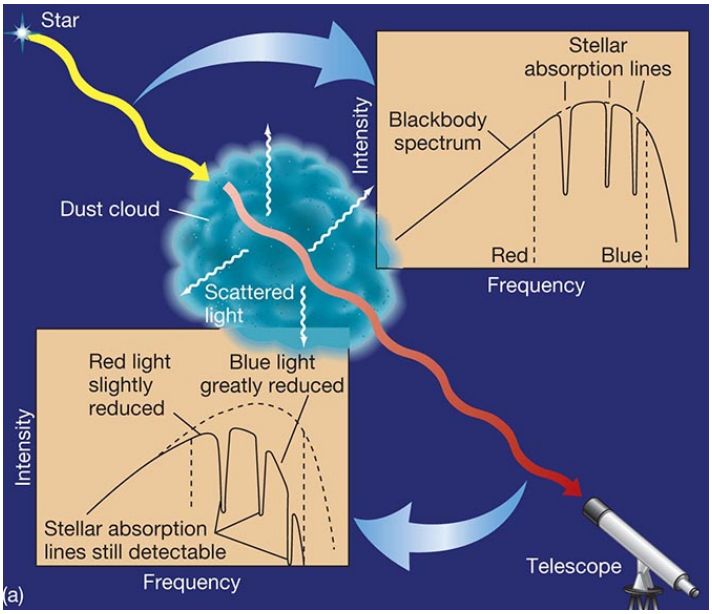

Figure 1.4: The principle of reddening by interstellar dust. Image credit: 2005 Pearson Prentice

The distribution of interstellar dust in the Milky Way:

Fig. 1.6 is a whole-sky optical view of the Milky Way. Interstellar dust blocks most of the visible light emitted from the stars located along the disk and makes the galactic plane opaque at optical wavelengths.

Fig. 1.7 is a whole-sky infrared view of the Milky Way. The infrared light is largely emitted by interstellar dust.

In images of the Milky Way (e.g. Figs. 1.6 and 1.7), it can be seen that most dust is distributed along the plane of the galaxy. This is reasonable: An indispensable component for forming cosmic dust is the availability of heavy elements, which are formed in stars. Population I stars, which are hot, young, and rich in heavy elements, are concentrated in the discs of spiral galaxies, like the Milky Way (Bergh 1975; Unavane 1995) . The high abundance of heavy elements suggests that the gas for forming Population I stars must have been recycled (incorporated into, and then expelled) by previous generations of stars (Gibson et al. 2003). Several star formation and destruction cycles release a lot of heavy elements into interstellar space, which are eventually incorporated into interstellar dust (Albada 1947).

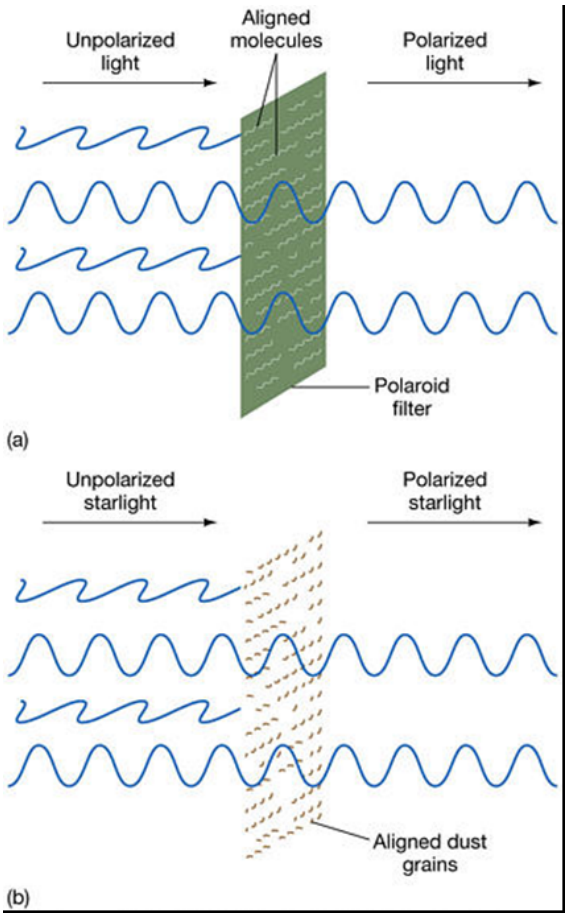

Figure 1.5: (a) Light becomes polarized as it passes through a polarizing medium.(b) The starlight becomes polarized as it passes through interstellar dust. The principle for both is the same. Image credit: 2005 Pearson Prentice Hall, Inc

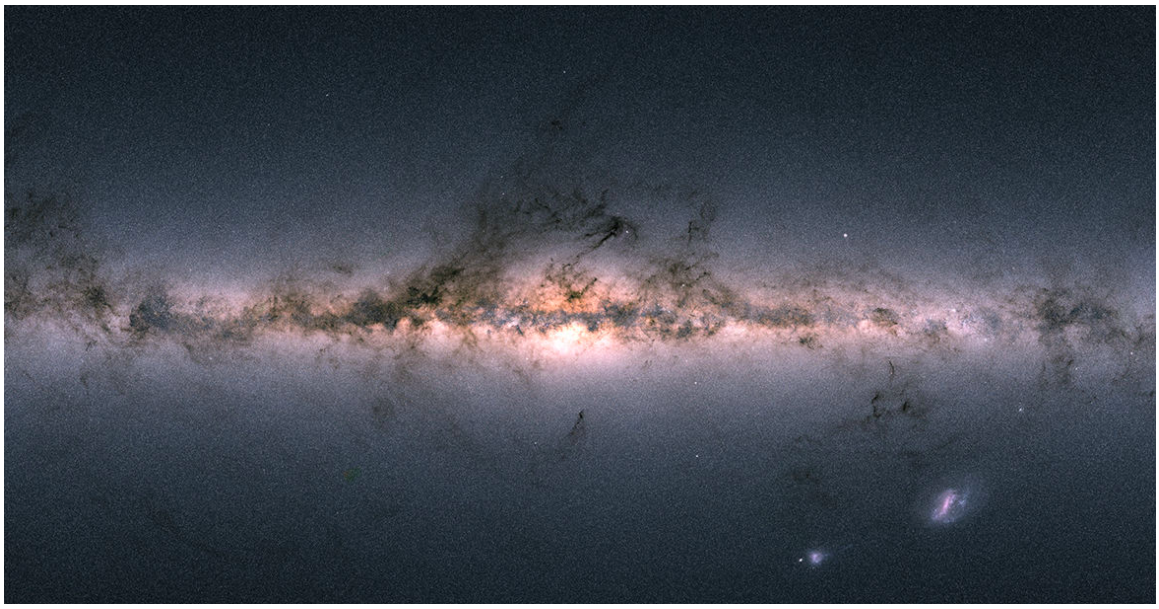

Figure 1.6: A whole-sky optical view of the Milky Way, released by the GAIA mission in 2018. Most of the dust is distributed in the plane of the disk. Image credit: ESA/Gaia/DPAC

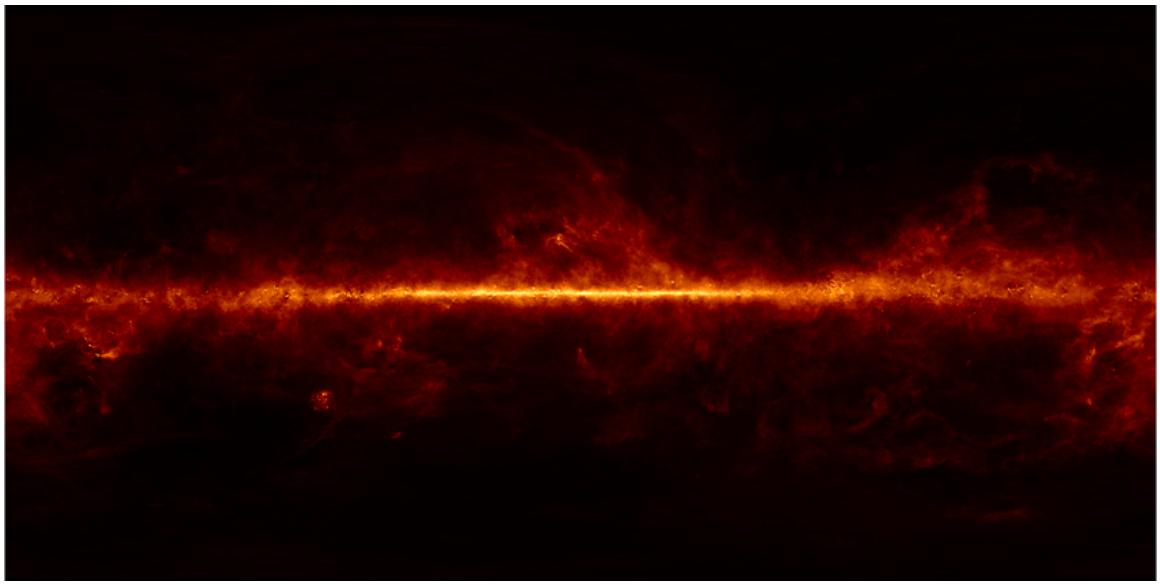

Figure 1.7: Galactic map of infrared emission by interstellar dust in the Milky Way. Image credit: 2005 Pearson Prentice Hall, Inc

1.1.2 Interplanetary dust

Interplanetary dust is cosmic dust created and found within planetary systems such as our Solar System.

Evidence for the distribution of interplanetary dust in our Solar System:

In the Solar System, interplanetary dust particles scatter sunlight and emit thermal radiation. At visible wavelengths, in dark sky conditions, we can see the zodiacal light as a faint, diffuse glow (Fig. 1.8) extending along the ecliptic. This phenomenon is caused by sunlight scattered by interplanetary dust.

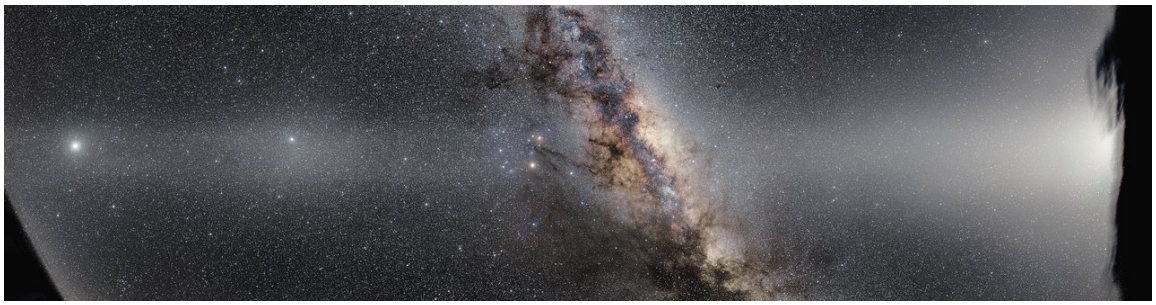

Figure 1.8: Zodiacal light and Milky Way at optical wavelengths. The horizontal glow is the zodiacal light, which is projected along the ecliptic. The disc of Milky Way crosses the zodiacal light at an angle of approximately 60°. Also visible are the huge clouds of dust obscuring the light from more distant stars in the disk. This image therefore shows cosmic dust both in our Solar System and in the Milky Way. Image credit: ESO/P. Horálek

As well as the evidence from remote sensing observations, there is also evidence from in situ detection of interplanetary dust by spacecraft. For instance, during Cassini's early cruise phase, its onboard Cosmic Dust Analyzer obtained two spectra of interplanetary dust particles (Hillier et al. 2007b).

The origins of interplanetary dust in our Solar System:

There are many sources of interplanetary dust particles: cometary activity (Kissel et al. 1986a), active asteroidal activity (Jewitt 2012), collisions in the inner Solar System and Kuiper Belt; from planets and moons without atmospheres, and even via planetary rings (Grün et al. 2001; Hillier et al. 2007b). Following are some examples of the sources of interplanetary dust particles:

When a comet approaches the Sun, it is heated up by the solar radiation, and then the sublimation of volatile gases frees and expels dust grains into space, via gas drag (Huebner et al. 2006). The solar wind accelerates the charged dust particles released from the surface of the comet (Gunell et al. 2015). Figure 1.9 shows an image of an active comet, 67P/Churyumov-Gerasimenko.

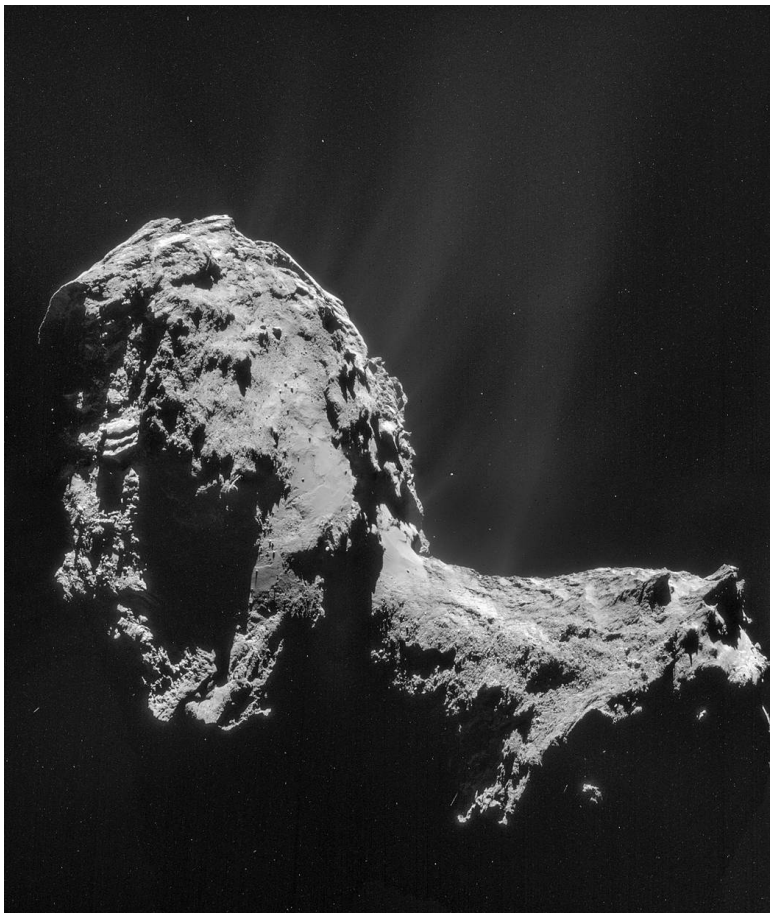

Figure 1.9: The active comet, comet 67P/Churyumov-Gerasimenko, is emitting dust. This composite is a mosaic composed from four individual images taken at a distance of 31 kilometers from the comet by Rosetta's navigation camera (NavCam) on Nov. 20, 2014. Copyright: ESA/Rosetta/NAVCAM, CC BY-SA IGO 3.0

Active Asteroids are the small bodies which are dynamically like asteroid but lose mass, like comets (Jewitt 2012). They also emit dust into space. For instance, a faint dust trail left behind by 3200 Phaethon, which is the source of the annual Geminids meteor shower, was captured by the Wide-Field Imager for Solar Probe (WISPR) camera onboard the Parker Solar Probe in 2018 (Fig. 1.10).

The micrometeorite impact gardening (Rietmeijer 1998) and the asteroid-

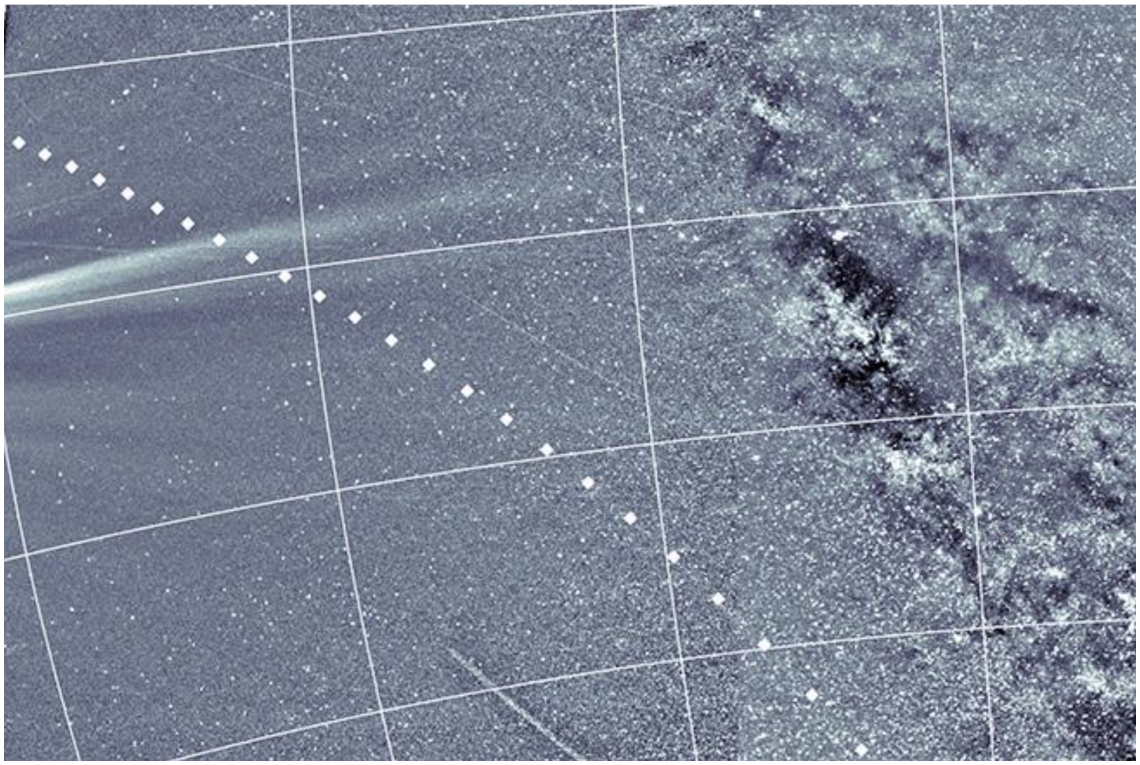

Figure 1.10: The image of dust trail of asteroid 3200 Phaethon captured by the Wide-Field Imager for Solar Probe (WISPR), a U.S. Naval Research Laboratory-built camera on Nov. 5, 2018. The trail, imaged for the first time, can be seen in the places where the white dots are omitted. Copyright: U.S. Naval Research Laboratory Corporate Communications

asteroid impacts (Dohnanyi 1976) are also major sources of interplanetary dust in the inner solar system.

1.1.3 Planetary dust

The last type of cosmic dust is planetary dust or circumplanetary dust, which is also what this thesis focuses on. Planetary dust is cosmic dust gravitationally bound to a central body, e.g. a planet or a smaller planetary body, such as a moon. Planetary dust includes dust rings and tori around the giant planets, ejecta dust clouds above atmosphereless moons, and rings and ejecta around smaller planetary bodies throughout the Solar System (Spahn et al. 2019).

The planetary dust populations in the solar system are described in detail by Spahn et al. (2019), who stated the possible planetary dust sources include:

micrometeoroid erosion of the surface of atmosphereless bodies, active volcanoes and geysers, as well as the capture of exogenous particles.

In this thesis, a compositional analysis of planetary dust particles in Saturn's diffuse and extended E-ring (Fig. 1.11) is undertaken. These dust particles mainly originate from the active cryovolcanoes (Fig. 1.12) on Saturn's icy moon Enceladus (Pang et al. 1984; Spahn et al. 2006a,b; Kempf et al. 2010).

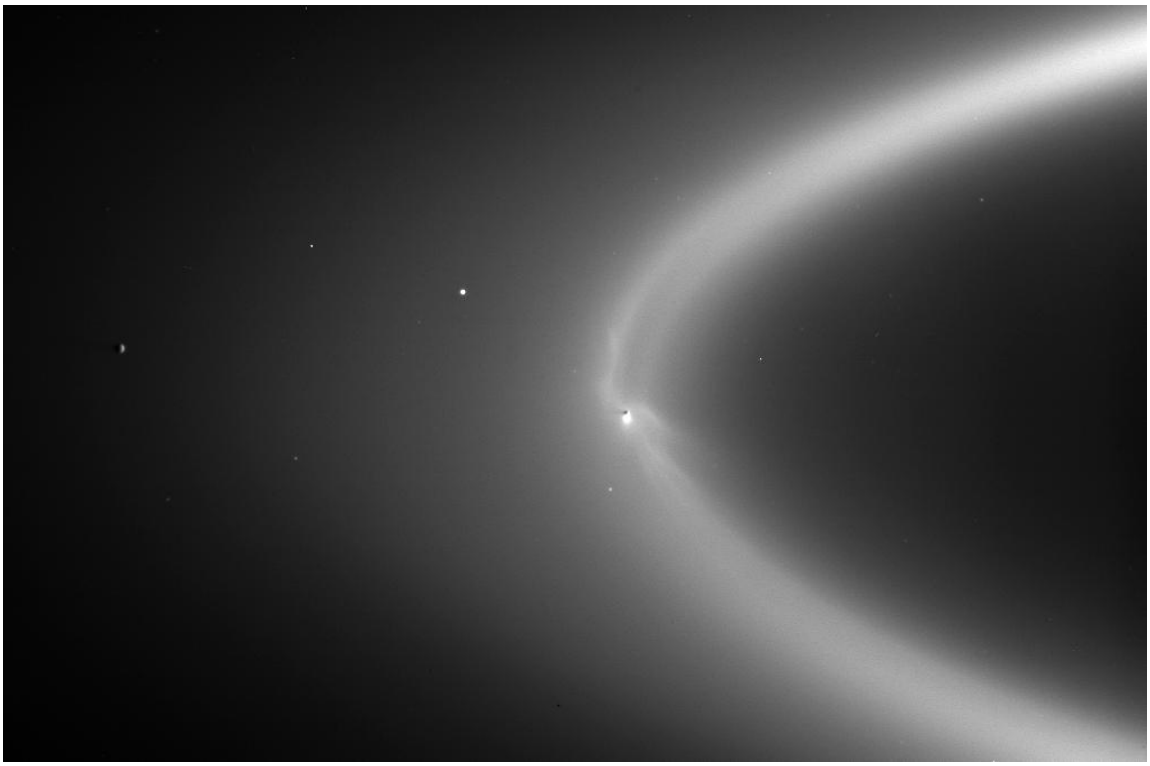

Figure 1.11: The Saturn's large diffuse E-ring, which is formed from micron and sub-micron, and Saturn's moon Enceladus, which is the dark spot inside the bright flare. The bright flare is the plume from its south pole. Image credit: NASA/JPL/Space Science Institute

Planetary dust is destroyed by a range of processes, such as erosion due to sublimation and plasma sputtering, or collisions with moons, planets or rings. Planetary dust can also evolve into interplanetary dust, after escape from the gravity of the planetary central body. Therefore, observed planetary dust particles in a system indicate an ongoing or recent source, to refresh and sustain the population.

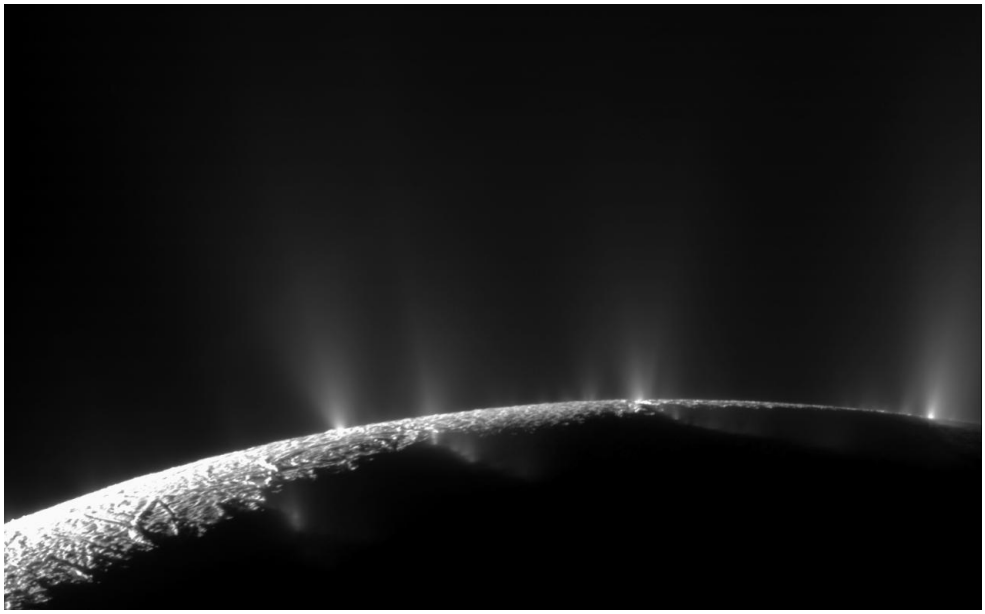

Figure 1.12: Cryovolcanoes erupting from fractures in the surface of Enceladus, the main sources of Saturn's E-ring material. Image credit: NASA/JPL/Space Science Institute

1.2 The Cassini-Huygens mission

The Cassini-Huygens mission was an international joint endeavor, mainly involving NASA, the European Space Agency (ESA) and the Italian space agency (ASI). The major aim of this mission was to investigate the Saturnian system: the planet Saturn, its moons and rings. The Cassini-Huygens spacecraft was composed of two probes: The Cassini orbiter and the Huygens lander, designed to measure the atmosphere and surface of Saturn largest moon, Titan. The spacecraft was launched on October 15, 1997, with a gravity assist from Jupiter in 2000 supplying speed for its journey to Saturn, and finally arrived at the Saturnian system on June 30, 2004 (Fig. 1.13). On December 24, 2004, the spacecraft released the Huygens lander at Saturn's moon Titan. After 13 years of orbiting Saturn and studying the Saturnian system, Cassini orbiter ended its mission by diving into Saturn's atmosphere finally on September 15, 2017 (Dougherty et al. 2018).

The scientific objectives of the Cassini-Huygens mission involved Saturn, its magnetosphere, ring system, satellites:

Saturn: To study the physical properties, structure, composition, and dynamics of its atmosphere; Saturn's rotation rate and internal structure.

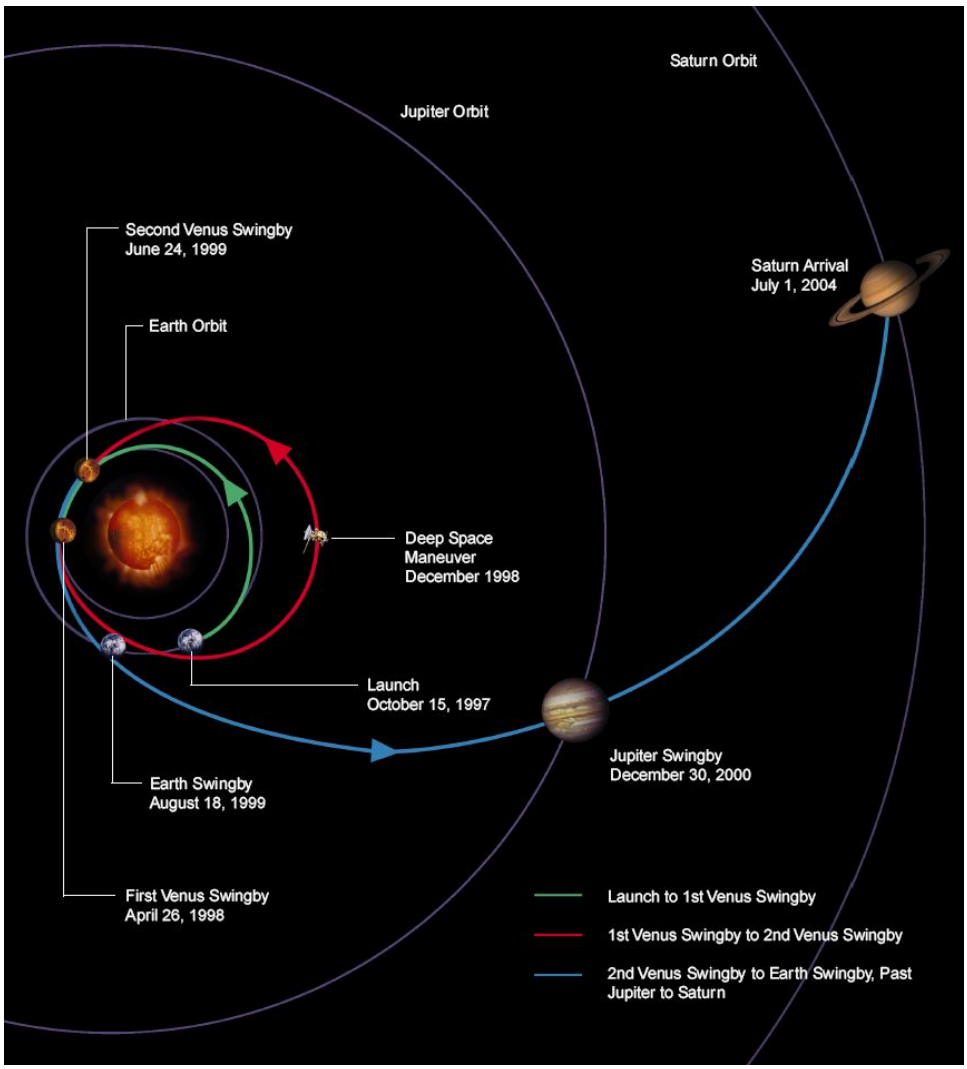

Figure 1.13: Cassini-Huygens spacecraft's trajectory from Earth to Saturn. Image credit: NASA/JPL

The magnetosphere: To observe the configuration and temporal variability of Saturn's magnetosphere and study the interactions between the magnetosphere and ionosphere as well as satellites.

Saturn's rings: To investigate the composition and size distribution of ring material; determine the structure and dynamics of the rings as well as the age of the rings; explore the interaction between the rings and the embedded moons, Saturn's magnetosphere, ionosphere, and atmosphere.

Icy satellites: To map their surface geologies and compositions and determine their geological histories; Determine their bulk compositions, internal structure and physical processes.

Titan: To determine the structure, composition of Titan's atmosphere as well as seasonal changes; to determine the topography, composition and physical state of the surface and infer Titan's internal structure;

To achieve these Scientific objectives the Cassini orbiter and Huygens probe were equipped with the following instruments: (Cassini-Huygens-Group 2018)

Cassini orbiter:

- Remote Sensing instruments (Ultraviolet, visible, Infrared and microwave):

- Ultraviolet imaging spectrograph (UVIS): To capture images of the ultraviolet light reflected off objects to analyze their structures and compositions.

- Visible and infrared mapping spectrometer (VIMS): To capture images of visible and infrared light to analyze the compositions, temperatures and structures of moons' surfaces, the rings, and the atmospheres of Saturn and Titan.

- Composite infrared spectrometer (CIRS): To measure the infrared radiation emitted and reflected from atmospheres, rings and surfaces in the Saturn system to determine their temperatures, thermal properties, structure and compositions.

- Imaging science subsystem (ISS): To capture images in visible light, infrared and ultraviolet (wavelength ranging from 0.2 to 1.1 μm) of Saturn, its rings, and its moons with both a wide-angle camera (WAC) and a narrow-angle camera (NAC).

- Radio science subsystem (RSS): To study the gravity fields around objects, the structures and compositions of atmospheres, surface properties of objects, as well as structures and particle sizes of rings through analyzing the radio signals altered by objects between Cassini and the Earth.

- Radar: To map Titan's surface by measuring reflected radar waves which is

able to penetrate the thick haze surrounding Titan; as well as to receive radio waves emitted by Saturn or its moons.

In situ instruments (fields, particles and waves):

- Ion and neutral mass spectrometer (INMS): To measure in situ the composition of charged particles (protons and heavier ions) and neutral particles (atoms and molecules) with a quadrupole mass spectrometer.

- Cosmic dust analyzer (CDA): To measure in situ the size, speed, charge and composition of dust grains.

- Radio and plasma wave instrument (RPWS): To determine the electric and magnetic fields, the electron/ion density, temperature in the interplanetary medium and Saturn's magnetosphere;

- Cassini plasma spectrometer (CAPS): To measure in situ the charge, flux and composition of charged particles.

- Magnetospheric imaging instrument (MIMI): To detect the energies, compositions, and populations of energetic charged particles and neutral atoms, as well as to capture images of the particles trapped in Saturn's magnetosphere in order to determine the configuration and dynamics of the magnetosphere and its interactions with the solar wind, Saturn's atmosphere.

- Dual technique magnetometer(MAG): To determine the strength and direction of Saturn's magnetic fields.

Huygens Lander:

- Descent Imager/Spectral Radiometer (DISR): To measure and visualize the radiant flux inside Titan's atmosphere.

- Huygens atmospheric structure instrument (HASI): To measured the physical properties and structure of Titan's atmosphere.

- Gas chromatograph and mass spectrometer (GC/MS): To measure the composition of Titan's atmosphere.

- Aerosol collector pyrolyzer (ACP): Sample aerosol particles from Titan's atmosphere and prepare and inject the samples into the GC/MS instrument for analysis.

- Surface science package (SSP): To determine the physical properties of Titan's surface.

- Doppler wind experiment (DWE): To measure the wind speed in Titan's atmosphere

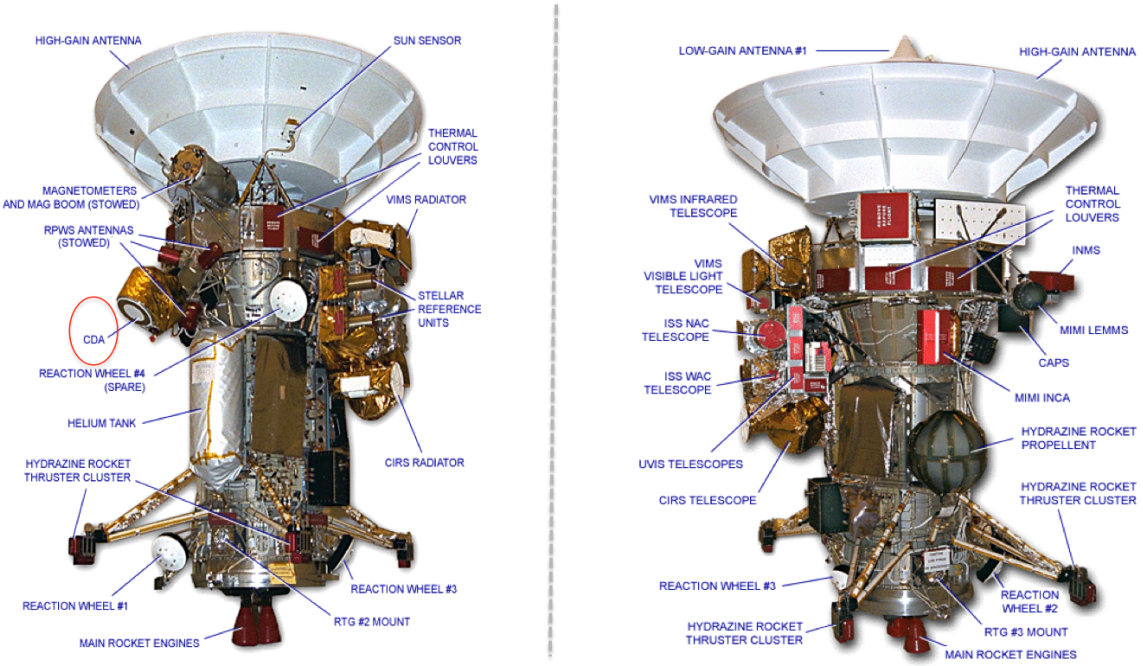

Figure 1.14: The Cassini orbiter with the onboard instruments. (Left): Plus Y side of the orbiter. (Right): Minus Y side of the orbiter. The Cosmic Dust Analyzer (CDA) is indicated on the left subimage. Image credit: NASA/solarsystem

1.3 The Saturnian system

Saturn is the sixth planet from the Sun. Its orbit is elliptical with an eccentricity of 0.053 (NASAwebsite 2019d) and a semi-major axis of approximately 9.58 AU (NASAwebsite 2020). It is the second-largest planet, in both mass and volume, after Jupiter, but with the lowest average density (0.687 g/cm^3) (NASAwebsite 2019d), even lower than that of liquid water.

Saturn is primarily composed of hydrogen and helium and is classified as a gas giant. However, despite the name, gas giants do not mainly consist of gas; on the contrary, the mass of the gaseous phase is only a small fraction of the total mass. For Saturn, only the outer 0.1 % of its total mass is in the gaseous phase, because at a certain depth the density of hydrogen reaches 0.01 g/cm^3, at which point the gaseous hydrogen became a non-ideal fluid (Fortney & Nettelmann 2009).

Both the temperature and pressure rise with increasing depth inside Saturn. At

its center, there is probably a core of iron and nickel surrounded by rocky material (silicon, oxygen and other compounds). This core is enveloped by a thicker layer of metallic hydrogen followed by a layer of liquid molecular hydrogen and liquid helium (Fortney et al. 2018). The outermost layer is its atmosphere, spanning approximately 1000 km and consisting mainly of molecular hydrogen and helium blanketed with clouds composed of ammonia crystals (upper clouds), or ammonium hydrosulfide or water (deeper clouds) (Martinez 2007).

Saturn's Magnetosphere

Saturn has an highly axisymmetric intrinsic magnetic field, probably generated by currents in the liquid metallic-hydrogen layer, called an interior metallic-hydrogen dynamo (Gombosi & Ingersoll 2010) (Stanley 2010). Its strength at the equatorial surface is 0.20 Gauss (20 μT) (Smith et al. 1980), slightly weaker than the magnetic field strength at the Earth's magnetic equator (around 0.05 Gauss) and one twentieth of that of the field around Jupiter (Smith et al. 1980). The magnetic field interacts with the solar wind and forms Saturn's magnetosphere, in which the motion of charged particles are dominated by Saturn's magnetic field of Saturn instead of the solar magnetic field.

The magnetopause, the boundary between Saturn's magnetosphere and the solar wind, is located at a distance of 16 to 27 Saturn radii from the Saturn's center (Gombosi et al. 2009). Therefore Enceladus, the focus of this thesis, is enveloped by Saturn's magnetosphere. However, Titan, Saturn's biggest moon, at the outermost edge of the E-ring, is sometimes outside the magnetosphere (Fig. 1.15).

Saturn's magnetosphere is populated by plasma originating from the solar wind, Saturn's ionosphere, the rings and the icy moons. Amongst those plasma source, Enceladus is the most relevant one by far. The plasma composition in Saturn's inner magnetosphere is dominated by hydronium ions (H_3O^+), water group ions (O^+, H_2O^+, OH^+), HO_2^+, O_2^+, and N^+ (Sittler et al. 2008). The Cassini mission discovered that Enceladus is the major source of these species: neutral water vapor is ejected into space from the geysers on Enceladus' South Polar Terrain (SPT) and subsequently ionised by charge exchange, electron impact ionization and photoionization (Sittler et al. 2008). The plasma composition in Saturn's outer magnetosphere is dominated by protons, originating from the solar wind and Saturn's ionosphere (Gombosi et al. 2009). Via the interchange instability mechanism, the plasma gradually moves outward and eventually escapes out of the magnetosphere (Gombosi et al. 2009). As on Earth, interaction between the solar wind and Saturn's magnetosphere also causes aurorae on the polar regions of Saturn (Galland Kivelson

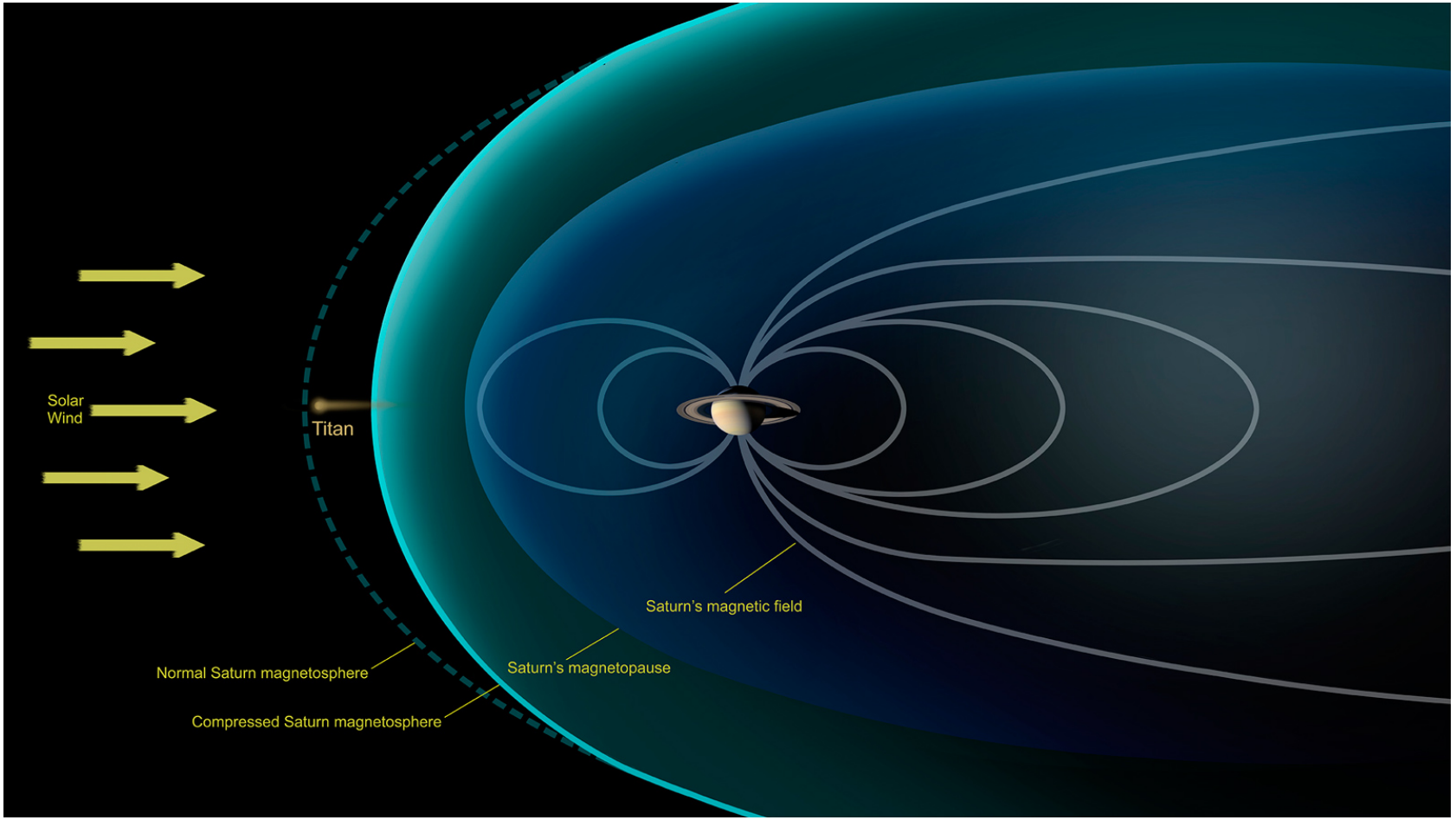

Figure 1.15: The distance of magnetopause to Saturn's center varies from 16 to 27 Saturn radii with orientation and time (Gombosi et al. 2009). Titan spends about 95 percent of the time within Saturn's magnetosphere. However, during a Cassini flyby in Dec. 2013, Titan happened to be on the sun-facing side of Saturn when a powerful surge in the solar wind caused by a solar outburst arrived and compressed the sunward side of Saturn's magnetosphere so that the magnetopause of Saturn was pushed inside Titan's orbit. Therefore, Titan was outside of the protection of Saturn's magnetosphere and thus exposed to the solar wind. Image credit: NASA/JPL-Caltech

2005).

Saturn's ring system and moons

Saturn possesses the most extensive ring system in the Solar System. These rings consist of small particles, ranging in size from less than a micrometer to over ten meters (Ohtsuki et al. 2020).

In 1859, James Clerk Maxwell firstly demonstrated that the rings are composed of numerous individual small particles, independently orbiting Saturn, instead of solid or continuous fluid structures, which would be unstable (Maxwell 1859; Ogilvie 2008). In 1895 his idea was proved through analyzing the spectroscopic features of the rings (Ogilvie 2008).

The main rings are, in decreasing distance from the Saturn, the broad A ring and B ring and then the narrow C ring. These dense main rings are primarily composed of particles ranging in size from 1 cm to 10 m (Marouf et al. 1983), the composition of which is mainly water. The extremely faint D Ring is just inside the C ring and closest to the planet. The narrow F Ring is just outside the A Ring. See the natural color mosaic of the unilluminated side of Saturn's inner rings taken by Cassini's narrow-angle camera on May 9, 2007 at url: https://photojournal.jpl.nasa.gov/figures/PIA08389_fig1.jpg.

Outside these inner rings are much fainter outer rings, named G and E (from inside to outside). The diffuse E-ring extends from Mimas' orbit to Titan's orbit, or from about 3.1 R_S to 20 R_S (Saturn's radius, R_S = 60330 km), and is the focus of this work. All the rings are separated by gaps, where the particle number density and thus brightness drops sharply. The largest of these gaps is the Cassini Division separating the A and B rings (Fig. 1.16).

Far beyond these rings is a tenuous and much larger ring, named the 'Phoebe ring' after its probable source moon. Radially, it extends from at least 128 R_S to 207 R_S and its vertical thickness is around 40 R_S (Verbiscer et al. 2009). Despite its huge size, the Phoebe ring is so tenuous that it is barely visible at optical wavelengths. The Phoebe ring is also dynamically unusual, tilted at an angle of 27° to Saturn's equator, with its particles in retrograde orbits (Verbiscer et al. 2009).

Saturn has numerous moons and they vary in mass, size, shape and orbit. The smallest moons are just 'moonlets' less than 1 kilometer in diameter, but the largest moon, Titan, is larger than the planet Mercury and the second largest moon in our Solar system after Jupiter's Ganymede. Over sixty Saturnian moons

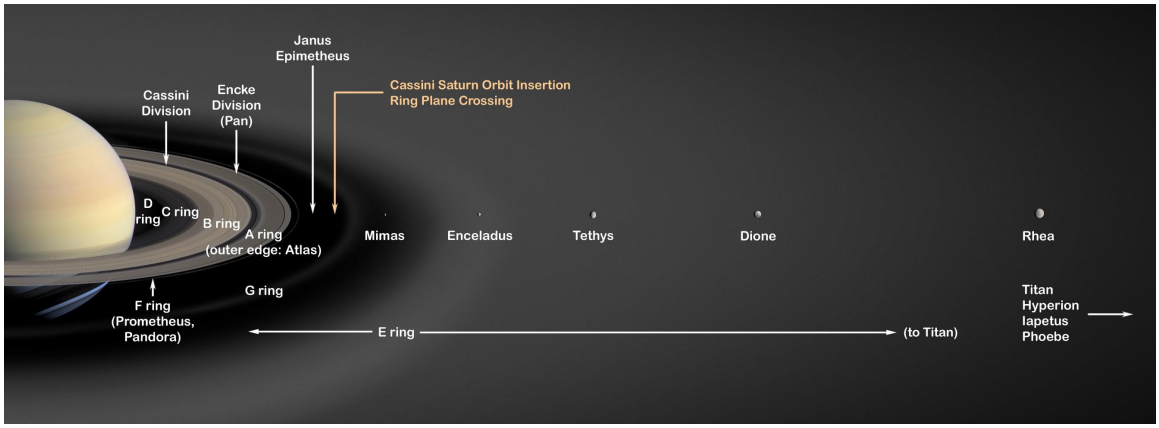

Figure 1.16: An artist's concept of Saturn's rings and major icy moons (url: https://solarsystem.nasa.gov/resources/12669/saturns-rings/). Image credit: NASA/JPL

have confirmed orbits. Among them, only seven moons are large enough to be spherical or near-spherical in shape. Of these, two in particular are notable for their astrobiological potential: One is Titan, which has a complex atmosphere consisting mostly of nitrogen ($\sim 95\%$) and methane ($\sim 5\%$), as well as experiencing Earth-like phenomena, such as rain and wind, and landscapes such as rivers and hydrocarbon lakes (Barnett 2020). Another is Enceladus, whose plume chemical composition shows comet-like features (Waite Jr et al. 2009; Waite et al. 2011). In addition, aqueously formed species, such as salts, silica and H_2, detected in Enceladus' plume indicate aqueous alteration of rocks, such as dissolution, hydration, oxidation, in Enceladus' history (Zolotov et al. 2011). Importantly, Enceladus has a global ocean below its surface (Patthoff & Kattenhorn 2011; Thomas et al. 2015) and there is evidence for ongoing hydrothermal activities on the ocean floor (Hsu et al. 2015).

The ring system and some of the moons are interrelated: Some are sources of ring materials, some are sinks and some are responsible for the formation of ring gaps. Importantly, there are several icy moons embedded in the E-ring: Mimas ($r_M = 3.07\ R_S$), Enceladus ($r_E = 3.95\ R_S$), Tethys ($r_{Th} = 4.88\ R_S$), Dione ($r_D = 6.25\ R_S$), Rhea ($r_R = 8.73\ R_S$), as well as the distant Titan ($r_{Ti} = 20.25\ R_S$) (Kempf et al. 2018), which are covered by icy dust or snow and can exchange material with E-ring (Le Gall et al. 2019). Amongst them, Enceladus is the major source of E-ring dust and the icy particles originating in the plume of Enceladus supply almost the entire E-ring (Kempf et al. 2018).

1.4 Saturn's E-ring, Enceladus and its subsurface ocean

Saturn's E-ring, its moon Enceladus, and the moon's subsurface ocean are intimately connected, and will be discussed in turn in the following subsections

1.4.1 E-ring

The Saturn's E-ring was firstly detected by Earth-based optical observations in the red spectral region at Allegheny Observatory during Earth's crossing Saturn's ring plane in 1966 (Feibelman 1967). However, scientists only obtained detailed information on the E-ring when the Cassini spacecraft arrived at the Saturn system in 2004. In this section, I will introduce firstly the historical observations before Cassini mission and then briefly cover the Cassini observations.

Pre-Cassini observations of the E-ring

Observations before the Cassini mission were mainly remote observations, including ground based observations, such as by the 1.8 m Perkins Telescope in Lowell Observatory (Baum et al. 1981) and by the 10 m W. M. Keck telescope in Mauna Kea Observatories (De Pater et al. 1996, 2004), and space telescope observations, such as by the Hubble Space Telescope (HST) (Nicholson et al. 1996). Some early spacecraft measurements, such as Voyager imaging during their flybys, were also performed (Stone & Miner 1981, 1982). Those observations produced the following information:

Earlier observations indicated the E-ring showing blue photometric colour at optical wavelengths, which can be explained in terms of Mie scattering by a sharp size distribution of ice spheres with an effective diameter of 2 to 2.5 μm (Pang et al. 1984). The blue color was confirmed by the observations of HST (Nicholson et al. 1996) and Keck telescope (De Pater et al. 2004) during Earth's ring plane crossing in August 1995. This indicated the E-ring consists of predominantly micron-sized ice particles, and implied those ice particles were created from liquid water.

HST observations of Saturn's ring system during the crossings in 1995 indicated that the E-ring particle size seems to have a spatially uniform distribution and the measured vertical thickness of E-ring gradually increases with distance from Saturn, interrupted by a local minimum ($\sim$ 8000 km) near the orbit of Enceladus ($\sim$ 4 R_S

from Saturn), and reaches $\sim$ 15000 km at 7.5 R_S from Saturn (Nicholson et al. 1996). The edge-on brightness profile of the E-ring obtained by ground-based observations in March 1980 showed a sharp peak, corresponding to the maximum density of ring material, in the vicinity of the orbit of Enceladus at about 4 R_S (Baum et al. 1981). This, coincident with the minimum vertical ring thickness, suggested Enceladus could be the dominant source of the E-ring materials. A model explaining the origin of Saturn's E-ring indicated that high-velocity collisions of E-ring particles with embedded satellites generate ejecta to supply E-ring with particles and the Enceladus is the primary source of E-ring ring material (Hamilton & Burns 1994).

Near-infrared (1.24 to 2.26 μm) images of Saturn's E-ring obtained with the W.M. Keck telescope in August 1995 showed the icy moon Tethys could be a secondary source of the E-ring material (De Pater et al. 2004).

Cassini Observations of the E-ring

The Cassini spacecraft, as the first space probe orbiting Saturn, offered scientists opportunities for in situ observations of the E-ring. It carried several instruments, which were able to measure the E-ring in different ways:

- The Imaging Science Subsystem (ISS)

  The Imaging Science Subsystem (ISS) onboard the Cassini orbiter consisted of two framing cameras: a narrow angle camera and a wide angle camera (Barnett 2013).

  The following descriptions about the process to obtain the mosaic of the Saturn system in this paragraph are from: https://photojournal.jpl.nasa.gov/catalog/PIA17172. On July 19, 2013, the Cassini orbiter flew into Saturn's shadow so that its Imaging Science Subsystem (ISS) could acquire a panoramic mosaic of the Saturn system using the unique viewing geometry, during which the sun was blocked by Saturn and the grains within the rings scattered sufficient solar radiation to make details in the rings visible. Finally, a natural-color mosaic was created using 141 wide-angle images taken with different spectral filters. It can be seen that at optical wavelengths the E-ring appears blue (Fig. 1.17). This blue color is consistent with previous pre-Cassini observations, which indicated that this color was produced from micron-sized icy particles with a very narrow size distribution (Pang et al. 1984).

- Cosmic Dust Analyzer (CDA)

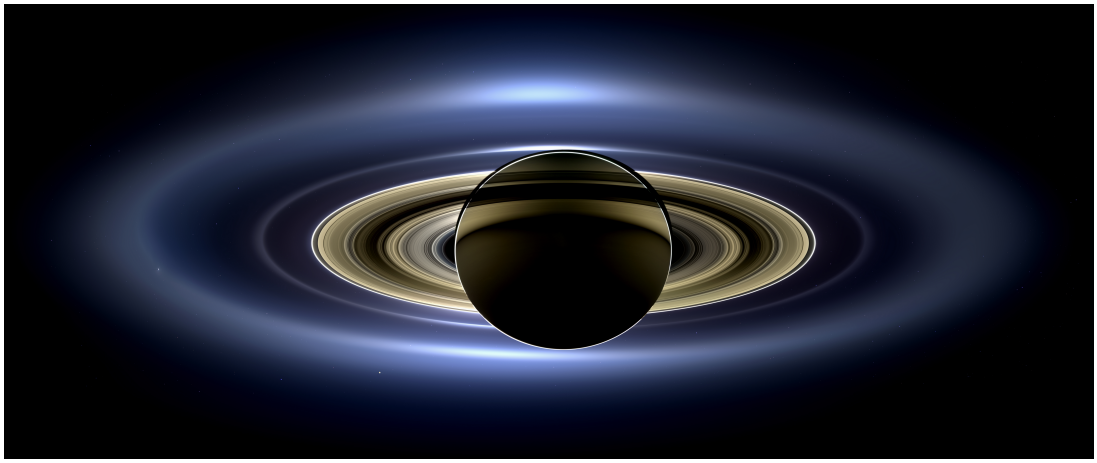

Figure 1.17: This is a natural-color view of Saturn, its ring system and some of its moons. The outermost blue ring in this image is the E-ring. This image was taken by the Cassini Orbiter and spans about 651591 kilometers. Image credit: NASA/JPL-Caltech/SSI

There were two independent components in the Cosmic Dust Analyzer (CDA) instrument, which perform the dust measurements: the High Rate Detector (HRD) and the Dust Analyzer (DA). The HRD could quantitatively measure particle flux, and the mass distribution of the E-ring and could work well in dust rich environments due to its high counting rate capability (Srama et al. 2004), but it was only sensitive to particles larger than about 1 μm, depending on their impact velocity. The DA could provide much more information about a dust particles traversing its entrance grid system and/or impacting on its impact target, such as the electric charge, the impact direction, the impact speed, mass and, most important of all, the chemical composition. However, it had a much lower counting rate capability and thus could work only in low number density dust environments (Srama et al. 2004). In the inner core of the E-ring, where the DA was saturated, HRD measurements implied the DA dust impact rates exceeding 1000 per minute (Kempf 2008).

The first in situ direct compositional measurement of the Saturn's E-ring during Cassini's first E-ring crossing in October 2004 confirmed that the particles in E-ring are predominantly composed of water ice, with minor exceptions (Hillier et al. 2007a). Further analysis of the E-ring in situ CDA data indicated that besides the almost pure water ice particles there are also a population of organic rich ice particles (Postberg et al. 2008; Khawaja 2017; Postberg et al. 2018b) and a population of salt rich ice particles (Postberg et al. 2009b) in the E-ring.

Using the HRD data of CDA produced during Cassini's close flyby of Enceladus on 14 July 2005, combining with the evidence for geophysical activities near Enceladus' south pole revealed by other CDA instruments, Spahn et al. (2006a) confirmed that the major source of the E-ring dust is the plume ejected from the SPT of Enceladus.

Cassini also found nanometre-sized silica particles in E-ring, which imply ongoing high-temperature ($> 90°C$) hydrothermal reactions in the source of the particles, the subsurface ocean of Enceladus (Hsu et al. 2015).

- Radio and Plasma Wave Science (RPWS)

  'The Radio and Plasma Wave Science, or RPWS, instrument detected radio and plasma waves, as well as the plasma medium through which Cassini passed, using a suite of antennas and sensors.' - quoted verbatim from a NASA webpage with the title 'Radio and Plasma Wave Science (RPWS)' at: https://solarsystem.nasa.gov/missions/cassini/mission/spacecraft/cassini-orbiter/radio-and-plasma-wave-science/.

  Impacts on a spacecraft body can release a cloud of charged particles and thus result in voltage impulses at the input to the electric antenna preamplifiers of the RPWS, so that the rate of impacts can be measured by the RPWS (Kurth et al. 2006; Gurnett et al. 1983). In addition, the estimated charge yield of the impact combining with other considerations (e.g. the assumed impact speed) can be used to estimate the mass and size of the impact grains (Kurth et al. 2006). Therefore, the RPWS instrument could undertake in situ studies of the E-ring.

  There were some advantages for RPWS in detecting dust compared with the CDA. Firstly, the RPWS has a much larger collecting area than CDA since the entire spacecraft worked as a dust impact target (Kurth et al. 2006). More importantly, unlike the CDA, which needed favorable spacecraft attitudes to perform the measurements, the RPWS did not rely on a specific spacecraft orientation to detect dust (Kurth et al. 2006). Therefore, it was possible for RPWS to detect dust continuously to some extent through the orbital tour and thus to obtain a larger picture of the dust distribution in the E-ring (Kurth et al. 2006).

  Based on the results of previous studies that the E-ring is mainly composed of tiny water ice grains, Kurth et al. (2006) concluded the typical size of grains detected by the RPWS were a few microns in radius. In addition, the structure of the E-ring was also evaluated: Radially, the number densities of ice grains reach their maximum in the range of 0.0005 m^{-3} near the orbit of

Enceladus (Kurth et al. 2006). This is in agreement with previous optical measurements and supports the suggestion that Enceladus is the major source for E-ring grains (Kurth et al. 2006). The vertical dust number density profile of the E-ring near the orbit of Enceladus obeys a Gaussian distribution with its maximum near the geometric equator and a scale height of about 2800 km, over which the number density drops by a factor of e (~ 2.71828) despite some non-Gaussian variation near the peak number density (Kurth et al. 2006).

The electrostatic potential of E-ring particles

Both the charge-sensitive grid system of the CDA, and the RPWS instrument itself, were able to detect the charges on the impacting micron-sized particles, and both of their investigations show that all the E-ring particles detected inside the orbit of Saturn's moon Rhea (8.73 R_S from Saturn center) were negatively charged, while particles outside Rhea's orbit were found to be on a positive potential of about 3 V (Kempf et al. 2006).

The size of E-ring

The diffuse E-ring is the second outermost ring after the Phoebe ring. The in situ CDA measurements during the first year of Cassini's orbital tour (2004 - 2005) found that the E-ring particles extends outwards at least to the orbit of Titan (Srama et al. 2006). The in situ CDA measurements during the Cassini's F-ring orbits showed the E-ring particles extends inwards almost all the way to the F-ring (Linti 2018). Therefore, the E-ring is so extremely extensive that it encompasses many moons or moonlets, six of which are icy monns: Mimas (3.07 R_S), Enceladus (3.95 R_S), Tethys (4.88 R_S), Dione (6.25 R_S), Rhea (8.73 R_S), and Titan (20 R_S) (Kempf et al. 2018).

The short lifetime of the E-ring particles

The micron-sized E-ring particles' lifetimes are rather short compared to those of main ring particles. The lives of E-ring particles come to the end due to several factors.

Firstly, sputtering erosion of E-ring particles by magnetospheric ions (plasma) leads the loss of mass of E-ring particles. If staying near the Enceladus orbit ($\sim 3.5 - -6.0 R_S$ from Saturn center.), the characteristic lifetimes of micrometer-sized ice particles would be approximately 50 years and that of the ice particles of $\sim 0.1 \mu m$

size is only a few year (Jurac et al. 2001; Kempf et al. 2018). However, the orbits of E-ring particles evolved continually due to the combined effects of planetary oblateness, radiation pressure, plasma drag and the Lorentz force (Juhász et al. 2007; Kempf et al. 2018). As a results, the E-ring particles slowly drift outward (Dikarev 1999). As they moved away from Saturn, the plasma density in space decreases and thus the sputtering erosion gets weaker, so these E-ring particles' characteristic lifetime due to sputtering gets prolonged (Horányi et al. 2008).

Secondly, the dynamical evolution of the particles orbits could eject the E-ring particles out of the E-ring (Horanyi et al. 1992; Juhász & Horanyi 2002; Juhász et al. 2007; Kempf et al. 2018). In addition to the Saturn's gravitation field, E-ring particle dynamics is also affected by other forces. Dust particles are charged by collection of ion and electrons from plasma, impacts with other dust particles, secondary electron emission and the photoelectric effect caused by solar UV photons (Grün et al. 1984). Because they are charged, they are accelerated by the Lorentz Force due to Saturn's magnetic and co-rotation electric field. Plasma drag can also accelerate the E-ring particles because they are travelling slowly than the plasma, which tends to co-rotate with planetary spin as the co-rotating magnetosphere sweeps the plasma along. Radiation pressure and gravity also play a role in the motion of the E-ring particles (Juhász & Horanyi 2002). Besides, the sputtering erosion of E-ring particles particles in the magnetosphere leads to changes in the ratios of forces acting upon them, as well as their eventual distribution within (or without) the Saturnian system.

Moreover, some dynamics studies suggest particles within a certain initial size range could attain high eccentricities at early stage due to the solar radiation pressure and thus rapidly collide with main rings or Saturn due to the rapid decrease of their pericenters (Horanyi et al. 1992; Juhász et al. 2007; Kempf et al. 2018).

At last, the moons engulfed in the E-ring are also important sinks for the E-ring particles, which continually bombard and deposit on these moons(Kempf et al. 2018).

In short, there are four major loss mechanisms for E-ring particles (Juhász et al. 2007; Kempf et al. 2018): 1) Sputtering erosion by the magnetospheric plasma the particles are exposed to; 2) Ejection from the E-ring - forming high speed streams of particles leaving Saturn, after acceleration by Saturn's magnetosphere and plasma drag, 3) Moving inward and hitting the main rings or Saturn; 4) Collisions with the embedded moons.

The lifetime of a specific particle in the E-ring varies with the particle's own properties, such as its initial size, initial velocity, and orbital eccentricity (Juhász et al. 2007; Kempf et al. 2008). The E-ring particle dynamics studies of Juhász

et al. (2007) suggest that particle lifetimes are expected to be less than 200 years. According to the estimation of Horányi et al. (2008), the lifetime of a micron sized particle in E-ring could be expected to 600 years.

The short grain lifetimes imply that those currently in orbit are 'fresh', and the particles are therefore expected to retain a lot of chemical information about their source - Enceladus.

1.4.2 Enceladus and its subsurface ocean

Enceladus

Enceladus is the sixth-largest moon of Saturn. Its mass is $\sim 1.08 \times 10^{20}$ kg (Jacobson et al. 2006). Its effective radius derived from ISS images is of 252.1 $\pm$ 0.2 km (Porco et al. 2006), about 0.15 times that of Earth's moon. Based on the mass and the effective radius of Enceladus, Porco et al. (2006) computed the mean density of Enceladus is $1608.3 \pm 4.5\,\mathrm{kg\,m^{-3}}$. This density implies it has a rocky core. Enceladus orbits Saturn at a mean distance of 3.95 R_S from the Saturn's center with orbital period of 32.9 hours (1.37 days). Enceladus is tidally locked with Saturn, i.e. rotating synchronously with its orbital period, keeping the same face toward Saturn (Stark et al. 2018).

Enceladus' 2:1 mean-motion orbital resonance with Dione maintains an orbital eccentricity of 0.0047. This small eccentricity results in tidal deformation of Enceladus, with the resulting energy dissipation as the major heat source for Enceladus' geologic activity (Běhounková et al. 2012; Choblet et al. 2017). Libration (Hurford et al. 2009) or obliquity heating (Tyler 2009) (although contested - e.g. (Chen & Nimmo 2011)) could provide Enceladus with an additional heat source. Besides, there could be also chemical heating, from serpentinisation, as a minor but possible heat source (Nissen et al. 2015). Enceladus' surface is composed mainly of water ice (Postberg et al. 2018a). The young and relatively crater-free surface, especially in the southern hemisphere, implies Enceladus is geologically active (Nimmo & Porco 2014).

Between February 2005 and December 2015 the Cassini orbiter made 23 flybys of Enceladus, with closest approaches ranging from $\sim$ 25 km (E5, in October 2008) to $\sim$ 4999 km (E22, in December, 2015), to carry out measurements of the properties of Enceladus (Henin 2018). A large amount of information about surface of Enceladus and the plume erupting from the SPT was obtained or confirmed: 1) The surface is dominated by water ice with some organics and CO_2 coincident with prominent fractures in the SPT, and NH_3 might be general present (Postberg et al.

2018a); 2) There is a tenuous atmosphere around Enceladus filled with water-ion plasma (Porco et al. 2006); 3) The landscape near the south pole is almost free of impact craters, and littered with house-sized ice boulders(Barnett 2018; Porco et al. 2006); 4) Four prominent $\sim$ 130 km long fractures named 'Tiger Stripes' cross a shallow basin centred on the south pole (Fig. 1.18) (Porco et al. 2006); 5) The region south of $\sim 55°$S latitude is circumscribed by an continuous chain of twisting fractures and ridges (Fig. 1.18) (Porco et al. 2006); 6) The SPT is anomalously warm and has the highest temperatures measured at/near the surface of Enceladus, possibly up to 197 K (Goguen et al. 2013), coincident with the tiger stripes, indicating endogenic heat sources beneath the SPT; 7) Plume of water vapor and icy particles, fed by narrow jets, emanate from the SPT of Enceladus (Figure 1.12) and some of these icy particles are ejected into space feeding the E-ring (Kempf et al. 2010, 2018); 8) Molecular hydrogen, a sign of water-rock reaction through hydrothermal processes and thermodynamic disequilibrium in Enceladus' ocean, exists in the Enceladus plume (Waite et al. 2017).

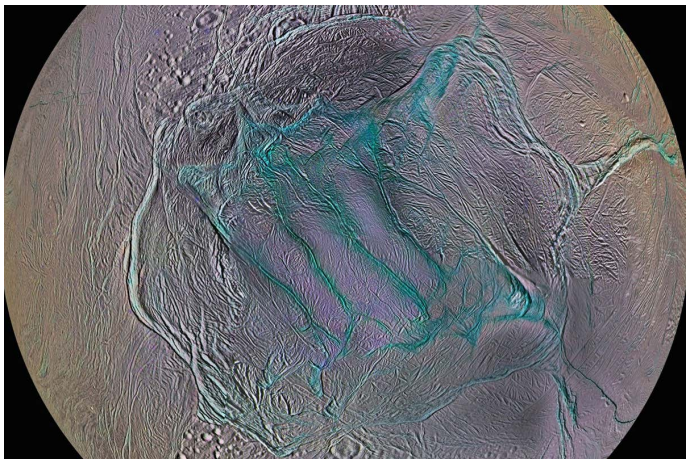

Figure 1.18: Tiger stripes in the South Polar Terrain (SPT) circumscribed by a continuous chain of twisting fractures and ridges, using a false color scheme in which fractured areas appear blue. Image credit:NASA/JPL-Caltech/SSI/Lunar and Planetary Institute, Paul Schenk (LPI, Houston)

The Cassini Plasma Spectrometer (CAPS) detected singly charged nanometer sized grains in the Enceladus plume during E3, E5, E7, E17, and E18 flybys, and the negative grains dominate the positive grains (Dong et al. 2015).

Enceladus' subsurface ocean

A model was proposed in 2008 to explain the formation of icy particles inside Enceladus. According to the model, the icy particles arise from condensation and growth of water vapor in channels of variable width. The large flux of particles suggest there must be liquid water below Enceladus' south pole (Schmidt et al. 2008). Furthermore, the Cassini spacecraft detected salt-rich icy particles in Saturn's E-ring and the plume of Enceladus, which can only originate from a subsurface ocean, currently or formerly in contact with a rocky core (Postberg et al. 2009b, 2011). This was the first solid evidence of an ocean beneath the SPT of Enceladus. Models aiming to explain the shape of Enceladus (Collins & Goodman 2007), thermal anomaly on the SPT (Tobie et al. 2008) and vapour production (Nimmo et al. 2007) also support the existence of a subsurface ocean beneath the SPT of Enceladus.

In 2014, through analyzing the Doppler data from three spacecraft flybys, the quadrupole gravity field of Enceladus was obtained, hinting that a regional subsurface ocean would be 30 km to 40 km under the SPT surface and extend up to southern latitudes of about 50° (Iess et al. 2014). However, other research suggested that the subsurface ocean is likely to be global instead of regional (Thomas et al. 2015; Patthoff & Kattenhorn 2011) and the ice shell over the subsurface ocean in the SPT also much thinner (Thomas et al. 2015). The first suggestion of a global subsurface ocean was made in 2011 by Patthoff and Kattenhorn's analysis of the fracture patterns in the SPT (Patthoff & Kattenhorn 2011).

In 2015 Thomas et al. (2015) determined the moon's precise rotation state by analyzing ISS measurements taken between January 2005 and April 2012 of control points (surface features, usually craters) on the surface of Enceladus, and found a forced physical libration of $\sim 0.120°$, which is too large for a rigid connection between Enceladus' surface and its core and thus implies a global ocean separating them. To explain the heat required preventing a subsurface ocean from freezing, Roberts (2015) proposed that the rocky core is likely unconsolidated and filled with interstitial ice and water. Čadek et al. (2016) developed an interior structure model composed of a rocky core and an ice shell, separated by an internal ocean, satisfying observed gravity, shape, and libration data. This model predicts that the core is 180-185 km in radius, the lower limit of the internal ocean density is 1030 kg/m^3, and the average thickness of the ice shell is between 18 and 22 km. The ice thickness in the south polar region could be less than 5 km (Čadek et al. 2016). In 2017 the microwave thermal emission of south polar terrain observed using Cassini's RADAR instrument also suggest that ice shell above the subsurface ocean at the south polar

region is only a few km thick (Le Gall et al. 2017).

Teolis et al. (2017) concluded that the gaseous component of Enceladus' plume varies dramatically and randomly in fluxes, speeds and densities both spatially along the tiger stripes and temporally between flyby observations, from the measurements of INMS during multiple low-altitude flybys through Enceladus' plume, in combination with the previous imaging and spectrographic results of ISS and UVIS. These spatiotemporal variabilities may result from tidal stress fields related to the subsurface structure and the complex physical processes of Enceladus (Teolis et al. 2017). Ingersoll et al. (2019) reported a time variability of the plume's solid particle mass flux and velocity over a range of timescales, by studying the plume's brightness data obtained by the ISS from 2005 to 2017 and attributed these variations to corresponding physical processes: A periodic diurnal variation is caused by the tidal stresses as Enceladus travels through its eccentric orbit. A periodic decadal variation is caused by the tidal stresses related to the orbital resonance with Dione. Aperiodic variations on timescales of months may be caused by ice build up and flow along the walls of the fissures connecting the inner ocean to the surface. The intricate spatial and temporal variabilities in both the gaseous component and solid component of Enceladus' plume provide very useful information for understanding the origin and mechanism of the plume as well as their physical and chemical relationship to the subsurface ocean (Teolis et al. 2017).

Although both the salt-rich ice grains in plume (Postberg et al. 2011) and E-ring (Postberg et al. 2009b), which will be discussed in detail in Chapters 4 and 5, and the estimated depth and thickness of the subsurface ocean (Čadek et al. 2016) imply the existence of rock-water contact or even rock–water interactions in regions surrounding the rocky core of Enceladus, the first solid evidence of ongoing hydrothermal activities came from the silica-rich, nanometer-sized stream particles originating from the Saturnian system (Hsu et al. 2015). These stream particles are interpreted as nanometer-sized SiO_2 (silica) particles, initially embedded in icy grains emitted from Enceladus' subsurface ocean and released through plasma sputtering erosion in Saturn's E-ring, to be finally accelerated by the co-rotating electric field and escape from the gravity of Saturn. The narrow size distribution (2 to 8 nanometers in radius) of the silica stream particles indicates ongoing high-temperature ($> 90°C$), high pH ($\sim 8 - 10.5$) and moderate salinity ($< 4\%$) hydrothermal reactions, with the hydrothermal products quickly transported from the rocky ocean floor by convection currents and escaping from Enceladus' ocean (Hsu et al. 2015). Further evidence for hydrothermal processes was provided by the discovery of molecular hydrogen in the Enceladus plume, detected by INMS during Enceladus flybys. Molecular hydrogen is a product of hydrothermal processes,

such as serpentinisation, and potentially provides a source of chemical energy for autotrophic microorganism (if present) (Waite et al. 2017).

Complex macromolecular organic material with molecular masses of over 200 atomic mass units has been detected in ice grains emitted from the subsurface ocean of Enceladus (Postberg et al. 2018b) and oxygen- and nitrogen bearing funtional groups are considered to exist in these macromolecular organic compounds (Postberg et al. 2018b). The discovery of the macromolecular organics in icy grains suggest the existence of a thin, refractory and insoluble organic-rich film on top of the oceanic water, where upwelling bubbles burst to produce organic nucleation cores - droplets or flakes of organic material. There are many ways to explain the formation of the macromolecular organics. They could arise from the accretion of organic-containing primordial material during the formation of the icy moon, or via synthesis from small molecular precursors during hydrothermal activities at the bottom of its subsurface ocean. Even synthesis by extraterrestrial life cannot be completely ruled out (Postberg et al. 2018b). Subsequently, low mass volatile organics, including amines, carbonyls, and aromatic compounds, were detected in the E-ring organic-bearing ice grains and these low mass organics could be precursors for hydrothermal abiotic synthesis of biologically relevant organic compounds (Khawaja et al. 2019).

The discovery of salt-rich icy grains, evidence of long term hydrothermal activity, existence of molecular hydrogen in the Enceladus plume and the evidence of the complex macromolecular organic material imply the internal ocean of Enceladus could be habitable for life (McKay et al. 2018). Choblet et al. (2017) built a model to explain the mechanism which produces the high heat power ($>$ 20 billion watts) required for the presence of a global ocean underneath the ice shell of Enceladus, the reduced ice-shell thickness in the SPT as well as the salty ocean and ongoing hydrothermal activity. This model indicates that the rocky core of Enceladus is porous and water-filled, inside which tidal friction generates more than 10 GW of heat, and water flows with temperatures exceeding 363 K, welling up and forming powerful (1–5 GW) hotspots at the seafloor, particularly at the south pole. The high temperature of the hot water flows favours intense water-rock interaction. The upwelling water flows transport hydrothermal products, which include life sustaining elements, from the core to the plume sources. The calculations predict endogenic activity in the core can be sustained for tens of millions to billions of years. The long timescale implies there could be enough time for life to originate and develop.

In this thesis, I will describe new discoveries about the chemical characteristics of the internal ocean water and discuss the astrobiological potential of Enceladus.

Chapter 2

Instruments and Methodology

2.1 The Cosmic Dust Analyzer

2.1.1 The structure of Cosmic Dust Analyzer

The Cosmic Dust Analyzer (CDA) was designed to in situ characterize micron and sub-micron cosmic dust particles. It consists of two independent subsystems: 1) the High Rate Detector (HRD); and 2) the Dust Analyzer (DA).

The High Rate Detector (HRD) is designed to quantitatively measure particle flux, corresponding to impact rates, and masses throughout the Saturnian system, using two separate polyvinylidene fluoride (PVDF) sensors. It has a high ($\leq 10^4$ s^{-1}) counting rate capability and thus can work well in dust-rich environments, such as ring plane and plume crossings (Srama et al. 2004).

The Dust Analyzer (DA) is designed to determine the electric charge, impact direction, impact speed, mass and chemical composition of individual dust particles, which enter the CDA. However, its counting rate capability is only 1 s^{-1}, and it is easily over-saturated in dust rich environments, such as during ring plane and Enceladus plume crossings (Srama et al. 2004; Kempf 2008).

The Dust Analyzer (DA) is composed of three subsystems: a charge sensing unit (QP detector), a classic impact ionization detector (IID) and a chemical analyzer (CA), which is actually a time-of-flight mass spectrometer (Srama et al. 2004):

The charge sensing unit (QP detector) is designed to measure the charges and velocities of charged dust particles entering the Dust Analyzer (DA), which are obtained by analysing the QP signal (Srama et al. 2004). It mainly consists of four

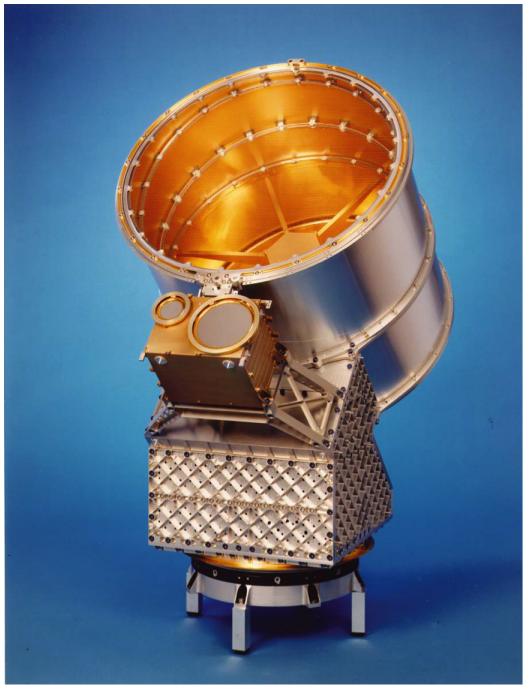

(a) The Cosmic Dust Analyzer

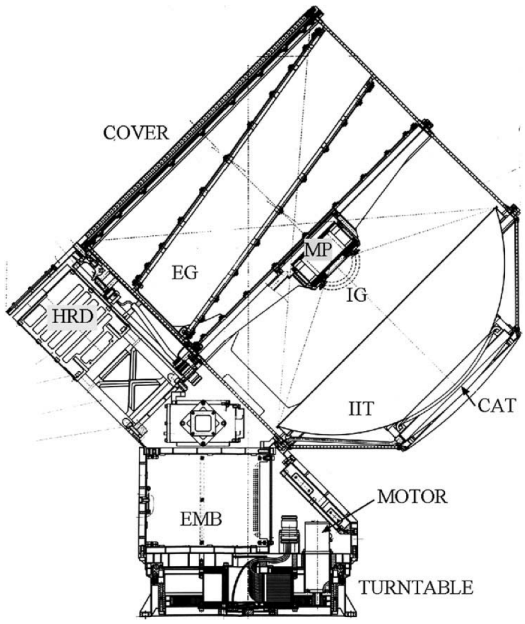

(b) Side view of a technical drawing of the Cosmic Dust Analyzer

Figure 2.1: The Cosmic Dust Analyzer (CDA) is mounted on a turntable, which, driven by a motor, enables the instrument to rotate by 270°. The Electronics Main Box (EMB) is attached to the turntable, above which are the main components of CDA: the High Rate Detector (HRD) and the Dust Analyzer (DA). Both are mounted at 45° with respect to the articulation axis of the turntable. The High Rate Detector (HRD) with two circular dust sensors is roughly central and the Dust Analyzer (DA) is above the HRD. The components of the DA are labeled in subfigure (b); The Entrance Grids (EG) are located in the entrance. The Multiplier (MP) is located in the center of the DA and its backside is visible in the photograph left. The Ion Grid (IG) is in front of the MP. The large gold Impact Ionization Target (IIT) and the small Rhodium Chemical Analyser Target (CAT) are located at the far end, with the CAT at the middle of the IIT. Image credit: Adapted from (Srama et al. 2004).

stainless steel entrance grids (EG), each of which has a transmission of 95%, towards the front of CDA and a charge sensitive amplifier. The innermost grid and outermost grid are grounded and only the central two grids are connected to this amplifier to produce the QP signal.

The IID and the chemical analyzer (CA) utilize different impact targets but share a multiplier (MP) and an ion grid mounted in front of the multiplier (Fig. 2.1). The impact target of the ionization detector (IID) is 41 cm diameter, gold plated, hemispherical Impact Ionization Target (IIT), with a chemical analyzer grid at the center of it. The impact target of the chemical analyzer is the small rhodium inner Chemical Analyzer Target (CAT) (16 cm in diameter) inserted in the gold IIT. These targets are attached to two different charge amplifiers, which measure negative ion charge at the CAT (QC signal) and at the IIT (QT signal). The IIT as well as the chemical analyzer grid are electrically grounded (nominal zero potential), whereas the CAT is on a potential of +1000 V; and there is 3 mm distance between the CAT and chemical analyzer grid, which works as the acceleration grid. This results a very strong electric field in between, which separates the impact charges generated at the impact targets immediately and accelerates the positive ions to a very high velocity quickly, passing through the chemical analyzer grid and then entrance the space between the chemical analyzer grid (68% transmission) and the Ion Grid (IG) (with a potential of -350 V). The space provides a flight path length of 230 mm and a cone-shaped electric field, which is caused by the curved shape of the target and the grids and continues to accelerate and focuses the positive ions onto the Ion Grid (QI signal) and the Multiplier (MP signal), giving the elemental composition of the impact particles (Fig. 2.2) (Srama et al. 2004).

2.1.2 The working principle of the Chemical Analyzer

As shown in Fig. 2.2, the innermost grid and outermost grid are grounded and when a charged particle passes through the entrance grids (EG) after entering the CDA, it induces a charge signal corresponding directly to the charge of the particle on the two central entrance grids, which are connected to an amplifier. As a result, the amplifier amplifies and outputs a voltage signal (QP), which is used to calculate the velocity and incident angle of the incident particle (Srama et al. 2004; Kempf et al. 2008).

Finally, the particle will impact either the sensor walls, the IIT or the CAT and will be vaporized and ionized due to the high energy. If it impacts on the wall, no further useful signal will be produced. If it impacts on the IIT or (passing through the Chemical Analyzer Grid) on the CAT, fragments (ejecta) of impacting

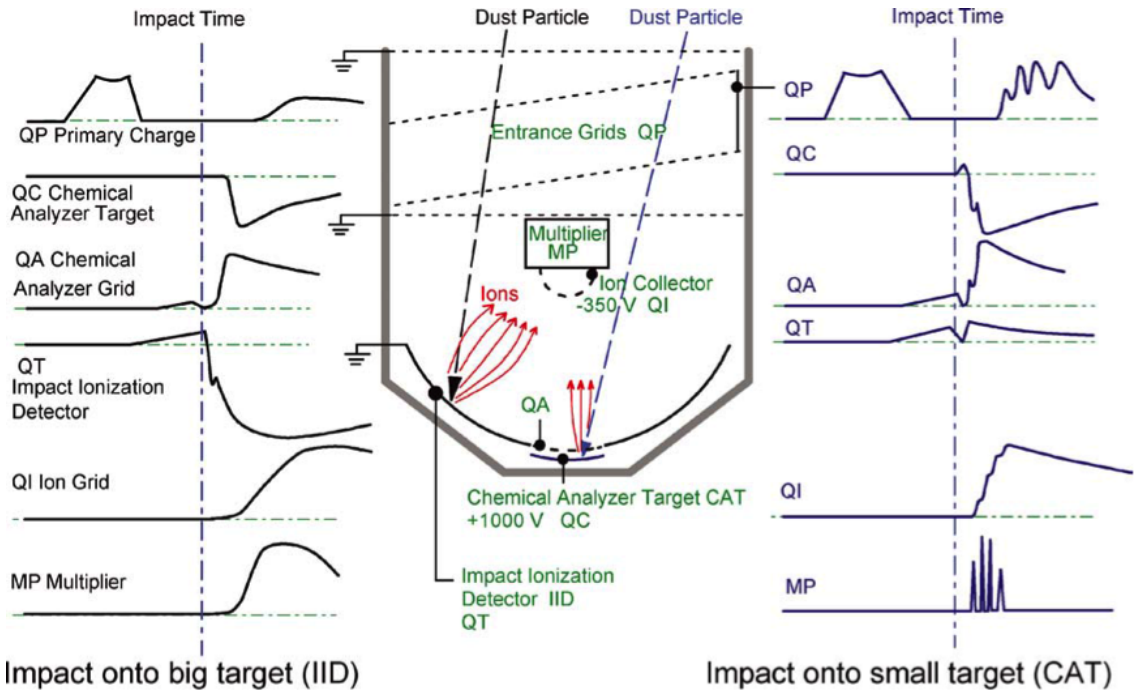

Figure 2.2: The scheme of the structure of the Dust Analyzer (middle), the Hypervelocity impact signals of dust grains onto the Impact Ionization Target (IIT) (left) and onto the Chemical Analyzer Target (CAT) (right). Only if a dust particle impacts on the CAT at a high enough speed, will a useful time-of-flight mass spectrum be outputted by the multiplier. Image credit: Srama et al. (2004).

particle and target, as well as neutral atoms, ions and electrons (impact plasma) will be produced. The negatively charged components (electrons and anions) and the positively charged components cations will be separated by the electric fields between the targets and relevant ion grids. As a result, electrons and anions are collected by the IIT or the CAT, with the amplifiers attached to the targets providing the negative charge signals, QT and QC, respectively. Simultaneously, the cations are accelerated towards the Ion Grid. They pass through the Chemical Analyzer Grid (if the impact occurred on the CAT) and the Ion Grid (QI) and are finally received by the Multiplier (MP). Amplifiers attached to the Ion Grid, the Chemical Analyzer Grid and the Multiplier (MP) output positive charge and voltage signals: QA, QI and MP, respectively. However, only CAT imacts create spectra with better seperation due to the much stronger electric field of the accelerator grid. with the spectra created by CAT imacts the elemental composition of the impacting dust grain is analyzed. The signal QI is used to determine the quantity of cations reaching the multiplier and to judge if the impact is a single impact. If it is a double or triple impact, the mass spectra overlap, complicating interpretation. Therefore, only the mass spectrum from a single impact is useful (Srama et al. 2004).

Before an impact is detected, the QC, QT, and QI channels works at very low sampling frequencies, and the MP sampling is inactive. The outputs of these amplifiers are continuously compared with a threshold, and if the threshold is exceeded, the DA is triggered and spectrum recording starts. The DA can be triggered by exceeding the thresholds on either the CAT, which collects enough negative charges or the multiplier (MP) itself, which receives the first abundant cation species. In the latter case, spectrum recording can be triggered up to several μs after the actual impact on the CAT. As a consequence, the mass line of the triggering ion itself, such as hydronium ions (H_3O^+) for water dominated particles, as well as signatures of species with lower masses than the triggering ion, do not appear in the spectra.

Once the DA is triggered, the sampling frequencies of channels QC, QT, and QI are increased, and high frequency sampling of MP is activated. The spectra from the MP channel are logarithmically amplified, sampled at 100 MHz, and digitized with 8 bit resolution for a period of 6.4 μs and recorded. If the DA was impact triggered and all ions are singly charged, the recorded mass range is from approximately 0u to 190u (atomic mass units). If the DA is triggered by a mass line, the recorded mass range is shifted to higher masses, depending on the trigger species. For example, for a hydronium ion (H_3O^+) trigger, the mass range may reach 230u.

2.1.3 The principle of impact ionization

When a dust particle impacts the surface of a solid target at sufficiently high velocity (> 1 km/s), the impact kinetic energy is converted into internal energy, which partially vaporizes and ionizes the impacting particle as well as a tiny part of the target. The impact ionization process is illustrated in Fig. 2.3. The shock wave induced by impact compresses the impinging particle to form a high temperature, high pressure and dense plasma cloud. This cloud expands, with some electrons escaping the expanding plasma cloud due to their faster expanding velocities, leading to charge separation and a positively charged cloud. This process may be accompanied by recombination of ions and electrons during the expansion. At the final stage, the cloud reaches a partially dissociated state with residual ions. Eventually, the residual positive charge and negative charge are separated by an strong applied electric field, and subsequently the residual negative charges are collected by the target and the most of the residual positive ions are transferred into a mass spectrometer (Mocker et al. 2012; Austin 2003).

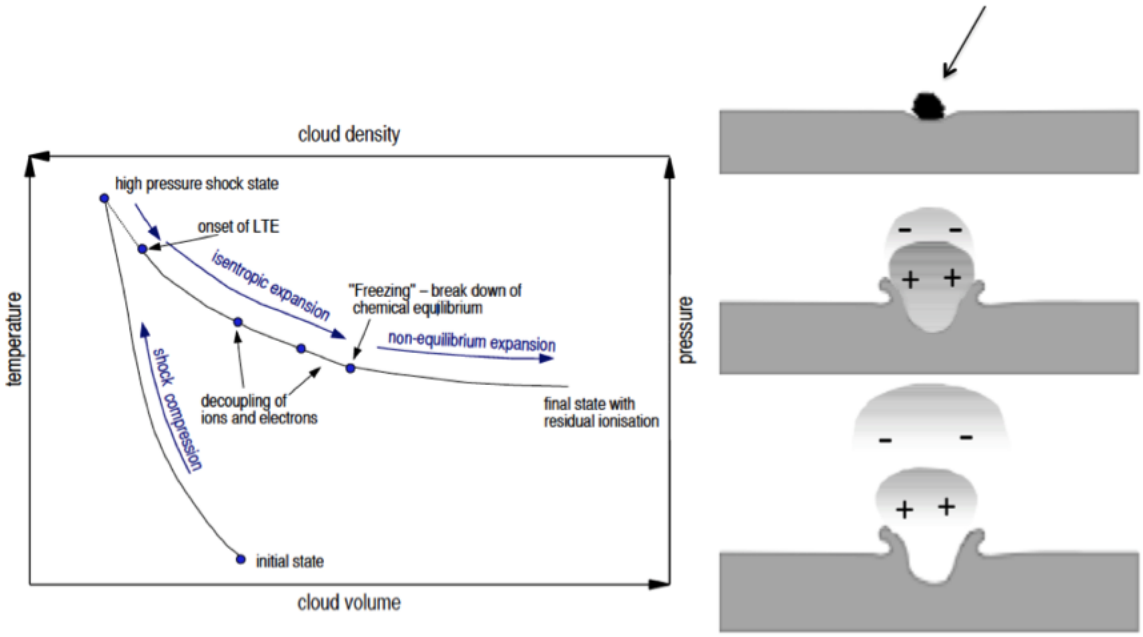

Figure 2.3: (Left) The process of shock wave ionization (Note: LTE is the abbreviation for local thermodynamic equilibrium.) (Image Credit: (Mocker 2011)); (Right) A schematic of the impact ionization mechanism (Image Credit: (Austin 2003)): (1) A micron-sized particle impacts the surface of a target, melting and forming a crater. (2) A cloud of vapor and ions forms. (3) The cloud expands at different speeds, with the more mobile electrons dispersing faster.

2.1.4 CDA Impact Event Data

Here, I will describe the processes and data product relevant to impacts of particles on the CAT.

1) The impact charge yield and QC signal

The impact charge yield (Q) has a power law relationship with the particle mass (m) and impact speed (v) (Dietzel et al. 1973; Ratcliff et al. 1997):

$$Q = c \cdot m^{\alpha} \cdot v^{\beta}. \tag{2.1}$$

Here, c is a constant, m is the mass of the impacting particle and v is the impact speed. Exponent α is generally assumed to be close to 1, and β is between 1 and 6 depending on the materials of projectiles and impact speed ranges (Ratcliff et al. 1997).

The negative charge produced during a CAT impact will be collected by CAT to produce the QC signal. The QC signal is proportional to the impact yield and thus can be used, in combination with the impact speed, to estimate the mass and size of an impacting particle (Srama 2009).

2) QI amplitude

From the QI amplitude an ion yield may be derived, which represents the charge of positive ions, originating from both the impact particle and the target, collected at the ion grids in front of the multiplier. After an impact occurs, dependent on impact velocity, grid transmission and electric field, a certain part of the positive ions produced by impact are focused to and pass through the ion grid. For the CDA, the $\sim 50\%$ of the incoming ions pass through the grid and reach the multiplier to generate the TOF spectrum. The total ion yield is proportional to the number of positive ions produced by an impact (Q in Eq. 2.1) and thus can be also used, in combination with the impact speed, to evaluate the mass and size of an impacting particle (Postberg et al. 2006; Srama 2009).

As well as enabling the number of cations which form a spectrum to be estimated, the QI signal can also show if the spectrum was formed by a single impactor. For single impact, there is only one maximum on the QI curve (Fig. 2.4). During the high dust fluxes, double or triple impacts may occur, in which two or three particles impact the Chemical Target during spectrum recording, making spectral interpretation difficult, if not impossible.

3) The time of flight (ToF) mass spectrum:

In general, a time of flight mass spectrum can be described by the following

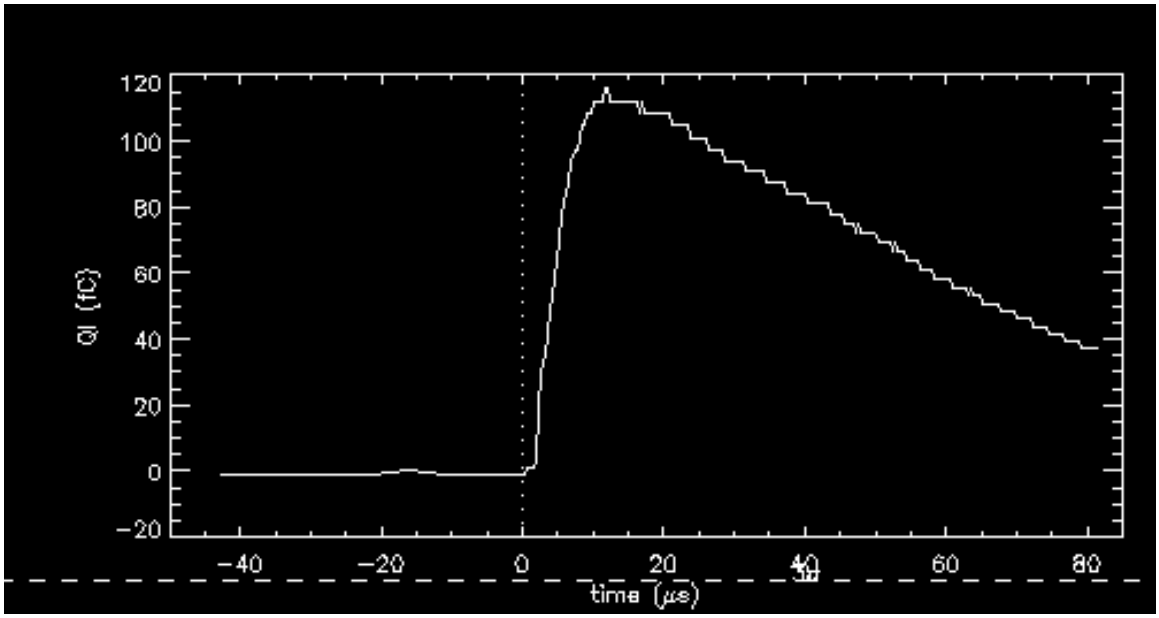

Figure 2.4: QI curve of a single impact CDA spectrum. The profiles of QI curves help us to judge the quality of an impact: For the QI signal of a good impact, the rising time (the charging time) is very short (~ 10 μs) and the RC delay time (the discharging time of a RC circuit) is much longer ($> \sim 100$ μs). Therefore, the shape of the QI signal should be a very steep rising slope after the trigger time, followed by a slow dropping slope.

function of ion mass and charge:

$$t = b + a \cdot \sqrt{m/q} \tag{2.2}$$

Where t is the time of flight, m is the mass of an ion, and q is the charge of the ion. Apart from at the very highest impact velocities ($> \sim 100$ km/s), the peaks in CDA spectra are due to singly charged ions only. The spectra can therefore be calibrated onto a mass scale by using known, or derived, a and b parameters.

- Accuracy and parameters a and b:

  Parameter a is called the **stretch-parameter**, which is, neglecting the initial ion kinetic energy from the impact, in principle determined by the dimensions and electric field configuration of the instrument. In addition, the stretch parameter, a, is also affected by the initial speed (kinetic energy) of the ions and the projectile materials (Mocker 2011; Mocker et al. 2012). This increase of the complexity for determining the parameter. However, a can be determined via laboratory experiments. The calibration experiments were done using the Heidelberg dust accelerator, which can accelerate charged particles to a wide range of speeds. The particles of different projectile materials (metals, carbon and Polyaniline coated or Polypyrrole coated polystyrene latex), masses and impact speeds (2 - 70 km/s) are tested and the results indicate that the stretch parameter increase slightly with the increase of impact speed, and vice versa and only varies by less than 1% around a value of $a = 4.8 \times 10^{-7}$ (Stübig 2002). Unfortunately, icy particles can not be tested with this accelerator, because they can not be charged or coated with chargeable materials to accelerate. According to previous experience, for CDA spectra of E-ring icy particles, the stretch parameter also does not vary much, usually from 4.72 $\times 10^{-7}$ to 4.80 $\times 10^{-7}$. The stretch parameter of the CDA spectra of plume icy particles is higher (around 5.00 $\times 10^{-7}$) and has larger deviation. The reason for this is that, to avoid damage to the CDA due to the high impact rate during plume traversals, the acceleration voltage, and with that the strength of the electric field between the CAT and the multiplier, was reduced.

  Parameter b is the so-called **shift parameter**, which represents the time offset between the trigger time relative to the impact time: $b = t_{trigger} - t_{impact}$. The shift-parameter b can be unique for every single spectrum due to the different triggering methods and other effects, so it is determined manually by assigning ion masses to peaks of known species (Mocker 2011; Mocker et al. 2012).

- Precision and Mass Resolution:

The precision of spectra is described by their mass resolution. In this work I use the IUPAC definition for resolution in mass spectrometry, by which the mass resolution of a mass spectrometer is defined as:

$$R = m/\Delta m \tag{2.3}$$

where R is the resolution, m is the mass of the ion of interest and Δm is the peak full width at half maximum (FWHM). For CDA, the mass resolution is relatively low and has been determined in the laboratory to be between 10 and 50, depending on the atomic mass of the ions (approximately 1 u - 190 u) (Srama et al. 2004). This is primarily because of the constant sampling rate of the instrument, although other effects, such as ion energetics and curved trajectories can also broaden peaks and reduce the apparent resolution (Hillier et al. 2006). The mass resolution of CDA is in most cases not high enough to distinguish peaks related to isotopes, such as $Na^+(Na^{35}Cl)$ and $Na^+(Na^{37}Cl)$ or to enable near isobaric chemical compounds to be definitively identified.

2.2 Analogue spectra by Infrared Laser Induced Liquid Beam Ion Desorption Time of Fight Mass Spectrometer (IR-LILBID-TOF-MS)

The CDA spectra can only offer qualitative analysis of the composition of icy particles in space, i.e. what kinds of ions or substances causing these ions could exist in the icy particles. However, in order to obtain more detailed information about the composition of icy particles, such as the quantities or ratios of substances showing their peaks in the CDA spectra and the detection limits of some potential substances, laboratory analogue experiments need to be done.

2.2.1 Techniques for simulating impacts of ice grains onto the CAT in CDA and mimicking analogue spectra

Although laboratory simulation of hypervelocity cosmic dust is possible for refractory materials, such as metals, minerals and some organic polymers (often utilizing conductive coatings (Hillier et al. 2009; Fielding et al. 2015), the controlled acceleration of single, micron and submicron sized ice grains has not yet been achieved. Instead, other techniques have been adapted and enhanced

to simulate such processes. Usually, the Infrared Laser Induced Liquid Beam Ion Desorption (IR-LILBID) method, which is a specific type of Matrix Assisted Laser Desorption/Ionization (MALDI) method, is used to simulate the impact ionization process of icy particles onto a target of a space instrument. In LILBID a narrow beam of an aqueous solution with the sample is ionized and desorbed by a focused infrared laser. Subsequently, the ions and charged clusters are transported into and analyzed by a time of flight mass spectrometer (ToF-MS).

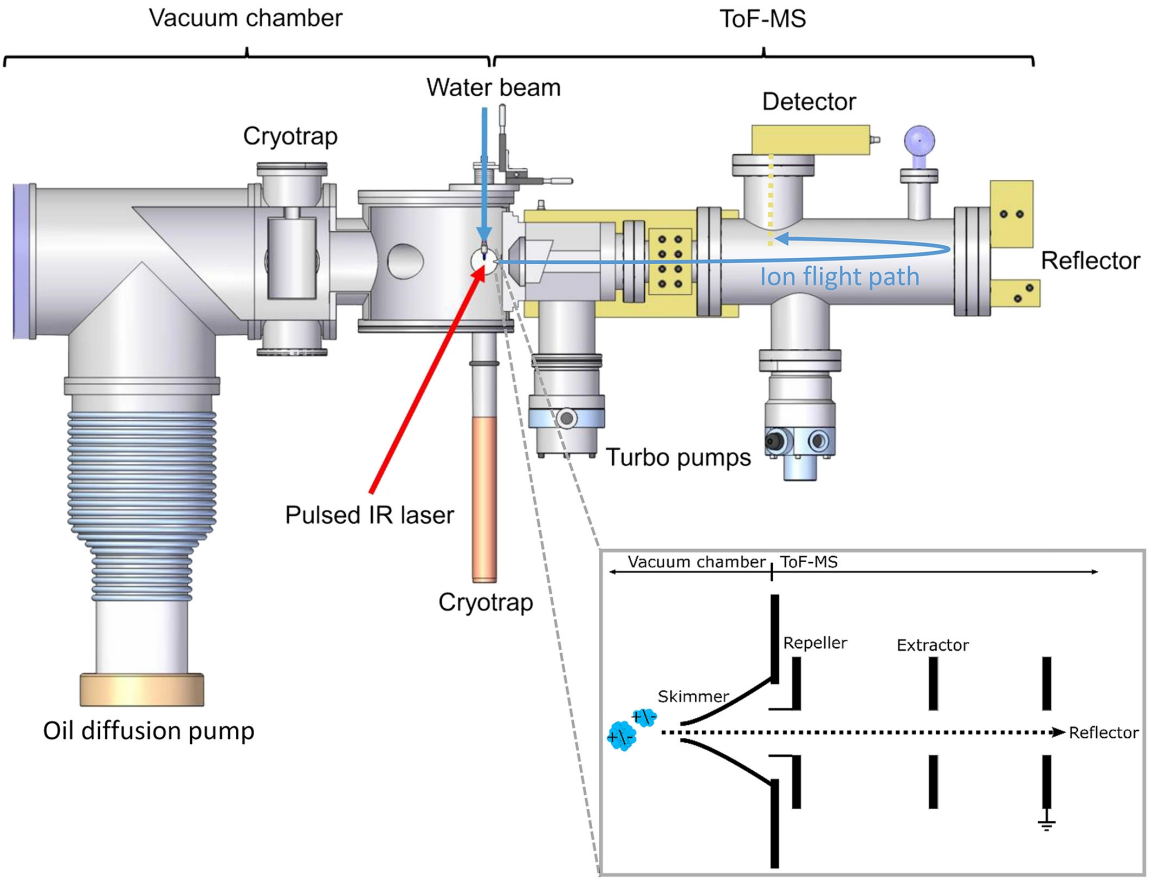

Figure 2.5: The experimental setup for simulating impacts of ice grains onto the Chemical Analyzer Target (CAT) in CDA. Inset is a schematic illustrating the instrument configuration for the principle of delayed extraction. The acceleration electric field is applied between the repeller electrode and extractor electrode. The oil diffusion pump shown has been replaced by a turbo pump. Cited from Klenner et al. (2019).

Fig. 2.5 shows the layout of the Infrared Laser Induced Liquid Beam Ion Desorption Time of Fight Mass Spectrometer (IR-LILBID-TOF-MS) used to produce analogue spectra for this thesis. The working principle is as follows:

A vacuum chamber with an internal pressure of approximately 5×10^{-5} mbar is connected to a Time of flight spectrometer, which is at a much lower pressure of approximately 1×10^{-7} mbar. A liquid beam ($12 - 22\,\mu$m in diameter) of an aqueous solution analogous to icy particles in composition is vertically injected via a quartz nozzle into this vacuum chamber with a flow speed of $0.17 - 0.20$ ml/min. Two cryotraps, together with multiple turbo pumps, help maintain a suitable vacuum. The liquid beam is irradiated with a focused and pulsed infrared laser (20 Hz, 7 ns pulse length; maximum power density $\approx 1150\,\mathrm{MW/cm^2}$), at a wavelength of 2840 nm, which matches the absorption frequency of the OH-stretch vibration of water molecules. By absorbing the laser energy, the liquid beam is heated up and explosively disperses into atomic, molecular, ionic and macroscopic fragments, which subsequently drift through a skimmer (to produce a better-collimated spray of ions) into an acceleration region and are, depending on their polarity, transferred into a reflectron-type Time-of-Flight mass spectrometer.

2.2.2 Impact speed simulation

For icy particles with a specific composition, the pattern of peaks or the profile of spectra generated during an impact is primarily influenced by impact speed (impact energy), which can be simulated by adjusting the energy density of the infrared laser on the water beam as well as the delay time of the gated mass spectrometer, using the principle of delayed extraction (Klenner et al. 2019). For a fixed delay time, higher laser energy densities correspond to higher energy (higher speed impact) and lower laser energy densities correspond to lower impact speeds.

However, the LILBID process differs from the impact process of icy particles on a target in that the laser affects a larger region of water than an impact and the energy transferred to the atoms and molecules by the laser is below their nominal ionization potentials. It is actually the formation of charged species during dispersion accomplished by mechanical breakup of the liquid matrix into charged fragments, producing more slower, larger, clusters and the drift region in the spectrometer is also big (Charvat & Abel 2007; Wiederschein et al. 2015). Thus, adjusting laser density must be combined with another method - delay extraction to achieve high impact speed simulation.

Delayed extraction is a method to select ions depending on their initial velocities by setting a delay time. There is a drift region between the site of 'ionization' (Depending on the laser energy, it isn't strictly 'ionization' - it's the formation of charged species during dispersion of the liquid.) and the beginning of the acceleration region. After dispersion, the fragments firstly drift freely with their initial velocities,

with part of them passing through the skimmer, until the acceleration voltage is activated. The delay time is the time span between the laser shot on the liquid beam (dispersion) and the activation of the acceleration voltages between a repeller electrode and an extractor electrode. Once activated, the acceleration voltage is maintained for a certain duration (30 μs is used here), and the late arriving ions are blocked by the potential barrier of the repeller electrode. In other words, ions are selected based on their initial velocities. The initial velocities of ions dispersed from the liquid beam are inverse correlated with their masses, so lower mass means higher initial velocities and shorter drift time. Thus, ions are also selected based on their mass. Lower delay time selects comparatively more fast low mass ions and fewer slow high mass ions; and thus mimics high impact speeds, which produces more low mass ions or clusters due to the high energy. In contrast, high delay time selects comparatively more slow high mass ions and fewer fast low mass ions, and thus mimics low impact speeds. In this way, the spectral profiles from different impact speeds are simulated by adjusting the delay time in addition to the laser's energy density (Klenner et al. 2019).

However, higher delay time allows more ions or clusters at all masses to enter the acceleration region and thus amplifies all peaks, which conflicts with the fact that lower impact speeds produce lower ion yield and correspondingly lower peaks. To counteract this effect, the laser energy must be reduced. For the same reason, a higher laser energy density has to be used to increase all peaks amplitudes at lower delay times.

Different impact speeds can thus be simulated through the combination of adjusting the energy density and delay time. According to Klenner et al. (2019), the analogue experiments with the setup in our laboratory can simulate impact speeds ranging between $3 - 21\,\mathrm{km/s}$, which are typical impact speeds of icy particles on CDA in the Saturnian system.

2.3 Comparison of the principles and spectra of impact ionization in CDA and laser ionization in IR-LILBID-TOF-MS

In CDA the energy for ionization comes from the kinetic energy of the high speed grains whereas in IR-LILBID-TOF-MS the energy for ionization comes from the Infrared laser.

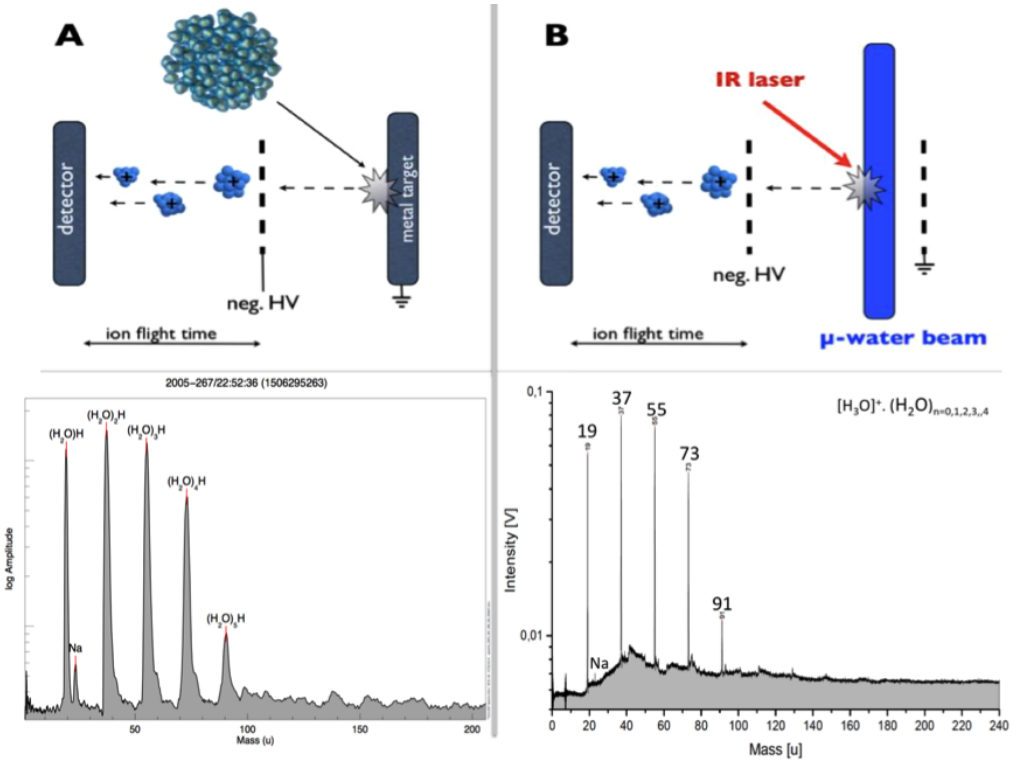

Figure 2.6: (A) High speed impact ionization of a micron-sized ice grain on the CDA Target and the CDA spectrum; (b) Laser ionization of liquid beam with a diameter of 12 to 20 μm and the laboratory spectrum. The compositions of the ice grain and the liquid beam are similar so their spectral profiles are similar, but the laboratory spectrum has much higher mass resolution. Image Credit: (Adapted from Postberg et al. (2009b) supplement therein).

The analogue experimental setup is much more precise in mass measurement than CDA. The mass resolution of CDA is only approximately 10 - 50 $m/\Delta m$, but the mass resolution of the analogue experimental setup is approximately 800 $m/\Delta m$.

2.4 Main compositional types of ice grains in the E-ring and Enceladus' plume

The CDA onboard the Cassini spacecraft produced thousands of ToF mass spectra of ice particles in the E-ring and Enceladus' plume. Some of them are salt poor and others are salt rich. Postberg et al. (2008, 2009b) classified the majority of these spectra, based on their peak features, into three major types, reflecting three compositionally distinct families of ice particles: Type-1, Type-2 and Type-3. I will introduce these three types of spectra and their corresponding ice grains in the following part of this section:

The salt-poor ice spectra possess abundant hydronium-water cluster peaks and tiny or no salt-water cluster peaks (usually $Na^+(H_2O)_n$, n=1, 2...), and thus their respective ice particles contain trace salt (the salt to water molar ratio is usually between 10^{-8} and 10^{-5}). They are further classified into two types based on the existence of a broad organic fragment related peak (26 u - 29 u in mass): Type-1 spectra do not have this peak and thus result from almost pure water ice particles; Type-2 show this peak and result from organic-enriched, salt-poor ice particles. The organic feature varies widely: many show only subtle organic peaks and a few show abundant organic peaks typically occurring with some high mass peaks. In addition, in the case of high impact speeds, the salt-poor ice spectra may occasionally show peaks from Rh, the target material (Fig. 2.9). In contrast, the salt-rich ice spectra are characterised by significant salt-related peaks but tiny (if any) water cluster peaks, and are named Type-3 (Fig. 2.7) (Postberg et al. 2018a). The salt to water molar ratio of their representative ice grains (Type-3 grains) is $> 10^{-3}$ (Table 2.1) (Postberg et al. 2018a). Impacts of Type-2 particles on average produce higher total ion yields than of Type-1 particles, implying a larger size on average (Postberg et al. 2018a). Impacts of Type-3 particles on average produce total ion yields several times higher than of Type-1 particles, implying a considerably large size (Postberg et al. 2011). Therefore, Type-3 particles have the largest average size and Type-1 particles have the smallest average size among these three compositional types of particles. Besides, based on the evaluation of about 10000 E-ring ice grains spectra, the abundance of each types are obtained (Table 2.1) (Postberg et al. 2018a).

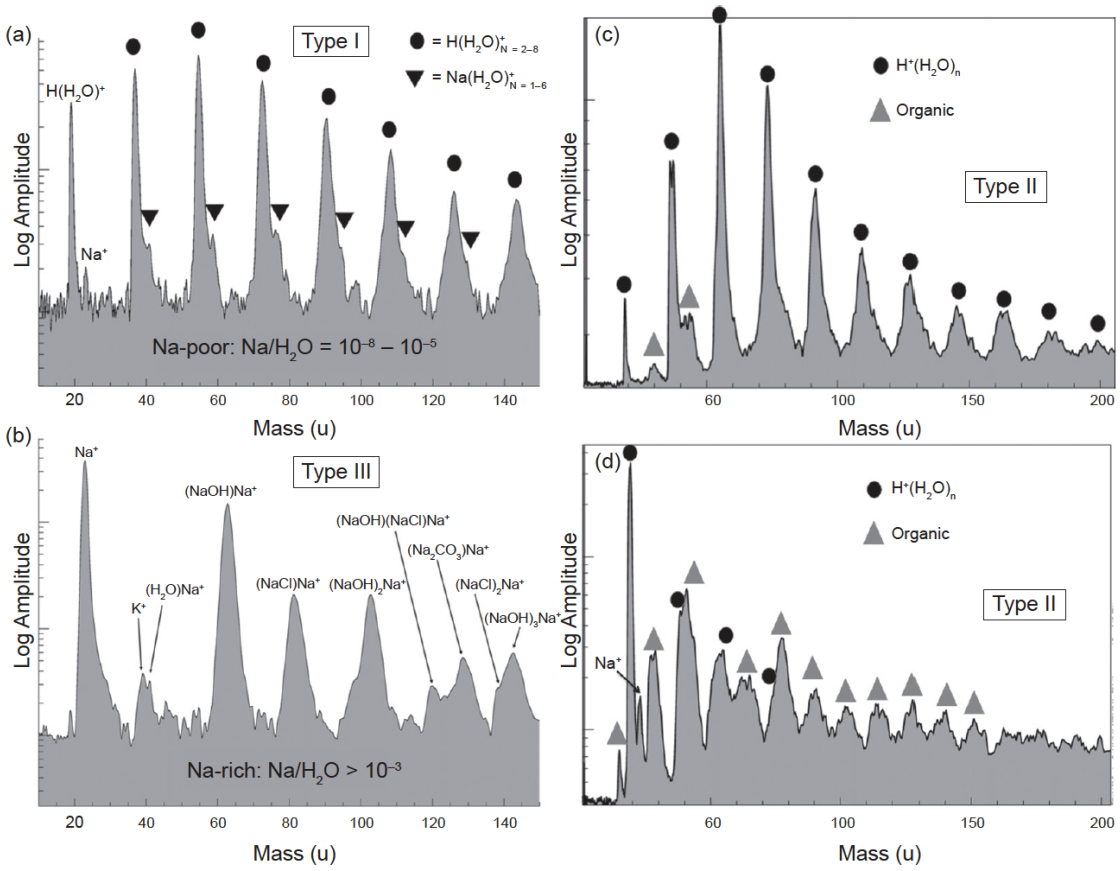

Figure 2.7: The three major CDA mass spectral types representative of ice grains. (a): Type-1 spectra show mostly water with only traces of salt (usually salt-water cluster peaks). (b): Type-3 spectra exhibit strong salt peaks. (c) and (d): Type-2 spectra show low salt features and a broad peak at 26 u - 29 u in mass. Their organic features show a wide variety: Many are similar to Type-1 with additional subtle peaks in agreement with low mass molecular organic cations carrying only 1-3 carbon atoms [subfigure (c)] (Khawaja et al. 2019). A few Type 2 spectra show abundant organic peaks, some of which are at high masses of up to $\sim$ 200 u [subfigure (d)]. Image Credit: (Postberg et al. 2009b, 2018a)

Table 2.1 illustrates the compositional features, the average abundances and the relative size of the three compositional types of ice grains measured in the E-ring:

Type	Salt-poor		Salt-rich
	Type-1	Type-2	Type-3
Composition	Almost pure water ice with trace Na and/or K alkali salt and Na/H_2O mole ratio on the order of 10^{-7}.	Water ice with trace Na and/or K alkali salt plus organic compounds, which can vary dramatically in fraction and composition among grains. Sometimes silicates exist.	Water ices with abundant Na and/or K alkali salt (0.5-2 % by mass on average, with K compounds being less abundant) Na/H_2O mole ratio above 10^{-3}
Average Abundance	$\sim 65\%$	$\sim 25\%$	$\sim 10\%$
Average Size	small	medium	large

Table 2.1: The compositional features, the average abundance and the relative average size of the three compositional types of ice grains measured in the E-ring (Postberg et al. 2008, 2009b, 2018a)

Besides the three main spectral types there are a few 'transition' spectral types, which are characteristically between two types, such as Type-2/3 spectra showing both organic peaks and salt peaks, Type-1/3 spectra showing both obvious water cluster peaks and salt peaks. These transition spectral types only form a very small fraction of the data set of ice particle spectra.

All of the three main types of spectra (Type-1, Type-2 and Type-3) and their respective particles have been extensively analysed (Hillier et al. 2007a; Postberg et al. 2008, 2009b, 2011, 2018b; Khawaja et al. 2019). However, in order to deeply explore the properties of the Type-3 salt rich spectra and ice particles from both E-ring and in Enceladus plume and their implication on the subsurface ocean composition, the further classification (into subtypes) must be done and the distribution and evolution of the subtypes must be analysed firstly. Furthermore, in order to quantify the concentration of the main chemicals and the detection limits of the potential important geochemical substances in the subsurface ocean, the spectra mimic work must be done. This thesis focuses on these works.

2.5 The formation mechanism of water clusters and salt clusters

The majority of CDA spectra from Saturnian E-ring and Enceladus plume particles are due to impacts on the CAT of water ice dominated grains. Water-cluster peaks dominate the majority of these mass spectra. Therefore, understanding the behavior of water molecules in impact spectra is critical for identifying non-water species embedded in the ice particles, such as salts and organics.

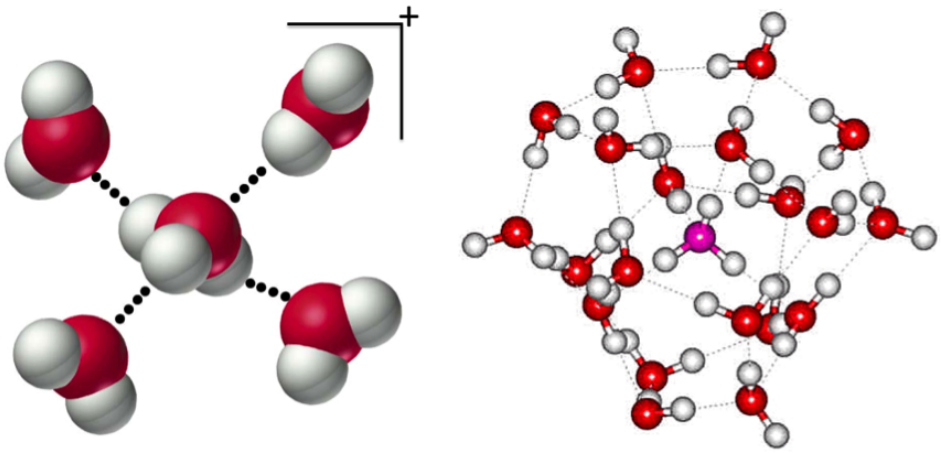

Figure 2.8: (Left panel): Clustering of neutral water molecules with a hydronium as a core. Three partially positively charged hydrogen atoms of the hydronium core form bonds with the oxygen atoms of the neighboring neutral water molecules. The entire cluster is singly positively charged. (Right panel): Large clusters could be formed via this process. Image Credit: (Postberg et al. 2008) & http://www1.lsbu.ac.uk/water/magic.html (20.10.2019)

In the impact plasma cloud from salt-poor ice particles in CDA, or the laser dispersed salt-poor water solution beam in the laboratory setup, water molecules tend to form hydroxide ions (OH^-) and hydronium ions (H_3O^+). In the presence of neutral water molecules clusters with hydronium as an ion core form (Fig. 2.8). Thus, hydronium-water cluster peaks $[H_3O]^+ (H_2O)_n$ (n = 1, 2, 3...) dominate in the spectra of salt-poor ice particles. The maximum size of observed hydronium-water cluster peaks, and the relative amplitudes of these cluster peaks, varies depending on the impacting speeds for CDA or laser power and delay time in the laboratory. With increasing impact speed, the maximum size of observed hydronium-water clusters decreases and the maxima of the profile of the hydronium-water cluster peaks shifts to the low mass end (Fig. 2.9).

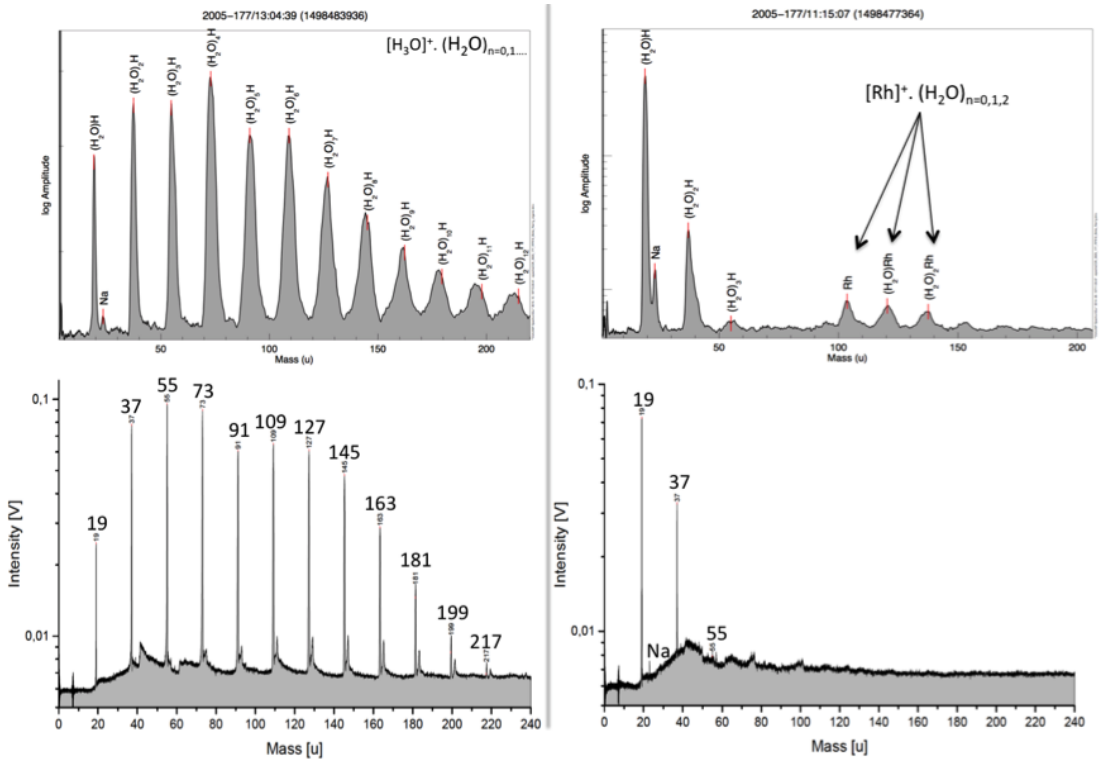

Figure 2.9: Salt-poor CDA mass spectra from E-ring ice particle impacts (Top) and their respective analogue laboratory mass spectra (Bottom). The hydronium H_3O^+ mass line at 19 u is followed by a sequence of water cluster peaks with periodic intervals of 18 u due to $[H_3O]^+(H_2O)_n$. The presence of water clusters varies with impact speed or energy density: Low impact speeds corresponding to low energy densities result in more large water clusters and thus more higher mass water cluster peaks (Left). In contrast, high impact speeds corresponding to high energy densities result in more small clusters and fewer large water clusters and thus fewer higher mass water cluster peaks (Right). In addition, high impact speeds also produce more Rh and Rh-water clusters peaks in CDA spectra due to the high energy densities (Top Right). Image Credit: (Khawaja 2017)

In addition, other ion species, e.g. sodium cations (Na^+), can also form an ion core for water clusters. Therefore, some peaks of salt-water clusters may also be observed in salt poor spectra (Fig. 2.10)

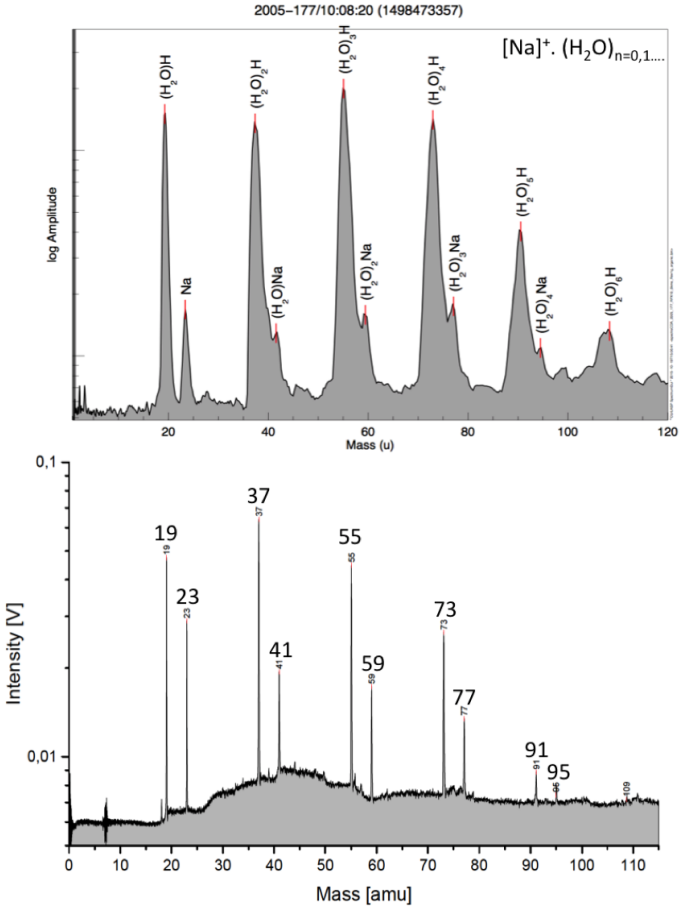

Figure 2.10: Water-water and Na-water cluster peaks in a CDA spectrum (Top) and an analogue laboratory spectrum (Bottom). Image Credit: (Khawaja 2017)

Furthermore, in CDA the target material rhodium can also be ionized during impacts and thus peaks from rhodium cations (Rh^+) and rhodium-water clusters ($Rh^+(H_2O)_n$) can also be observed in some CDA spectra, especially in high impact speed cases, which produce higher energy densities for ionization (Fig. 2.9).

The following kinds of water cluster peaks are usually observed in CDA and laboratory salt poor spectra:

- H_3O^+ plus neutral water clusters: $[H_3O]^+(H_2O)_n$
- Na^+ plus neutral water clusters: $Na^+(H_2O)_n$
- Rh^+ plus neutral water clusters: $Rh^+(H_2O)_n$ (only in CDA spectra)

However, in the impact plasma cloud of alkali salt-rich ice particles in CDA or the laser dispersed, alkali salt-rich water solution beam in the laboratory setup,

the ionisation or the dispersion of water is suppressed due to the interaction with alkali and salt ions, which already exist in the salt solution. Salt ions act as cores to be attached to and thus to form a cluster, such as $Na^+(NaOH)_n$, $Na^+(NaCl)_n$, $Na^+(Na_2CO_3)_n$. These processes suppress the formation of water clusters and thus the salt-related peaks dominate in the spectra of salt-rich ice particles.

The following kinds of salt cluster or salt-water cluster peaks are usually observed in CDA and laboratory 'salt-rich' spectra:

- Na^+ plus salt clusters: $Na^+(NaCl)_n$, $Na^+(NaOH)_n$, $Na^+(Na_2CO_3)_n$ and their combinations thereof, such as $Na^+(NaCl)(NaOH)$.
- Na^+ plus neutral water clusters: $Na^+(H_2O)_n$

  (In CDA salt rich spectra only $Na^+(H_2O)$ is visible sometimes and the higher orders of clusters (n >= 2) are usually suppressed, but in laboratory salt rich spectra the higher orders of clusters (n is up to 3) are still usually visible.)

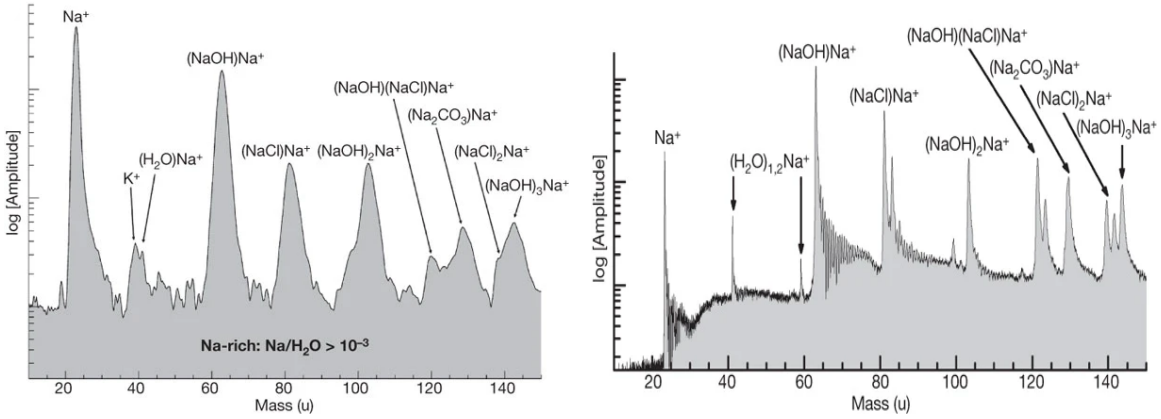

(a) A co-added sodium salt-rich CDA mass spectrum

(b) An analogue laboratory mass spectrum

Figure 2.11: A co-added sodium salt-rich CDA mass spectrum from E-ring ice particle impacts (Left) and its respective analogue laboratory mass spectrum (Right). Most of the water cluster peaks are suppressed by salt cluster peaks. The concentration of sodium in the analogue solution and hence the ice grains, is approximately 0.1 M. Image Credit: (Postberg et al. 2009b).

Chapter 3

The motivation and goals of this work

3.1 The motivation and goals of this work

The subsurface ocean of Enceladus is one of the most promising habitable extraterrestrial environments in our solar system (Parkinson et al. 2008; McKay et al. 2018; Taubner et al. 2020), and its habitability thus currently one of the most attractive topics in the field of astrobiology. The habitability of Enceladus' subsurface ocean is closely related to its geochemical environment (Sekine et al. 2019; Glein & Waite 2020; Ray et al. 2020; Hao et al. 2020), which also provides valuable information about the formation and evolution of Enceladus. Understanding the current state of this environment can thus provide crucial constraints for geochemical models (Glein et al. 2008; Matson et al. 2007; Zolotov 2007; Ray et al. 2020; Taubner et al. 2020; Glein & Waite 2020). Exploration of the habitability and geochemical conditions in Enceladus, on one hand, is helpful for future in situ investigations of Enceladus (Ray et al. 2020), and on other hand, provides clues for understanding the habitability and the internal processes of subsurface oceans within other icy moons in our solar system (Parkinson et al. 2008), such as Europa, and even extrasolar icy moons (Tjoa et al. 2020).

Postberg et al. (2009b) discovered sodium-rich E-ring grains in CDA data, which indicated Enceladus' subsurface ocean had been in contact with its rocky core. Subsequently, Hsu et al. (2015) used saturnian stream particle spectra to confirm that this process was ongoing. Building on these discoveries, the work presented in this thesis investigates further constraints on the composition of Enceladus' subsurface ocean, via CDA spectral analysis and spectral analogue experiments. In particular, this work differs from Postberg et al. (2009b)'s previous work as follows:

Firstly, Postberg et al. (2009b) used the average spectrum of approximately one hundred E-ring Type-3 CDA spectra, inferring the detailed composition through analogous laboratory experiments. In this work, over 1000 CDA spectra, including those of both E-ring and plume particles, have been analyzed. Every spectrum was individually examined, and compositional diversity within the Type-3 CDA spectra family investigated. Subsequently, the compositional diversity of the salt rich ice particles, the primary factor in the observed diversity of Type-3 spectra, was quantified and the concentration parameter spaces for different salt rich ice particles were determined using analogue experiments. Finally, spectra were searched for compounds other than the ones identified by Postberg et al. (2009b), and the particle concentration upper limits for compounds of interest, which were not found in the Type 3 spectra, inferred via laboratory analogue experiments. These detection limits allow the Enceladean subsurface ocean composition, intimately related to its habitability and geochemistry, to be further constrained.

Chapter 4

Compositional variation in Type-3 salt-rich ice grains, as revealed by their spectra

4.1 Introduction

In this chapter I will discuss the salt-rich grains emitted from Enceladus, and which are believed to be frozen droplets of the moon's subsurface ocean. In the following, spectra may be described as X-rich - this is a shorthand way to refer to the composition of the grains which generated the spectra.

4.1.1 Ice grain formation processes

Saturn's E-ring is composed mainly of μm and sub-μm sized icy dust particles originating from cryovolcanic plume on the south polar fractured zone of Saturn's icy moon Enceladus. Both salt poor and salt rich ice grains have been detected in the E-ring through CDA spectra analysis. As mentioned in Chapter 2, the salt poor ice grains and their spectra are classified into two major types: Type-1 and Type-2, based on the existence of organic peaks in the spectra (Postberg et al. 2008, 2018a). Meanwhile, the salt rich ice grains and their spectra are known as Type-3 (Postberg et al. 2009b, 2018a)(Fig. 4.1).

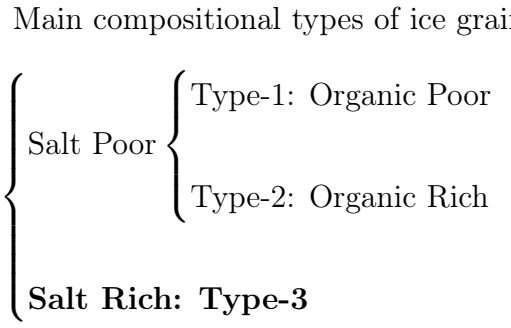

Figure 4.1: Main compositional types of ice grains

The generally accepted view is that the large differences in salt concentration of the ice grains is proposed to be caused by their different formation processes. The salt-poor ice grains (Type-1 and Type-2) are formed by the condensation of water vapor ascending from a liquid reservoir, with subsequent growth in ice channels during passage to the vents. However, salt-rich grains (Type-3) originate from frozen sub-micron- to micron-sized aerosol-like droplets dispersed from the salty seawater, so they preserve the chemical composition of Enceladus' subsurface ocean, which is in contact with the rock core and has dissolved salts and other compounds from it. During transport in the channels, these salt-rich droplets condense additional water from the supersaturated water vapor, in which they travel (Fig. 4.2). Since the vapor phase is salt poor, the condensed layer on the salt-rich core is nearly pure water ice. The structure of a recently erupted Type-3 grain in space is therefore expected to be a salt-rich icy core, which has the same composition as the ocean water, covered by a salt poor icy shell. Once exposed into the outer space environment, a grain's outer shell will be eroded gradually due to plasma sputtering. Thus, the salt concentrations of the E-ring salt rich grains, which have lost their salt-poor shells partly or completely, dependent on their ages, are assumed to be a lower limit of the salinity of the surface water of Enceladus' subsurface ocean (Postberg et al. 2009b).

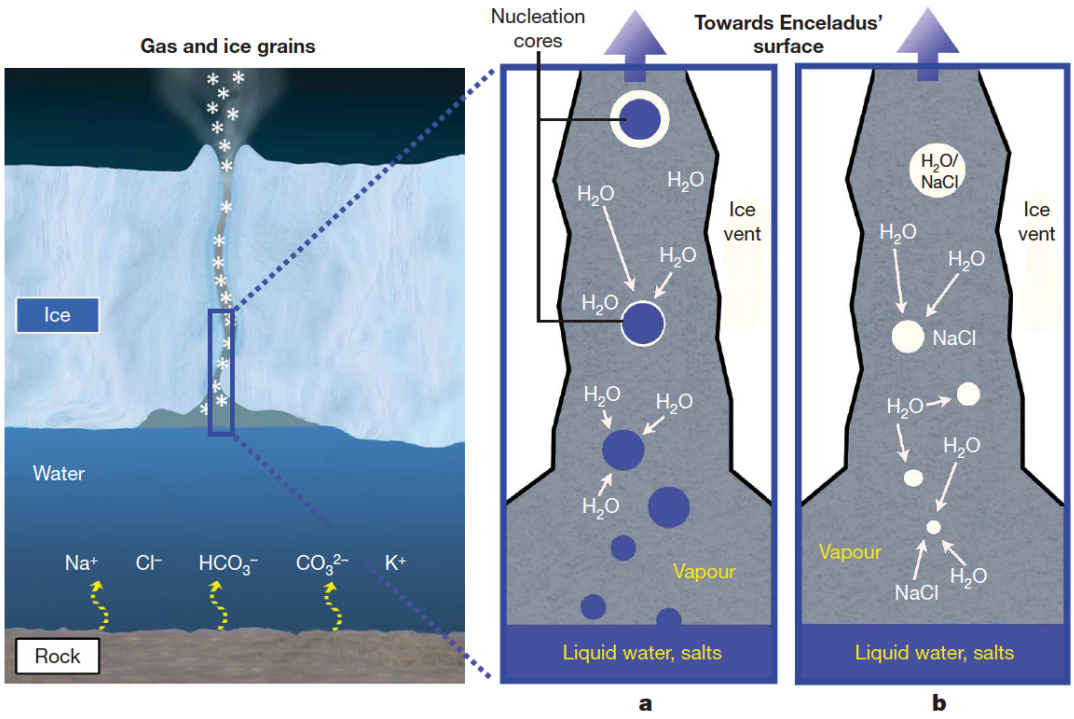

Figure 4.2: **Schematic of how ice particles with very different salt content are formed through liquid dispersion and condensation from vapour.** a) Salt-rich ice grains (Type-3). Dispersion of the surface of the liquid reservoir generates sub-micron- to micron-sized aerosol-like droplets (blue), which preserve the liquid reservoir's composition and condense some additional water from the supersaturated gas that drags them towards the surface. b) Salt-poor ice grains (Type-1). These ice grains are formed by condensation of water vapour ascending from the liquid reservoir with subsequent growth in ice channels during transport to the vents. Initially, the grains have the same low ratio of salt/water as the vapour. However, they may become enriched with trace salt through direct (collision) or indirect interaction (such as via crack walls) with the salt-rich grains. Image Credit: Postberg et al. (2009b)

4.1.2 Research objectives

Peaks suspected to be due to small amounts of organics also appear in some spectra of the salt-rich ice grains. It has been theorized that biogenic organics could be dissolved in the subsurface ocean, based on evidence which supports the existence of ongoing hydrothermal activity at the bottom of Enceladus' subsurface ocean (Hsu et al. 2015; Waite et al. 2017), which could therefore support chemoautotrophic ecosystems. Molecular hydrogen, the food of some chemoautotrophic microbes

on Earth, has been detected in Enceladus' plume (Waite et al. 2017), further strengthening the case that the subsurface ocean is habitable.

In order to look for more subtle, low concentration substances, whether organic or inorganic, it is necessary to first understand and analyze the variations in both salt composition and salt concentration. Understanding these variations in the composition of ocean originated ice grains is the first step to mimicking the spectra in laboratory, through which quantitative physical and chemical information about Enceladus' subsurface ocean water can be obtained.

Therefore, in this chapter the spectra of salt-rich ice grains, and by inference the compositions of salt-rich ice grains, were classified into subtypes. Following this process, searching for organic peaks and an analysis of their orbital distribution and orbital/physical evolution was undertaken.

4.2 The properties of the datasets

The original CDA dataset used in this thesis includes 1077 selected spectra, which appeared to be due to impacts of salt rich particles at first sight and obtained from 15 CDA samplings of the E-ring between 2004 and 2008. Sampling distances from Saturn's center were between 3.5 R_S and 21.0 R_S (R_S = Radius of Saturn). The impact speeds of the ice grains onto the CDA target range from 3.8 km/s to 16.2 km/s. The detailed listing of the used spectral data obtained from the 15 sampling periods is given in Appendix A.1.

Most spectra recording was impact triggered spectra which typically have a parameter 'b' ranging from -0.4 μs to 0 μs or low mass line, such as H^+ (1 u), H_2^+ (2 u), and $^{12}C^+$ (12 u), triggered spectra. The earliest line trigger (H^+) is at -0.48 μs. In the line triggered spectra the trigger line and any lower mass peaks are not recorded. For above two sort of spectra, both H_3O^+ (19 u) and Na^+ (23 u) peaks are still recorded. However, there are also some H_3O^+ (19 u) triggered (The typical b parameters are between -2.12 μs and -1.8 μs) or Na^+ (23 u) triggered (The typical b parameters are between 2.35 μs to -2.12 μs) spectra, in which, as a result, the triggered peaks are missing. In these cases the following assumption is applied: The triggering peak is higher than the unrecorded lower mass peaks. This makes sense, since the unrecorded lower mass peaks, whose corresponding ions arrive at the MP earlier, fail to trigger the DA. Therefore, the following conclusions are derived: 1) if Na^+ (23 u) triggered, the Na^+ (23 u) is higher than the unrecorded lower mass peaks (including peak H_3O^+ (19 u)); 2) If H_3O^+ (19 u) triggered, the peak H_3O^+

(19 u) is higher than any in the lower mass range, but whether it is higher or lower than peak Na^+ (23 u) is unknown.

With the above assumption and the criteria for Type-3 spectra (Postberg et al. 2009b, 2018a), all spectra in the dataset can be assigned, according to the existence and relative amplitudes of water peaks and salt peaks, into Type-3 spectra or non-Type-3.

As a result, 995 spectra from the 1100 spectra in the original dataset can be assigned to Type-3 spectra, and will be further classified and analyzed in this thesis. The rest 105 spectra can not be assigned to Type-3 spectra and thus are not analyzed in this thesis.

4.3 Methodology

In general, the following operations were carried out to classify and investigate the spectra.

4.3.1 Peak threshold for CDA spectra

3σ (here σ is the standard deviation of local noise.) is set as the peak threshold. It means if the value of a bump in a spectrum $> 3\sigma$, it is treat as a peak. Otherwise, it is not is treat as a peak. After calibrating the baseline of a CDA spectrum, the approximation that the spectrum has an uniform σ is accepted. Therefore, the σ can be measured in a selected mass range (or Time-of-flight range) far from peaks.

4.3.2 Classification of the potential preliminary classified salt-rich spectra

The first step is to judge whether these 1077 potential preliminary classified salt-rich spectra (The peak H_3O^+ (19 u), if existing, is lower than the peak Na^+ (23 u) or peak K^+ (39 u). Otherwise, they are salt poor spectra: Type-1 or Type-2.) are really salt-rich spectra. All spectra in the dataset can be classified into one of the following 3 broad types (Type-3, Type-5, Type-?) by applying the specified criteria:

1. If the H_3O^+ (19 u) peak amplitude, if existing, is lower than those of the Na^+ (23 u) or K^+ (39 u) peaks, and there are other Na^+ cluster or K^+ cluster peaks

aside from Na^+ (23 u) and K^+ (39 u), the spectra are classified into **Type-3**.

2. If the H_3O^+ (19 u) peak amplitude, if existing, is lower than those of Na^+ (23 u) or K^+ (39 u), and there are no other Na^+ cluster or K^+ cluster aside from Na^+ (23 u) and K^+ (39 u), the spectra are defined as a new type: **Type-5**, which is considered to be created by ultra salt-rich ice grains (Nölle 2021) and not discussed in this thesis.

3. The mass range of the spectra start from the mass corresponding to the peak of H_3O^+ (19 u), so the spectra are suspected to be H_3O^+ (19 u) triggered. In this case, whether the H_3O^+ (19 u) peak amplitude is higher than those of Na^+ (23 u) and K^+ (39 u) or not (if they are recorded) is not observable. To deal with this situation, two criteria are used:

   (a) If peak $H_3O^+(H_2O)$ (37 u) is not detected, the peak H_3O^+ (19 u) is speculated to be lower than peak Na^+ (23 u) and thus the spectrum is classified into **Type-3**. Since peak $H_3O^+(H_2O)$ (37 u) is never detected in Type-3 spectra, where both H_3O^+ (19 u) or Na^+ (23 u) are recorded, this speculation is very safe.

   (b) If peak $H_3O^+(H_2O)$ (37 u) is detected, it is difficult to speculate whether peak H_3O^+ (19 u) is lower than Na^+ (23 u) or not, since in many spectra if peak $H_3O^+(H_2O)$ (37 u) is detected, peak H_3O^+ (19 u) is higher than peak Na^+ (23 u). Therefore, these spectra are assigned to **Type-?**

4. The mass range of the spectra start from the mass corresponding to the peak of Na^+ (23 u) or K^+ (39 u), so the spectra are suspected to be Na^+ (23 u) or K^+ (39 u) triggered. In this case, whether the H_3O^+ peak amplitude is higher than those of Na^+ (23 u) and K^+ (39 u) or not (if they are recorded) is not observable. However, since a spectrum is triggered by the its first peak which is high enough (if not impact triggered), the peak H_3O^+ (19 u) is supposed to lower than Na^+ (23 u) or K^+ (39 u) triggered. Otherwise, the peak H_3O^+ (19 u) triggers the spectra. Therefore, these spectra are classified into **Type-3**.

5. In cases where the calibration is too uncertain. The spectra are assigned to **Type-?**

4.3.3 Sub-classification of the Type-3 spectra into several subtypes

According to the existence and relative amplitudes of salt peaks, into Type-3 spectra or non-Type-3, all Type-3 spectra in the data set can be classified into subtypes.

4.3.4 Co-adding the spectra of subtypes

To reduce the effects of compositional variation between individual ice particles of a certain subtype and reveal hidden peaks produced by trace substances in the ice particles of a certain subtype, the spectra of the same subtypes are co-added to produce co-added spectra representing the subtypes. In addition, in order to estimate the overall composition of the Na-rich group (Section 4.4.2) Type-3 particles and reveal hidden peaks produced by trace substances in this group of ice particles, the spectra of major subtypes were co-added, which will be reproduced through laboratory experiments in Chapter 7 to determine the detection limits for the trace substances.

The software used for spectra co-adding is 'Browser', developed by Sascha Kempf. The spectra have different amplitudes and/or total integrated signal levels, due to variations in particle size and impact conditions, and were therefore normalised before co-adding. To reduce the influence of poor quality (e.g. noisy, late-triggered, saturated peaks) spectra on the sum spectrum, the following conditions and preprocessing steps were applied before co-adding:

Preprocessing before co-adding

1. Spectra with uncertain subtype classification were excluded.
2. Only spectra with a peak QI value of between 5 fC and 500 fC are used.
3. Spectra with no Na^+ (23 u) peak, due to Na^+ triggering the recording, are excluded.
4. Spectra with severely inverted (saturated) peaks are excluded.
5. Spectral baselines are manually corrected.

4.3.5 Statistics and plotting:

The CDA does not have the ability to explore directly the formation processes of ice grains under the surface of Enceladus. It can only explore the ice grains in space during plume flybys and E-ring traversals. CDA did not collect mass spectra of sufficiently good quality for a detailed investigation of variations in the salt-rich spectra during plume flybys, because it was not designed for the high impact fluxes. Therefore, spectra obtained from the E-ring are the main source of useful data for

understanding the range of CDA Type-3 spectra, despite the increased potential for grain evolution between formation and detection.

Apart from their compositions, Cassini's CDA instrument can obtain three observable physical/dynamical parameters about the grains, either directly or indirectly: distances from Saturn at the time of impact, impact speeds and rough directions, and the sizes of grains.

- Saturnian distance/particle age: The distance between Saturn's center and Cassini is accurately known through trajectory reconstruction (Bellerose et al. 2019) and information from e.g. Cassini's communications systems (RSS), as well as imaging (Bordi et al. 2005), and its unit used in my work is R_S. Distance from Saturn correlates approximately with the age of E-ring ice grains, as they move away from Saturn under the action of Saturn's oblate gravity field, plasma drag and electromagnetic forces (Horanyi et al. 1992). Therefore, the distribution of E-ring grains with distance at least partially reflects their dynamical evolution with time.

- Impact speeds: The charge-sensitive dust trajectory sensor (the QP detector) carried by CDA is suitable for detecting dusts with diameter bigger than ~ 3 μm (Kempf et al. 2006), which produce too many ions during impact. As a result, QI value is between 5 - 10 pC, which is too high for CDA to produce good spectra, i.e. the spectra are severely distorted. Therefore, the impact speeds of the particles corresponding to the spectra used in this work can not be measured by the dust trajectory sensor on CDA and an indirect method is used to estimate the impact speeds in this work. The impact speeds are estimated based on an approximation - E-ring particles orbit Saturn in the prograde direction in the ring plane. Knowing the distance from Saturn's center at which a grain was detected, the mass of Saturn and the speed of Cassini relative to Saturn, the impact speed - the relative speed between a particle and Cassini can be easily estimated. Although this "Kepler ram speed" assumes the grains to be in circular orbits, travelling directly down the boresight of the CDA instrument, which may not be the case, it provides a reasonable estimate for the average impact speed of an ensemble of grains.

- Grain sizes: The size and mass of ice grains is not measurable directly. The mass of an ice particle can be estimated with follow empirical equation (Eq. 4.1) (Srama 2009).

$$\log m = -4.15 + 0.588 \log QI - 5.59 \log v - 1.44 \log v \log QI \qquad (4.1)$$

m: The mass of one ice grain in kg

QI: The total positive charge collected at the ion grid after an impact

v: The impact speed calculated as above in km per second

To simplify the problem, all ice particles are regarded as spheres, so the mass, density and equivalent radius of one ice grain are described by the following equation:

$$m = \rho \frac{4}{3} \pi r^3 \tag{4.2}$$

Since the major component of the grains is water ice, the density is approximated as $1.0 \times 10^3\,\mathrm{kg/m^3}$.

In Section 4.4 correlations of Type-3 grain composition with distance to Saturn, impact speed and grain size are investigated in order to speculate on the evolution of the various salty icy grains in space.

4.3.6 The relation between impact speeds and important peak amplitude ratios in co-added spectra

In order to evaluate the peak ratio variation with impact speed, CDA spectra in different impact speed intervals were co-added. The spectra were normalised before co-adding. The same conditions and preprocessing steps as that in Section 4.3.4 were applied to reduce the influence of poor quality.

The impact speed were divided into four intervals: [3.8, 5] (3.8 km/s $\leq$ v $\leq$ 5 km/s), (5, 7] (5 km/s $<$ v $\leq$ 7 km/s), (7, 10] (7 km/s $<$ v $\leq$ 10 km/s), (10, 14.8] (10 km/s $<$ v $\leq$ 14.8 km/s).

The super carbonate rich subtype (A) and chloride rich subtypes (C,D, and E) are analyzed separately. The peak Na^+ (23 u) was always as the reference peak. The important salt peaks were analyzed.

4.4 Results

In this section, the analysis results of the compositional variation in Type-3 salt-rich ice grains, as revealed by their spectra are described in detail and discussed deeply.

4.4.1 Preliminary results of peaks analysis

Although the evidence of ongoing hydrothermal activity at the bottom of Enceladus' subsurface ocean (Hsu et al. 2015; Waite et al. 2017), along with Molecular hydrogen (Waite et al. 2017), imply that the subsurface ocean is habitable and plenty of organic could be dissolved in the salt rich ocean water, unfortunately I did not find any frequent and significant organic peaks in the Type-3 salt-rich spectra investigated for this work. The could mean the aforementioned 'suspected organics peaks' may be not from organics, and therefore the concentration of organics dissolved in Enceladus ocean is not high enough to be detected by Cassini. Other possible reasons for the lack of any obvious organic peaks in Type-3 spectra may be that peak suppression or random 'noise' is removing or hiding small peaks arising from low concentrations of organics.

Instead, it is found that the strong magnitude of the variations is somewhat surprising, although the variations between the E-ring CDA Type-3 spectra are known previously. If not the result of variations in impact speed or particle size (see below), then it may imply a strong variation of salty ice grain compositions in the E-ring, despite a common origin in the global subsurface ocean of Enceladus.

This variation may have formed prior to grain eruption from the 'tiger stripes' across the south polar region of Enceladus, or in space after eruption. It is likely however, that both stages would contribute to producing a range of ice grain compositions. It is therefore important to explore the causes of the variation.

4.4.2 Preliminary classification of spectra of E-ring salt-rich ice grains

The results of this preliminary classification process are shown in Table 4.1.

Type Name	Properties	Number	Percentage
Type-5	Ultra salt-rich spectra	14	1.3%
Type-3	Salt-rich spectra	995	92.4%
Type-?	Uncertain	68	6.3%
Total		1077	100%

Table 4.1: Preliminary classification of spectra from E-ring salt-rich ice grains

Type-5 spectra are considered to be created by ultra salt-rich ice grains, which

are believed to be significantly altered by space weathering of Type-3 ice grains (Nölle 2021). Therefore, the compositional signature of the Enceladus subsurface ocean is lost and thus they are not analyzed in this thesis. Type-? are also not analyzed, due to the uncertainties in spectral identification and poor quality peak profiles. Type-3 spectra, the majority of spectra in the dataset, are the focus of this work, because they reflect the composition of the Enceladean subsurface ocean. These spectra will be further classified into subtypes and statistically analysed.

Most Type-3 spectra possess strong sodium-related mass lines and tiny or no potassium-related mass lines. Only a small number of Type-3 spectra show the inverse case - strong potassium-related and tiny sodium-related mass lines. There are also a number of spectra showing both sets of strong mass lines. Therefore, at the first stage Type-3 spectra can be divided into three groups according to the presence and the intensity of the sodium- and potassium-related mass lines, which reflect the concentration of sodium and potassium in the salt-rich ice grains. The three groups are defined as following:

Na-rich group: Na-related peaks dominate these spectra with only tiny, or no, K-related peaks. This group represents the majority of CDA Type-3 spectra and shows strong internal variation, enabling it to be further classified into several subtypes.

The spectrum in Fig. 4.3 is an example of a typical member of the Na-rich group.

K-rich group: K-related peaks dominate these spectra, with only tiny, or no, Na-related peaks; The spectra of this group are not further sub-classified, due to its small population. All spectra of this group therefore belong to a single subtype: Subtype K.

Fig. 4.4 shows a typical example of a subtype K spectrum.

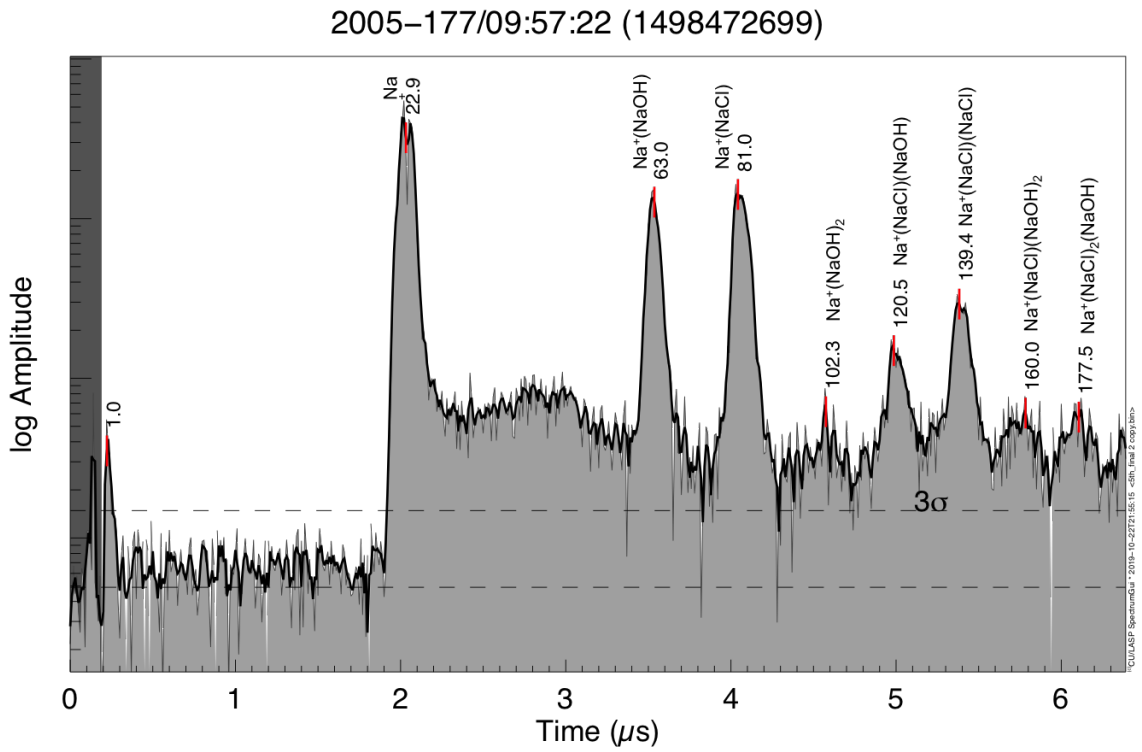

Figure 4.3: A typical Na-rich group member spectrum. Impact speed: 8.6 km/s. Stretch parameter a = 477 ns. Shift parameter b = -0.249 μs. (The peak on the far right may not show its maximum, so I can not label it.)

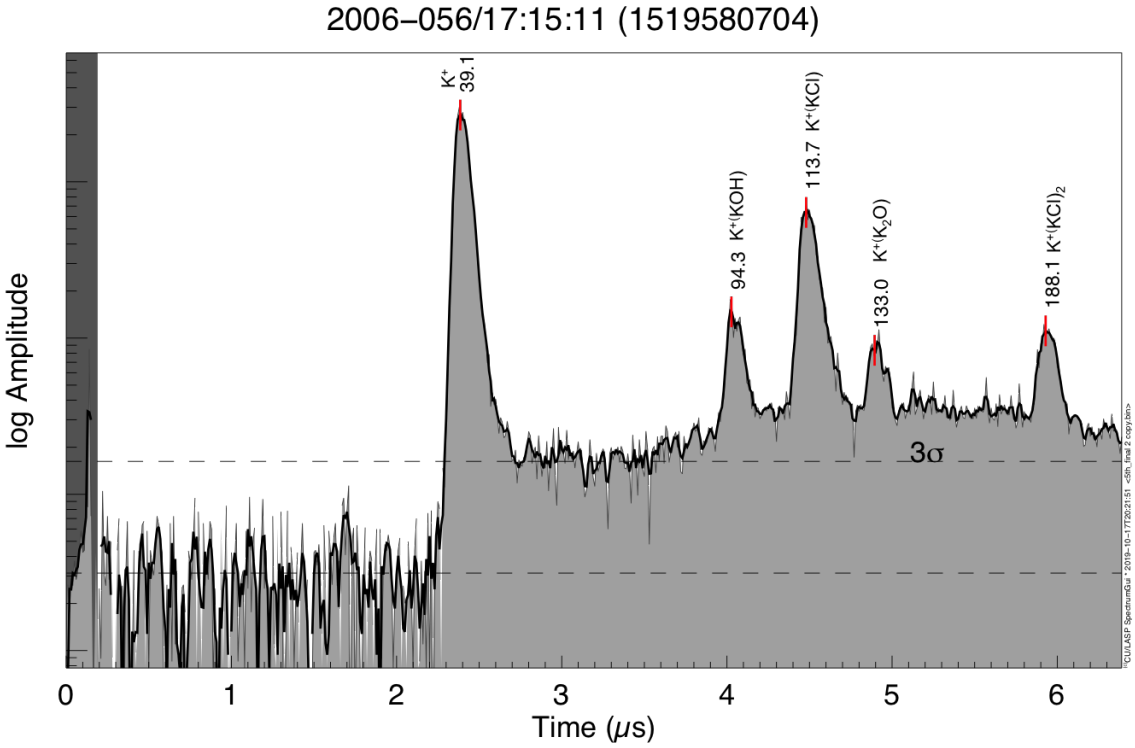

Figure 4.4: A typical K-rich group member spectrum (Subtype K). Impact speed: 5.6 km/s. Stretch parameter a = 475 ns. Shift parameter b = -0.585 μs.

Fig. B.1 in Appendix shows the co-added spectrum of subtype K. To illustrate the actual peak amplitudes - and hence their ratios - the spectra are shown on both logarithmic (in the upper figure panel) and linear (in the lower figure panel) scales.

Na and K-rich group: Both Na- and K-related peaks are present, and the amplitudes of the Na^+ (23 u) and K^+ (39 u) peaks are comparable. The spectra of this group are not further sub-classified due to its small population. All spectra of this group therefore belong to a single subtype: Subtype NaK.

Fig. 4.5 shows a typical example of a subtype NaK spectrum.

Fig. B.2 in Appendix shows the co-added spectrum of Subtype K. To illustrate the actual peak amplitudes - and hence their ratios - the spectra are shown on both logarithmic (in the upper figure panels) and linear (in the lower figure panels) scales.

The pie chart Fig. 4.6 shows the fractions of the three different major groups of Na, K and Na/K bearing Type-3 grains.

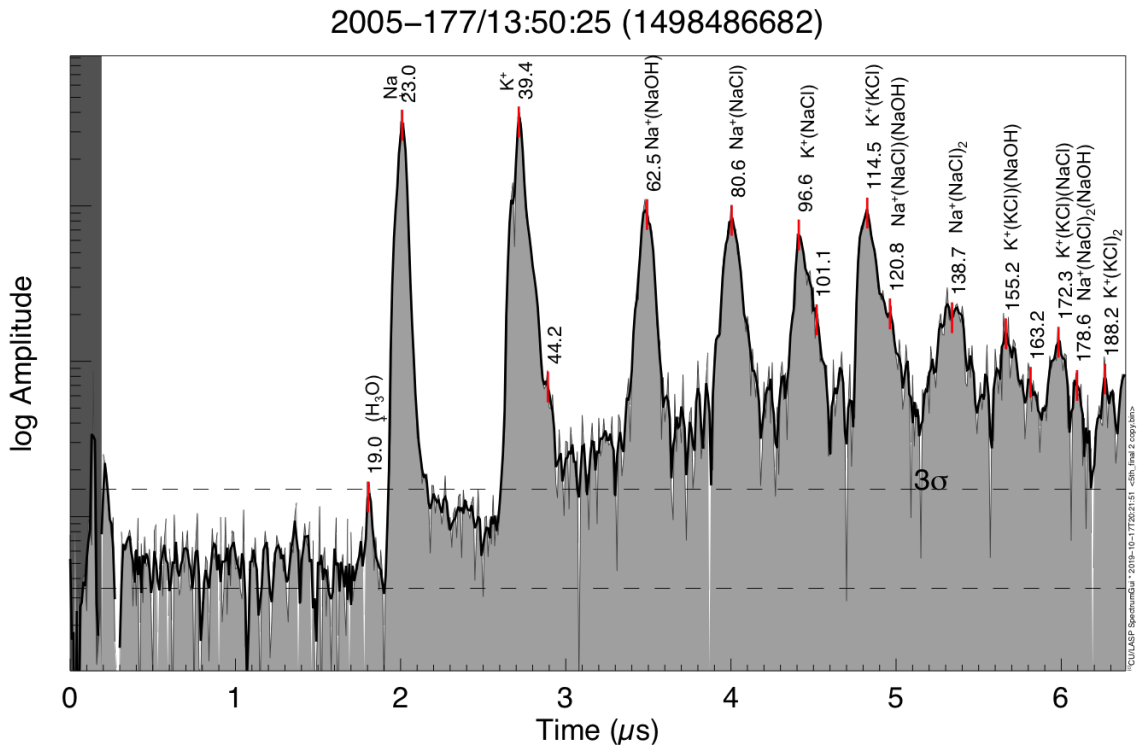

Figure 4.5: A typical Na and K-rich group member spectrum (Subtype NaK). Impact speed: 8.0 km/s. Stretch parameter a = 477 ns. Shift parameter b = -0.278 μs.

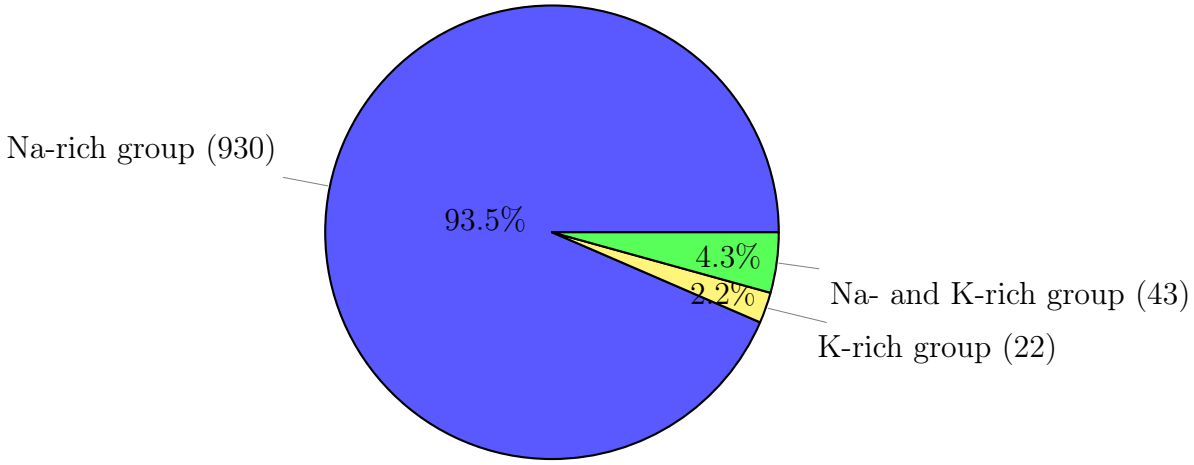

Figure 4.6: The fractions of the three groups of Type-3 (995 spectra in total).

Fig. 4.6 clearly demonstrates that: 1) Sodium is the major metal ion in Enceladus subsurface ocean; 2) the 'K-rich group' and 'Na- and K-rich group' are rare in quantity and proportion.

4.4.3 Further classification of the spectra of E-ring Na-rich ice grains

Further investigation reveals that the spectra of E-ring Na-rich ice grains are very diverse. Therefore, it is necessary to do the further classification for the further research.

92.7% (863 out of 930) of the 'Na-rich' Type-3 spectra have typical spectral profiles and exhibit a range of regularly reoccurring features. Therefore, they are named as *typical* Na-rich Type-3 spectra and corresponding ice particles are named *typical* Na rich Type-3 ice particles. The rest of Type-3 spectra (67 spectra) do not have typical spectral profiles, because they have more complex peaks or profiles, which are either too distorted to recognize or contaminated with unclear ion species. Therefore, they are named as *atypical* Na-rich Type-3 spectra and the corresponding ice particles are named *atypical* Na-rich Type-3 ice particles. (Fig. 4.7).

The *typical* Type-3 spectra can be further classified based on the presence and the relative amplitudes of representative peaks related to specific anions, such as Na^+ (23u), NaOH-related peaks, NaCl-related peaks and Na_2CO_3-related peaks. In this case, related peaks are the base cation peak (e.g. NaOH, NaCl etc.) and other clusters containing it. The *atypical* Type-3 spectra are not further classified, because they are a minority and non-representative sample, and entirely assigned

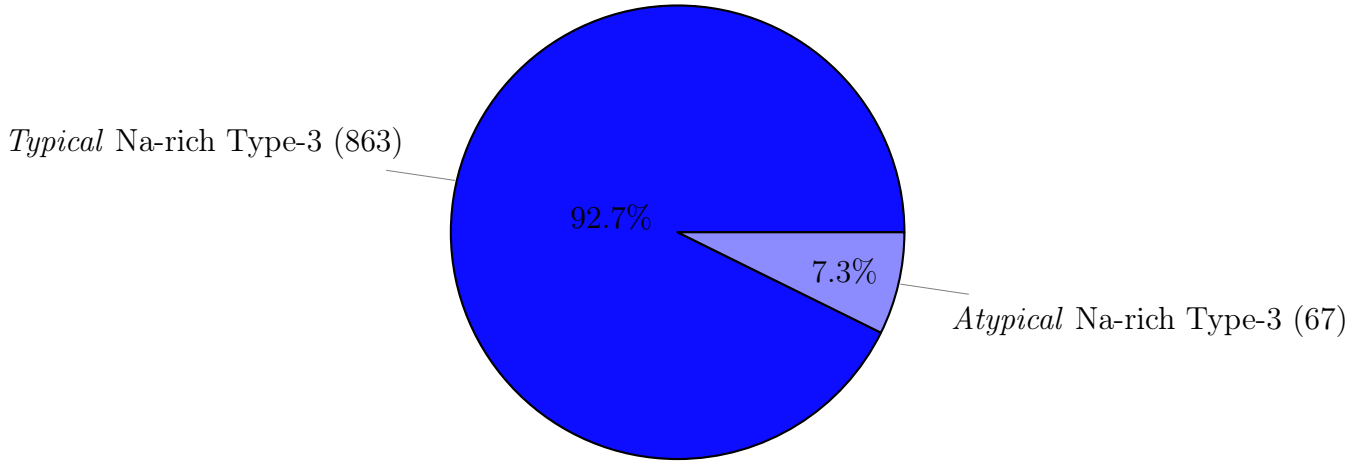

Figure 4.7: The fractions of typical and atypical Na-rich Type-3 spectra of Na rich group (930 spectra in total).

into a single Subtype Na-?. The 'K-rich group' and 'Na- and K-rich group' spectra are also not further classified, due to their rarity as previously mentioned.

Sub-classification criteria for the *typical* Na-rich spectra:

The high amplitude 'signature' peak at 23 u, corresponding to Na^+, is the common feature of the Na-rich CDA Type-3 spectra. As well as this peak, there are also other Na-related peaks. The existence and the relative amplitudes of these Na-related peaks vary obviously for Na-rich CDA Type-3 spectra, and thus can be used as the criteria for the sub-classification of the Na-rich CDA Type-3 spectra as well as the corresponding ice grains. Using these criteria, the *typical* Na-rich CDA Type-3 spectra can be sub-classified.

Na-related peaks used for sub-classification are classified into four main classes based upon the anions they contain:

1. The OH^- related peaks:
   $Na^+(NaOH)$, $Na^+(NaOH)_2$, $Na^+(NaCl)(NaOH)$, $Na^+(Na_2CO_3)(NaOH)$...
   (Note: OH^- could also come from the breakup of water molecules, as evidenced by the fact that even if an NaOH-free solution is initially used in the laboratory experiments, these peaks are still present and significant.)
2. The CO_3^{2-} related peaks:
   $Na^+(Na_2CO_3)$, $Na^+(Na_2CO_3)(NaOH)$...
3. Peak $Na^+(Na_2O)$ (85u):
   Peak $Na^+(Na_2O)$ (85u) appears concurrently with large $Na^+(Na_2CO_3)$ peaks.

Thus, Na_2O is considered to be due to the breakup of Na_2CO_3 at high impact speeds. This peak is considered as the defining feature of 'super carbonate-rich' spectra.

4. The Cl^- related peaks:
   $Na^+(NaCl)$, $Na^+(NaCl)_2$, $Na^+(NaCl)(NaOH)$...

The definition of the subtypes of the *typical* Na-rich spectra:

The five majority subtypes of spectra: A, B, C, D and L will be introduced first, followed by the minority subtypes (H and E) in detail.

- **The major subtypes:** There are five major subtypes: A, B, C, D and L. Subtype A and Subtype B share some common feature, so they are introduced together firstly. Subtype C and Subtype D share some common feature, so they are introduced together. Subtype L is introduced at the last.

  Subtype A and subtype B:

  Both Subtype A and Subtype B have OH^- related peaks and lack Chloride related peaks. The difference is at the relative amplitude of CO_3^{2-} related peaks and the existence of peak $Na^+(Na_2O)$ (85 u). Their definition are as following:

  Subtype A is the most carbonate rich subtype. The definition of Subtype A spectra is:

  1. Both the OH^- related peaks and the CO_3^{2-} related peaks are detectable (higher than 3σ).
  2. The Cl^- related peaks are, if at all, lower than 3σ.
  3. Peak $Na^+(Na_2O)$ (85 u) is detectable or, if not, the amplitude of peak Na_2CO_3 (129 u) is bigger than 0.2 times [1] that of peak $Na^+(NaOH)$ (63 u). This is the defining criteria to distinguish Subtype A from Subtype B.

  In addition, there are also some other features which most Subtype A spectra possess, and which can aid the identification/classification of these spectra.

  1. Three peaks at masses Na^+ (23 u), $Na^+(NaOH)$ (63 u) and Na_2CO_3 (129 u) are usually very high, with similar amplitudes, and also very wide. Other peaks within the spectra are very small compared to these three peaks and the spectra are thus described as having a 'trident' shape.

[1] The determination and the discussion of the threshold are in Appendix C.

2. If the spectra have high S/N, peak $Na^+(Na_2O)$ (85 u) is usually detectable, which is never seen in the spectra of other subtypes and thus unique for subtype A.

Fig. B.3 in Appendix shows a typical example of subtype A spectra. Fig. 4.8 shows the co-added spectra of subtype A. To illustrate the actual peak amplitudes - and hence their ratios - the spectra are shown on both logarithmic (in the upper figure panel) and linear (in the lower figure panel) scales.

Subtype B, as with subtype A, is also chloride poor, and it is often believed to contain a small amount of carbonate, because the spectra often show a small peak at around 129 u, identified as $Na^+(Na_2CO_3)$. The definition of Subtype B spectra is:

1. At least two OH^- related peaks are visible.
2. The Cl^- related peaks are not detectable (lower than 3σ, if at all).
3. The peak $Na^+(Na_2O)$ (85 u) is not detectable (lower than 3σ, if at all).
4. If a peak $Na^+(Na_2CO_3)$ (129 u) is present then it has to be less than or equal to 0.2 times the amplitude of $Na^+(NaOH)$ (63 u).

As with Subtype A, there are also some other features which most Subtype B spectra possess and which aid identification.

1. All peaks are very narrow.
2. Only peak Na^+ (23 u) and OH^- related peaks (such as $Na^+(NaOH)$ (63 u)) always are by far the largest peaks in the spectra.
3. Almost half of the spectra have a small peak at approximately 129 u (higher than 3σ), apart from in the low signal to noise cases [2].

Fig. B.4 in Appendix shows a typical example of subtype B spectra. Fig. 4.9 shows the co-added spectra of subtype. To illustrate the actual peak amplitudes - and hence their ratios - the spectra are shown on both logarithmic (in the upper figure panels) and linear (in the lower figure panels) scales.

Subtype C and Subtype D:

These two subtypes are very similar: Both lack CO_3^{2-} related peaks and possess Cl^- related peaks. The only difference in definition between them is that in Subtype C spectra the first OH^- related peak - $Na^+(NaOH)$ (63 u) is higher than the first Cl^- related peak $Na^+(NaCl)$ (81 u); in contrast, in Subtype D spectra the first OH^- related peak - $Na^+(NaOH)$ (63 u) is lower than the first Cl^- related peak $Na^+(NaCl)$ (81 u). This means that if the

[2]It is likely that the non-detection of the peak $Na^+(Na_2CO_3)$ (129 u) in these spectra is due to the noise level, rather than the lack of carbonate in the grains.

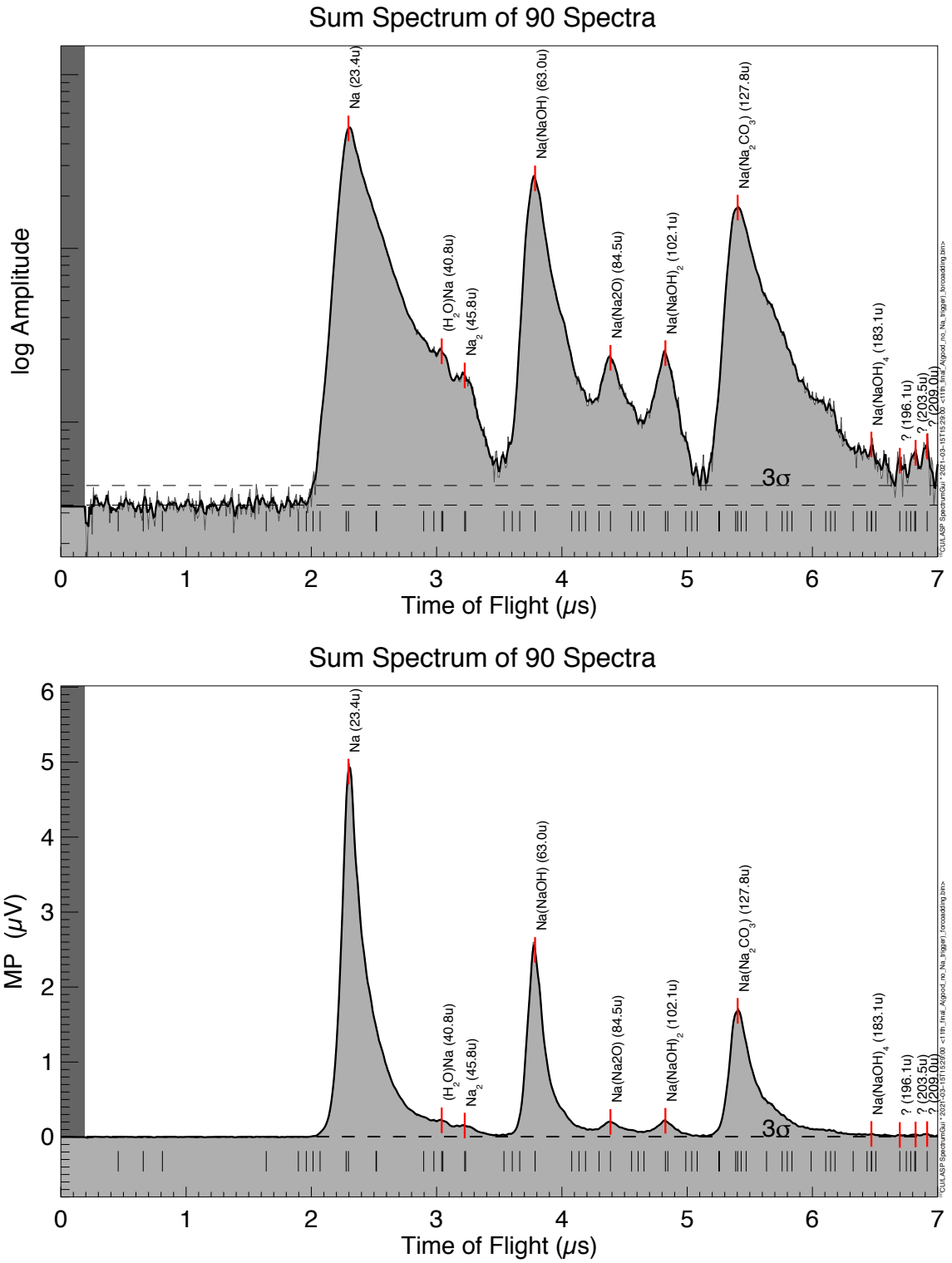

Figure 4.8: The co-added subtype A spectrum (upper panel: logarithmic amplitude scale; lower panel: linear amplitude scale).

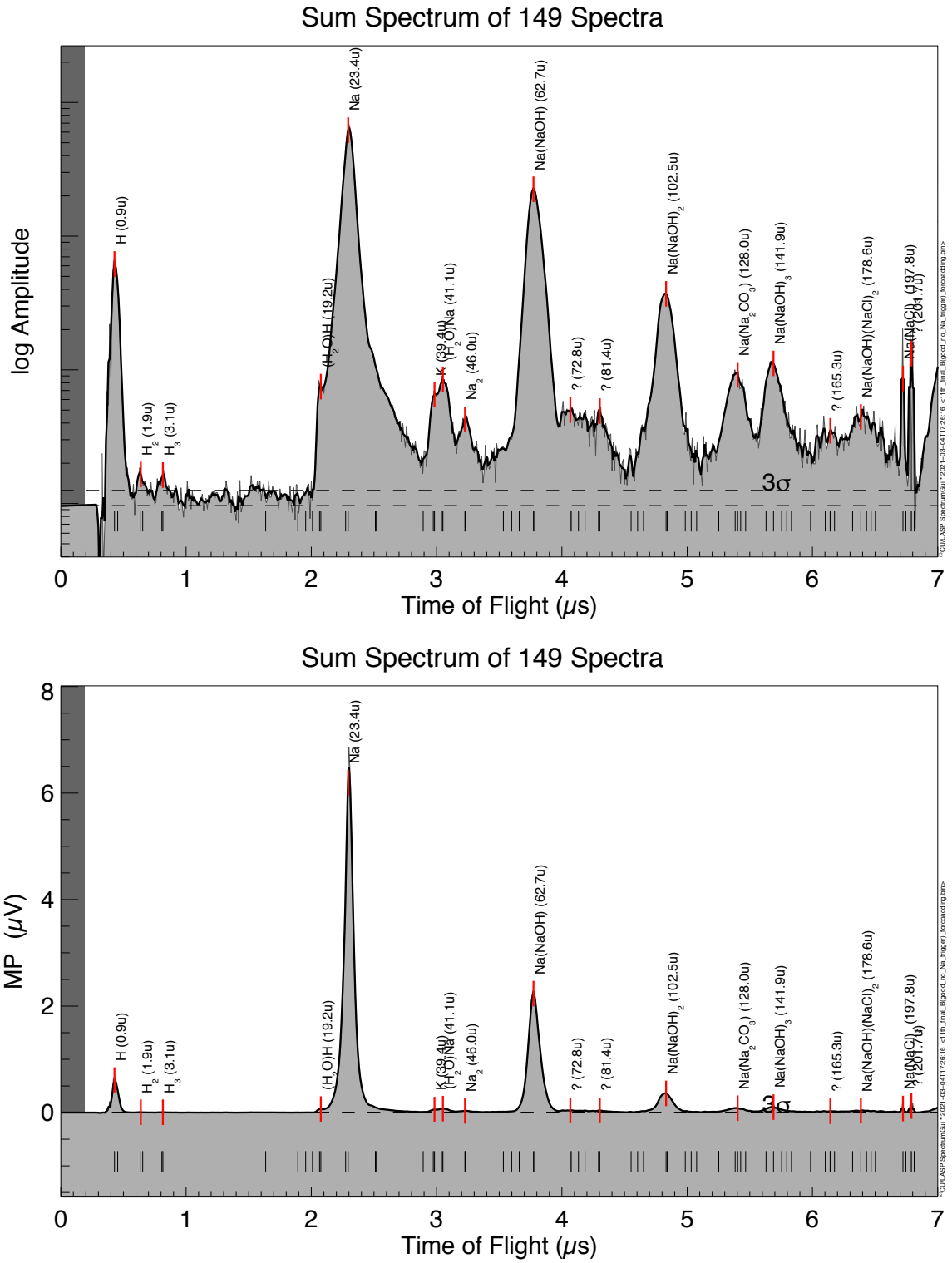

Figure 4.9: The co-added Subtype B spectrum (upper panel: logarithmic amplitude scale; lower panel: linear amplitude scale).

impact velocities are the same, the ice grains of Subtype D spectra are richer in chloride compared to those of Subtype C. An additional difference (although not used in the definition) between these two kinds of spectra is that peaks in Subtype D spectra are usually wider than those in Subtype C.

The definition of **Subtype C** spectra:

1. Both OH^- and Cl^- related peaks are visible.
2. The CO_3^{2-} related are, if at all, lower than 3σ.
3. The first OH^- related peak - Na^+(NaOH) (63 u) is higher than the first Cl^- related peak - Na^+(NaCl) (81 u).

Fig. B.5 in Appendix shows an example of typical Subtype C spectra. Fig. 4.10 shows the co-added spectra of subtype. To illustrate the actual peak amplitudes - and hence their ratios - the spectra are shown on both logarithmic (in the upper panel) and linear (in the lower panel) scales.

The definition of **Subtype D** spectra:

1. Both OH^- and Cl^- related peaks are visible.
2. The CO_3^{2-} related peaks are lower than 3σ.
3. The first OH^- related peak - Na^+(NaOH) (63 u) is lower than the first Cl^- related peak Na^+(NaCl) (81 u).

Fig. B.6 in Appendix shows an example of typical Subtype D spectra. Fig. 4.11 shows the co-added spectra of Subtype D. To illustrate the actual peak amplitudes - and hence their ratios - the spectra are shown on both logarithmic (in the upper panel) and linear (in the lower panel) scales.

Subtype L:

The last subtype is **Subtype L**. It is named as L due to the 'low' amplitude of peaks other than peak Na^+ (23 u) and Na^+(OH) (63 u), i.e. all other peaks are lower than 3σ. In most time, although higher than 3σ, peak Na^+(NaOH) (63 u) is much lower than peak Na^+ (23 u). Another important feature is that Subtype L spectra have low S/N, so they show too few details (Characteristic peaks) to be assigned to other subtypes. The composition is therefore not well constrained.

The definition of **Subtype L** spectra is:

1. Cl^- and CO_3^{2-} related peaks are not detectable (lower than 3σ) in a one spectrum.
2. Apart from the large peak Na^+ (23 u) (or Na^+ (23 u) as the trigger peak), there is only the first OH^- related peak Na^+(NaOH) (63 u) in a spectrum.

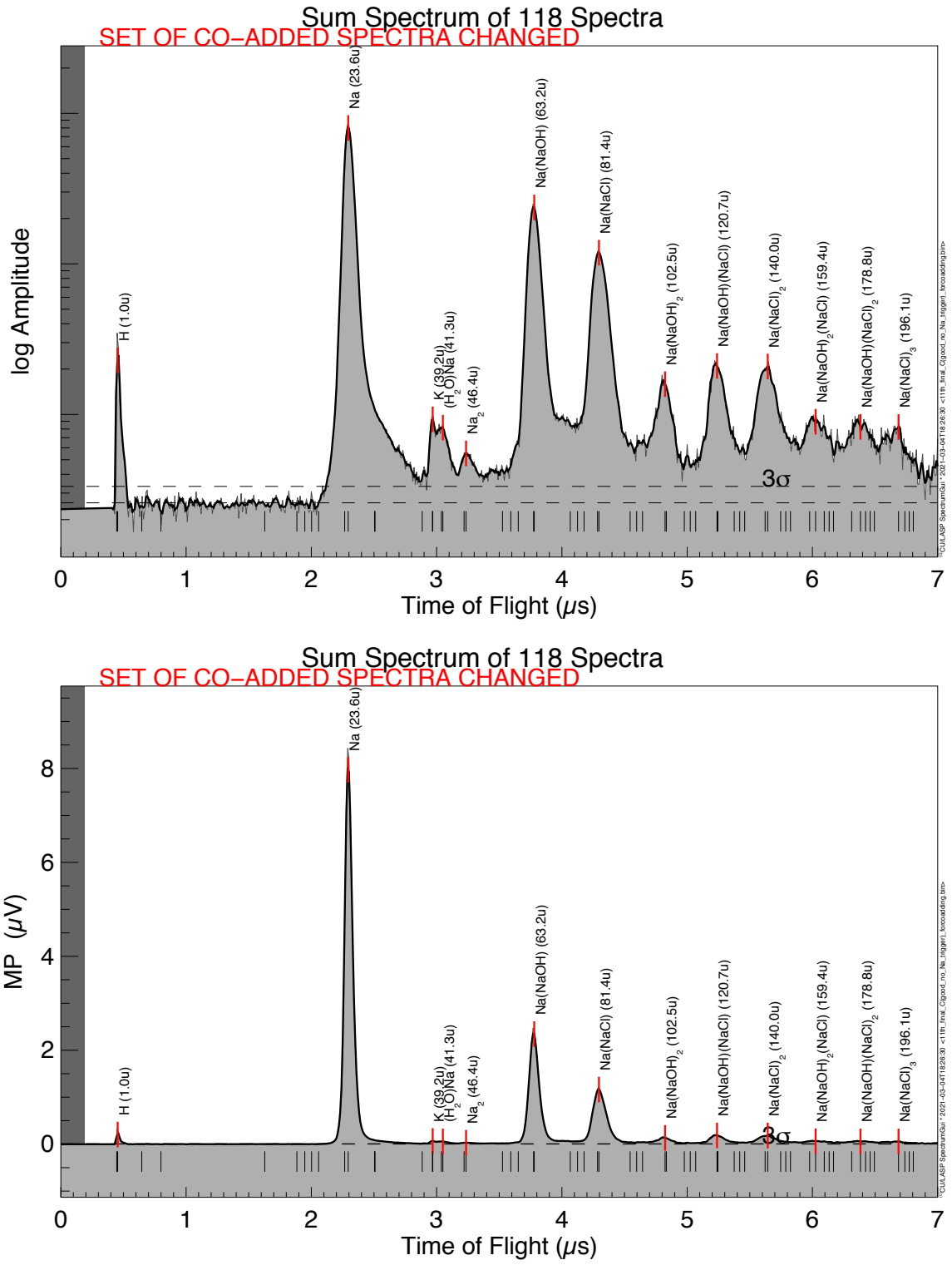

Figure 4.10: The co-added Subtype C spectrum (upper panel: logarithmic amplitude scale; lower panel: linear amplitude scale).

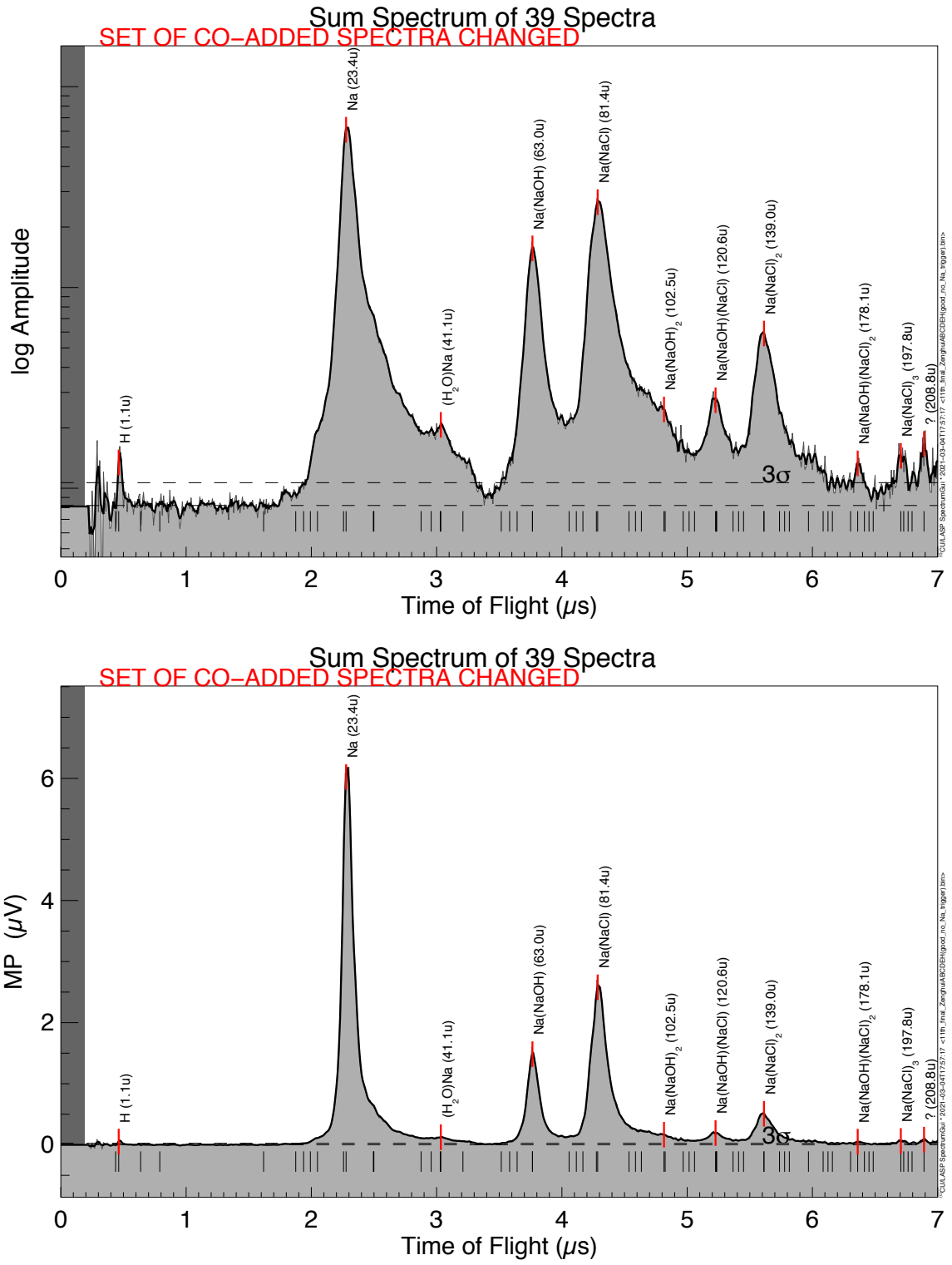

Figure 4.11: The co-added Subtype D spectrum (upper panel: logarithmic amplitude scale; lower panel: linear amplitude scale).

Fig. B.7 in Appendix shows a typical example of subtype L spectra. Fig. 4.12 shows the co-added spectrum of Subtype L. To illustrate the actual peak amplitudes - and hence their ratios - the spectra are shown on both logarithmic (in the upper figure panel) and linear (in the lower figure panel) scales. In the co-added spectrum peak $Na^+(NaOH)_2$ (103 u) becomes significant. It seems that peak at mass 73 u (or 72 u) and at mass 81 u appears in the co-added spectrum, but the existence of these two peaks is uncertain because these two peaks are so flat. The appearance of peak $Na^+(NaOH)_2$ (103 u) implies that the ice particles producing subtype L spectra could have the similar composition as the ice particles producing Subtype B spectra.

Fig. 4.17 provides an overview of the final results of the classification of potential salt rich spectra:

- **The minor subtypes:**

  Subtype H looks like a hybrid of the carbonate and chloride subtypes. Their definition is therefore:

  The OH^- related peaks, the Cl^- related peaks and the CO_3^{2-} related peaks coexist in the same spectrum.

  Fig. B.8 in Appendix shows a typical example of subtype H spectra. Fig. 4.13 shows the co-added spectrum of Subtype H. To illustrate the actual peak amplitudes - and hence their ratios - the spectra are shown on both logarithmic (in the upper figure panel) and linear (in the lower figure panel) scales.

  Members of this subtype are very rare in the dataset considered here, with only 14 identified.

  Subtype E is an extremely chloride rich spectral subtype and it is defined by:

  Only the Cl^- related salt peaks are visible, and both OH^- and CO_3^{2-} related peaks are absent.

  Members of Subtype E are extremely rare in the dataset considered here, with only 3 identified. Two of these three Subtype E spectra have very low QI values (1 fC and 2 fC, respectively) and are suspected to be Na-triggered. Thus, the peak Na^+ (23 u) is not recorded in these two spectra. There is only one Subtype E spectrum with peak Na^+ (23 u) recorded, and it is considered as the only archetypal example of Subtype spectra. Thus, it is impossible to co-add Subtype E spectra. Fig. 4.14 shows the only archetypal example of a subtype E spectrum. As with subtype D spectra, the peaks of this Subtype E spectrum are very wide in comparison to the peaks in subtype B and C spectra.

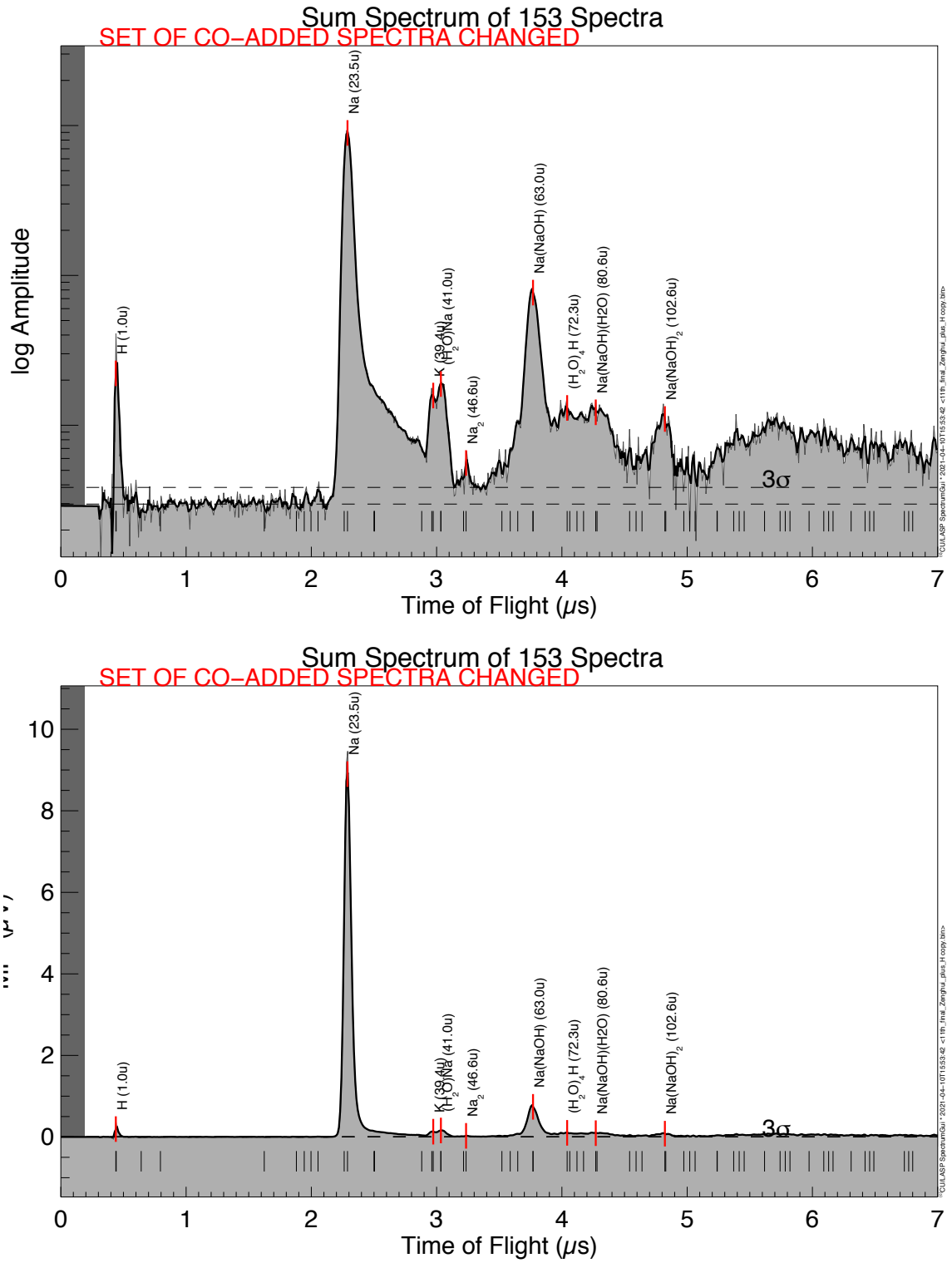

Figure 4.12: The co-added Subtype L spectrum (upper panel: logarithmic amplitude scale; lower panel: linear amplitude scale).

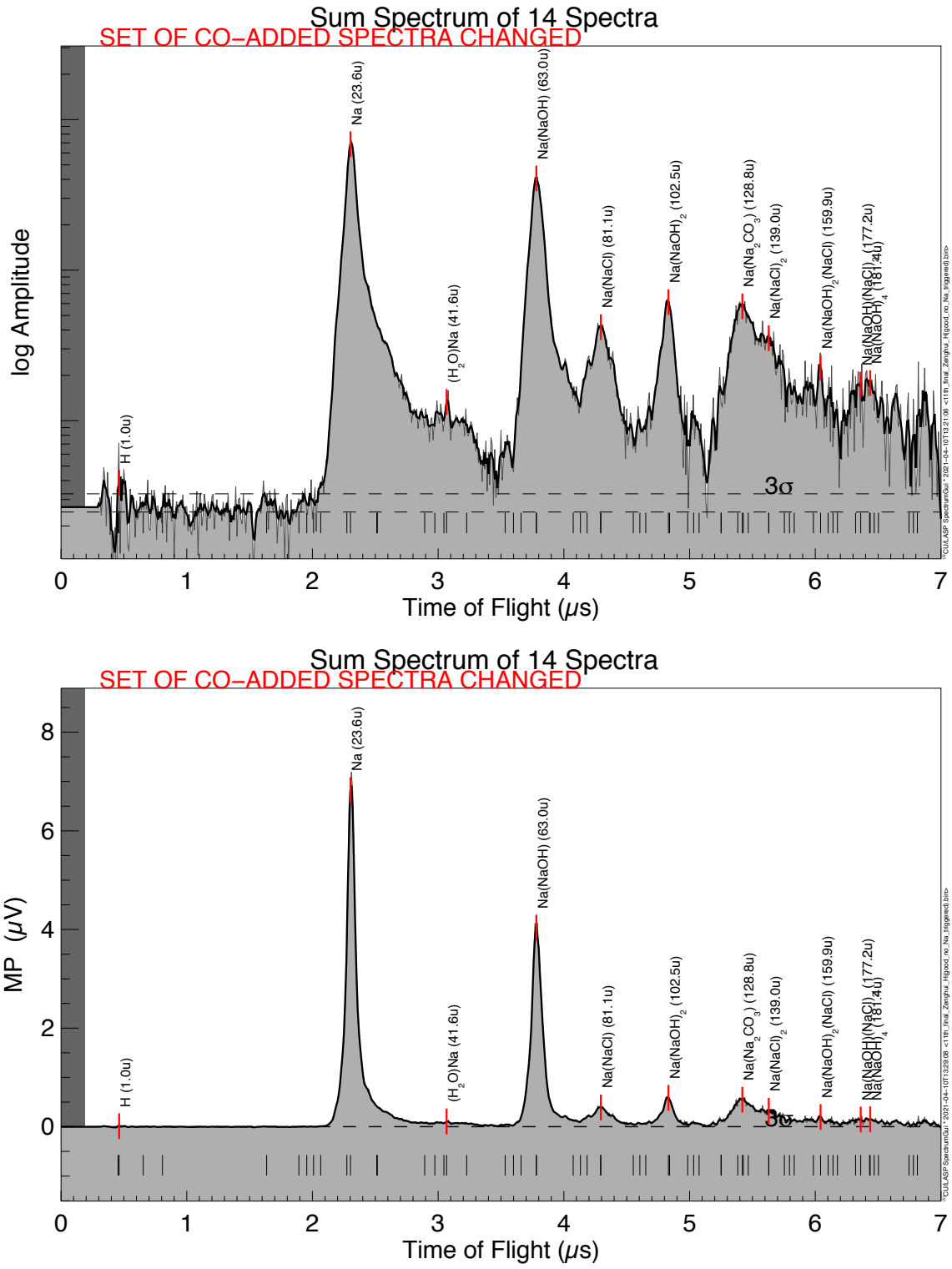

Figure 4.13: The co-added Subtype H spectrum (upper panel: logarithmic amplitude scale; lower panel: linear amplitude scale).

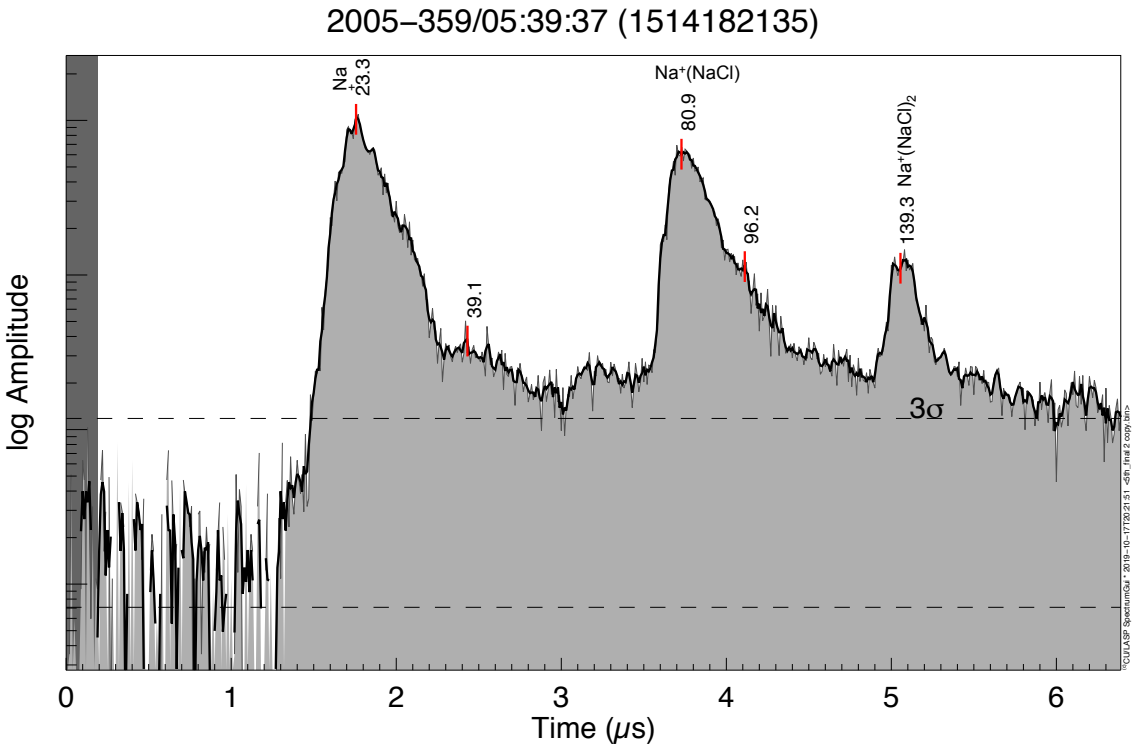

Figure 4.14: The archetypal Subtype E spectrum. Impact speed: 7.1 km/s. Stretch parameter a = 473 ns. Shift parameter b = -0.527 μs.

Subtype E spectra can only be mimicked with acidic solutions of NaCl (pH $\leq$ 2) in our laboratory. Since there is only 3 spectra of this subtype, a statistically-relevant analysis here is not appropriate and Subtype E will not be considered further.

There are 863 *typical* CDA Type-3 salt-rich spectra in total, which can be classified into these subtypes. Table 4.2 shows a summary of the definitions of the subtypes of *typical* CDA Type-3 salt-rich spectra, classified based on the the presence and relative amplitudes of salt cluster peaks. The numbers of spectra in each subtypes are also listed.

Subtype		Chloride poor		Mix	Chloride rich			None
		A	B	H	C	D	E	L
Number		151	190	15	155	62	3	287
Salt Cluster Peak	OH^-	+	+ (at least 2)	+	+	+	-	+ (only 1)
	CO_3^{2-}	+	+/-	+	-	-	-	-
	O^{2-}	+/(- 129 u > 0.2×63 u)	-	+	-	-	-	-
	Cl^-	-	-	+/-	+	+	+	-
	Other features		129 u ≤ 0.2×63 u		63 u > 81 u	63 u ≤ 81 u		

Table 4.2: The definitions of the subtypes of *typical* CDA Type-3 salt-rich spectra and the numbers of spectra in each subtypes. There are 863 *typical* CDA Type-3 salt-rich spectra in total, which are able to be classified into these subtypes. A + sign denotes the present of particular component related peaks and a - sign denotes the absence of particular component related peaks. The > and < signs refer to the relative amplitudes of two peaks.

Co-added spectra from different subtypes of Na-rich group Type-3 spectra

Fig. 4.15 shows the co-added spectrum from the Subtypes A, B, C, D, E and H, in which Subtypes E and H are minor subtypes. Fig. 4.16 shows the co-added spectrum from the Subtypes A, B, C and D, all of which are major subtypes. Subtype L spectra are not used for co-adding, because they contain few informative salt peaks, such as Cl^- related peaks and CO_3^{2-} related peaks. These two co-added spectra are almost the same, since the total number of the extra spectra from Subtypes E and H in Fig. 4.15 is only 14. Both these two co-added spectra are similar to the co-added spectrum in the Fig. 1(b) in Postberg et al. (2009b), which is co-added from the spectra of Na-rich water-ice particles. The difference is that the Cl^- related peaks and CO_3^{2-} related peaks are relatively high in this work, i.e, peak $Na^+(NaCl)$ (81 u) and peak $Na^+(Na_2CO_3)$ (129 u) are significantly higher than peak $Na^+(NaOH)_2$ (103 u) in this work, which is not the case in Postberg et al. (2009b).

- Co-added spectrum of subtypes of A, B, C, D, E, H spectra

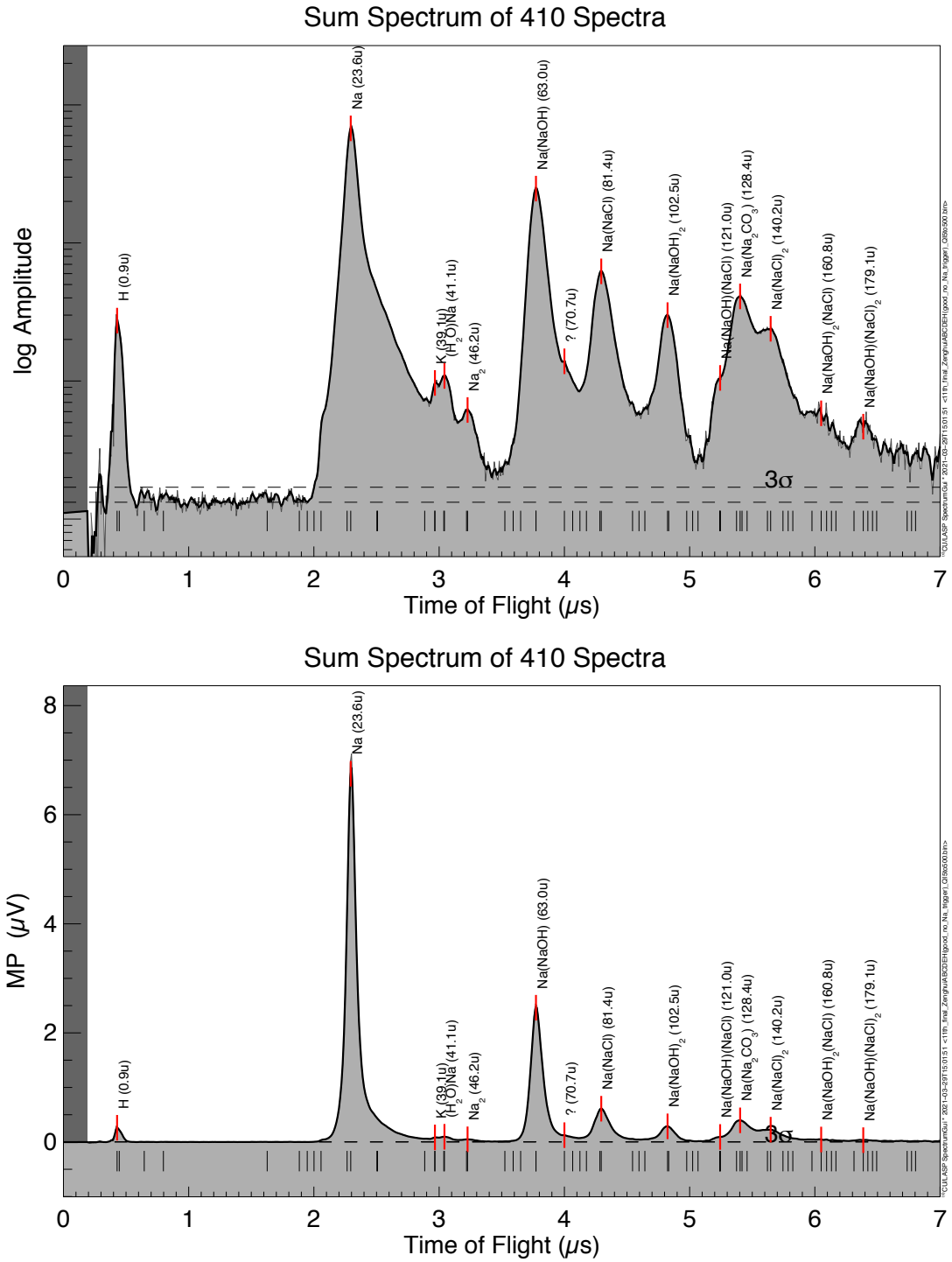

Figure 4.15: The co-added spectrum of Subtypes A, B, C, D, E and H. (upper panel: logarithmic amplitude scale; lower panel: linear amplitude scale).

- Co-added spectrum of subtypes of A, B, C, D spectra

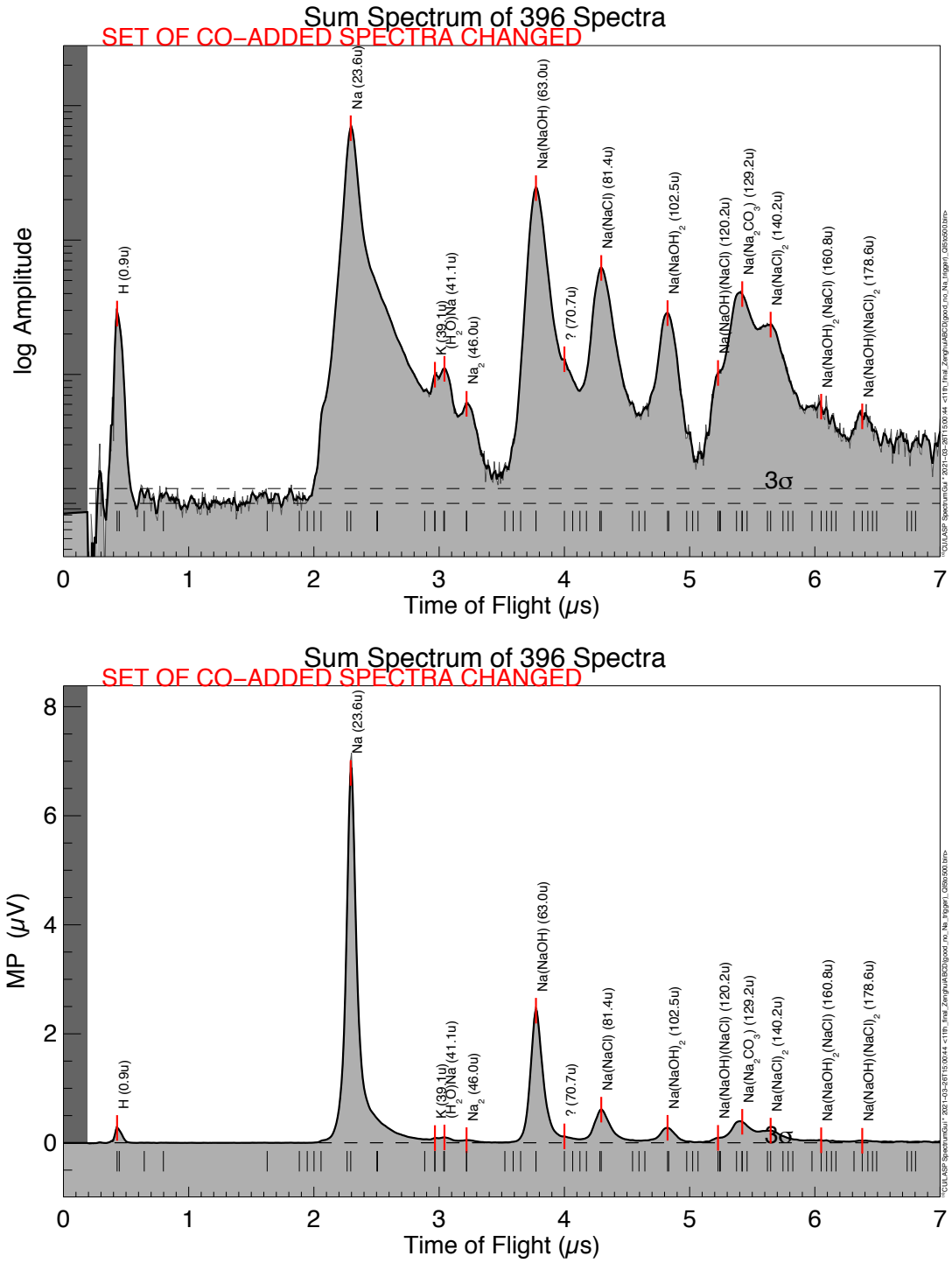

Figure 4.16: The co-added spectrum of Subtypes A, B, C, and D. (upper panel: logarithmic amplitude scale; lower panel: linear amplitude scale).

The classification of all of the spectra

Fig. 4.17 provides an overview of the final result of the classification of all of the spectra in the original dataset used in this thesis:

- Type-5: Ultra salt-rich spectra (14)
- Type-3: Salt-rich spectra (995)
  - Na-rich group (930)
    - Typical (863)
      - Subtype A (155)
      - Subtype B (186)
      - Subtype H (15)
      - Subtype C (155)
      - Subtype D (62)
      - Subtype E (3)
      - Subtype L (287)
    - Atypical: Subtype Na-? (67)
  - K-rich group: Subtype K (22)
  - Na- and K-rich group: Subtype NaK (43)
- Type-?: Suspected salt-rich spectra (68)

Figure 4.17: Further sub-classification of spectra of E-ring salt-rich ice grains (1077 spectra in total). The numbers in brackets are the numbers of spectra of corresponding types/groups/subtypes.

4.4.4 The impact speed of different spectral subtypes

Table 4.2 demonstrates that only Subtypes A, B, C, D, L have large enough sample sizes for a reliable statistical analysis, with small margins of error and high confidences. In addition, all of them are Na-rich spectra, potentially better suited for comparison. Therefore, only these 5 major subtypes (845 spectra in total) are used for statistical analysis to explore the distribution and the evolution of the concentration of carbonate and chloride in the E-ring salt rich ice grains.

Poor quality spectra and their statistical effect

Some spectra from the major subtypes, especially from Subtype A, are considered to be poor quality spectra or unreliable spectra, primarily due to uncertainties in their sub-classification, for two reasons:

- The tops of some important peaks are so flat (usually happening in spectra with low mass resolution) that it is hard to determine the position of peak maxima.
- Spectral profiles are distorted to the point that some peak maxima are shifted.

The combination of these issues introduces doubt about the calibration of these spectra, with ensuing uncertainty in the assignment of spectral subtypes. Fig. 4.18 shows an example of bad quality Subtype A spectrum:

Table 4.3 lists the number and percentage of bad quality spectra in every major subtype.

Subtype	A	B	C	D	L	Sum
Number of total spectra	155	186	155	62	287	845
Number of good quality spectra	126	181	144	55	287	793
Number of bad quality spectra	29	5	11	7	0	52
Percentage of bad quality spectra	18.7 %	2.7 %	7.1 %	11.3 %	0 %	6.2 %

Table 4.3: The numbers of total spectra, good quality spectra, bad quality spectra for each major subtype, as well as the percentage of bad quality spectra for each major subtype.

Table 4.3 shows the numbers of total spectra, good quality spectra, bad quality spectra for each major subtype, as well as the percentage of bad quality spectra for each major subtype. It indicates that 793 from 845 spectra are considered to have good quality, i.e. the peak calibrations have high certainty. It also indicates that Subtype A and Subtype D have more than 10 % poor quality spectra. These two subtypes usually have broader peaks, and the inclusion of poor quality spectra may bias the statistical results. However, removing over 10% of these spectra is undesirable, and to quantify any bias the statistical behavior of the subtypes both including and excluding the bad quality spectra was investigated.

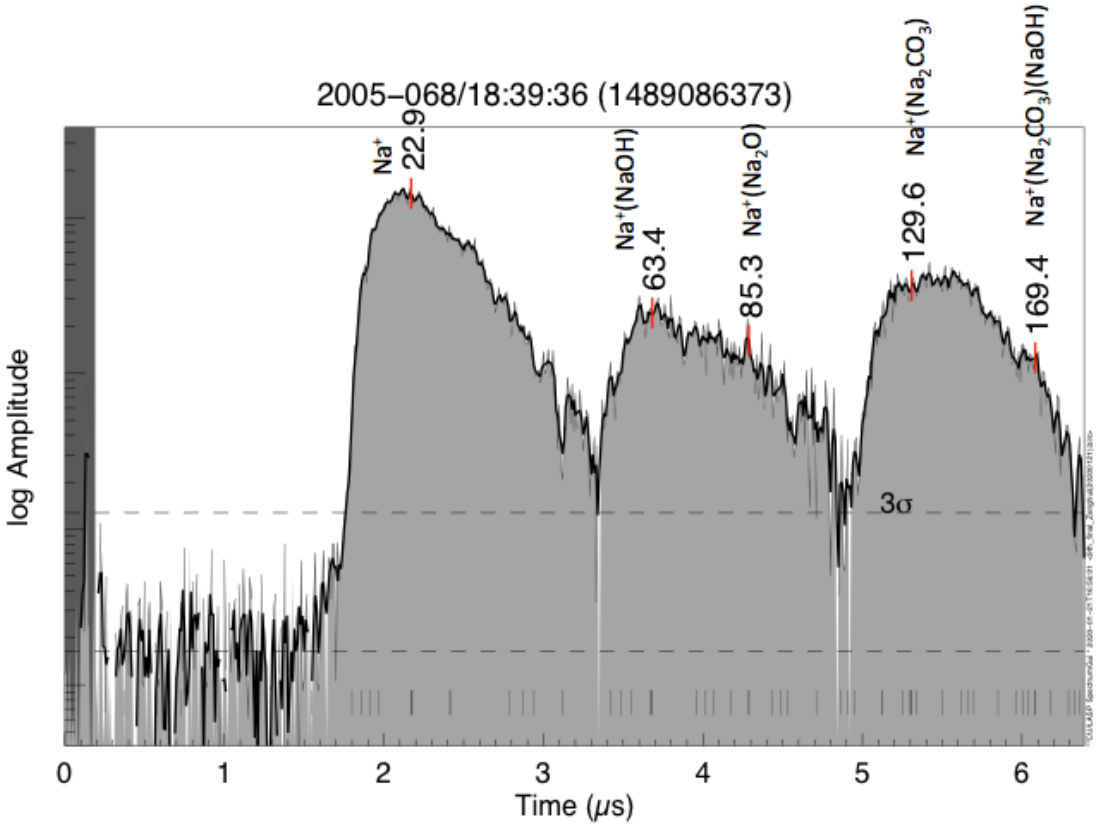

Figure 4.18: A typical low quality Subtype A spectrum. Impact speed: 8.4 km/s. Stretch parameter a = 475 ns. Shift parameter b = -0.100 μs. The top of the peak approximately located at 129 u is so flat that it is hard to determine where the maximum is. Therefore, there is some uncertainty on whether it is peak Na_3CO_3. If it is not, the spectra is not Subtype A. Therefore, there is some uncertainty about the subtype of this spectrum and it thus is considered as a bad quality Subtype A spectrum.

The aim of the statistical analysis is to analyse the distribution of Na-rich ice grains with different compositions with respect to distance to Saturn and the sizes of the particles. To achieve this, first the distributions with respect to impact speeds have to be considered, so that the influence of impact speeds on spectral appearance can be minimized.

Impact speed distribution of subtypes, and artifacts caused by impact speeds:

The plot in Fig. 4.19 shows the distribution of the five major spectral subtypes, including bad quality spectra, with impact speed, which shows the effect of impact speed on the subtypes. The plot corresponding to the five major spectral subtypes excluding bad quality spectra shows the similar trends and is attached in Appendix (Fig. E.1). The plots demonstrate following trends:

The percentage of each bin of Subtype B spectra appears to have a positive linear correlation with impact speed, which is particularly obvious for higher impact speeds (≥ 9 km/s). In contrast, Subtype L spectra show a negative linear correlation with impact speed, which is also particularly obvious for higher impact speeds (≥ 8 km/s). The imply that the high impact speeds (high specific kinetic energy) are more likely to convert Subtype L spectra to Subtype B spectra, which could be explained by that the high impact speeds cause higher signal to noise ratio so that more Cl^- related peaks extend the 3σ threshold to be detectable. In addition, Subtype A spectra, even if to a lesser extent, also show a negative linear correlation with impact speed. This could mean high impact speeds (high specific kinetic energy) are more likely to destroy CO_3^{2-} related peaks, so that some Subtype A spectra are converted to Subtype B spectra. Subtypes C and D spectra do not show these kinds of linear correlation. This means impact speeds do not influence the behavior of Cl^- related peaks obviously in the range of 3.5 km/s to 16.6 km/s.

The distribution of the spectral subtypes is impact speed dependent to some extent, at least for Subtypes A, B and L. To minimise this effect, such that variations of the intrinsic property of the grains, their composition, are not swamped or hidden by variations in the extrinsic property of their impact speeds, a subsample of the data, over a restricted range of impact speed, can be used.

It can be seen that the proportions of the various spectral subtypes do not change too much with impact speed in the range between 5 km/s and 8 km/s, which includes $\sim 59\%$ of the population.

Therefore, spectra obtained at impact speeds between 5 km/s and 8 km/s

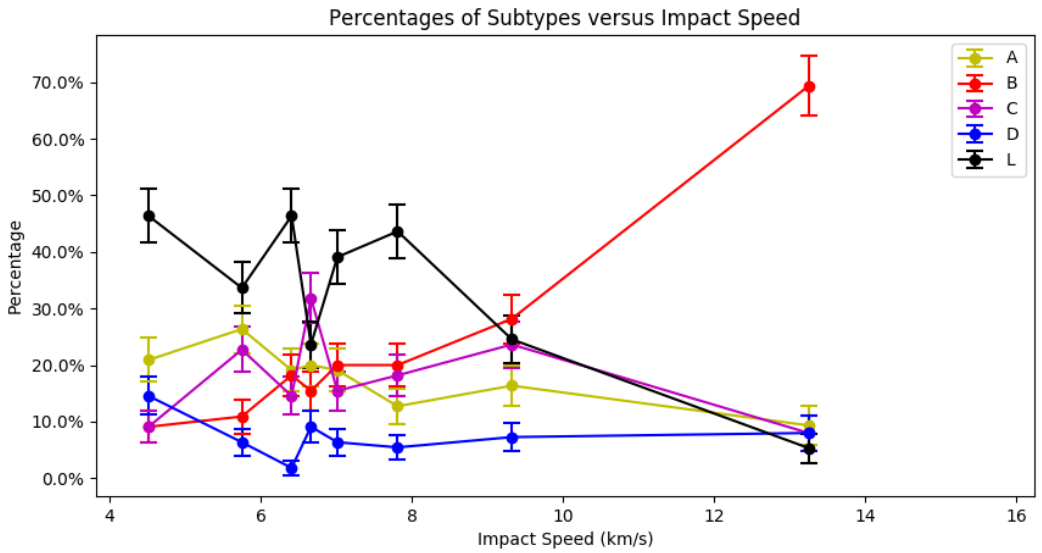

Bin	1	2	3	4	5	6	7	8	Sum
Spectra number	110	110	110	110	110	110	110	75	845
Speed (km/s)	3.8 - 5.2	5.2 - 6.3	6.3 - 6.5	6.5 - 6.8	6.8 - 7.2	7.2 - 8.4	8.4 - 10.3	10.3 - 16.2	3.8 - 16.2

Figure 4.19: Speed distribution of major Na-rich subtypes, including poor quality spectra. The data is divided into 8 bins according to their impact speeds. The horizontal axis indicates the impact speeds of the spectra. The percentage axis (vertical axis) indicates the percentage of subtypes in each bin. The error bars indicate the standard errors of the proportion of sample for each bin. The table below shows the number and the impact speed range of the spectra in each bin and the total spectra (Sum).

can be used to plot and analyze trends with distance and grain size of the spectra subtypes, minimizing the effects of impact speeds.

4.4.5 Distribution of spectral subtypes with Saturnian distance

As previously discussed in Section 4.3.5, ice particles drift outward from Saturn mainly due to the action of plasma drag. Therefore, greater distance implies older age and thus the distance distribution may represent the evolution of the chemical composition of ice particles with time.

In this section, the plot of the distribution of spectral subtypes with distance, including the unreliable (bad quality) spectra, is shown (Fig. 4.20). The number of spectra in each bin are shown below the plots. The plot of the distribution of spectral subtypes with distance, excluding the unreliable (bad quality) spectra, shows the similar trend and thus is attached in Appendix (Fig. E.2).

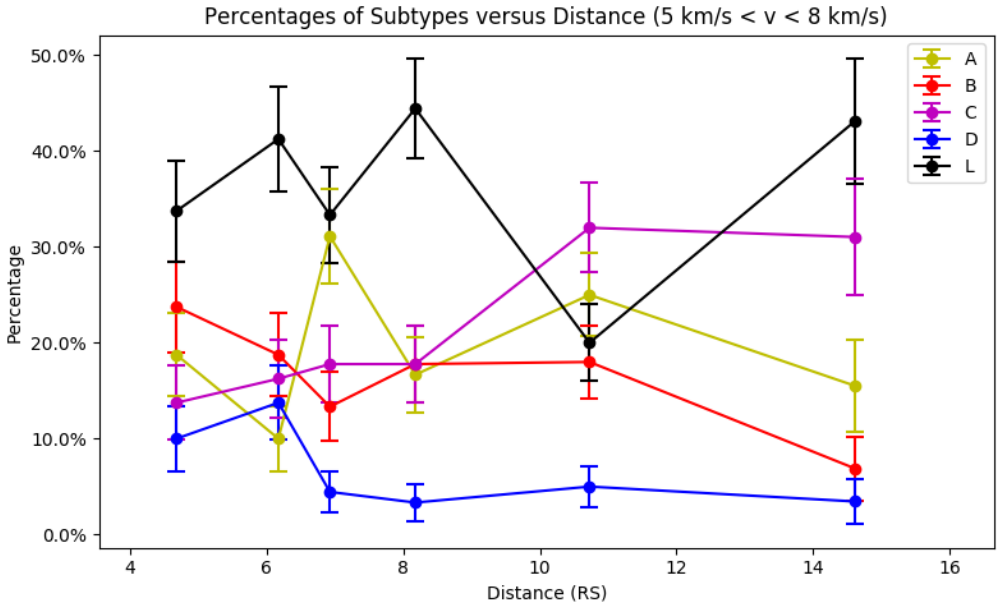

Bin	1	2	3	4	5	6	Sum
Spectra number	80	80	90	90	100	58	498
Distance (R_S)	3.6 - 5.8	5.8 - 6.5	6.5 - 7.3	7.3 - 9.0	9.0 - 12.4	12.6 - 16.6	3.6 - 16.6

Figure 4.20: Percentage distribution of all major subtypes of spectra, including the poor quality data, as a function of Saturnian distance. Only spectra due to impacts at speeds between 5 - 8 km/s were considered. The data is divided into 6 bins according to the distances of the particles to the Saturn center. The horizontal axis of the plot indicates the distance of the ice grains to the Saturn center in R_S. The percentage axis (vertical axis) of the plot indicates the percentage of each bin. The error bars indicate the standard error of the proportion of sample for each bin. The table below shows the number and the distance range of particles of the spectra in each bin and the total spectra (Sum).

From the plots following trends are observed: Subtype B exhibits slightly, monotonically decreasing relative abundances with Saturnian distance, especially from the 5th bin (7.3 to 9.0 R_S) to the 6th bin (12.6 to 16.6 R_S). The proportion of subtype C spectra exhibits an increases from the 4th bin (7.3 to 9.0 R_S) to the 5th

bin (9.0 to 12.4 R_S), whereas subtype D exhibits a small drop after 6 R_S, after which subtype D is flat. Subtype A exhibits an increase from the 2nd bin (5.8 to 6.5 R_S) to the 3rd bin (6.5 to 7.3 R_S) and falls back in the 4th bin (7.3 to 9.0 R_S). Subtype L spectra show a dip in the 5th bin (7.3 to 9.0 R_S), after which subtype L shows a significant increase, which is coincident with the significant decrease of subtype B.

Distribution of carbonate-rich and chloride-rich spectral subtypes with Saturnian distance:

Whether or in what relative rate the carbonate and chloride in the salt-rich Saturnian E-ring ice particles are lost with Saturnian distance or age has not been investigated before. Here, the carbonate-rich and chloride-rich spectral subtypes are analyzed together to make a comparison.

Although the profiles of Subtype A spectra and Subtype B spectra are clearly different, both Subtypes A and B spectra are chloride-poor spectra. In addition, all Subtype A spectra show a significant carbonate related peak $Na^+(Na_2CO_3)$ (129 u), and 84 from the 186 Subtype B spectra also show a small but significant peak $Na^+(Na_2CO_3)$ (129 u). Therefore, these spectra are considered as carbonate rich spectra. All spectra of Subtypes C, D and E show significant chloride related peak $Na^+(Na_2CO_3)$ (81 u) and thus are considered as chloride rich spectra.

Fig. 4.21 and 4.22 show the percentage distributions of carbonate rich spectra and chloride rich spectra, including the poor quality data and excluding the poor quality data, respectively, as a function of Saturnian distance. Only spectra due to impacts at speeds between 5 - 8 km/s were considered.

It can be seen that in the first two bins (3.6 to 6.9 R_S) the error bars of the carbonate rich spectra and chloride rich spectra are overlapped, which means the proportions of carbonate rich spectra and chloride rich spectra are similar. In the third bin (6.9 to 8.7 R_S) the error bars are separated Fig. 4.21 or almost separated Fig. 4.22 and the proportion of carbonate rich spectra are higher than that of the chloride rich spectra. It implies that either the loss of chloride exceeds the loss of carbonate between 6.9 R_S and 8.7 R_S. This statement is also supported by the Fig. 4.20 and Fig. E.2, in which the Subtype A (super carbonate rich) shows a significant increase, coinciding with the significant drop of Subtype D (highly chloride rich) between 6.5 R_S and 7.3 R_S (the third bin). However, due to the big error bars this statement is not a solid conclusion. From the third bin (6.9 to 8.7 R_S) to the last bin (10.5 to 16.2 R_S) in Fig. 4.21 and Fig. 4.22, the proportion of carbonate rich spectra monotonously decreases and the proportion of chloride rich spectra monotonously

increases. In the last bin the proportion of carbonate rich spectra is significantly lower than the proportion of chloride rich spectra. This implies that the loss of the carbonate exceeds the loss of the chloride outside approximate 8 R_S.

In summary, one possible explanation for Fig. 4.21 and Fig. 4.22 is at far Saturnian distance (inside $\sim$ 8.7 R_S the loss of chloride exceeds the loss of carbonate, and at far Saturnian distance (outside $\sim$ 8.7 R_S) the loss of carbonate exceeds the loss of chloride,

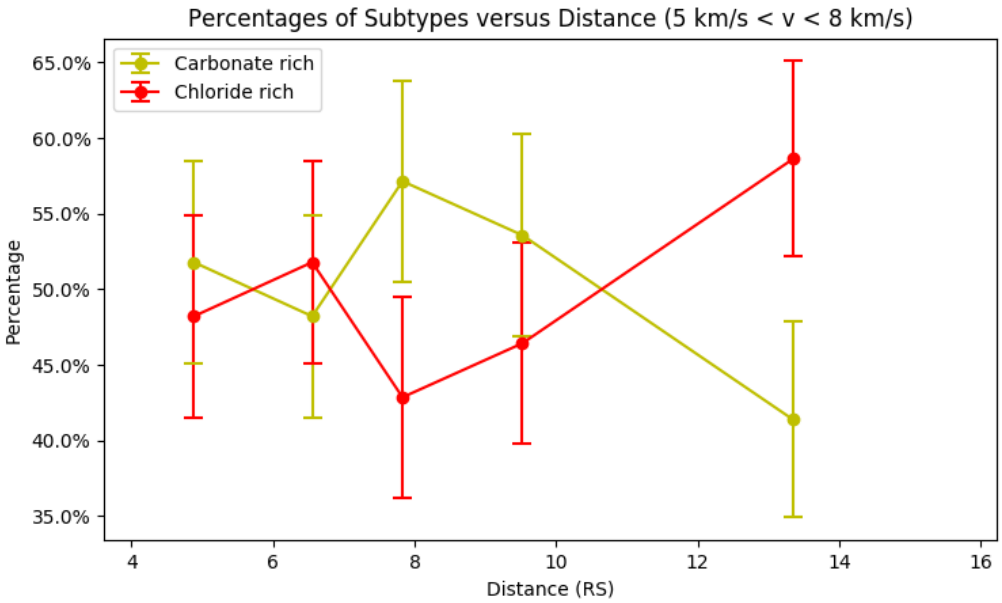

Bin	1	2	3	4	5	Sum
Spectra number	56	56	56	56	58	282
Distance (R_S)	3.6 - 6.2	6.2 - 6.9	6.9 - 8.7	8.7 - 10.3	10.5 - 16.2	3.6 - 16.2

Figure 4.21: Percentage distribution of carbonate rich spectra and chloride rich spectra, including the poor quality data, as a function of Saturnian distance. Only spectra due to impacts at speeds between 5 - 8 km/s were considered. The data is divided into 5 bins according to the distances of the particles to the Saturn center. The horizontal axis of the plot indicates the distance of the ice grains to the Saturn center in R_S. The percentage axis (vertical axis) of the plot indicates the percentage of each bin. The error bars indicate the standard error of the proportion of sample for each bin. The table below shows the number and the distance range of particles of the spectra in each bin and the total spectra (Sum).

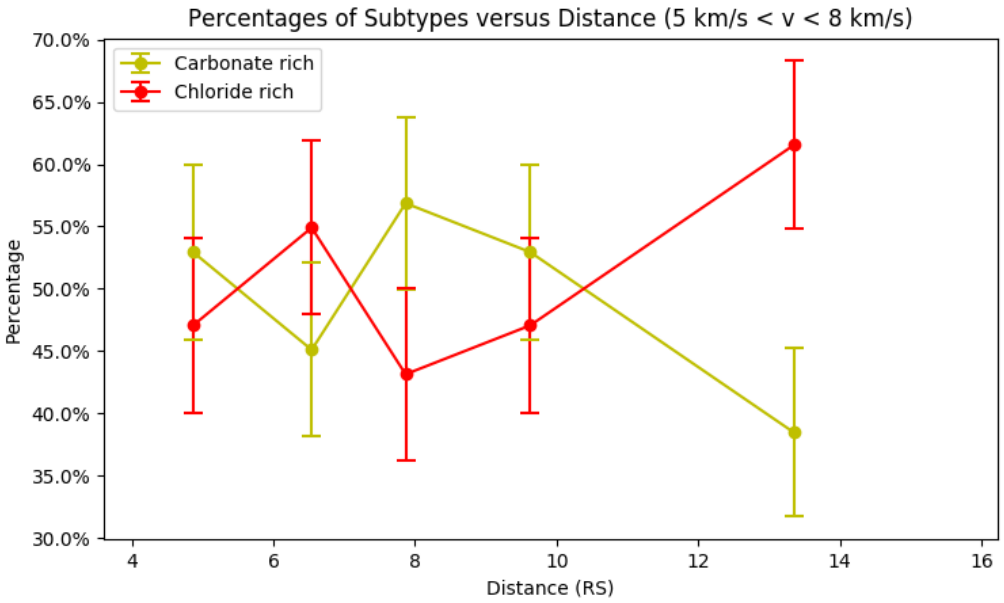

Bin	1	2	3	4	5	Sum
Spectra number	51	51	51	51	52	256
Distance (R_S)	3.6 - 6.1	6.1 - 7.0	7.0 - 8.8	8.8 - 10.5	10.5 - 16.2	3.6 - 16.2

Figure 4.22: Percentage distribution of carbonate rich spectra and chloride rich spectra, excluding the poor quality data, as a function of Saturnian distance. Only spectra due to impacts at speeds between 5 - 8 km/s were considered. The data is divided into 5 bins according to the distances of the particles to the Saturn center. The horizontal axis of the plot indicates the distance of the ice grains to the Saturn center in R_S. The percentage axis (vertical axis) of the plot indicates the percentage of each bin. The error bars indicate the standard error of the proportion of sample for each bin. The table below shows the number and the distance range of particles of the spectra in each bin and the total spectra (Sum).

Further evidence for the potential loss of chloride with time in near Saturnian distance

Making the assumption that the ratio of the amplitudes of peak Na^+(NaCl) (81 u) and peak Na^+(NaOH) (63 u) in the chloride-rich spectra (Subtype C and Subtype D) reflects the relative concentrations of the sodium chloride and sodium hydroxide in ice particles, the above lost chloride hypothesis' can be investigated by examining the evolution of the 81 u/63 u peak amplitude ratio of chloride-rich spectra with the icy particles' distances to Saturn. Although subtype E spectra are also chloride-rich spectra, they do not have peak Na^+(NaOH) (63 u) and thus are not used for peak amplitude ratio analysis.

In total, there are over 200 E-ring chloride-rich (Subtypes C and D) present in the dataset (Table 4.2), but not all of them can be used for a quantitative analysis, because some factors alter peak amplitudes and therefore the derived amplitude ratios: 1) impact speeds, 2) elevated baselines, and 3) low quality peak shapes. Therefore, a subset of spectra was selected and reduced before peak amplitude ratio calculation. As with the earlier analysis, in order to reduce the effects of impact speed on the spectral appearance, only those spectra generated by particles with impact speeds between 5 km/s and 8 km/s are selected. To reduce quantitative inaccuracy due to unsuitable peak shapes, only spectra with well defined peaks were selected. Specifically, spectra with following features were excluded:

1. Impact speeds lower than 5 km/s or higher than 8 km/s.
2. QI smaller than 5 fC or larger than 500 fC. (Spectra with QI lower than 5 fC usually have too low peak ratio noise ratios; Spectra with QI higher than 500 fC usually have severely distorted peaks shapes.)
3. The peak amplitudes at 129 u or 63 u are lower than 3σ (the standard deviation of the local noise).

After this process, 117 chloride-rich spectra (Subtype C and Subtype D) were suitable for further evaluation. The baselines of the remaining spectra were manually corrected to reduce the effect of elevated baselines. The resulting distribution of the amplitude ratios (Peak Na^+(NaCl) (81 u) to peak Na^+(NaOH) (63 u)) with Saturnian distance is shown in Fig. 4.23.

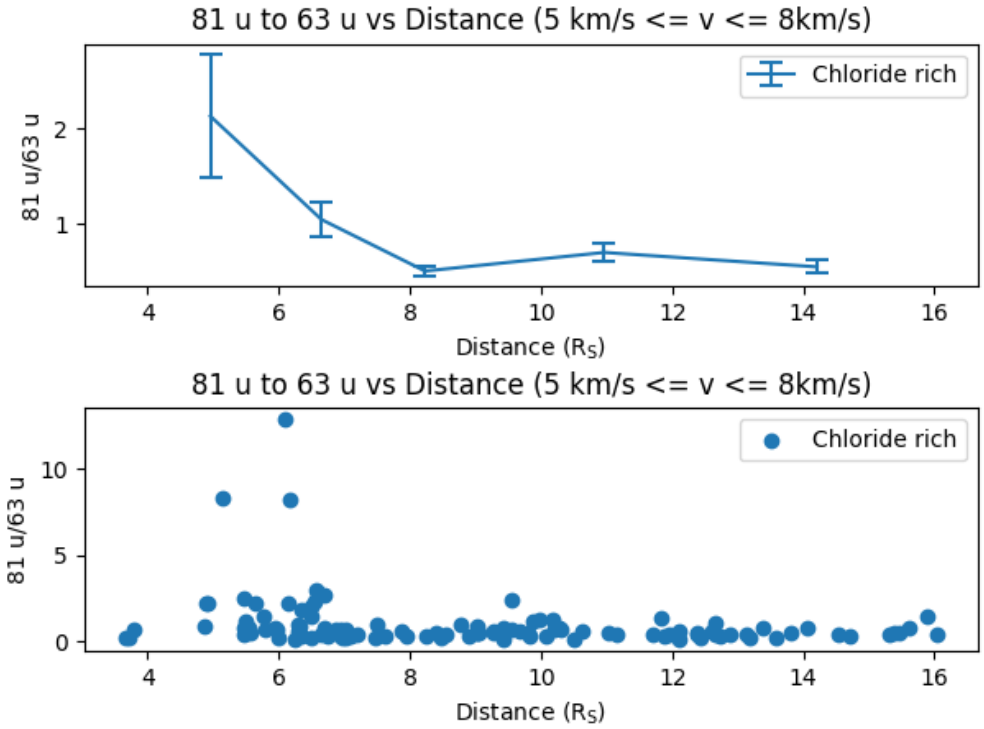

Bin	1	2	3	4	5	Sum
Bin Size	24	24	24	24	21	117
Distance (R_S)	3.7 - 6.3	6.3 - 7.0	7.0 - 9.4	9.5 - 12.4	12.4 - 16.0	3.7 - 16.0

Figure 4.23: The 81 u/63 u peak amplitude ratios of the chloride-rich spectra (Subtypes C and D) as a function of Saturnian distance. Only spectra from impacts at speeds between 5 km/s and 8 km/s and with QI value between 5 fC and 500 fC are used. The data is divided into 5 data bins according to the distances of the particles to the Saturn center. The upper panel of the figure shows the average values of the peak amplitude ratios in each data bin, with the error bars showing the standard error of the mean of the peak amplitude ratio of sample for each bin. The lower panel of the figure shows the peak amplitude ratios for individual spectra. The table below shows the number and the distance range of the spectra in each bin and the total spectra (Sum).

Fig. 4.23 shows a potential decreasing trend of this ratio with distance (time) from approximate 4 R_S to approximate 8.5 R_S. After 8.5 R_S the trend is flat. This is potentially the further evidence for the loss of chloride in ice particles with time.

However, given the scatter of the data points in the plot, it is difficult to draw a solid conclusion.

No significant trend evidence for the potential loss of carbonate with time

Figs. 4.20 and E.2 in Appendix show no trend for the proportion of subtype A spectra with Saturnian distance, and only a slightly decreasing trend for subtype B. Whether carbonate is lost from the grains is therefore not shown in these plots. However, to search for potential hidden, subtle spatial or temporal trends, the same approach as undertaken for the chloride spectra was applied to the carbonate-rich spectra.

As discussed above all subtype A spectra and the subtype B spectra with peak $Na^+(Na_2CO_3)$ (129 u) are considered as carbonate rich spectra. They will be analyzed together to investigate if, and how, the amplitudes of carbonate- and hydroxide-related peaks change with Saturnian distance.

In total, 239 E-ring carbonate-rich (subtypes A spectra and B spectra with a significant peak $Na^+(Na_2CO_3)$ (129 u)) (155 subtype A spectra and 84 subtype B spectra) have been identified in the dataset (Table 4.2), although for the same reasons described for the chloride-rich dataset, not all of them can be used for quantitative peak amplitude analysis. Here, I only consider the good quality spectra. Specifically, spectra with following features are excluded:

1. Generated by particles impacting at speeds lower than 5 km/s or higher than 8 km/s.
2. QI amplitude smaller than 5 fC or larger than 500 fC.
3. The peak amplitudes at 129 u or 63 u are lower than 3σ (the standard deviation of the local noise).

As with the chloride-rich spectra, this process reduced the number of spectra suitable for further analysis. Finally, 121 carbonate-rich and chloride-poor spectra (subtypes A and B with a significant peak $Na^+(Na_2CO_3)$ (129 u)) were selected to evaluate the distribution of the amplitudes ratios of peaks 129 u and 63 u with respect to Saturnian distance. As before, the baselines of the spectra were manually corrected in the cases where baselines were elevated or distorted. The resulting distribution is shown in Fig. 4.24.

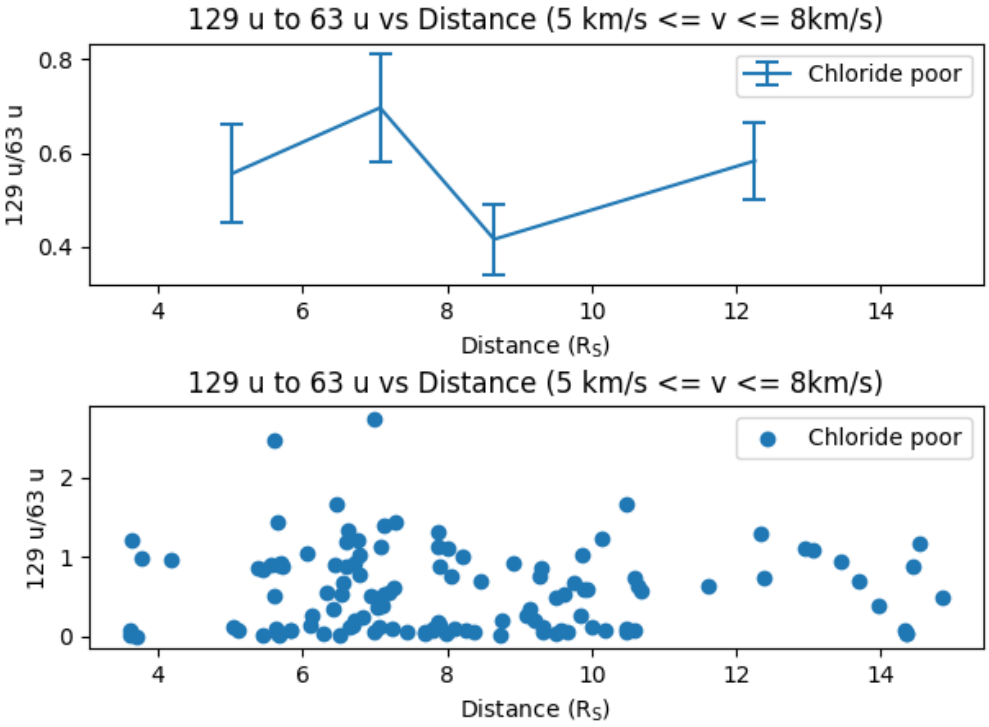

Bin	1	2	3	4	Sum
Bin Size	30	30	30	31	121
Distance (R_S)	3.6 - 6.4	6.5 - 7.7	7.7 - 9.6	9.7 - 14.8	3.6 - 14.8

Figure 4.24: The 129 u/63 u peak amplitude ratios of the Subtype A spectra and Subtype B spectra with a significant peak Na^+(Na_2CO_3) (129 u) (carbonate-rich and chloride-poor) as a function of Saturnian distance. Only spectra with impact speeds between 5 km/s and 8 km/s are used. The data is divided into 4 data bins according to the distances of the particles to the Saturn center. The upper panel of the figure shows the average values of the peak amplitude ratios in each data bin, with the error bars showing the standard error of the mean of the peak amplitude ratio of sample for each bin. The lower panel of the figure shows the peak amplitude ratios for individual spectra. The table below shows the number and the distance range of the spectra in each bin and the total spectra (Sum).

No statistically significant trends of this ratio with distance (time) are apparent. This may mean that carbonate is not lost from the grains as they age. However, unlike the Subtypes C and D spectra, which have no clear boundary, Subtype A

spectra and Subtype B spectra are very different in appearance, combined purely because of the presence of a carbonate peak. Therefore, it makes sense to analyze Subtypes A and B spectra separately. Unfortunately, the results still do not show significant trends, based on the large error bars (See Appendix F).

Therefore, the conclusion is that the distribution of amplitude ratio of peaks 129 u and 63 u does not show any statistically significant trend that the carbonate is lost from the grains with the Saturnian distance. This conclusion does not agree with Fig. 4.21 and Fig. 4.22, which show the loss of the carbonate exceeds the loss of the chloride at far Saturnian distance (outside ~ 8.7 R_S). One possible explanation for this inconsistency is that the amplitude ratio of peaks 129 u and 63 u does not really represent the concentration of carbonate in the ice particles.

4.4.6 Distribution of spectral subtypes with calculated grain size

As with the analysis of subtype distribution with Saturnian distance, the effects of impact speed were minimized by considering only those spectra generated by particles impacts at speeds between 5 and 8 km/s.

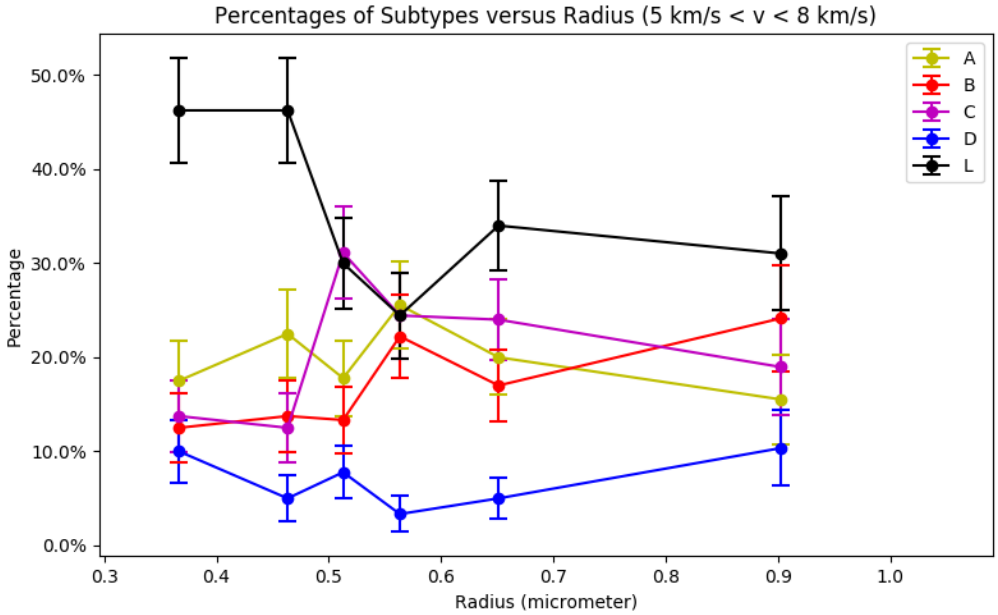

Bin	1	2	3	4	5	6	Sum
Spectra number	80	80	90	90	100	58	498
Radius (μm)	0.3 - 0.4	0.4 - 0.5	0.5 - 0.5	0.5 - 0.6	0.6 - 0.7	0.7 - 1.1	0.3 - 1.1

Figure 4.25: The relative abundances of all major spectra subtypes as a function of their derived particle size. Only particles with impact speeds between 5 km/s and 8 km/s are used. The data is divided into 6 bin according to the particle radius. The percentage axis (vertical axis) of the plot indicates the percentage of each bin. The horizontal axis of the plot indicates the particle radius in μm. The table below shows the number and the range of the particle radius of the spectra in each bin and the total spectra (Sum).

Fig 4.25 shows the distribution of the five major subtypes of the total spectra (including good and bad spectra) with grains radius. The plot corresponding to good quality spectra shows the similar trend and is attached in the Appendix (Fig. E.3). The plots show following trends:

Subtype L grains represent a significant proportion of the smallest grains, in

good agreement with the fact that the recording of many Subtype L spectra is Na triggered due to the low ion yield. The radius distribution of Subtype C grains shows a vague peak at around 0.5 μm, but other subtypes' size distributions show no clear trend.

4.4.7 The relation between impact speeds and important peak amplitude ratios derived via spectra co-adding

Peak amplitude ratios reference to Na^+ (23 u) for Subtype A

The amplitude ratios of peak $Na^+(NaOH)$ (63 u) to Na^+ (23 u), $Na^+(Na_2O)$ (85 u) to Na^+ (23 u), $Na^+(NaOH)_2$ (103 u) to Na^+ (23 u) and $Na^+(Na_2CO_3)$ (129 u) to Na^+ (23 u) of the co-added spectrum of super carbonate rich subtype (Subtype A) are listed in Table 4.4, which demonstrates that the amplitude ratios of 85 u to 23 u and 129 u to 23 u monotonically decrease with impact speed, but the amplitude ratios of 63 u to 23 u and 129 u to 103 u do not.

Bin	1	2	3	4	Total
Impact Speed (km/s)	[3.8, 5]	(5, 7]	(7, 10]	(10, 14.8]	[3.8, 14.8]
Spectra number	9	51	25	5	90
63 u/23 u	0.57	0.49	0.60	0.40	
85 u/23 u	0.12	0.05	0.04	0.03	
103 u/23 u	0.10	0.05	0.04	0.06	
129 u/23 u	0.63	0.37	0.27	0.19	

Table 4.4: The amplitude ratios of some typical peaks to peak Na^+ (23 u) of the co-added spectra in different impact speed intervals for super carbonate rich Type-3 CDA spectra (subtype A).

Peak amplitude ratios reference to Na^+ (23 u) for subtypes C, D, and E

The amplitude ratios of peak $Na^+(NaOH)$ (63 u) to Na^+ (23 u), $Na^+(NaCl)_2$ (81 u) to Na^+ (23 u) and $Na^+(NaOH)_2$ (103 u) to Na^+ (23 u) of the co-added spectra of chloride-rich Subtypes (C,D, and E) are listed in Table 4.5, which demonstrates that there is not monotonic trend for the three ratios.

Bin	1	2	3	4	Total
Impact Speed (km/s)	[3.8, 5]	(5, 7]	(7, 10]	(10, 14.8]	[3.8, 14.8]
Spectra number	10	92	47	9	158
63 u/23 u	0.10	0.25	0.34	0.18	
81 u/23 u	0.20	0.16	0.20	0.17	
103 u/23 u	N.A.	0.016	0.019	0.008	

Table 4.5: The amplitude ratios of some typical peaks to peak Na^+ (23 u) in the co-added spectra in different impact speed intervals for chloride rich Type-3 CDA spectra (Subtypes C, D and E). Peak amplitude ratio 103 u/23 u is not available for the co-added spectrum in the [3.8, 5] km/s impact speed interval, because the peak 103 u is located on the right flank of the broad peak 81 u and thus the real amplitude of peak 103 u is not known.

4.5 Discussion

4.5.1 The identification of peak at 81 u

Both ion $Na^+(Na^{35}Cl)$ (81 u) and ion $Na(NaOH)(H_2O)^+$ (81 u) share the same mass 81 u, so if a peak at 81 u is detected in CDA spectra, it is hard to tell which ion it represent without further evidence. Fortunately, chloride's second abundant isotope ^{35}Cl is also significant, i.e. the abundance ratio of of ^{35}Cl to ^{37}Cl is ~ 0.3. Therefore, if the amplitude of the peak at 81 u to the peak at 83 u is approximately 10:3, the peak at 81 u is supposed to be $Na^+(Na^{35}Cl)$ (81 u) and the peak at 83 u is supposed to be $Na^+(Na^{37}Cl)$ (83 u). Even so, due to the low resolution of CDA spectra, peak 81 u are peak at 83 u are not separable in most spectra. Only in some very good spectra, a shoulder is observed at the high mass side of peak at 81 u. This shoulder is probably $Na^+(Na^{37}Cl)$ (83 u). Therefore, $Na^+(Na^{35}Cl)$ (81 u) and ion $Na(NaOH)(H_2O)^+$ (81 u) can be distinguished through analogy to the laboratory spectra.

The laboratory spectra show that:

- Peak $Na(NaOH)(H_2O)^+$ (81 u) was not detected in the spectra of chloride-rich ($C_{(NaCl)} = 0.1$ M) solutions, but was detected in the spectra of chloride-poor ($C_{(NaCl)} = 0.001$ M) solutions. See Fig. 4.26.
- If a laboratory spectrum is calibrated so that $Na^+(NaOH)_2$ (103 u) is lower

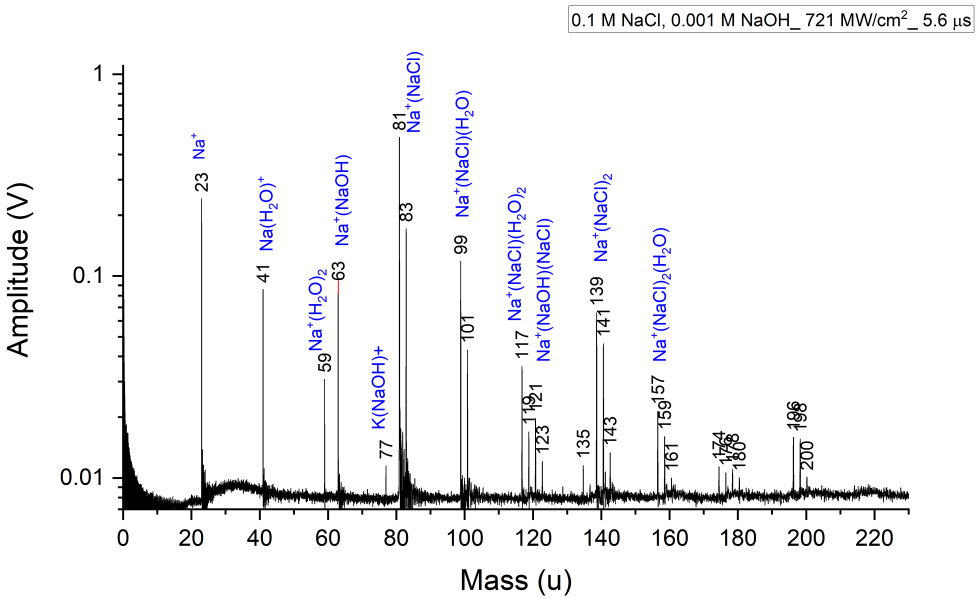

(a) A laboratory chloride-rich Spectrum. The amplitude ratio of peak at 81 u to peak at 83 u is $\sim 10:3$, so the peak at 81 u is $Na(NaCl)^+$ (81 u).

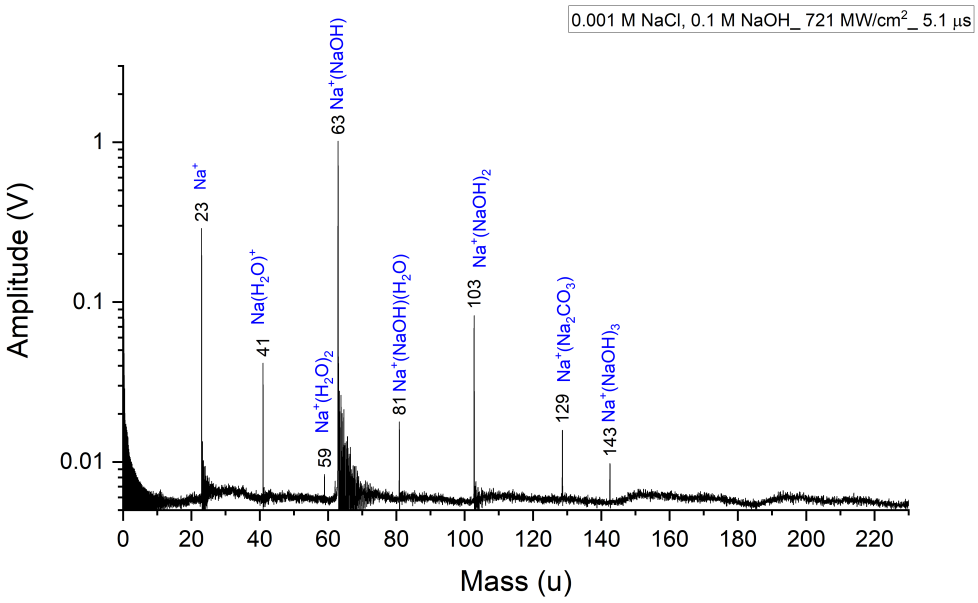

(b) A laboratory chloride poor Spectrum. There is not peak at 83 u, so the peak at 81 u is $Na(NaOH)(H_2O)^+$ (81 u).

Figure 4.26: A laboratory chloride-rich Spectrum and a laboratory chloride-poor Spectrum. The laser intensity of both spectra is 721 MW/cm^2

than peak Na^+ (23 u), which is the case for all CDA Type-3 spectra, peak $Na(NaOH)(H_2O)^+$ (81 u) is lower than peak $Na(H_2O)^+$ (41 u). See Fig. 4.26b.

- If the peak $Na^+(NaOH)$ (63 u) is similar high as peak Na^+ (23 u), the peak $Na(NaOH)(H_2O)^+$ (81 u) is lower than 0.1 times the amplitude of $Na(H_2O)^+$ (41 u). See Fig. D.1 in Appendix.
- If the peak $Na^+(NaOH)$ (63 u) is approximately equal or lower than 0.6 times the amplitude of peak Na^+ (23 u), peak $Na(NaOH)(H_2O)^+$ (81 u) is not detected. See Fig. D.2 in Appendix.

Therefore, following conclusion are obtained:

- If the peak $Na(H_2O)^+$ (41 u) is not detected in CDA spectra, the peak at 81 u, if detected, is supposed to be $Na^+(NaOH)$ (81 u) instead of $Na(NaOH)(H_2O)^+$ (81 u).
- If the peak $Na^+(NaOH)$ (63 u) is lower than Na^+ (23 u) in CDA spectra, the peak $Na(NaOH)(H_2O)^+$ (81 u) is supposed to be also lower than 0.1 times the amplitude of $Na(H_2O)^+$ (41 u).
- If peak $Na^+(NaOH)$ (63 u) is approximately equal or lower than 0.6 times the amplitude of peak Na^+ (23 u) in CDA spectra, the peak at 81 u, if detected, is supposed to be $Na^+(NaOH)$ (81 u) instead of $Na(NaOH)(H_2O)^+$ (81 u).

In Na-rich Type-3 CDA spectra peak $Na(H_2O)^+$ (41 u) is usually tiny (SNR < 10) or absent. For most CDA spectra, peak $Na^+(NaOH)$ (63 u) is lower than Na^+ (23 u). Besides, in the co-added spectrum of all good Subtypes A, B, H, C, D, and E, the peak $Na^+(NaOH)$ (63 u) is just approximate 42% of peak Na^+ (23 u). Therefore, the peak at 81 u in Na-rich CDA Type-3 spectra is always considered as $Na^+(NaOH)$ (81 u) instead of peak $Na(NaOH)(H_2O)^+$ (81 u).

4.5.2 The popularly mutual exclusion between carbonate and chloride

In order of Subtypes A, B, C, and D, the CO_3^{2-} related peaks varies from strong to weak and then to undetectable; and Cl^- related peaks varies from undetectable to weak and then to strong. This implies a 'spectrum' of composition for most Na-rich Type-3 ice particles.

It is notable that the presence of CO_3^{2-} related peaks and Cl^- related peaks are mutually exclusive, with only 15 exceptions out of 863 *typical* Na-rich Type-3 spectra.

It seems like that Cl^- and CO_3^{2-} are rarely detected in the same ice grains. A hypothesis to explain this discovery is that Cl^- and CO_3^{2-} are basically separated for currently unknown reasons during the ice particle formation process under surface. Another hypothesis is that some unknown mechanisms remove the CO_3^{2-} from some ice particles and Cl^- from other ice particles in the space.

4.5.3 The potential revolution trend of carbonate-rich Subtypes (A and B with peak $Na(Na_2CO_3)$ (129 u))

Although no significant revolution trend for carbonate-rich subtypes (A and B with peak $Na(Na_2CO_3)$ (129 u)) from 3.8 R_S to 14.8 R_S can be concluded from Figs. 4.24, F.1 and F.2 due to the big error bars, Figs. 4.21 and 4.22 do imply the loss of chloride in far Saturation distance (outside $\sim$ 8.7 R_S).

If carbonate is indeed being lost from the grains, a possible reaction pathway, initiated by energetic photons as for the chloride loss pathway, is as follows:

Potential photo-chemical reactions in E-ring carbonate-rich Type-3 icy particles

$$Na_2CO_3 + H_2O \xrightarrow{photon} 2\,NaOH + 2\,CO_2\uparrow$$

In this reaction, the carbonate is lost but the sodium remains in the ice particles. Thus, some Subtype A particles may gradually convert to Subtype B.

4.5.4 The revolution of chloride-rich Subtypes (C and D)

Figs. 4.21, 4.22 and 4.23 imply the loss of chloride in near Saturation distance (insides $\sim$ 8.7 R_S). A potential chloride loss mechanism from Type-3 grains in space is raised as following to explain the observation.

Potential chloride loss mechanism from Type-3 grains

High energy radiation, such as UV, is present in the E-ring environment, deriving mainly from the Sun (Morfill et al. 1983). These high energy photons provide energy for photo-chemical reactions, or sputtering, in icy particles. A potential photo-chemical reaction likely to contribute to loss of chloride from the grains is as follows:

$$NaCl + H_2O \xrightarrow{photon} NaOH + HCl\uparrow$$

In this reaction, the chloride is lost but the sodium remains in the ice particles. Thus, Subtype D particles are able to gradually convert into Subtype C particles.

4.5.5 The potential relation between Subtype B and Subtype L

Like Subtype B spectra, Subtype L spectra also show no carbonate- and chloride-related peaks. Fig. 4.19 shows the inverse trends with impact speed Subtype B and Subtype L show obviously, and implies that lower impact speed produces less Subtype B spectra but more Subtype L; and, in contrast, higher impact speed produces more Subtype B and less Subtype L. In addition, the Subtype L ice particles represent a significant proportion of the smallest grains (Fig. 4.25), in good agreement with the fact that the recording of many Subtype L spectra is Na triggered due to the low ion yield. Thus, one possible explanation is that the Subtype L ice particles actually have the similar compositions as Subtype B ice particles but smaller sizes. Thus, only if the high impact speed is high enough, enough ions yield is produced to make the second NaOH related peak ($Na^+(NaOH)_2$) significant. Unfortunately, the hypothesis cannot be tested with the IR-LILBID-TOF-MS in laboratory.

4.5.6 The possible impact speed dependent conversion between Subtype A spectra and Subtype B spectra of carbonate-rich ice particles

Amongst of the four co-added spectra of the four main Subtypes (A, B, C and D) (Section 4.4.3), all of the co-added spectra of Subtypes B, C, D spectra show H^+

line (Figs. 4.9, 4.10 and 4.11), which means some of them are recorded at impact speeds above 10 - 11 km/s, because only impact speeds higher than 10 - 11 km/s can produce H^+ line in CDA spectra (Postberg et al. 2009a; Fiege et al. 2014). However, the H^+ line is also probably attributed by contamination (Postberg et al. 2009a). Only the co-added spectrum of Subtype A spectra does not show H^+ line, which means all of the Subtype A spectra used for co-adding should be recorded below 10 - 11 km/s. Although 5 of 90 Subtype A spectra used for co-adding have estimated impact speeds between 10 km/s and 14.8 km/s (Table 4.4), but estimated impact speed could deviate from the actual impact speed a lot, if the particle does not orbit in the prograde direction in circular orbit in the ring plane. Therefore, all the actual impact speeds of the particles corresponding to Subtype A spectra could be lower than 10 - 11 km/s. Combining with that the peak amplitude ratio of 129 u to 23 u decrease with impact speed (Table 4.4), and that Subtype A spectra dominate and Subtype B spectra is absent during low speed plume flybys (E17, E18, E21), a hypnosis is proposed: Carbonate signatures are suppressed at high impact speed, i.e, the relative amplitude of peak Na(Na_2CO_3) (129 u) decreases with impact speed. As a result, some Subtype A spectra tend to become Subtype B at high impact speed. on the contrary, some Subtype B spectra tend to become Subtype A at low impact speed.

4.5.7 The possible physical mechanism for the different behaviors of carbonate and chloride related ions in high speed impact

The carbonate related peaks (peaks at masses 85 u and 129 u) and the chloride related peaks (Peak at mass 81 u) behave differently with impact speed (Section 4.5.6, Tables 4.4 and 4.5). This phenomena could be explained by the difference of the structures of the CO_3^- and Cl^-: former is a polyatomic ion, which can decompose at higher energy, but later is a monoatomic ion, which cannot decompose.

One physically plausible explanation for the decrease of the amplitude ratios of carbonate peaks (Peaks at masses 85 u and 129 u) to peak Na^+ (23 u) with impact speeds could be that carbonate ion dissociation or decomposition may occur (Eq. 4.3) at higher speeds (higher energy densities).

$$Na_2CO_3 + H_2O \xrightarrow{high\,energy\,(high\ \ impact\ \ speed)} 2NaOH + 2\,CO_2\uparrow \tag{4.3}$$

There are also other potential explanations for the inverse correlation between

the amplitude ratios of carbonate related peaks (peaks at masses 85 u and 129 u) to peak Na^+ (23 u) and the impact speeds. For example, the higher impact speeds (or high energies intensity) lead to shorter lived, more rapidly dispersing plasma clouds. As a result, the clusters do not have time to form, or the relative speeds of the ions result in inefficient clustering. Or, the amplitude of the Na peak could be increasing with increasing impact velocity.

In contrast, chloride can not be break up even in higher speed, because Cl^- is a monoatomic ion, instead of a polyatomic ion, like CO_3^-. Thus, the amplitude ratios of chloride related peak (peaks at mass 81 u) to peak Na^+ (23 u) should not have a certain monotonic relation with the impact speeds. This is consistent with Table 4.5.

Chapter 5

Enceladus Plume Grain Compositions

5.1 Introduction

The plume along the four 'Tiger Stripes' in the south polar terrain of Enceladus are the main source of Saturn's icy E-ring particles (Spahn et al. 2006a,b). Cassini images show there are two kinds of particle sources in the plume: slow diffuse sources and faster and more collimated jet-like sources (Spitale & Porco 2007; Hansen et al. 2008; Postberg et al. 2011; Spitale et al. 2015). Previous analyses of the chemical composition of icy particles freshly ejected from the sources indicate that salt-rich ice particles have larger sizes and dominate the total flux of ejected dust grains larger than approximately 0.2 μm in radius (the detection threshold of the CDA) ($>$ 99% in mass and $\sim$ 70% in particle numbers (Postberg et al. 2011)), but they are depleted in the population escaping into the E-ring of Saturn (Postberg et al. 2011). This means that most of the salt-rich particles deposit as 'snow' on the surface of the south polar region, because their speeds are lower than the two body escape velocity of the Enceladus-Saturn system (Kempf et al. 2010, 2018).

Understanding the distribution of subtypes in the plume is important, as the ratios of various subtypes of icy particles in the plume can reflect the composition of the subsurface ocean, as well as provide information on grain formation and evolution.

5.2 Dataset

Cassini undertook multiple Enceladus plume traversals between 2004 and 2017 (Henin 2018). However, only flybys E17 (March, 2012), E18 (April, 2012) and E21 (October, 2015) produced some spectra of salt-rich grains, that can be subclassified into subtypes. CDA was not designed for the high ice particles number density condition in the plume. The maximum spectral recording rate of the three flybys was limited to ~ 0.6 s^{-1} (Postberg et al. 2018a). Therefore, an unusual setting is used to cope with the high particle flux, resulting a reduced spectral resolution. The trajectory of all three flybys: E17, E18 and E21 led Cassini to fly almost horizontally over the south polar region (SPT) (Postberg et al. 2018a) with altitudes at the closest approach (CA)s $\sim$ 74 to 76 km, $\sim$ 74 to 76 km and $\sim$ 48 to 49 km and flyby speeds $\sim$ 7.5 km/s and $\sim$ 7.5 km/s and $\sim$ 8.5 km/s, respectively (NASAwebsite 2019b,a,c; Khawaja et al. 2017; Postberg et al. 2018a).

Table 5.1 shows basic dynamical information for these three flybys.

Encounter Name	Altitude (km)	Date	Closest Approach (CA) Time	Speed at CA (km/s)
E17	$\sim$ 74 to 76	March 27, 2012	18:30:09	$\sim$ 7.5
E18	$\sim$ 74 to 76	April 14, 2012	14:01:38	$\sim$ 7.5
E21	$\sim$ 48 to 49	October 28, 2015	15:22:42	$\sim$ 8.5

Table 5.1: Cassini-Enceladus configuration for flybys E17, E18 and E21 (NASAwebsite 2019b,a,c; Khawaja et al. 2017; Postberg et al. 2018a). The date and time used are in Coordinated Universal Time (UTC).

Despite the low resolution compared to most E-ring spectra, some of these spectra are able to be classified into different types, such as Type-1, Type-2, Type-3 (Postberg et al. 2018a) and Type-2/3; and even subclassified into different subtypes (for Type-3), such as A, B, H, C, D, E.

5.3 Plume particle salt-rich subtype distribution

This work only focuses on the spectra of salt-rich plume particles. Table A.2 in Appendix indicates the subtype distribution of the spectra of salt-rich plume

particles measured during flybys E17, E18, and E21. The sampling time and assigned subtype of the spectra are shown, together with the Closest Approach (CA) Times of each flyby. In this data set there are in total 32 spectra of salt-rich (Type-3 and Type-2/3) plume particles, which have good enough quality for further classification. In flyby E17 the number of classifiable salt-rich plume particles sampled is 14 and the period of these samplings with respect to the closets approach time is from - 2 min 47 s to +2 min 54 s. In flyby E18 the number of classifiable salt-rich plume particles sampled is 8 and the period of these samplings with respect to the closets approach time is from - 2 min 54 s to 2 min 1 s. In flyby E21 the number of classifiable salt-rich plume particles sampled is 10 and the period of these samplings with respect to the closets approach time is from - 2 min 53 s to - 0 min 13 s.

With the exceptions of a single E17 spectrum, categorized as Type-2/3 due to its abundant organic-related peaks, and a single E21 spectrum, difficult to distinguish between Type-3 (Subtype A) and Type-2/3 due to its low mass resolution, all other salt-rich spectra are recognizably Type-3 spectra. Despite their reduced resolution, almost 80% of these Type-3 spectra can be reliably classified into subtypes of *typical* Type-3 salt-rich spectra, according to the criteria in Section 4.4.3 on Page 73, with around 20% spectra ambiguous enough to allow classification into alternative subtypes.

Table 5.2 shows the relative proportions of the spectral subtypes for the three flybys. Subtype A clearly dominates in plume Type-3 spectra, unlike in the sample of E-ring Type-3 spectra (Table 4.2 on Page 86).

	A	B	H	C	D	E	L	Total
E17	7.5	2	1.5	1	2.5	0.5	0	13
E18	6.5	0	0.5	1	0	0	0	8
E21	7	1	1.5	0	0	0	1	9.5
Sum	21	0	3.5	2	2.5	0.5	1	30.5
Percentage	68.9%	0.0%	11.5%	6.6%	8.2%	1.6%	3.3%	100.0%

Table 5.2: Proportions of the spectral subtypes of the plume salt-rich icy particles. The spectra with ambiguous subtypes are weighted 0.5 for each possible subtype. Carbonate-rich Subtype A dominate the classified plume salt-rich spectra, unlike in the E-ring itself.

Fig. 5.1 shows the separate subtype distributions for *typical* Na-rich Type-3 E-ring and plume ice particles. The contrast between the two distributions is clear: 1) In the E-ring, Subtypes A, B, C, D and L are found in comparable numbers, but

in the plume environment Subtype A dominates, Subtype B is absent and other subtypes are found much less frequently; 2) the proportion of Subtype H in the plume environment is a higher than in the E-ring. Both distributions are very poor in Subtype E spectra.

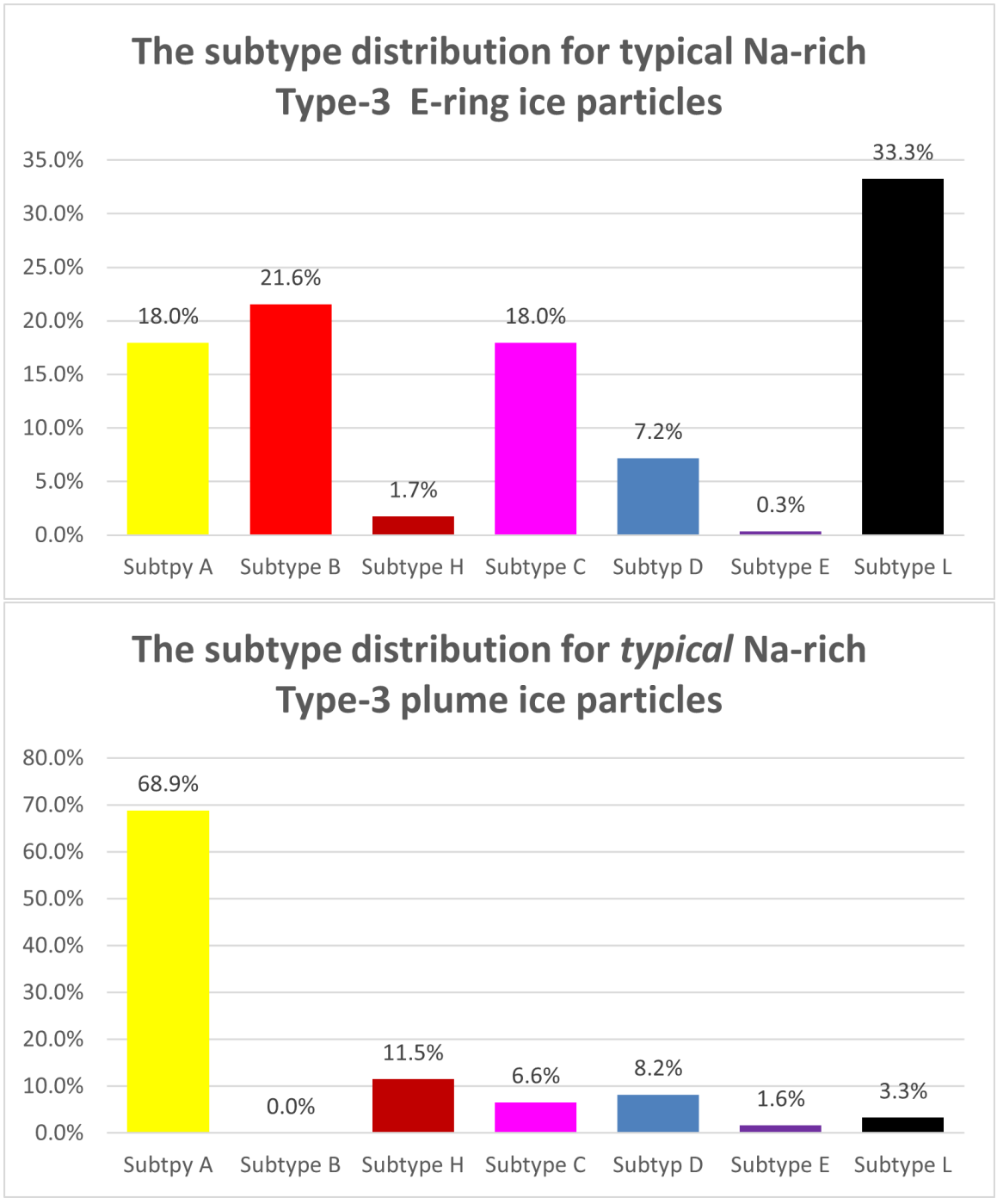

Figure 5.1: E-ring *typical* Na-rich Type-3 subtype distribution (upper panel) and plume *typical* Na-rich Type-3 subtype distribution (lower panel).

5.4 Discussion

All E-ring Type-3 icy particles originate from the plume and escaped from the gravity of Enceladus due to their high velocity (The three-body escape speed of the Saturn–Enceladus system is $\sim$ 207 m/s (Kempf et al. 2010)). Fig. 5.1 shows that the population of subtypes of the Type-3 icy particles changes dramatically from the plume environment to the E-ring, demonstrated by the dramatic decrease in the fraction of Subtype A spectra produced. This phenomenon is difficult to explain. Since the subtype distributions with distance to Saturn of the E-ring salt rich particles (Figs. 4.20 and E.2) do not show clear decreasing trend for the ratio of Subtype A particles, it seems like that space weathering does not decompose the carbonate in E-ring Subtype A ice particles significantly. Three potential explanations are raised for the dramatic decrease in the fraction of Subtype A spectra from the plume to the E-ring:

1. The first potential explanation is that space weathering would remove most of carbonate from the fresh plume Subtype A ice particles within a short time (such as a few days). Then, the rest carbonate in these ice particles becomes relatively stable after these particles arrive E-ring.

2. The second potential explanation is that the decomposition of Subtype A particles by space weathering does not reduce the fraction of Subtype A particles (more correctly, the spectra) quickly since these ice particles are erupted from the fractures on the icy surface of Enceladus. Therefore, the decrease in the proportion of Subtype A from the plume environment to the E-ring could be not attributed to space weathering. In this case, to explain the big difference between the subtype distributions in plume and in E-ring, I would assume that most Subtype A icy particles cannot escape from the gravity of Enceladus to enter the E-ring due to their low velocities. There are two hypotheses which could explain their low velocities:

    1) Subtype A particles are prone to forming with large sizes, but their kinetic energies, acquired during acceleration by ascending gas in the channels connecting the subsurface ocean to space, are not much larger than those of the other subtypes. As velocity is inversely proportional to the square root of particle mass for a given kinetic energy, the acquired velocities of these large Subtype A particles are small compared to those of other particles. Thus, only a small fraction of the Subtype A particles have high enough velocities to overcome the gravity of Enceladus and become E-ring particles. However, there is no indication from the data to supporting

this hypothesis, i.e. the QI values of the plume Subtype A spectra are not higher than the QI values of the spectra of other plume subtypes.

2) The slow diffuse sources tend to produce carbonate rich Subtype A particles and the faster and more collimated jet-like sources tend to produce carbonate-poor subtypes of particles. Therefore, as with the previous hypothesis, only a fraction of the Subtype A particle population has high enough velocities to escape to become E-ring particles. Unfortunately, this hypothesis cannot be verified by Cassini flyby data due to the low spatial resolution of CDA sampling.

Dynamic modeling should be done to verify above assumption and hypotheses in future.

3. Low impact speed lead to Subtype A spectra. The speeds of Cassini at the closest approaches are between 7.5 km/s and 8.5 km/s for all three flybys (E17, E18 and E21). The speeds of plume particles relative to the surface of Enceladus are usually lower than 500 m/s (Kempf et al. 2010) and can be neglected. Therefore, the impact speeds of plumes particles on CDA are approximately between 7.5 km/s and 8.5 km/s. One assumption is that in this impact speed range the carbonate rich ice particles prefer to produce Subtype A spectra rather than Subtype B spectra. The lacking of hydrogen line in the co-added spectrum of Subtype A (Fig. 4.8) also implies that the impact speeds of Subtype A spectra are below 10 to 11 km/s (Postberg et al. 2009a; Fiege et al. 2014). This assumption could partly explain the high proportion of Subtype A spectra and the lacking of Subtype B spectra in plume traversals, but it is hard to explain that the total proportion of Subtypes A and B spectra are much higher than the total proportion of Subtypes C and D.

Chapter 6

Laboratory mass spectra mimicking and concentration parameter space determination

6.1 Introduction

In this chapter research on mimicking - creating analogue solutions representing - the major subtypes of the *typical* spectra of the Na-rich E-ring and plume ice particles (Subtypes A, B, C and D), which could reflect the major salt composition of Enceladus' subsurface ocean, is reported. Through spectra mimicking, the concentration ranges of major substances, and the upper limits for the concentrations of trace substances, can be estimated. In the laboratory, the impact ionization process for volatile (water) rich grain impacts is simulated by the dispersion of a liquid beam of solution in a diameter of 12 μm to 22 μm.

6.2 Methodology

The strategies for mass spectra mimicking and concentration parameter space determination are described in detail in this section.

6.2.1 Settings of the experimental setup

The setup used for simulating impacts of ice grains onto the CAT in CDA and mimicking analogue spectra mimic is described in Section 2.2.1. The parameters used for this chapter are as following:

- Flash lamp power: 5.30 J.
- Laser intensity: 94.3%.
- Delay time range: 4.9 - 5.9 μs.
- Nozzle inner diameter: 15 μm, 16 μm, 20 μm, and 22 μm.
- Water flow range: 0.17 - 0.20 ml/min.

The laser setting of a flash lamp power of 5.30 J and a laser intensity of 94.3% corresponds to the laser power density of 721 mW/cm^2, which is the energy flux at focus of the infrared laser, where the water beam is located. The value is calculated by me and Fabian Klenner, who measured the power densities for different settings fitted a function between the laser power density and laser settings.

According previous calibration experiments (Klenner et al. 2019) and my personal communication with Fabian Klenner, the laser power density of 721 mW/cm^2, cooperate with proper solution and delay time, is suitable for mimicking Type-3 CDA spectra from impacts across the intermediate speed range (5-9 km/s). In Fabian Klenner's paper (Klenner et al. 2019), spectra of up to three settings could be co-added to accurately mimic one impact speed range, but the goal in this work is not to mimic impact speed ranges accurately, but just mimicking the impact speeds roughly for reproducing the general profiles and major peaks of the CDA spectra. Therefore, for simplification only one setting was used for mimicking one impact intermediate speed range.

The laser setting is not the only option. If increasing the Flash lamp power (The maximum value: 5.46 J) and laser intensity (The maximum value: 100%), the corresponding laser power intensity is increased (The maximum power intensity is 1150 mW/cm^2.), the similar spectral profiles can still be reproduced with the peak amplitudes increased, via increasing the delay time slight.

Varying the nozzle inner diameter and water flow in above ranges does not influence the spectral profiles.

6.2.2 The major salts forming the major subtypes *typical* CDA spectra of the Na-rich ice particles

Since the dominant salt peaks in the *typical* sodium-rich Type-3 CDA spectra are mainly related to CO_3^{2-}, OH^- and Cl^- (Section 4.4.3 and Table 4.2), it is believed that salt Na_2CO_3, NaOH and NaCl are the major salts in the corresponding ice particles. Therefore, the three salt are used to mimic the major subtypes of the *typical* sodium-rich CDA spectra (Subtypes A, B, C and D).

6.2.3 Understanding the relative ionization efficiencies of salts

For identical experimental conditions, ion production efficiencies vary between different salts, and the resulting spectral peak amplitudes therefore differ. Understanding the behaviour of the amplitude ratios of these peaks, the relative efficiencies or abilities of different salts to form ions in solution, as well as to form peaks in spectra are therefore helpful. Therefore, the relative ionization efficiency is defined as following:

Definition of relative ionization efficiency as used in this thesis:

For a solution of two salts with the same concentrations, the amplitude ratio of their first salt peaks (corresponding to the lowest mass molecular ions), exclusively caused by the salts themselves, is defined as their relative ionization efficiency, which represent of the relative efficiency or ability of the two salts to form ions in solution, as well as to form peaks in spectra.

For example, for a solution containing 0.05 M NaCl and 0.05 M Na_2CO_3 concentrations, the peak from Na^+(NaCl) (81 u and the isotope 83 u at a ratio of approximately 3:1) is the first peak exclusively caused by NaCl, and similarly the peak from $Na^+(Na_2CO_3)$ (129 u) is the first (lowest mass) peak exclusively caused by Na_2CO_3. The amplitude ratio of the 81 u and 129 u peaks thus represents the relative ionization efficiencies of NaCl and Na_2CO_3 at a concentration of 0.05 M of both salts.

This definition can be applied to NaCl, Na_2CO_3 and $NaHSO_4$, because their first salt peaks - the sodiated molecular ions (Na^+(NaCl) (81 u), $Na^+(Na_2CO_3)$ (129 u), $Na^+(Na_2SO_4)$ (165 u)) - are exclusively formed by elements from the salts. However, it cannot be applied to NaOH, as all NaOH related peaks, such as Na^+(NaOH) and

$Na^+(NaOH)_2$, are partially generated by the water matrix, which can provide OH^- ions that, in combination with Na^+ from other salt components, can produce NaOH related peaks. Thus, even pure NaCl solutions have been demonstrated to produce $Na^+(NaOH)_n$ (n = 1, 2, 3 ...). Moreover, the abundance of the OH^- is the crucial indicator for the pH value.

In this chapter, the relative ionization efficiencies of two of the three major salts Na_2CO_3 and NaCl, were measured. A further salt, Na_2SO_4, was also investigated. Although not yet observed in E-ring grains, sulfates are considered important for constraining planetary geochemistry, such as the degree of leaching from a chondritic core (Kargel 1991). Besides, the relation between the relative amplitudes of peak $Na^+(NaOH)$ (63 u) to $Na^+(NaCl)$ (81 u) or $Na^+(Na_2CO_3)$ (129 u) and the concentrations of NaOH and Na_2CO_3 or NaCl are measured, because it is also a useful indicator of the relative peak producing ability.

The ions to detect, the salt used, the first salt peaks related to these ions and the corresponding molecular ions masses corresponding to these salt peaks are listed in Table 6.1.

Ion	Salt used	First salt peak	Peak mass
Cl^-	NaCl	$Na^+(NaCl)$	81 u
CO_3^{2-}	Na_2CO_3	$Na^+(Na_2CO_3)$	129 u
OH^-	NaOH	$Na^+(NaOH)$	63 u
SO_4^{2-}	$NaHSO_4$	$Na^+(Na_2SO_4)$	165 u

Table 6.1: The ions to detect, the salt used, the first salt peaks related to these ions and the corresponding molecular ions masses corresponding to these salt peaks.

6.2.4 Spectra mimicking

The methodology used to determine the salt concentrations required to mimic - or create analogues of - the major subtypes of CDA spectra of Saturn's E-ring salt-rich ice particles is as following:

The spectral profile produced by the LILBID system, i.e. the general pattern of peak amplitudes - for a certain composition of solution depends mainly on the flash lamp power, laser intensity and delay time (Klenner et al. 2019). The Type-3 CDA spectra corresponding to the impact speed range from 5 km/s to 9 km/s are mimicked in this work. For the preliminary mimicking work, the flash lamp power was held at 5.30 J and the laser density at 94.3% (justified in Section 6.2.1), with

salt concentrations and LILBID delay times varied to make the resulting laboratory spectra match the CDA spectra as closely as possible. Finally, the archetypal spectra of different subtypes are produced, which match the good Type CDA spectra of the main subtypes: A, B, C, D.

6.2.5 Exploring the concentration parameter space for major subtypes

Gradual changes in the concentrations of the spectral end members of one specific spectrum type were found to produce similarly gradual changes in the spectral peak amplitudes and profile. Starting from the concentrations of salts for the archetypal spectra of different subtypes, the concentrations of the end members were varied (both increased and decreased) until the profile of the resulting spectrum no longer fulfilled the definition of its corresponding subtype (See Section 4.4.3 on Page 73). In this way, the concentration parameter space of Na_2CO_3, NaOH and NaCl, was explored for every individual subtype.

6.3 Results and discussion

6.3.1 The range of the total concentration of Na^+

In this chapter, the experiments were designed to mimic the CDA spectra of Saturn's E-ring salt-rich ice particles, so the major cation in the solution is Na^+. The range of the Na^+ was firstly determined via experiments.

The experiments indicate that the total concentration of Na^+ in the solution must be higher than approximately 0.1 M for most water peaks to be suppressed and for the spectra to fit the criteria of Type-3 CDA spectra (See Section 4.3.2 on Page 63). An example is shown in Appendix D.2. Thus, 0.1 M was adopted as the lower boundary of the total Na^+ concentration. Interestingly, if the total Na^+ concentration becomes too high, the salt peaks' amplitudes begin to drop, due to the effect of strong charge recombination (Wiederschein et al. 2015). As impact ionization mass spectra (i.e. the CDA spectra) can be accurately reproduced with the LILBID system (Klenner et al. 2019), it is reasonable to assume that the charge recombination effects also occur in the CDA impact ionization process. In the LILBID laboratory spectra, once the total Na^+ concentration is over 0.4 M, the salt peak amplitudes are severely suppressed. Furthermore at concentration above

0.5 M ice frequently forms in the opening of the nozzle, creating blockages which prevent further measurement. Therefore, 0.4 M is taken as an approximate upper boundary of the total Na^+ concentration in the solutions for spectra mimicking in the laboratory, as well as in Type-3 CDA spectra.

In conclusion, the constraint for the total Na^+ concentration is as following:

$$0.1\ \text{M} < 2C_{(\text{Na}_2\text{CO}_3)} + C_{(\text{NaCl})} + C_{(\text{NaOH})} < 0.4\ \text{M} \tag{6.1}$$

6.3.2 Relative ionization efficiencies of Salts

The relative ionization efficiencies of two substances varies with the applied laser intensity and the delay time prior to ion extraction. The relative ionization efficiencies of two substance may also vary with their total concentration in solution, but this variation is small across the range of realistic concentrations used to mimic the Type-3 spectra here (The total concentration of Na^+ is between 0.1 M and 0.4 M). The ratios of CO_3^{2-} containing sodium salts were found to be independent of whether the bicarbonate salt was used, and therefore Na_2CO_3 was chosen for relative ionization efficiencies determination and spectra mimicking.

The measurement of the relative ionization efficiencies are carried out with the range of Na_2CO_3 between 0.1 M and 0.3 M.

The measured values of relative ionization efficiencies of Na_2CO_3 to NaCl and Na_2CO_3 to $NaHSO_4$ are shown in Table 6.2. The measured values of relative ionization of NaOH to NaCl and NaOH to Na_2CO_3 are shown in Table 6.3.

Substances	Concentration	Ratio	pH	Peak mass	Relative ionization efficiency
Na_2CO_3 : NaCl	0.05 M, 0.05 M	1:1		129 u : 81 u	$\approx 4:1$
Na_2CO_3 : $NaHSO_4$	0.05 M, 0.05 M	1:1		165 u : 129 u	$\approx 1.2:1$

Table 6.2: Relative ionization efficiencies

From Table 6.2, it can be concluded that the relative ionization efficiencies of Na_2CO_3 and $NaHSO_4$ are similar and much higher than the relative ionization efficiency of NaCl.

Substances	Concentration	Ratio	pH	Peak mass	Peak amplitude ratio
NaOH : NaCl	0.1 M, 0.01 M	10:1	13	63 u : 81 u	$\approx 46:1$
NaOH : NaCl	0.1 M, 0.1 M	1:1	12.5	63 u : 81 u	$\approx 10:1$
NaOH : NaCl	0.01 M, 0.1 M	1 : 10	12	63 u : 81 u	$\approx 1:1$
NaOH : NaCl	0.001 M, 0.1 M	1 : 100	8	63 u : 81 u	$\approx 1:4$
NaOH : Na_2CO_3	0 M, 0.05 M	0 : 1	12	63 u : 129 u	$\approx 1:1$
NaOH : Na_2CO_3	0 M, 0.1 M	0 : 1	12	63 u : 129 u	$\approx 1:1$
NaOH : Na_2CO_3	0.001 M, 0.1 M	1 : 100		63 u : 129 u	$\approx 1:1$
NaOH : Na_2CO_3	0.01 M, 0.1 M	1 : 10		63 u : 129 u	$\approx 1:1$
NaOH : Na_2CO_3	0.1 M, 0.1 M	1 : 1		63 u : 129 u	$\approx 1:1$
NaOH : Na_2CO_3	0.1 M, 0.01 M	10 : 1		63 u : 129 u	$\approx 4:1$
NaOH : Na_2CO_3	0.1 M, 0.001 M	100 : 1	13	63 u : 129 u	$\approx 10:1$

Table 6.3: The relation between the relative amplitudes of peak Na^+(NaOH) to Na^+(Na_2CO_3) or Na^+(Na_2CO_3) and the concentration of NaOH and Na_2CO_3 or NaCl.

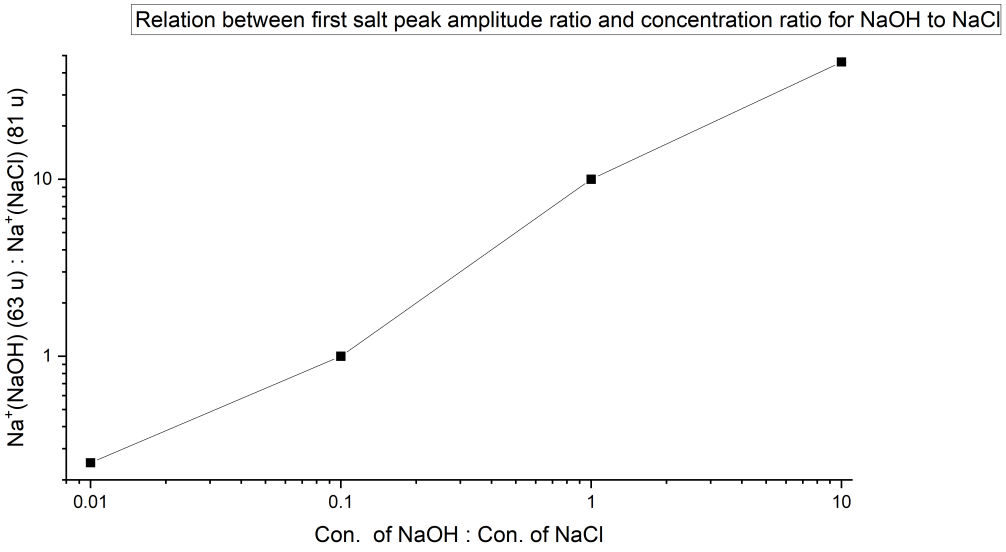

Figure 6.1: The relation between the first salt peak amplitude ratio and the concentration ratio for NaOH to NaCl. Four solutions are measured. The concentrations of the NaOH and NaCl for each solution are listed in Table 6.3. The total concentration of Na^+ is between 0.101 M to 0.2 M. Laser power intensity: ~ 721 mW/cm^2. Delay time: 5.1 μs. Note: The numbers in the axes are in logarithmic scale.

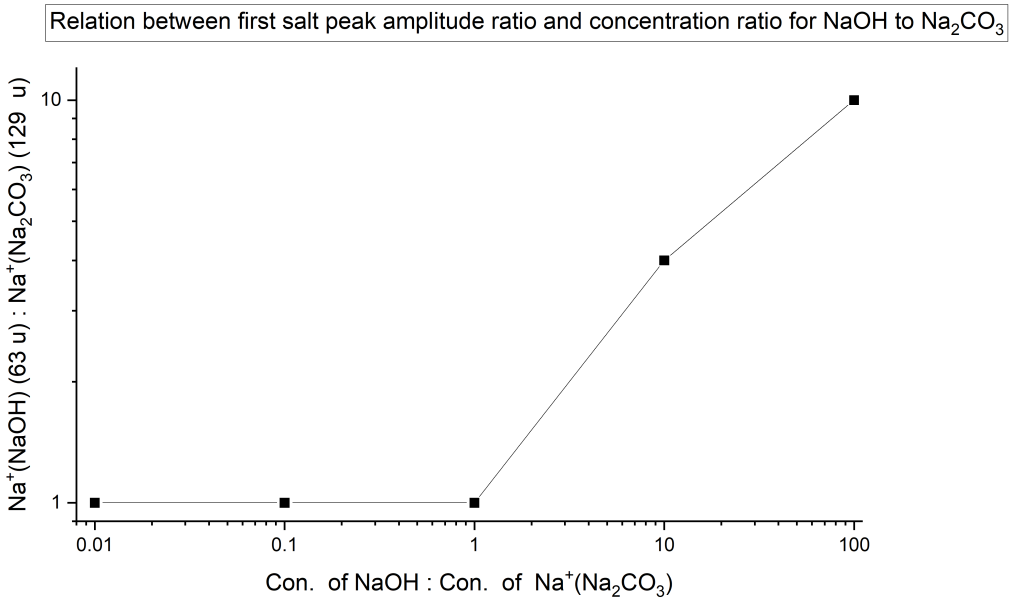

Figure 6.2: The relation between the first salt peak amplitude ratio and the concentration ratio for NaOH to Na_2CO_3. Five solutions are measured. The concentrations of the NaOH and Na_2CO_3 for each solution are listed in Table 6.3. The total concentration of Na^+ is between 0.2 M to 0.3 M. Laser power intensity: $\sim$ 721 mW/cm^2. Delay time: 5.4 μs. Note: The numbers in the axes are in logarithmic scale.

From Table 6.3, it can be concluded that the apparent relative ionization efficiencies of NaOH is higher than the relative ionization efficiencies of NaCl and lower than the relative ionization efficiencies of Na_2CO_3. The amplitude of the peak at Na^+(NaOH) (63 u) will be equal to that of peak Na^+(NaCl) (81 u) when the concentration ratio of NaOH to NaCl is approximately 1:10. Similarly, for the peaks at Na^+(NaOH) (63 u) and Na_2CO_3 (129 u), the concentration ratio of NaOH to Na_2CO_3 could range from 0:1 to approximately 1:1. These conclusions aid in determining the concentrations of substances during spectral mimicking, as will be described in the following section.

6.3.3 Spectra Mimicking

One or more of the peaks related to NaOH, NaCl and Na_2CO_3 appear constantly, and are usually of significant amplitude, in the spectra of the major subtypes (A, B, C, D) of sodium-rich CDA spectra. The three salts are believed to be the major sodium-bearing substances in Type-3 E-ring grains, and in general those responsible for the majority of spectral features (Postberg et al. 2009b). The three salts were therefore chosen to produce solutions to mimic the major subtypes (A, B, C, D) of sodium-rich Type-3 spectra.

The diversity of CDA spectra implies that the concentrations of the major substances are equally diverse between the different subtypes of grains. Subtypes A and B spectra have carbonate and hydroxide related peaks but no chloride related peaks. Therefore, the corresponding ice grains are carbonate rich and chloride poor. In contrast, Subtype C and D spectra have chloride and hydroxide related peaks but none from carbonate. Therefore, the corresponding ice grains are chloride rich and carbonate poor.

Dominant spectral end member and recessive spectral end member

Here, the substances whose relevant peaks are present at statistically significant (e.g. $> 3\sigma$) levels above the baseline are defined as dominant spectral end members and the substances whose relevant peaks are below this level - i.e. undetectable - as recessive spectral end members. According to this definition, for Subtype A and Subtype B, Na_2CO_3 is the dominant spectral end member, and NaCl is the recessive spectral end member; for Subtype C and Subtype D, NaCl is the dominant salt, and Na_2CO_3 is the recessive salt. Since all NaOH related salt peaks are also contributed by the matrix - water. These two concept does not apply for NaOH.

Through spectra mimicking, the rough range of concentrations of the dominant spectral end members and an upper limit for the concentration of the recessive end member can be experimentally determined.

6.3.4 Mimicking archetypal spectra for individual subtypes

Interdependencies of the different salt concentrations, in particular with respect to e.g. the pH of the solutions and the availability of Na^+ ions, made determining suitable analogue mixtures for the different subtypes complicated. Via a trial and error approach, the salt solution compositions shown in Tables 6.4 and 6.5 for archetypal Subtype A, Subtype B and Subtype C spectra were found. As the spectral profiles of Subtypes C and D are very similar, with the only difference being whether peak 81 u is higher than peak 63 u or vice versa, only the archetypal Subtype C spectrum for chloride-rich solutions was mimicked. These concentrations were then used as the initial compositions for exploring the parameter space of the major spectral subtypes (A, B, C, D).

Subtype	Concentration (M)		Upper limit (M)	pH	Salinity (g/kg)
	NaOH	Na_2CO_3	NaCl		
A	0	0.05	0.001	11.5 - 12 [1]	5.3
B	0.1	0.0001	0.005	$\sim$ 13	4

Table 6.4: Best case solution salt concentrations for carbonate rich and chloride poor spectra (Subtypes A and B).

Subtype	Concentration (M)		Upper limit (M)	pH	Salinity (g/kg)
	NaOH	NaCl	Na_2CO_3		
C/D	0.015 - 0.02	0.1	0.0001	12 - 12.5 [2]	6.6

Table 6.5: Best case solution salt concentrations for carbonate poor and chloride rich spectra (Subtypes C and D).

[1] The color of pH strip is between the colors corresponding to these two values.

[2] The color of pH strip is between the colors corresponding to these two values.

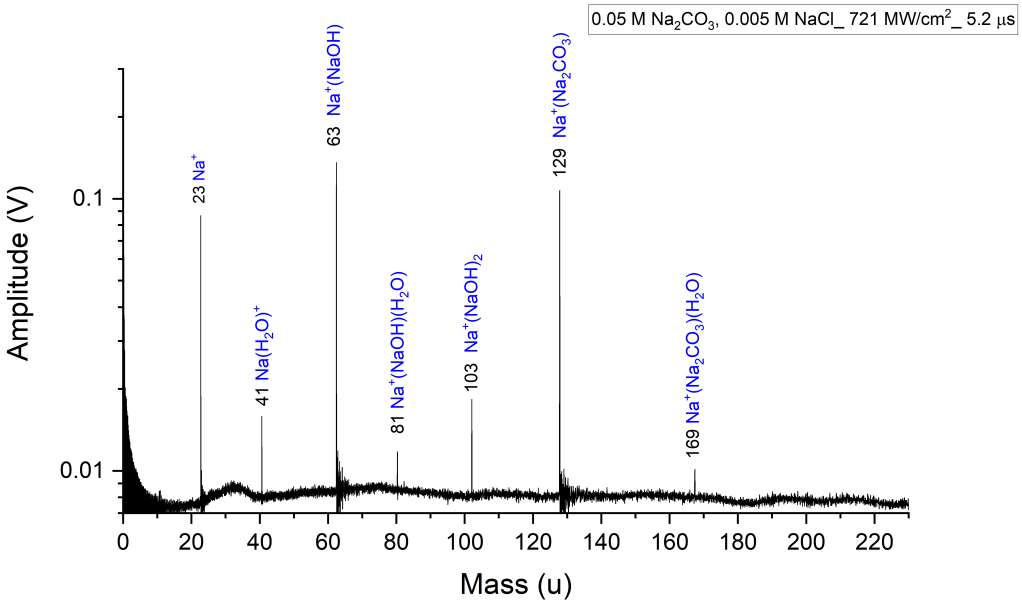

Figure 6.3: A archetypal Subtype A spectrum. The composition of the solution: 0.05 M Na_2CO_3 and 0.005 M NaCl. The power density: $\sim$ 721 MW/cm^2. The delay time τ: 5.2 μs.

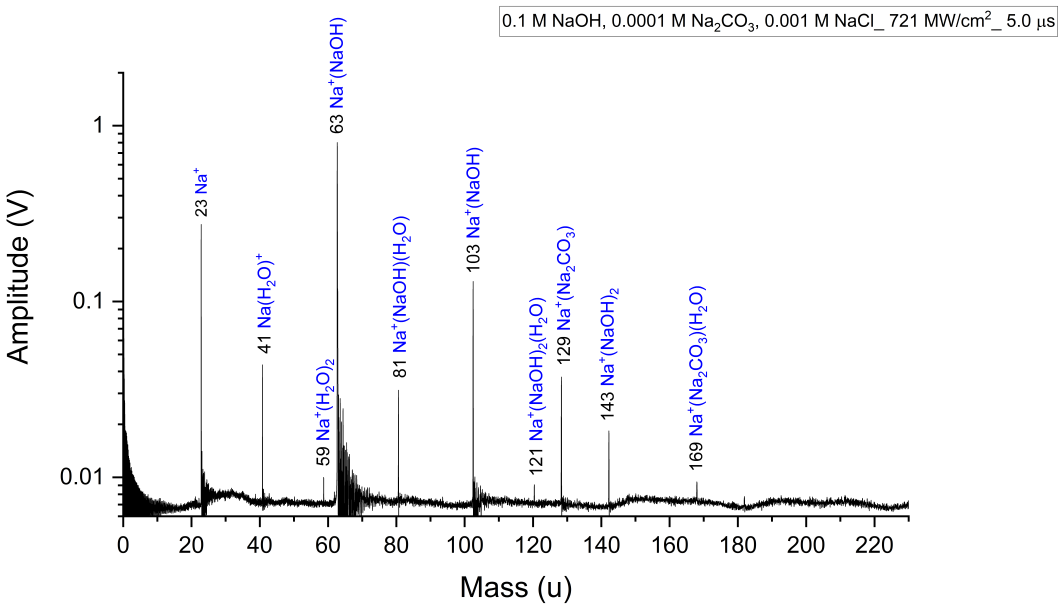

Figure 6.4: A archetypal Subtype B spectrum. The composition of the solution: 0.1 M NaOH, 0.0001 M Na_2CO_3 and 0.001 M NaCl. The power density: $\sim$ 721 MW/cm^2. The delay time τ: 5.0 μs.

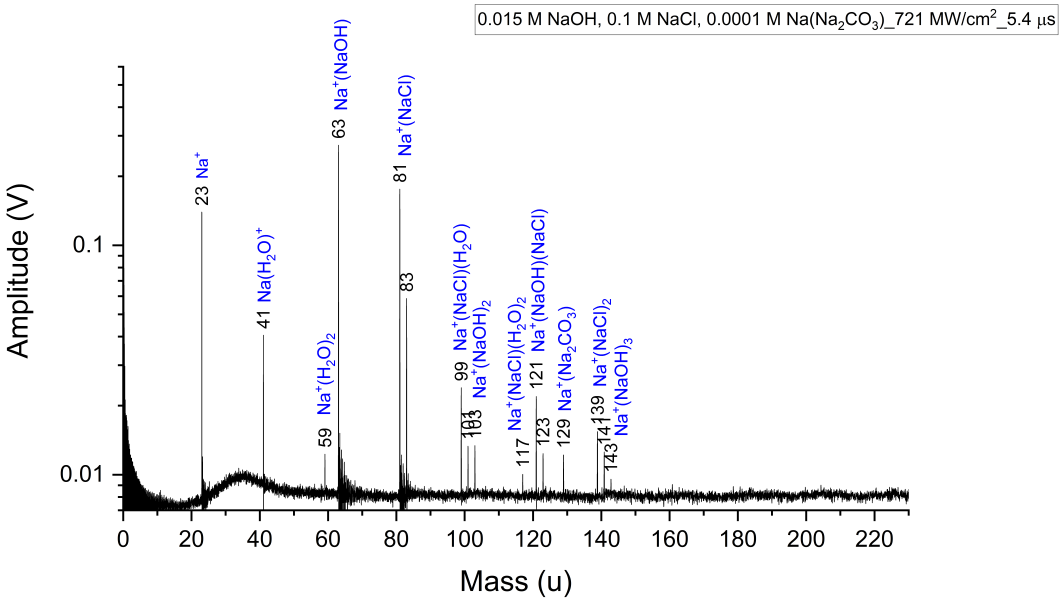

Figure 6.5: A archetypal Subtype C/D spectrum. The composition of the solution: 0.015 M NaOH and 0.1 M NaCl and 0.0001 M Na_2CO_3. The power density: $\sim$ 721 MW/cm^2. The delay time τ: 5.4 μs.

6.3.5 Concentration parameter space for subtypes

The results of the concentration parameter space mimicking are as following:

1) Constraints on the total concentration of the three spectral end members:

As discussed in Section 6.3.1, these constraints can be expressed as following inequality, in which C is the concentration of the subscripted salt:

$$0.1 \text{ M} < 2C_{(\text{Na}_2\text{CO}_3)} + C_{(\text{NaCl})} + C_{(\text{NaOH})} < 0.4 \text{ M} \tag{5.1}$$

The upper boundary of 0.4 M is much lower than the solubilities of these salts at 0 °C (for Na_2CO_3 it is 0.66 M; for NaOH it is 10.45 M; and for NaCl it is 6.1 M), and the concentration upper limit used for spectral mimicking is therefore physically plausible.

2) Determination of upper limits of recessive spectral end members:

The upper limit of a recessive end member is defined as the concentration at which the highest relevant peak (Na^+(NaCl) (81 u) for NaCl and $Na^+(Na_2CO_3)$ (129 u) for Na_2CO_3 is at 9-15 $\times$ σ_{lab} (local standard deviation of the local

baseline in laboratory analogue spectra), corresponding to 3-5 $\times$ σ (local standard deviation of the local baseline in E-ring Type-3 CDA Spectra) (See Section 7.2.3).

The experiments shows that for the best solution mimicking Subtype A spectra (0.05 M Na_2CO_3), the concentration upper limit of NaCl is 0.001 M (Table 6.4). Correspondingly, the concentration fraction of the upper limits of NaCl is as following:

$$C_{(\mathrm{NaCl})}/(C_{(\mathrm{Na_2CO_3})} + C_{(\mathrm{NaOH})}) < 0.02 \tag{6.2}$$

The experiments shows that for the best solution mimicking Subtype B spectra (0.1 M NaOH and 0.0001 M Na_2CO_3), the concentration upper limit of NaCl is 0.005 M (Table 6.4). Correspondingly, the concentration fraction of the upper limits of NaCl is as following:

$$C_{(\mathrm{NaCl})}/(C_{(\mathrm{Na_2CO_3})} + C_{(\mathrm{NaOH})}) < 0.05 \tag{6.3}$$

The experiments shows that for the best solution mimicking Subtypes C and D spectra (0.015 M to 0.02 M NaOH and 0.1 M NaCl), the concentration upper limit of Na_2CO_3 is 0.001 M (Table 6.5). Correspondingly, the concentration fraction of the upper limits of Na_2CO_3 is as following:

$$C_{(\mathrm{Na_2CO_3})}/(C_{(\mathrm{NaOH}))} + C_{(\mathrm{NaCl})}) \leq 0.00083 \text{ to } 0.00087 \tag{6.4}$$

These ratio about the the upper limits NaCl for Subtype A and Subtype B is close (Eqs. 6.2 and 6.3). The variation of the ratio about the upper limits of Na_2CO_3 is small (Eq. 6.4). Besides, range of the interval of total Na^+ is small (Eq. 5.1). Therefore, for plotting the following approximations are taken.

For carbonate rich and chloride poor spectra (Subtype A and Subtype B), Eq. 6.5 is used.

$$C_{(\mathrm{NaCl})}/(C_{(\mathrm{Na_2CO_3})} + C_{(\mathrm{NaOH})}) < 0.03 \tag{6.5}$$

For chloride rich and carbonate poor spectra (Subtype C and Subtype D), Eq. 6.6 is used.

$$C_{(\mathrm{Na_2CO_3})}/(C_{(\mathrm{NaOH}))} + C_{(\mathrm{NaCl})}) < 0.0009 \tag{6.6}$$

3) The boundary concentration ratio between two dominant end members in Subtypes A and B:

For Subtypes A and B, the dominant end members are Na_2CO_3 and NaOH. The concentration boundary between these two dominant end members is defined as the ratio of concentrations of Na_2CO_3 to NaOH, at which the ratio of the amplitudes of the 129 u to 63 u peaks in mimicked spectra is roughly equivalent to the boundary peak amplitude ratio distinguishing Subtype A and Subtype B CDA spectra.

The criteria for discriminating Subtype A and Subtype B in Section 4.4.3 are applied here. However, peak $Na^+(Na_2O)$ (85 u) in LILBID spectra could be not detected if the general peak amplitudes are low. Therefore, the 0.2 amplitude ratio of peak Na_2CO_3 (129 u) to peak $Na^+(NaOH)$ (63 u) is used to discriminating Subtype A and Subtype B in the LILBID spectra.

To convert this boundary peak amplitude ratio (0.2) into one applicable to the salt concentrations used in the laboratory, spectral mimicking using carbonate rich solutions with different concentration ratios of Na_2CO_3 to NaOH was performed. The results (Table 6.6) show that a concentration ratio (Na_2CO_3 to NaOH) of 9:1 reproduces the A-B boundary peak amplitude ratio of 0.2.

129 u/63 u	0.089	0.126	0.213
Concentration	0.1 M NaOH, 0.002 M **Na_2CO_3**	0.1 M NaOH, 0.005 M **Na_2CO_3**	0.09 M NaOH, 0.01 M **Na_2CO_3**
Concentration ratio of NaOH to Na_2CO_3	50:1	20:1	**9:1**
pH	13	13	**12.5**

Table 6.6: Concentrations tested to reproduce the 129 u to 63 u boundary peak ratio between Subtype A and Subtype B spectra. A concentration ratio of 9:1 for Na_2CO_3 to NaOH corresponds to the boundary peak amplitude ratio of 0.2 (the last column).

The ranges of the concentration ratios of Na_2CO_3 to NaOH for Subtypes A and B spectra can therefore be described as follows:

For Subtype A:

$$C_{(Na_2CO_3)}/C_{(NaOH)} > 9 \tag{6.7}$$

For Subtype B:

$$C_{(Na_2CO_3)}/C_{(NaOH)} \leq 9 \tag{6.8}$$

4) The boundary concentration ratio between dominant end members in Subtypes C and D:

For Subtypes C and D the dominant end members are NaCl and NaOH. The concentration boundary between these two dominant end members is defined as the ratio of the concentrations of NaCl to NaOH, at which the 81 u to 63 u peak amplitude ratio in mimicked spectra is roughly equivalent to the boundary peak amplitude ratio distinguishing Subtype C and D in CDA spectra. Unlike the case of Subtypes A and B, this ratio has already been specified as 1:1 in the definition of Subtypes C and D (See Table 4.2 on Page 86). Therefore, the aim of the performed laboratory experiments was to find the concentration ratio of NaCl and NaOH which reproduces this peak ratio. Spectra mimicking using a range of chloride-rich solutions with different concentration ratios of NaCl to NaOH produced the results shown in Table 6.7.

81u/63u	0.09	**1:1**	12.5
Concentration	0.05M NaCl, 0.05M NaOH	**0.12M NaCl, 0.01M NaOH**	0.1M NaCl
Concentration ratio of NaCl to NaOH	1:1	**12:1**	Pure NaCl
pH	12.5	**12**	5

Table 6.7: Concentrations tested to reproduce the 81 u to 63 u boundary peak ratio between Subtype C and Subtype D spectra. A concentration ratio of 12:1 for NaCl to NaOH corresponds to the observed boundary peak amplitude ratio of 1:1, highlighted in bold.

The results show that the concentration ratio of NaCl to NaOH, 12:1, reproduces the boundary peak amplitude ratio of 1:1. Therefore, this concentration ratio is the boundary between Subtype C and Subtype D in concentration parameter space and the range of the concentration ratio of NaCl to NaOH for Subtype C and Subtype D spectra can be described by following inequalities, respectively:

For Subtype C:

$$C_{(\mathrm{NaCl})}/C_{(\mathrm{NaOH})} < 12 \tag{6.9}$$

For Subtype D:

$$C_{(\mathrm{NaCl})}/C_{(\mathrm{NaOH})} \geq 12 \tag{6.10}$$

In summary, the concentration parameter space of the three end members is under the following constraints:

- Common constraints for all subtypes:

$$0.1\ \mathrm{M} < 2C_{(\mathrm{Na_2CO_3})} + C_{(\mathrm{NaCl})} + C_{(\mathrm{NaOH})} < 0.4\ \mathrm{M} \tag{6.11}$$

- Constraints for Subtype A:

$$C_{(\mathrm{NaCl})}/(C_{(\mathrm{Na_2CO_3})} + C_{(\mathrm{NaOH})}) < 0.03 \tag{6.12}$$
$$C_{(\mathrm{Na_2CO_3})}/C_{(\mathrm{NaOH})} > 9 \tag{6.13}$$

- Constraints for Subtype B:

$$C_{(\mathrm{NaCl})}/(C_{(\mathrm{Na_2CO_3})} + C_{(\mathrm{NaOH})}) < 0.03 \tag{6.14}$$
$$C_{(\mathrm{Na_2CO_3})}/C_{(\mathrm{NaOH})} < 9 \tag{6.15}$$

- Constraints for Subtype C:

$$C_{(\mathrm{Na_2CO_3}}/(C_{(\mathrm{NaOH}))} + C_{(\mathrm{NaCl})}) < 0.0009 \tag{6.16}$$
$$1 < C_{(\mathrm{NaCl})}/C_{(\mathrm{NaOH})} < 12 \tag{6.17}$$

- Constraints for Subtype D:

$$C_{(\mathrm{Na_2CO_3}}/(C_{(\mathrm{NaOH}))} + C_{(\mathrm{NaCl})}) < 0.0009 \tag{6.18}$$
$$C_{(\mathrm{NaCl})}/C_{(\mathrm{NaOH})} \geq 12 \tag{6.19}$$

Fig. 6.7 shows a 3D plot of the parameter space of the concentrations of the end members, demonstrating that the compositions of all the four subtypes are constrained in very narrow regions, with carbonate-rich/chloride-poor subtypes (A

and B) nearly completely separated from chloride-rich/carbonate-poor subtypes (C and D).

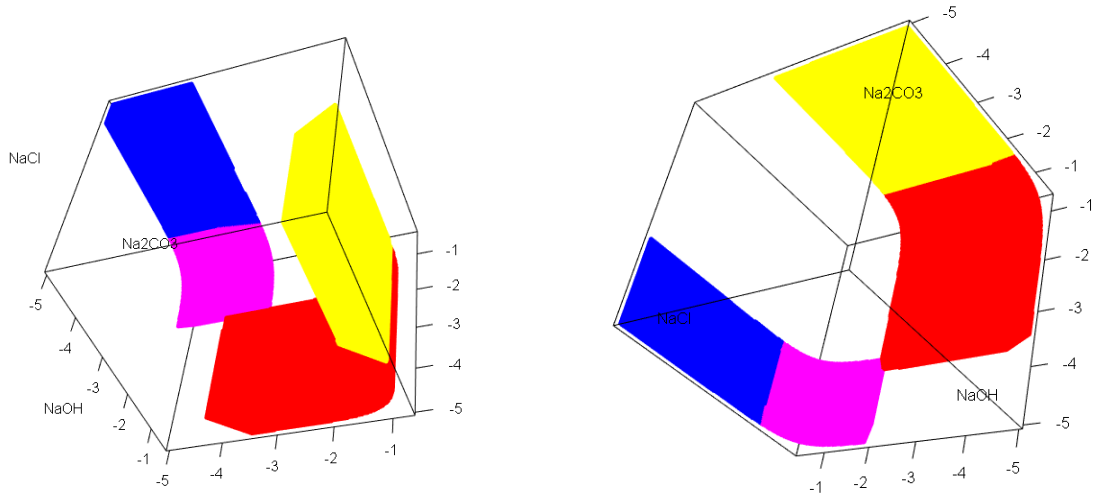

Figure 6.7: Two views of the 3D parameter space plot for Subtypes A (Yellow), B (Red), C (Magenta) and D (Blue). The three axes are in logarithmic scale and the numbers on the ticks indicate the order of magnitude of concentrations of the respective end members.

Chapter 7

Approximate CDA detection limit predictions for relevant geochemical and organic compounds

7.1 Introduction

Many geophysical and geochemical models to predict and explain the formation, evolution and composition of Enceladus have been constructed (Glein et al. 2008; Matson et al. 2007; Zolotov 2007; Ray et al. 2020; Taubner et al. 2020; Glein & Waite 2020). Measuring the concentrations or at the very least the detection limits of these compounds can provide crucial constraints for models and thus potentially verify or refute them.

Unfortunately, the composition of Enceladus' subsurface ocean water cannot be directly measured with current techniques. However, it can be inferred from the composition of the E-ring and plume salt-rich icy particles, which originate from the ocean water (Postberg et al. 2009b, 2011, 2018a). Salt-rich ice particles erupt from the fractures across Enceladus' south polar region, into space within a plume of gas and ice particles. The salt-rich ice particles preferentially own larger sizes (and thus larger masses) and slower speeds compared to salt-poor ice particles (Schmidt et al. 2008; Postberg et al. 2009b, 2018a). Most of the heavier, slower the salt-rich ice particles fall back to the surface of Enceladus as snow (Postberg et al. 2011; Schmidt et al. 2008; Kempf et al. 2010; Postberg et al. 2018a). Only a small fraction of the salt-rich icy particles which have the speeds over the three-body escape velocity of the Enceladus-Saturn system ($\sim$ 207 m/s) to escape from the gravity

of Enceladus-Saturn system to become E-ring particles (Kempf et al. 2010, 2018). From Fig. 5.1, it can be seen that the compositions of E-ring salt-rich particles are not necessarily equivalent to those of the plume salt-rich particles, which are supposed to be closer in composition to the subsurface ocean. The potential reasons could be that the salt-rich ice particles with different composition have different initial velocities (Section 5.4) and the space weathering, such as the plasma erosion sputtering (Juhász et al. 2007) and irradiation (Morfill et al. 1983), modifies the composition of the salt-rich ice particles (Sections 4.5.3, 4.5.4 and 5.4).

The quality of plume icy particle mass spectra is not high enough for reliable evaluation of individual ice particle compositions, so it is impossible to directly determine the bulk composition of the ocean solely with the mass spectra of the plume icy particle. Fortunately, many of the mass spectra of the relatively young E-ring icy particles are of higher quality, and can be used for the evaluation of individual ice particle compositions. Therefore, the bulk composition of the ocean water can be inferred via the combination of individual better quality spectra from the E-ring icy particles and distribution of plume compositional subtypes, which reflect the initial distribution of the compositional subtypes of the salt-rich ice particles formed under the surface of Enceladus' south polar region, and thus can be used to bias the (better quality) distribution of compositions of the individual salt-rich ice particles.

The concentrations of the dominant salt ions, including Na^+, K^+, Cl^-, OH^-, and CO_3^{2-}, can be evaluated by analyzing the peaks associated with combinations of the ions, and mimicking the spectral profiles (Section 6.3). Apart from these primary salt ions no frequent and significant peaks from other ions, whether inorganic or organic, are detected in *Typical* Na-rich Type-3 CDA spectra in the dataset investigated in this thesis. This absence means that, rather than directly measuring the concentrations of geochemically important ions within the grains from the spectra, CDA detection limits must be determined via LILBID spectral analogues.

Therefore, in this chapter the compositions of the salt-rich icy particles, including the concentrations of the primary salts and the detection limits of other species, are assessed via analysis of CDA flight mass spectra, using ion peak abundances derived from laboratory mass spectra of salt-rich aqueous solutions containing known concentrations of candidate minor species.

7.2 Methods

The major salts in the ice particles which originate from the subsurface sea water of Enceladus produce frequent and - for particular subtypes - common peaks in CDA mass spectra, which form the backgrounds on which the low amplitude peaks of trace substances (other ions, as well as those from organic compounds) will be visible if their concentrations are above the detection limits.

The concentrations of the major salts in individual salt-rich ice particles can be evaluated from the corresponding relationship between the corresponding peak amplitudes of the salts in CDA spectra and salt concentrations, which is evaluated via laboratory spectra mimicking. The concentrations of undetected trace ions or substances, if any, are by definition below the detection thresholds of the CDA, which are set by the dynamic range, resolution and baseline noise levels in CDA mass spectra. The concentrations of these undetected substances therefore cannot be determined via the direct analysis of CDA spectra, but the CDA detection limits of the ions can be identified through a combination of CDA spectra analysis and laboratory analogue experiments, as will be described below.

7.2.1 Mimicking co-added spectra of different subtypes of Type-3 spectra as template spectra to explore the detection limits of trace substances

The co-added spectra (Figs. 4.8, 4.9, 4.10 and 4.11) of different major CDA Type-3 subtypes were mimicked to create spectral analogues as templates spectra using the LILBID apparatus in the laboratory. These template spectra were then used to explore experimentally the detection limits of trace substances, .

Experimental settings to mimic the co-added spectra

A relatively high flash lamp power of 5.40 J was used to produce spectra with higher amplitude peaks. As with previous experiments (Section 6.2.1) a nozzle with an inner diameter of 15 - 22 μm and a water flow rate of 0.17 - 0.20 ml/min was used. To understand how the peak profiles and detection limits of substances vary with laser intensity and delay time, and therefore to impact speeds in space (Klenner et al. 2019), three combinations of laser intensity and delay time (Table 7.1) were used.

	Setting 1	Setting 2	Setting 3
Flash lamp power (J)	5.40	5.40	5.40
Laser Intensity	100%	100%	93.1%
Laser power density (mW/cm^2)	1080.8	1080.8	740.2
Delay Time (μs)	5.1	5.6	5.6
Corresponding impact speed	high	intermediate	low

Table 7.1: The three combinations of laser intensity and delay time corresponding to different impact speed ranges used for template spectrum mimicking and detection threshold determination. The laser setting of a flash lamp power of 5.40 J and a laser intensity of 100% (setting 1 and setting 2) corresponds to the laser power density of 1080.8 mW/cm^2; and the laser setting of a flash lamp power of 5.40 J and a laser intensity of 93.1% (setting 3) corresponds to the laser power density of 740.2 mW/cm^2.

Klenner et al. (2019) simulated Type-1 (NaCl concentrations of 10^{-7} M to 10^{-6} M) spectra and that work was used as the reference for impact speed mimicking. In Fabian Klenner's paper (Klenner et al. 2019), spectra of up to three settings could be co-added to accurately mimic one impact speed range, but the goal in this work is not to mimic impact speed ranges and the CDA spectra profiles accurately, but just mimicking the impact speeds roughly for CDA detection limits predictions. Therefore, it is not necessary for the settings to fully agree with the settings used by Fabian klenner. Here, for simplification only one setting is used for mimicking one impact speed range: setting 1 is used to mimic high impact speed ($\sim 11-13$ km/s) spectra, setting 2 is used to mimic intermediate impact speed ($\sim 8-10$ km/s) spectra and setting 3 used to mimic those generated at low impact speeds ($\sim 4-7$ km/s). For each mimicked impact speed range, corresponding detection limits could be experimentally derived.

Before measurements, the spectra for the three settings are calibrated by adjusting the position of the water beam and laser focus so that the spectral profiles for a certain setting are similar, i.e. they meet the same peak pattern criteria (Appendix G.2).

Analogue solutions of the template spectra

To measure the detection limits of trace compounds, spectra produced by the combined major components of the salt-rich solution (and therefore analogues to those produced by the ice particles) have to be created, with the analogue solutions

then used as the LILBID solvent matrix for the trace chemicals. Thus, laboratory experiments are required to find suitable solutions to reproduce these co-added spectra as 'template spectra'.

The CDA 'salt rich' spectra vary continuously from extremely carbonate-rich (Subtype A) to extremely chloride-rich (Subtype D). This implies that the composition of the salt-rich particles, and therefore the salt-rich solutions from which they derive, also varies continuously from extremely carbonate rich to extremely chloride rich. Producing an individual analogue solution for each spectrum is not necessary, as the spectra are already classified into four suitable subtypes based on visual/compositional similarity, and these subtypes can themselves be further divided into two (carbonate- or chloride-dominated) representative groups, which are mimicked with following two corresponding solutions, respectively.

1. **Mix 1: The representative solution for the chloride-poor subtypes (A and B):**

   The distribution of plume spectra (Fig. 5.1, lower panel) shows that the proportion of Subtype A spectra is larger than that of the Subtype B spectra and therefore a single solution, mimicking Subtype A spectra, was chosen to produce the template spectrum for the chloride-poor ice particles (and by extension, is assumed to be representative of chloride-poor brine sources within Enceladus). This solution is named Mix 1.

2. **Mix 2: The representative solution for chloride-rich subtypes (C and D):**

   The distribution of plume spectra (Fig. 5.1, lower panel) shows that the proportion of Subtype D spectra is just a little higher than that of Subtype C, implying that a solution designed to mimic spectra midway between Subtypes C and D in appearance is appropriate. A solution which produces spectra with similar Na^+(NaOH) (63 u) and Na^+(NaOH) (81 u) peak amplitudes was therefore chosen to produce the template spectrum for chloride-rich ice particles (and by extension, is assumed to be representative of chloride-rich brine sources within Enceladus). This solution is named Mix 2.

7.2.2 Measured substances

The following, geochemically-relevant, compounds (Table 7.2) were measured, and their detection limits for CDA determined, to provide information able to constrain geochemical models of Enceladus.

Ion or Molecule Name	Chemical Formula	Compound Used
Anions		
Sulfate	SO_4^{2-}	Na_2SO_4
Phosphate	PO_4^{3-} and HPO_4^{2-}	Na_3PO_4
Phosphite	PO_3^{3-} and HPO_3^{2-}	Na_2HPO_3
Nitrate	NO_3^-	$NaNO_3$
Fluoride	F^-	NaF
Bromide	Br^-	NaBr
Sulfide	S^{2-}	Na_2S
Cations		
Lithium	Li^+	LiCl
Ammonium	NH_4^+	NH_4Cl
Calcium	Ca^{2+}	$CaCl_2$
Ferrous	Fe^{2+}	$FeCl_2$
Magnesium	Mg^{2+}	$MgCl_2$
Mineral		
Silica	SiO_2	Amorphous SiO_2
Organic compounds		
Formic Acid	HCOOH	HCOOH
Formaldehyde	HCHO	HCHO

Table 7.2: The compounds measured to determine their spectral appearance and detection limits.

7.2.3 Evaluating approximate CDA detection limits

After dissolving a chemical into the Type-3 subtype template spectra analogue solutions, and generating LILBID spectra, identifiable peaks due to the added compound can be detected only if the concentration is high enough. These peaks can thus be used to evaluate the detection limits of the chemical.

In Section 4.3.1, 3σ (σ indicates the standard deviation of local noise value.) is used as the peak identification threshold in CDA spectra. Ideally, using the same criterion, if the amplitude of the chosen peak (usually the highest peak produced uniquely by a compound) produced by a particular concentration of a chemical, in a specific solution, is just above 3σ, the chemical is considered to be barely detectable and thus the used concentration is taken as the detection limit in the solution. However, there are two main problems to overcome when evaluating detection limits

through laboratory spectral analogues:

1. Laboratory spectra have much higher signal to noise ratios (SNR) than the flight CDA spectra, i.e. the ratio of the highest peak amplitude to the standard deviation of the 'global' spectrum noise in the laboratory spectra is approximately 3-5× that in the CDA spectra.

2. The mass resolution of CDA spectra is much lower than that of the LILBID spectrometer, i.e, the laboratory spectra with an about 20 times higher mass resolution than CDA flight spectra. In flight spectra the flanks of nearby peaks may therefore significantly overlap with peaks due to the minor components for which detection limits are being defined. As a result, the local baseline may be lifted by the flank of nearby peaks and thus much higher than 3σ in flight spectra, but not in the laboratory spectra. In other words, the flank of a nearby peak may overlap the peak under investigation (see, for example, Fig. 7.1).

Therefore, other methods for deriving the CDA detection limits from the laboratory spectra peak heights must be determined. In order to determine other methods, following basic assumption is made.

Assumption 7.2.1 *The amplification of signal (voltage) in CDA spectra is similar to that in laboratory spectra.*

Based on this assumption following two methods will be used in this thesis:

i) **Method 1: Peak identification threshold conversion based on signal to noise ratios**

This method converts the peak identification threshold in CDA spectra to the corresponding peak amplitudes in laboratory spectra, accounting for the larger noise level of CDA, and directly relates the concentration corresponding to the laboratory peak amplitude as the detection limit.

The first step is to choose one peak produced by the compound under investigation for detection limit determination. It is usually the highest peak or the second highest peak (if the highest relevant peak is too close to a significant background/template peak) containing ions due to the compound under investigation.

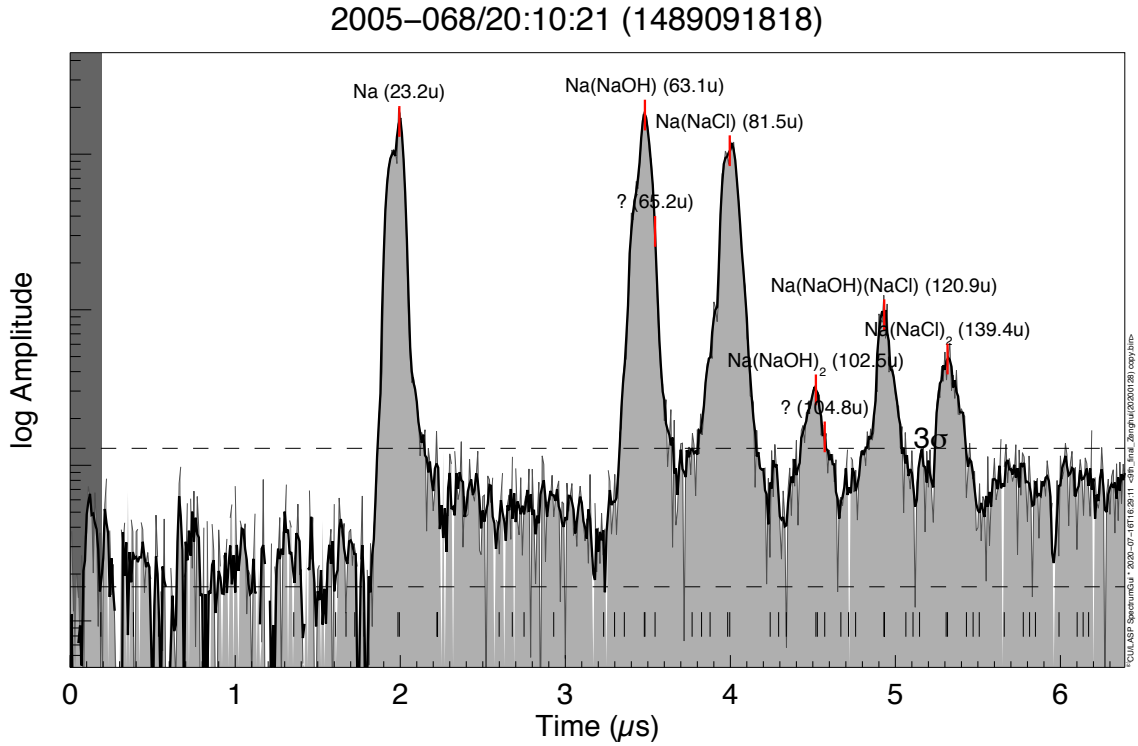

Figure 7.1: A subtype C spectrum. Stretch parameter a = 475 ns, shift parameter b = -0.287 μs. The highest peak produced by fluoride ions, $Na^+(NaF)$, has a mass of 65 u, which is overlapped by the right flank of $Na^+(NaOH)$ (63 u). As a result, the baseline at 65 u is much higher than 3σ (shown by the upper dashed line.) The amplitude ratio of the signal at 65 u to that at 63 u is $\approx$ 0.2. Other peaks produced by fluoride ions, such as $Na^+(NaF)(NaOH)$ (105 u), $Na^+(NaF)_2$ (107 u) and $Na^+(Na_2CO_3)(NaF)$ (171 u), either overlap with the flanks of nearby peaks (or even over the peak maxima) or are too low to be used to determine CDA detection limits.

- If the chosen peak produced by a 'compound of interest' is far from other significant peaks, the influence of the flanks of the other peaks is ignorable. In this case, the definition for CDA detection limits of a chemical is as follows: since the peak identification threshold in CDA spectra is 3σ, the corresponding CDA concentration of a 'compound of interest' is considered to be the CDA detection limit of the compound. Since the ratio of the highest peak amplitude to the standard deviation of the 'global' spectrum noise is approximately 3-5$\times$ that in the CDA spectra, the 3σ peak identification threshold for CDA spectra should be multiplied by a factor of 3 to 5 to convert to the corresponding peak amplitude in laboratory spectra, which is therefore between 9σ and 15σ. Accordingly, the corresponding laboratory concentration is treated as the detection limit.
- If the mass of the chosen peak produced by the 'compound of interest' is too close to the mass of a large template/background peak, the local baseline of the chosen peak is elevated. In this case, the definition for the CDA detection limit of a chemical is the ratio of the amplitude of the elevated flank at the position of a potential peak of interest to the amplitude of the nearby peak. Applying this same ratio to the laboratory spectra, the corresponding concentration is treated as the detection limit.

ii) **Method 2: Function fitting based on peak amplitude ratios**

This method does not use peak thresholds or amplitudes directly as the detection limits. Instead, it uses the ratios of peak amplitudes obtained from LILBID spectra of a range of concentrations of the 'compound of interest' to fit a linear function, which is then used to predict the detection limits in CDA spectra. Specifically, this method firstly uses laboratory template spectra of chloride or carbonate-rich solutions with different (known and systematically varied) concentrations of a particular compound, from which the peak amplitude ratio of peaks due to the compound and the matrix/template are measured. As the peak amplitude ratios tend to correlate with the concentration of the compound for which the detection limit is being determined, a linear function can be fitted (separately for each of the three LILBID settings) to predict the concentration corresponding to the amplitude ratio expected for a 3σ 'barely detected' peak in CDA spectra (if the baseline at the mass of the chosen peak is not significantly elevated be the flank of a nearby peak, i.e. elevated less or equal to 3σ) or the amplitude ratio based on the flank (if the baseline at the mass of the chosen peak is significantly elevated be the flank of a nearby peak, i.e. elevated over 3σ.). This predicted

concentration is then treated as the CDA detection limit of the compound under investigation.

Two different reference background peaks are used: Na^+ (23 u) and Na^+(NaOH) (63 u). The Na^+ peak is used because it is the highest peak in most spectra except those whose recording it triggers. The Na^+(NaOH) peak is used because this peak is closer to most peaks produced by the compound for which the detection limit is being determined, compared to peak Na^+ (23 u), allowing the effects of baseline changes, the different 'impact speed' regimes, and any variations in calibration accuracy to be minimised.

When fitting the linear function linking the concentrations and the peak amplitude ratios, both the concentration errors and peak amplitude ratio errors, which are measured independently, are taken into account. Thus, **Total Least squares (TLS) linear regression** is used. To perform the fitting and calculate the likelihood values, the **AstroML** (Machine Learning and Data Mining for Astronomy) python module is used.

7.2.4 Comparison of the two CDA detection limit evaluation methods

The two methods for evaluating approximate CDA detection limits for a variety of salts, mineral and low mass organic compounds will be compared in the following paragraphs.

Validity of Method 1

The validity of Method 1 is based on Assumption 7.2.1, from which, the following conclusion is deduced:

Although the noise levels for the CDA and laboratory analogue spectra are different, the ratio of the amplitudes of the chosen 'compound of interest' related peak to the amplitude of **the highest peak** are the same both in CDA and laboratory analogue spectra, if the composition of the salt rich ice particles and the solutions are the same.

The amplitude above which a peak is treated as statistically significant - i.e. real - in CDA spectra has to be converted to a peak amplitude threshold applicable to the laboratory analogue spectra. In CDA spectra, 3σ (σ represents the standard

deviation of the local spectrum baseline.) is used as the peak threshold, i.e. if a peak's amplitude is equal to, or greater than 3σ, the peak is statistically significant - it is real. The ratio of the standard deviation of the noise (in Volts) to the amplitude of the highest peak (in Volts) in the same spectrum is defined as the relative noise level. The relative noise level of the 'good' Type-3 CDA spectra (those selected for co-adding) is approximately 3-5$\times$ that of the high quality (the amplitude of the highest peak is between 0.7 V and 1.1 V and the spectral profiles fit the template spectra) laboratory spectra. The corresponding '3σ' peak threshold in laboratory analogue spectra is therefore approximately $9\sigma_{lab}$ to $15\sigma_{lab}$.

In addition, there are also some unaccounted factors, which could increase the uncertainty of the value of peak threshold, as following:

1. The amplitudes of peaks, in both CDA spectra and LIBID spectra, used to determine the peak thresholds have uncertainties.

2. In CDA spectra, due to the lower mass resolution, the local baseline could be elevated by the flanks of nearby salt peaks. If the nearby peak is a huge peak, such as peak $Na^+(NaOH)$ (63 u), the local baseline at the mass of chosen peak, such as $Na^+(NaF)$ (65 u), is elevated so significantly (much more than 20σ) that the Method 1 does not apply anymore. If the nearby peak is a small peak, such as peak $Na^+(NaOH)_2$ (103 u), the local baseline at the mass of chosen peak, such as $Mg^+(^{26}MgO)_2$ (105 u), could also be elevated by several σ. In this case, the Method 1 still applies.

3. It is very hard to choose the precise concentration of a compound of interest that exactly matches the signal to noise threshold, when carrying out the analogue experiment.

4. The CDA uses a logarithmic scale when converting from the DN units transmitted back to Earth into linear voltages. Therefore, for a high peak (especially if it's very sharp), the uncertainty in the maximum amplitude is much larger than the uncertainty in the amplitude of a small peak. By using the peak ratios the big uncertainties of the high peaks are introduced into the calculation.

5. The CDA spectra may go through a process of wavelet compression, which introduces uncertainties, or Lee filter, which preferentially remove lots of the low amplitude noise. The resulting uncertainties are hard to quantify.

6. The relation between the concentration of a certain substance and the amplitudes of the resulting peaks over the concentration range considered

in this work is just quasi-linear, rather than strictly linear, for both lab spectrometer and CDA. The influences caused by the deviation from the linearity will be investigated in the future.

All of the influences of these factors are negligible and difficult to quantitate. Therefore, for simplicity, they are neglected.

Factors affecting the precision of Method 1

The following factors could introduce errors into the approximate CDA detection limits calculated using Method 1.

1. **Shift of the spectral profiles of the laboratory spectra**

   Even with calibration (Appendix G.2) directly before the detection limit analogue experiments, the shift of the resulting spectral profiles still occurred. The spectral profile could shift either to low mass end, i.e, the relative amplitudes of lower mass peaks increase and the relative amplitude of higher mass peaks decrease, or to higher mass end, i.e, the relative amplitude of lower mass peaks decrease and the relative amplitude of higher mass peaks increase. Thus re-calibration was sometimes necessary. The errors caused by this factor are difficult to evaluate.

2. **Variation of the general level of peak amplitudes in laboratory spectra**

   If an analogue spectrum possesses the correct spectral profile (i.e. the relative amplitudes of the background spectral peaks are the same as the relative amplitudes of the peaks in the template spectrum (Figs. 7.2 and 7.3)), it is still possible for the overall spectral amplitude to vary during the few hours of measurement. Variations in instrument alignment, for example, introduce significant differences in response, resulting in day-to-day (or sometimes more or less frequent) changes in overall spectral amplitudes. Therefore, if the amplitude of the highest peak in a spectrum lay within 0.7 V to 1.1 V, the calibration was deemed acceptable (Appendix G.2). There is a $\sim 20\%$ variation around 0.9 V in the overall spectrum level. The amplitudes of peaks chosen for detection limit evaluation may also vary proportionally to variations in the overall spectrum amplitude level.

   Note: Both above two factors contribute the errors in the noise level and peak heights in the lab spectra

3. **The precision of the noise level or the relative height of the peak flank at the mass of the chosen peak in CDA spectra**

   The baseline correction, the mass of the chosen peak positioning, and the noise evaluation for CDA spectra introduce this kind of errors. 10 best CDA spectra for each 'compound of interest' were selected for coadding to produce one coaddded spectrum for each 'compound of interest'. Before coadding, the baseline of each individual spectrum was corrected and the spectral peak amplitudes are normalized. Afterwards, the baseline correction, the mass of the chosen peak positioning, and the noise evaluation were repeated three times on the co-added spectra to obtain the mean values and the deviations.

Validity of Method 2

The validity of this method is based on two prerequisites:

1. The ratio of the amplitude of the chosen 'compound of interest' related peak relative to the amplitude of **a reference peak** is the same in both CDA spectra and laboratory analogue spectra, if the composition of the salt rich ice particles and the solutions are the same. This is a conclusion of Assumption 7.2.1.

2. The relative amplitudes of the peaks related to the added 'compounds of interest' vary linearly with concentration in the ice particles, or solution of the same composition, if the concentration of the target detection limit compound is below a certain threshold. This initial assumption was subsequently verified for the laboratory spectra.

Factors affecting the precision of Method 2

The following factors may introduce errors into the approximate CDA detection limits calculated using Method 2.

1. **Variation of the spectral profiles of the laboratory analogue spectra**

   This is exactly the same as the first factor affecting the precision of Method 1.

2. **The relative amplitudes of the reference peaks**

   One or two suitable reference peaks must be chosen to reduce the effect of factor 1. The reference peaks should have following properties:

- The relative amplitude of the reference peak should not vary with impact speed significantly.

  The amplitudes of the peak Na^+(NaOH) (63 u) relative to Na^+ (23 u) peak do not vary with impact speeds significantly (Tables 4.4 and 4.4).

- The relative amplitude of the reference peaks should but not vary with composition too much.

  Only the Na^+ (23 u) and Na^+(NaOH) (63 u) peaks are detectable in all four major subtypes (A, B, C and D) of CDA spectra and they are usually two of the three highest peaks in individual Na-rich Type-3 CDA spectra and the two highest peaks in the four co-added spectra of the major subtypes (A, B, C and D) of CDA spectra in the dataset (Figs. 4.8, 4.9, 4.10 and 4.11), thus the amplitudes of these two peaks should roughly reflect the total concentration of Na^+, which is the major cations, and less dependent on the species of anions in the ice particles or the solutions.

- The reference peak should be close to the peak chosen for detection limit evaluation in order to reduce the effect of variations in spectral profiles on the peak amplitude ratio.

With the above constraints, the Na^+ (23 u) and Na^+(NaOH) (63 u) peaks were chosen as the reference peaks.

3. **The precision of the noise level or the relative height of the peak flank at the mass of the chosen peak in CDA spectra**

   This affects the precision of the chosen peak to reference peak ratios or noise to reference peak ratios in CDA spectra. These ratios are used for TLS linear fitting and thus affect the accuracy of the detection limits determined.

4. **The number of the data points available across suitable substance concentrations**

   The greater the number of the data points used to derive the relationship between peak amplitude ratios and concentrations, the smaller the uncertainty in the parameters of the linear regression. However, obtaining large number of data points is time consuming. Thus, in some cases the number of data points was constrained by LILBID availability, and for a few compounds further data points to confirm linearity should be collected in future.

The advantages and disadvantages of the two methods

Both methods are affected by variations in the spectral profiles of the laboratory analogue spectra. As well as this, the two methods have the following further advantages and disadvantages.

1. **Method 1:**

   - **Advantage**

     Only information about the concentration required to obtain 'compound of interest' peak amplitudes between $9\sigma_{lab}$ and $15\sigma_{lab}$ in laboratory analogue spectra (corresponding to 3σ in Type-3 CDA spectra) is required. If the measurement of this concentration is precise, the result is precise.

   - **Disadvantage**

     1) Method 1 is affected by the variation of the overall peak amplitudes of laboratory analogue spectra. During analogue to digital conversion onboard Cassini, information is lost concerning exact peak amplitudes. The nonlinear conversion applied by CDA means that this digitization process introduces larger uncertainties in the real amplitudes of larger peaks than smaller peaks, especially in the case of sharp peaks
     2) The accuracy of the measurements of the noise level or the relative height of the peak flank at the mass of the chosen peak in CDA spectra affects the accuracy of the evaluated detection limits.
     3) This method can only determine the detection limit of the compounds in CDA spectra, and it can not determine the actual concentration of the substances in the ice grains.

2. **Method 2:**

   - **Advantage**

     1) Method 2 is not affected by the variation of the overall peak amplitudes of laboratory analogue spectra.
     2) If a chosen peak for a 'compound of interest' is found in any spectra, the original concentration in the grains can be determined from measured peak amplitude ratios in arbitrary CDA spectra, using the fitted curves. The approach is valid for grains detected at speeds covered by the ranges considered in this work.

- **Disadvantage**
  1) Laboratory measurements of compounds over a range of concentrations, rather than just that which produces a 9 – 15 σ_{lab} high peak, are required. Otherwise, the parameters of the fitted line are not well constrained and therefore the predicted detection limits are not accurate. Data over at least three different concentrations are required. If there are only two data obtained from the measurement, the origin is also used.
  2) The accuracy of the measurements of the noise level or the relative height of the peak flank at the mass of the chosen peak in CDA spectra affects the accuracy of the evaluated detection limits.

7.2.5 Error Analysis

In this subsection the measurement errors, which include the errors on the concentration, individual peak amplitudes and peak amplitude ratios, followed by the predicted errors on the derived detection limits, will be introduced.

Measurement errors:

An initial stock solution of the template mixture (either chloride or carbonate-rich) was prepared. To this a known weight/volume of the compound under investigation was added and dissolved, a subsample of known volume was then extracted and further diluted, and this second process repeated until the desired concentration was reached.

- **Concentration Errors**

  The errors (standard deviation) in the concentration need to be calculated based on the method used to produce the solution and arise from errors in the weight of the solid substance and the volume of the (template/background) liquid during solution preparation and dilution. These can be combined using the standard error propagation formula.

  The weight of solid for initial concentration (for salt and silica): $X \pm \delta X$. The error is estimated from the balance and any possible losses during transfer. For the balance in the laboratory, the error is estimated to be 0.0005 g.

  The volume of liquid for the first solution (for formaldehyde and formic acid): $Y \pm \delta Y$. The error is estimated from the measurement scale on the side of the

container. For a 50 ml centrifuge tube with 2.5 mL graduations, the error is estimated to be 0.5 ml [1].

The concentration of the initial solution: $C \pm \delta C$, where the $C = X/Y$ and the error is shown in Eq. 7.1:

$$\delta C = C\sqrt{\left(\frac{\delta X}{X}\right)^2 + \left(\frac{\delta Y}{Y}\right)^2} \tag{7.1}$$

For a dilution step, a subsample ($n \pm \delta n$ ml) of the previous solution of concentration $C \pm \delta C$ was extracted, and made up to a new volume ($V \pm \delta V$ml) with additional Mix 1 or Mix 2 stock solution. The new concentration $\widetilde{C} \pm \delta\widetilde{C}$, where $\widetilde{C} = n/V$, is given by Eq. 7.2:

$$\delta\widetilde{C} = \widetilde{C}\sqrt{\left(\frac{\delta C}{C}\right)^2 + \left(\frac{\delta n}{n}\right)^2 + \left(\frac{\delta V}{V}\right)^2} \tag{7.2}$$

.

For further dilution steps the above calculation is repeated.

- **Peak Amplitude Errors**

  The error in peak amplitudes derives from:

  1) **Calibration error**

     Systematic errors are mainly due to imperfect calibration. Calibration involves many factors, such as the focus and alignment of the laser on the water beam and the position of the water beam relative to the skimmer at the entrance of the vacuum chamber. Therefore, although the setup is calibrated to reproduce the 'clean' templates before each set of measurements, it is impossible to achieve 'perfect calibration' - i.e. spectra identical to the original template spectrum. This error is difficult, if not impossible, to quantify and therefore efforts were made to reproduce the template spectra as exactly as possible to minimize this error. The effects of calibration and instrument setup accuracy have therefore not been included in the error calculations.

[1] To make the errors smaller, I usually only measure volumes at the scale lines, such as 5 ml, 7.5 ml, 10 ml, etc, not volumes between scale lines, such as 6 ml, 13 m, etc. If I have to measure a volume between the scale lines, I used a syringe.

2) **The non-linear response of the spectrometer** The function between the peak amplitude (the output voltage) and the amount of the corresponding ions arriving the Microchannel plate detector (MCP) amplifier of the fight mass spectrometer is non-linear for both the CDA and laboratory amplifiers. This is another systematic error.

3) **Random error**

Random error mainly arises from electronic noise in the spectrometer and digitiser, as well as random variations in the laser and the water beam. Noise from these sources is Gaussian noise.

Both calibration and random errors in peak amplitudes propagate to the peak amplitude ratio, in a similar way to the errors in the concentration.

- **The error on peak amplitude ratio**

Applying the standard error propagation formula, the peak amplitude ratio errors are calculated as follows. If the measured peak amplitudes for peak 1 and peak 2 are A_1 and A_2, and the amplitude errors/uncertainties in these two peaks are δA_1 and δA_2, respectively, the standard deviation of the peak ratio $R = \frac{A_1}{A_2}$ is shown in Eq. 7.3:

$$\delta R = R\sqrt{\left(\frac{\delta A_1}{A_1}\right)^2 + \left(\frac{\delta A_2}{A_1}\right)^2} \tag{7.3}$$

Deriving errors in the detection limits:

- **The detection limit error for Method 1**

The detection limit error of this method arises from two main sources:

1) **Uncertainty in peak amplitudes**

For most compound peaks, an amplitude of 3σ in CDA spectra is used as the criterion for detection limit. The 3σ in CDA spectra corresponds $9\sigma_{lab}$ and $15\sigma_{lab}$ in laboratory spectra, because the signal to noise ratio in the CDA spectra is 3 to 5 times as that in laboratory spectra. Thus, there is an uncertainty of $6\sigma_{lab}$ in laboratory spectra, which is hard to convert to concentration and thus is ignored.

2) **Uncertainty in concentration**

This error is calculated using the same approach as in Eqs. 7.1 and 7.2.

- **The detection limit error for Method 2**

  Using TLS fitting, the likelihood area (defined by the upper and lower limits of concentration and peak amplitude ratios) for different confidence intervals are obtained. For the 3σ (σ represents cumulative standard deviation for linear regression), 99.7%, likelihood area the corresponding detection limit error is then estimated.

7.3 Results

In this section the two solutions (Mix 1 and Mix 2) derived for template spectra mimicking are discussed firstly and then the example mimicked template LILBID spectra of the two solutions are presented. Finally the calculated CDA detection limits for the range of compounds shown in Table 7.5 are presented.

7.3.1 The composition of analogue solutions and the resulting laboratory template spectra

The typical compositions of the two brine mixture solutions: Mix 1 and Mix 2, which are the representative solutions for the carbonate-rich and chloride-rich ice particles (Section 7.2.1), respectively are given in Table 7.3.

	Na_2CO_3	NaOH	NaCl	KCl	Total Na^+	Salinity	pH
Mix 1	0.075M	0	0.002M	0.0003M	0.17M	0.80%	11.3
Mix 2	0	0.015M	0.15M	0.0003M	0.15M	0.91%	12.1

Table 7.3: The composition of the two brine mixture solutions. Mix 1 and Mix 2 are the representative solutions for the carbonate-rich and chloride-rich ice particles, respectively.

The concentrations of various salts are constrained and determined as discussed below.

- **Concentration of major salts**

  Major salts determine the dominant peaks in spectra and their general profiles. Na_2CO_3 is the major salt of Mix 1 and NaCl is the major salt of Mix 2. These

salts make up the overwhelming majority of the salts in the solutions, so their concentrations approach those of the total salt concentrations.

- **Concentration of minor salts**

  The minor salts produce the small peaks in the spectra, as well as adjust the relative peak amplitudes and pH values. The approximate concentrations of the minor salts are determined as follows:

  1) **Potassium in mixes 1 and 2**
     In order to evaluate the rough concentration of potassium, a co-added spectrum from the four main subtypes of Na-rich CDA Type-3 spectra was produced (Fig. 4.16). The peak amplitude ratios of peak K^+ (39 u) to peak Na^+ (23 u) in this coadded spectrum was evaluated as a reference. In reproducing this co-added spectrum, trace KCl was added to reproduce the rough peak amplitude ratio of K^+ (39 u) to peak Na^+ (23 u) in the co-added CDA spectrum. Since the spectrometer is much more sensitive to potassium than sodium, only approximately **0.0003 M** KCl is required.
  2) **Hydroxide in Mix 2**
     Mix 2 is used to mimic spectra on the boundary between subtypes C and D, which have similar amplitudes of the Na^+(NaOH) (63 u) and Na^+(NaOH) (81 u) peaks. and to achieve this, 0.015M NaOH is added. This increases the pH value to approximately that of Mix 1 and produces Na^+(NaOH) (63 u) and Na^+(NaOH) (81 u) peaks of similar amplitude.

Template spectra of Mix 1 and Mix 2 solutions

The template spectra of Mix 1 and Mix 2 solutions in three LILBID settings are present and discussed as following:

- **The template spectra of Mix 1 for the three different LILBID settings:**

  Fig. 7.2 shows the mimicked spectra of Mix 1 for the three LILBID settings described in Table 7.1.

  Note: The peak at mass 81 u in these spectra is exclusively or mainly [2] due to the water cluster of $Na^+(NaOH)(H_2O)$ (81 u) rather than $Na^+(Na^{35}Cl)$

[2]Since the abundance of ^{35}Cl is approximately 32% of the abundance of ^{37}Cl and the ringing of peak at mass 81 is very small, if the peak $Na^+(Na^{37}Cl)$ (83 u) just under the detection threshold

(81 u), because there is no peak $Na^+(Na^{37}Cl)$ (83 u) detected. In laboratory spectra the $Na^+(NaOH)(H_2O)$ (81 u) is accompanied by abundant water cluster peaks, such as the $Na^+(NaOH)(H_2O)$ (41 u), $Na^+(H_2O)_2$ (59 u) and $Na^+(NaOH)_2(H_2O)_2$ (99 u) peaks. For setting 1 (mimicking high impact speeds), the $Na^+(NaOH)(H_2O)$ (41 u) peak is higher than the $Na^+(NaOH)(H_2O)$ peak at 81 u. This mechanism of this phenomenon is discussed in Section 7.4.2. In contrast, in Type 3 CDA spectra only a small ($< 10\sigma$ if existing.) $Na^+(NaOH)(H_2O)$ (41 u) peak is infrequently detected, and higher mass water cluster peaks, such as those due to $Na^+(H_2O)_2$ (59 u) and $Na^+(NaOH)_2(H_2O)_2$ (99 u) are never detected. Therefore, the peak at mass 81 u in subtypes C and D salt-rich CDA spectra are attributable to $Na^+(Na^{35}Cl)$ (81 u) instead of $Na^+(NaOH)(H_2O)$. If a peak at mass 81 u in CDA spectra is high enough, its right flank decreases in amplitude more slowly than the left flank. This implies that there could be a hidden, unresolved, $Na^+(Na^{37}Cl)$ at 83 u. This is additional evidence that the peak at mass 81 u is $Na^+(Na^{35}Cl)$ (81 u) instead of $Na^+(NaOH)(H_2O)$ in salt-rich CDA Type-3 spectra.

- **The template spectra of Mix 2 for the three different LILBID settings:**

  Note:

  1. The mass 81 u peak in these spectra is due to $Na^+(Na^{35}Cl)$ (81 u) instead of $Na^+(NaOH)(H_2O)$ (81 u), because the 83 u peak, which corresponds to the 37 u Cl isotope cluster $Na^+(Na^{37}Cl)$, is present at equivalent amplitudes. The amplitude ratio of the 81 u to 83 u peaks, of approximately 10:3, corresponding to the isotopic abundance ratio of ^{35}Cl to ^{37}Cl in nature. Therefore the peak at 81 u is dominated by $Na^+(Na^{35}Cl)$ (81 u).
  2. There is a peak at mass 129 u, due to $Na^+(Na_2CO_3)$, although there is no carbonate added into Mix 2. It is attributed to the absorption of CO_2

(3σ) or hidden in the ringing of peak at mass 81 u, the peak $Na^+(Na^{35}Cl)$ (81 u) should be also significant, but much smaller than peak $Na^+(NaOH)(H_2O)$ (81 u).

Figure 7.2 *(following page)*: The template spectra of the Mix 1 solution for LILBID settings (Upper panel: setting 1, corresponding to impact speed range of 11 - 13 km/s; middle panel: setting 2, corresponding to impact speed of 8.5 - 11 km/s; lower panel: setting 3, corresponding to impact speed range of 6 - 7.5 km/s.).

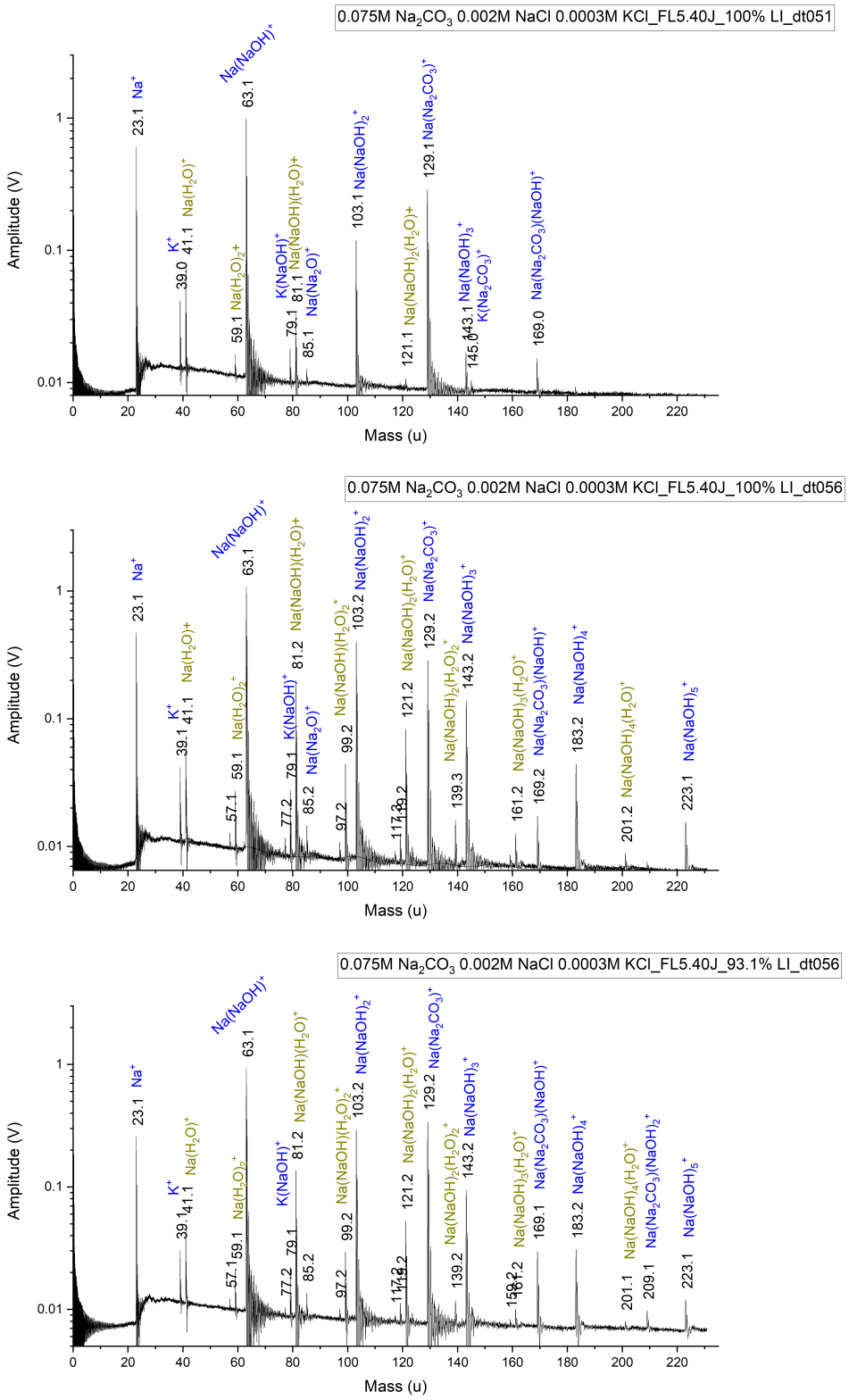
0.075M Na2CO3 0.002M NaCl 0.0003M KCl_FL5.40J_100% LI_dt051
Amplitude (V)
Mass (u)
23.1 Na+
39.0 K+
41.1 Na(H2O)+
59.1 Na(H2O)2+
63.1 Na(NaOH)+
79.1 K(NaOH)+
81.1 Na(NaOH)(H2O)+
85.1 Na(Na2O)+
103.1 Na(NaOH)2+
121.1 Na(NaOH)2(H2O)+
129.1 Na(Na2CO3)+
143.1 Na(NaOH)3+
145.0 K(Na2CO3)+
169.0 Na(Na2CO3)(NaOH)+
0.075M Na2CO3 0.002M NaCl 0.0003M KCl_FL5.40J_100% LI_dt056
Amplitude (V)
Mass (u)
23.1 Na+
39.1 K+
41.1 Na(H2O)+
57.1
59.1 Na(H2O)2+
63.1 Na(NaOH)+
77.2
79.1 K(NaOH)+
81.2 Na(NaOH)(H2O)+
85.2 Na(Na2O)+
97.2
99.2 Na(NaOH)(H2O)2+
103.2 Na(NaOH)2+
117.2
119.2
121.2 Na(NaOH)2(H2O)+
129.2 Na(Na2CO3)+
139.3
143.2 Na(NaOH)3+
161.2 Na(NaOH)3(H2O)+
169.2 Na(Na2CO3)(NaOH)+
183.2 Na(NaOH)4+
201.2 Na(NaOH)4(H2O)+
223.1 Na(NaOH)5+
0.075M Na2CO3 0.002M NaCl 0.0003M KCl_FL5.40J_93.1% LI_dt056
Amplitude (V)
Mass (u)
23.1 Na+
39.1 K+
41.1 Na(H2O)+
57.1
59.1 Na(H2O)2+
63.1 Na(NaOH)+
77.2
79.1 K(NaOH)+
81.2 Na(NaOH)(H2O)+
85.2
97.2
99.2 Na(NaOH)(H2O)2+
103.2 Na(NaOH)2+
117.2
119.2
121.2 Na(NaOH)2(H2O)+
129.2 Na(Na2CO3)+
139.2
143.2 Na(NaOH)3+
158.2
161.2 Na(NaOH)3(H2O)+
169.1 Na(Na2CO3)(NaOH)+
183.2 Na(NaOH)4+
201.1
209.1 Na(Na2CO3)(NaOH)2+
223.1 Na(NaOH)5+

from the air into the mix. The NaOH in the solution then reacts with it:

$$2\,OH^- + CO_2 \longrightarrow {CO_3}^{2-} + H_2O \tag{7.4}$$

This reaction occurs immediately once the solution is exposed to the air, so even if the solution is measured promptly after preparation, the 129 u peak is detectable. The amplitude of the $Na^+(Na_2CO_3)$ (129 u) peak increases with time, as the CO_2 from air continues to react with NaOH until it reaches equilibrium. The reaction rate therefore decreases gradually. The pH values does not change significantly in four days, if stored in a sealed container. As the peak at mass 129 u usually does not overlap with any peaks produced by the compounds whose detection limits are being determined, the presence of this peak is not considered to be a problem. However, to minimise any possible effects from e.g. pH changes as CO_2 is absorbed, and reduce the size of the 129 u peak, Mix 2 is always stored in a sealed container and usually less than one day old, and at most four days old, when it is used for detection limit determination.

7.3.2 Identification of suitable mass lines (peaks) for detection limits evaluation

In order to measure the detection limits of the compounds listed in Table 7.3, various amounts of the individual compounds were dissolved into the Mix 1 and Mix 2 solutions. The peaks attributable to the added substance were identified in the spectra and their amplitudes corresponding to the different concentrations then used to evaluate the detection limits. An example for sulfates follows:

Fig. 7.4 shows two LILBID spectra of Mix 2 containing different concentrations of Na_2SO_4 (142 u). In both spectra, the unique Na_2SO_4 related peak $Na^+(Na_2SO_4)$ (165 u) is marked in red. The upper plot shows the spectrum of Mix 2 with the higher concentration (0.0001 M) of Na_2SO_4 (165 u), in which the amplitude of peak $Na^+(Na_2SO_4)$ (165 u) is much higher than converted detection limit (9-15σ_{lab}) (corresponding to approximate 3σ in CDA spectra. See the description

Figure 7.3 *(following page)*: The template spectra of the Mix 2 solution for LILBID settings (Upper panel: setting 1, corresponding to impact speed range of 11 - 13 km/s; middle panel: setting 2, corresponding to impact speed of 8.5 - 11 km/s; lower panel: setting 3, corresponding to impact speed range of 6 - 7.5 km/s.).

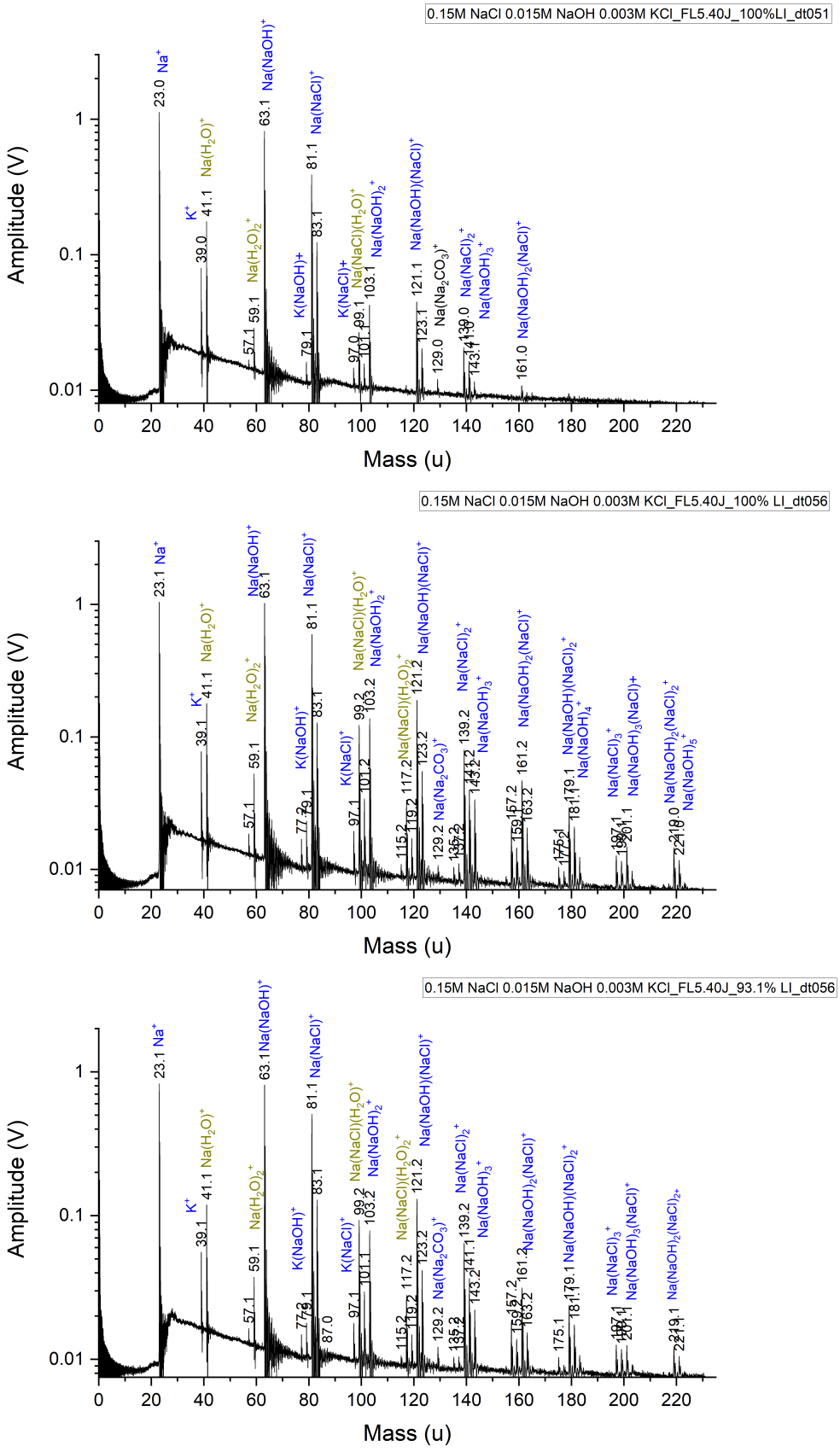
0.15M NaCl 0.015M NaOH 0.003M KCl_FL5.40J_100%LI_dt051
Amplitude (V)
Mass (u)
0.15M NaCl 0.015M NaOH 0.003M KCl_FL5.40J_100% LI_dt056
Amplitude (V)
Mass (u)
0.15M NaCl 0.015M NaOH 0.003M KCl_FL5.40J_93.1% LI_dt056
Amplitude (V)
Mass (u)

about method 1 in Section 7.2.3), here $\sigma_{lab} \approx 0.0002$ V, the baseline reduced peak amplitude ≈ 0.0133 V, and thus the amplitude of peak $Na^+(Na_2SO_4)$ (165 u) is $\sim 27 \times \sigma_{lab}$. The lower plot shows a spectrum of Mix 2 with a lower concentration (0.000002 M) of Na_2SO_4 (165 u), in which the amplitude of peak $Na^+(Na_2SO_4)$ (165 u) is between $9\sigma_{lab}$ and $15\sigma_{lab}$ (corresponding to approximate 3σ in CDA spectra), here $\sigma_{lab} \approx 0.00017$ V, the baseline reduced peak amplitude ≈ 0.00198 V, and thus the amplitude of peak $Na^+(Na_2SO_4)$ (165 u) is $\sim 12 \times \sigma_{lab}$. The concentration of Na_2SO_4 (and hence the SO_4^{2-} ion) used to produce the spectrum shown in this lower plot thus corresponds to the detection limit as defined via Method 1.

The suitable peaks used for determining detection limits

Table 7.4 lists the suitable peaks for detection limit determination. The peaks used may differ between Mix 1 and Mix 2 due to different background peaks, which may otherwise interfere with the substance peaks.

7.3.3 Approximate CDA detection limits prediction using Method 1 (Peak threshold conversion)

Table H.1 in Appendix lists the approximate CDA detection limits determined using Method 1 (Peak threshold conversion) (Section 7.2.3). The CDA detection limits vary with LILBID settings and solutions (Mix 1 and Mix 2).

Detection limits of chloride in Mix 1 and carbonate in Mix 2

Chloride is undetected in Subtypes A and B spectra, which are mimicked by Mix 1, but could possibly be present in corresponding salt-rich particles from the subsurface ocean. Similarly, carbonate is undetected in Subtypes C and D spectra, which are mimicked by Mix 2, but could possibly be present in corresponding salt-rich particles from the subsurface ocean. It is therefore important that their detection limits are determined.

1) **Chloride in Mix 1**

   The detection limit of chloride in the Mix 1 solution, above which chloride-related peaks are assumed to be visible in CDA spectra, has to be determined. The ideal method is to use the highest NaCl-related peak, $Na^+(Na^{35}Cl)$ (81 u), to judge the detectability of chloride-related peaks, i.e. if the amplitude

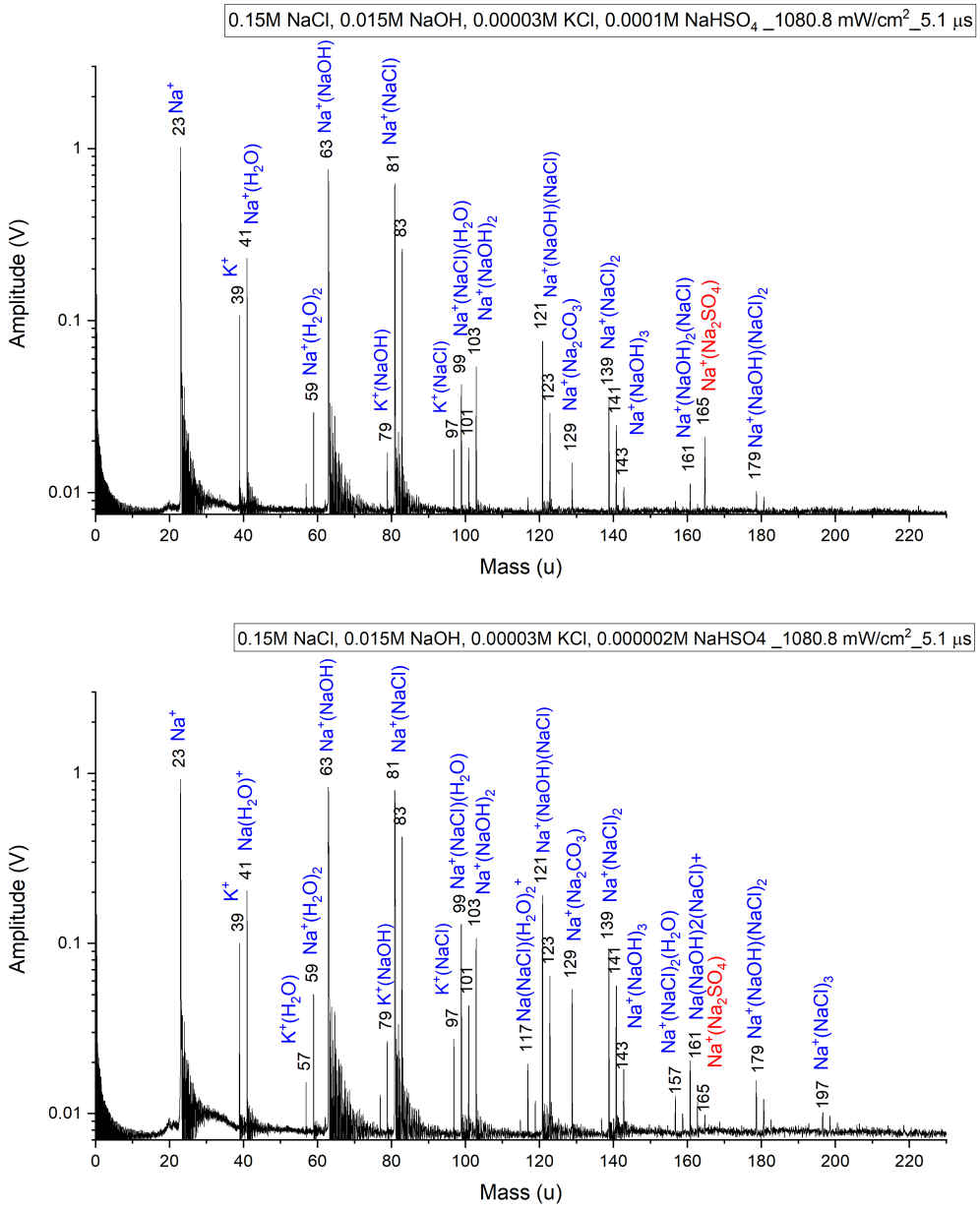

Figure 7.4: Spectra of Mix 2 solution with high (upper panel) and low (low panel) concentrations of SO_4^{2-} ions using setting 1 (Table 7.1). The mass line at 165 u, corresponding to $Na^+(Na_2SO_4)$, varies with the concentration of SO_4^{2-} ions in the solution. The lower figure shows the spectrum of Mix 2 with a lower concentration of Na_2SO_4, in which the amplitude of the mass line at 165 u is between $9\sigma_{lab}$ and $15\sigma_{lab}$ (corresponding to $\sim 3\sigma$ in CDA spectra), and thus represents the detection limit as evaluated via Method 1.

Compounds	**Peaks**	
	Mix 1	**Mix 2**
Anions		
Chloride (Cl^-)	$Na^+(Na^{37}Cl)$ (83 u)	N.A.
Carbonate (CO_3^{2-} and HCO_3^-)	N.A.	$Na^+(Na_2CO_3)$ (129 u)
Sulfate (SO_4^{2-})	$Na^+(Na_2SO_4)$ (165 u)	
Phosphate (PO_4^{3-} and HPO_4^{2-})	$Na^+(Na_3PO_4)$ (187 u) and $Na^+(Na_2HPO_4)$ (165 u)	
Phosphite (PO_3^{3-} and HPO_3^{2-})	$Na^+(Na_2HPO_3)$ (149 u)	
Nitrate (NO_3^-)	$Na^+(NaNO_3)$ (108 u)	
Fluoride (F^-)	$Na^+(NaF)$ (65 u) (all peaks close to gigantic background peaks)	
Bromide (Br^-)	$Na^+(NaBr)$ (125 u and 127 u)	
Sulfide (S^{2-})	$Na^+(Na_2S)$ (101 u)	$Na^+(NaSOSNa)$ (149 u)
Cations		
Lithium (Li^+)	$Na^+(LiOH)$ (47 u)	
Ammonium (NH_4^+)	NH_4^+ (18 u)	
Calcium (Ca^{2+})	——	$(CaOH)^+$ (57 u) or $(CaOH)^+(NaOH)$ (97 u)
Ferrous (Fe^{2+})	——	——
Magnesium (Mg^{2+})	——	$Na(^{26}MgO)_2$ (105 u)
Mineral		
Silica (SiO_2)	$Na^+(Na_2SiO_3)$ (145 u) or $Na^+(SiO_2)(NaOH)_2$ (163 u)	
Organic compounds		
Formic Acid (HCOOH)	$Na^+(NaCOOH)$ (91 u)	
Formaldehyde (HCHO)	$Na^+(HCHO)$ (53 u)	

Table 7.4: Peaks chosen for determining the detection limits of the compounds of interest. Chloride is a major compound instead of a compound of interest for Mix 1 and carbonate is a major compound instead of a compound of interest for Mix 2, so these two detection limits are not applicable (N.A.). The peaks for some compounds of interest and solutions are not given in the cases in which even if the compounds is saturated in the solutions, no related peaks are detected.

of this peak is between $9\sigma_{lab}$ and $15\sigma_{lab}$ in laboratory spectra, corresponding to 3σ in Type-3 CDA spectra, the corresponding concentration of chloride is considered as the CDA detection limit. However, this is difficult because the $Na^+(Na^{35}Cl)$ (81 u) peak, containing the most abundant chlorine isotope, ^{35}Cl, and the $Na^+(NaOH)(H_2O)$ (81 u) peak, which is significant in laboratory, but not detected in Type-3 CDA spectra (Section 4.5.1), have the same integer mass, so peaks related to these two ions can't be distinguished in laboratory spectra. Since the abundance of ^{35}Cl is approximately 32% of the abundance of ^{37}Cl, the abundance of the similar Na cluster containing the 37 u isotope of chlorine is approximately 32% of the abundance of that containing the 35 u isotope. Therefore, the peak $Na^+(Na^{37}Cl)$ (83 u) is also significant enough to be used to judge the detectability of chloride-related peaks. To make amplitude of peak at 81 u, which is caused exclusively by $Na^+(Na^{35}Cl)$ in Type-3 CDA spectra (Section 4.5.1), equal to 3σ in CDA spectra, the amplitude of peak $Na^+(Na^{37}Cl)$ (83 u) is supported to be 1σ in CDA spectra. Accordingly, the amplitude of peak 83 u is supported to be between 3σ and 5σ in laboratory spectra and the corresponding concentration of chloride is considered as the detection limit. The resulting NaCl concentration evaluated via Method 1 is 10($\pm$3) **mM** (Table H.1). Below this value, although the peak at 81 u (contributed to by both $Na^+(Na^{35}Cl)$ and $Na^+(NaOH)(H_2O)$) is still significant, the contribution of $Na^+(NaCl)$ (81 u) is considered insignificant and thus chloride-related peaks are assumed to be undetectable in the corresponding 'salt rich' CDA spectra.

2) **Carbonate in Mix 2**

The upper limit of carbonate in the Mix 2 solution, above which carbonate-related peaks are assumed to be visible in the corresponding 'salt rich' CDA spectra, was determined. Unfortunately, the upper limit measurement is complicated, because CO_2 from air can react with the NaOH in the solution to quickly produce carbonate. The CO_2 from air can produce detectable carbonate related peaks ($Na^+(Na_2CO_3)$ (129 u) and its water clusters) in spectra, because the LILBID technique is very sensitive to carbonate (Table 6.1). In order to understand the influence of the CO_2 from air, fresh Mix 2 solutions, free of added carbonate, and several Mix 2 solutions with varying concentrations of added sodium carbonate were prepared. Spectra from consecutive mixes were acquired as quickly as possible and the peak amplitudes at 129 u between the different solutions then compared. When the $Na^+(Na_2CO_3)$ (129 u) peak from a solution with added sodium carbonate was approximately 9 – $15\sigma_{lab}$ higher than that from the Mix 2 solution without additional carbonate in laboratory

spectra (equivalent to $\sim 3\sigma$ in CDA spectra), the concentration was considered to be the detection limit of carbonate for the Mix 2 solution. The resulting concentration evaluated via Method 1 is approximately **0.05 mM** (Table H.1).

Special cases

1. All relevant peaks are very close to significant background/template salt peaks:

   For fluoride, all of the related peaks are close to significant salt background peaks in CDA spectra. Thus, the '3σ' criterion is too low, and much higher peak amplitudes are required to determine the detection limits. The detection limits are evaluated using the ratio of the amplitude of the peak maximum of the background salt peak and the amplitude of the peak flank at the mass of the sought peak in CDA spectra. If the ratio of the peak amplitudes of the compound of the interest and the nearby background salt in laboratory spectra is higher than the maximum-to-flank ratio measured in CDA spectra, the substance peak is likely to be detectable in CDA spectra. Fig. 7.5a shows fluoride as an example: there are three fluoride-related peaks visible in this spectrum: 1) $Na^+(NaF)$ (65 u), which is only 2 u after a large background peak at 63 u; 2) $Na^+(NaF)(NaOH)$ (105 u), which is also only 2 u after a higher background peak due to $Na^+(NaOH)_2$ (103 u); and 3) $Na^+(NaF)_2$ at 107 u, lower than peak 105 u and only 2 u after the earlier fluorine-containing peak, $Na^+(NaF)(NaOH)$ (105 u). The peaks at 65 u and 105 u could therefore be hidden in the right flanks of background salt peaks, and peak 105 u could also be unresolvable from the peak at 103 u in CDA spectra. Fig. 7.5a shows an example high chloride concentration subtype C spectrum. The ratio of the spectrum amplitude at mass at 65 u to that at 63 u is ≈ 0.2 and the ratio at mass at 105 u to that at mass 103 u is ≈ 0.3. Therefore, if peak amplitude ratios for mass 65 u to 63 u or mass 105 u to 103 u are greater than 0.2 or 0.3 respectively in a fluoride-containing Mix 2 spectrum, the fluoride is considered to be at a concentration detectable in CDA spectra.

2. All relevant peaks are overlapped by background salt peaks:

   Some potential magnesium-related peaks, such as $(MgOH)^+$ (41 u), $(Mg^{35}Cl)^+$ (59 u), $Na^+(MgO)$ (63 u), $Na^+Mg(OH)_2$ (81 u), $Na^+Mg(OH^{37}Cl)$ (99 u) and $Na^+(MgCl)_2$ (117 u and 119 u), have the same (integer) masses as background/template salt peaks. Other potential peaks, however, have different masses to the background peaks (e.g. $(Mg^{37}Cl)^+$ (61 u), $Na^+(MgO)_2$ (105 u) and $Na^+(MgCO_3)$ (119 u)), or mass-to-charge ratios which produce

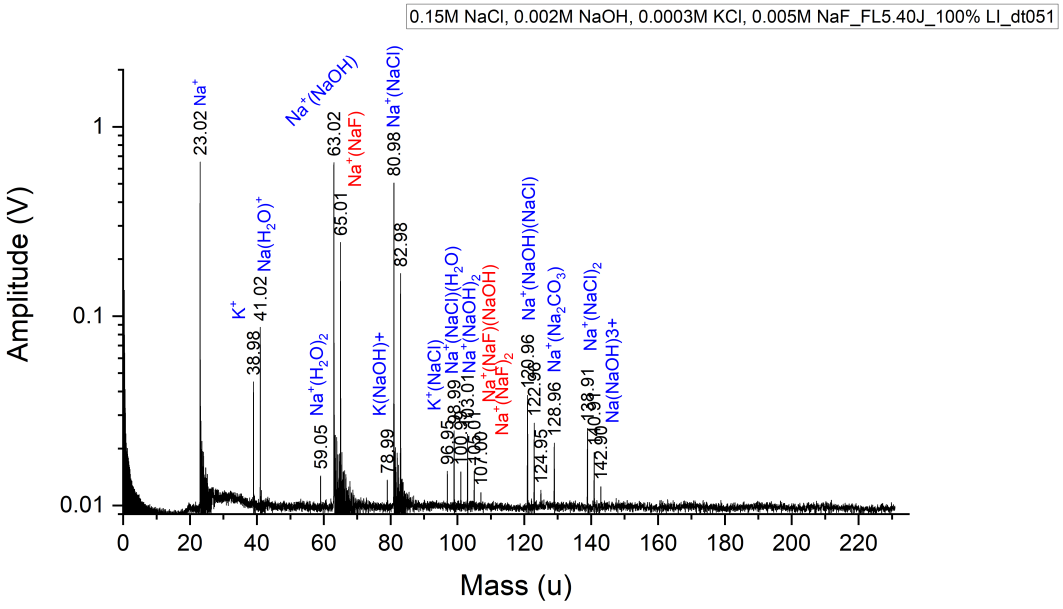

(a)

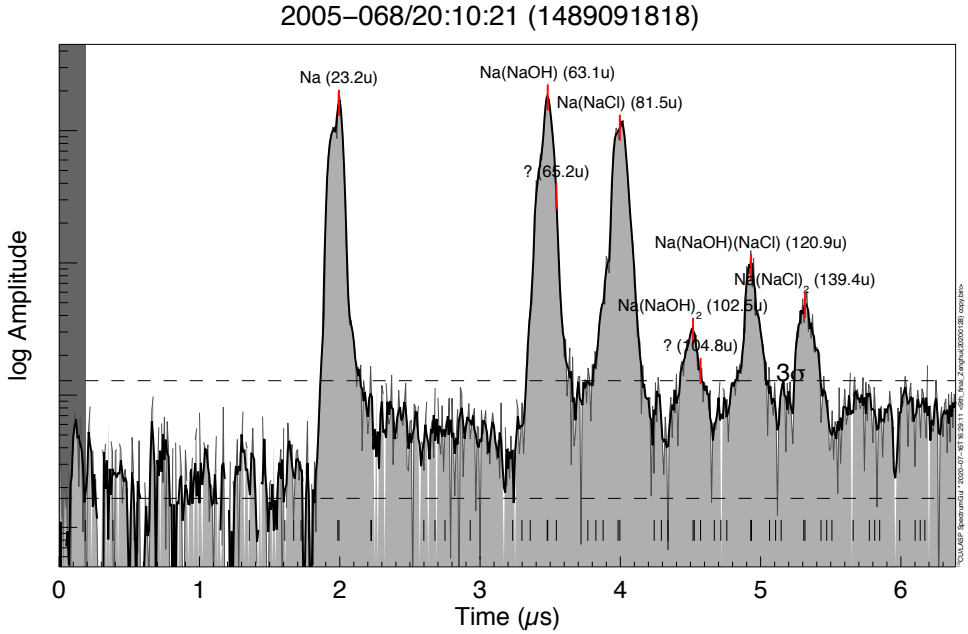

(b)

Figure 7.5: **(a):** A spectrum of 0.005 M fluoride in Mix 2 at setting 1. There are three fluoride related peaks visible in this spectrum: $Na^+(NaF)$ (65 u), $Na^+(NaF)(NaOH)$ (105 u) and $Na^+(NaF)_2$ (107 u). **(b):** A high chloride concentration Type-3 Subtype C CDA spectrum. Stretch parameter a = 475 ns. Shift parameter b = -0.287 μs. The red lines with question marks indicate the measurement points for amplitudes at masses of 65 u and 105 u.

peaks at earlier times (lower masses) in the spectra, such as Mg^{2+} (mass-to-charge ratio 12), but these potential peaks were never detected in the LILBID spectra of Mix 1 and Mix 2.

(1) For Mix 1

Fig G.2 in Appendix shows a spectrum of pure Mix 1 solution at setting 1 (upper spectrum) and a spectrum of a saturated (4.5 mM) solution of $MgCl_2$ in Mix 1 at setting 1 (lower spectrum). Both solutions were used shortly after preparation. Pure Mix 1 was measured first and then the saturated (4.5 mM) solution of $MgCl_2$ in Mix 1 was measured immediately afterwards. Comparing these spectra, it can be seen that the peaks whose masses are shared by both the background salt peaks and certain magnesium related peaks, in these two spectra, show no clear difference in their amplitudes, i.e. no significant extra amplitudes were observed in saturated solution of $MgCl_2$ in Mix 1 and the peak amplitude ratio of mass line at 83 u to mass line at 81 u also does not change. Other peaks, which should not overlap, as they have different (apparent, in the case of doubly-charged ions) masses than the background peaks are not detected. This holds true for all three settings. Therefore, no magnesium-related peaks are detected in the saturated solution of $MgCl_2$ in Mix 1.

(2) For Mix 2

The above situation is also true for the saturated (2.2 mM) solution of $MgCl_2$ in Mix 2 at setting 1. However, at settings 2 and 3 a small (9-15 σ_{lab} in laboratory spectra) $Na^+(MgO)_2$ peak at 105 u is visible in the saturated solution. Therefore, this concentration (2.2 mM) of the saturated solution in Mix 2 roughly corresponds to the CDA detection limit of magnesium ions in chloride-rich particles.

3. No relevant peak detected even if saturated solution:

For ferrous iron (Fe^{2+}) in Mixes 1 and 2, and calcium in Mix 1, no related peaks are detected even if they are saturated in the solutions, despite the fact that their diagnostic peaks do not have the same masses as the background peaks. Thus, their detection limits could not be evaluated with the methods described in this thesis, and their solubilities are instead used as upper limits.

7.3.4 Approximate CDA detection limits prediction using Method 2 (correlation between concentration and peak amplitude ratios)

In this subsection, the relationships between peak ratios and substance concentration over suitably low ranges are described. Subsequently, an example of detection limit prediction, via Total Least Squares (TLS) linear fitting of peak ratio changes as a function of concentration, is demonstrated and results for the remaining compounds are given.

Linear relationships between peak ratios and the concentrations of the dissolved substances

Laboratory spectra recorded in this work show that the ratio of the detection limit diagnostic peak amplitude to that of a reference peak (at 23 u or 63 u) varies linearly with the substance concentration in the mixture (e.g. Fig. 7.6), while this only remains below a particular concentration. Above a certain concentration, the linearity no longer holds. This phenomenon is assumed to be related to saturation of the measured substance in the mixture solution, the change in pH of the solution and/or the increase in the concentration of Na^+ contributed by the measured substance (Wiederschein et al. 2015). However, the concentration at which the trend departs from linearity is much higher than any possible detection limit, and thus the linear section of the ratio versus concentration plots can be used for fitting and prediction. Besides, if the amplitude of a peak is approaching to 10 σ_{lab} or lower, the peak amplitude is comparable with its uncertainty. In this case, using the two or more peaks with low amplitude for linear fitting could increase the uncertainty of the fitted parameters (slop and intercept), especially the slope, and even negative slope could be produced in rare cases. Figs 7.6 and 7.7 show an example linear relation for Na_2S in a Mix 2 solution with peaks at 23 u and 63 u used as the reference peaks, respectively.

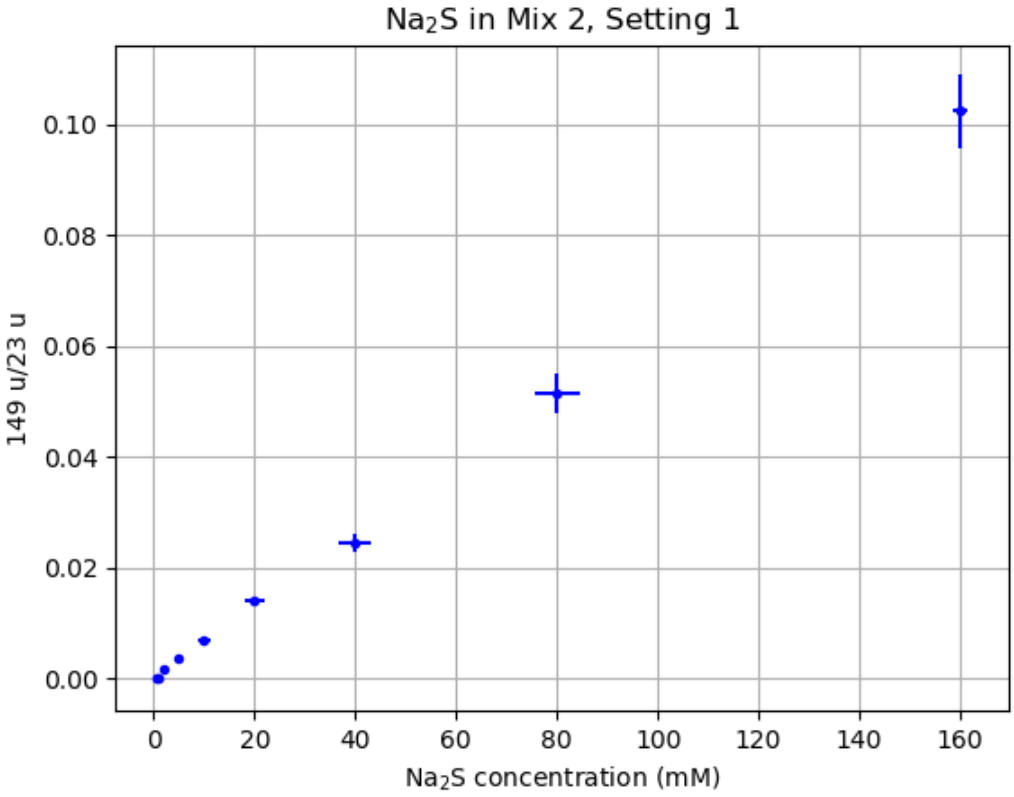

Figure 7.6: The linear relation between the peak amplitude ratio of 149 u to 23 u (Na^+) and the concentration of Na_2S. The peak at 149 u corresponds to Na^+(NaSOSNa), and is the most significant peak related to Na_2S in the spectrum of Na_2S dissolved in the Mix 2 solution.

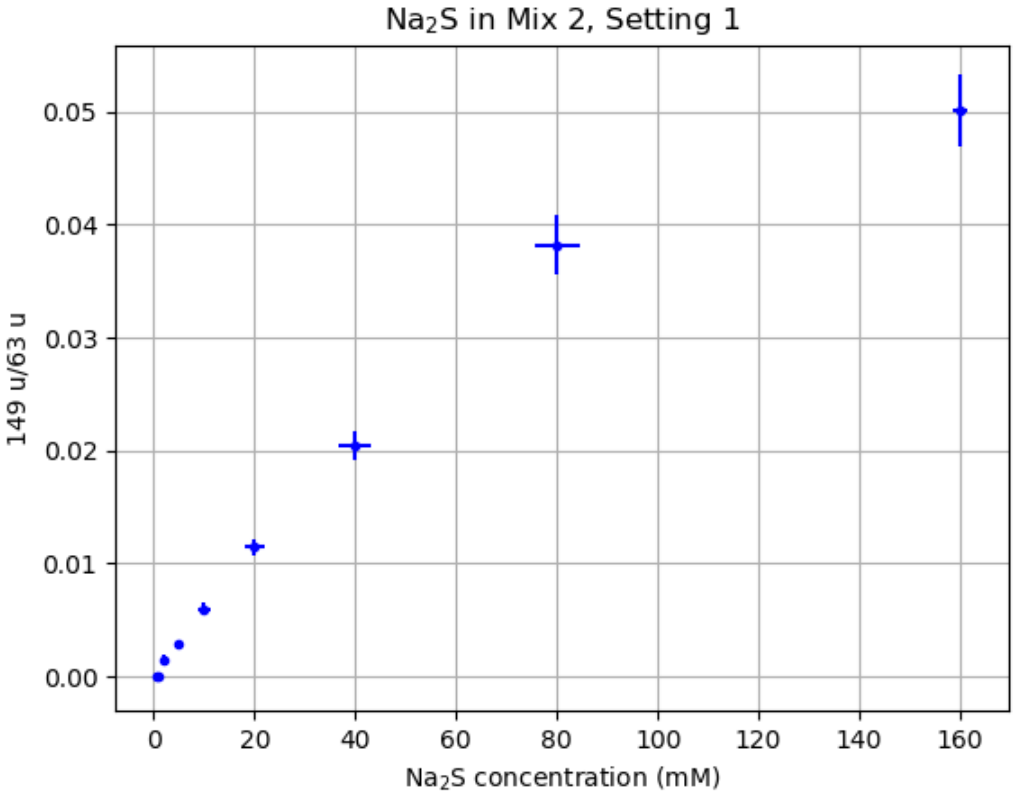

Figure 7.7: The linear relation between the peak amplitude ratio of 149 u to 63 u (Na^+(NaOH)) and the concentration of Na_2S. The peak at 149 u corresponds to Na^+(NaSOSNa), and is the most significant peak related to Na_2S in the spectrum of Na_2S dissolved in the Mix 2 solution. Below a concentration of 0.08 M Na_2S, the trend is linear, while at higher concentrations the trend departs from linearity.

Extrapolating a calibration curve to detection limits using TLS linear fitting

In order to predict the concentration of a substance corresponding to a certain peak ratio, the peak ratios are used as independent variables, represented by horizontal axis (x aixs), and the concentration are used as dependent variable, represented by vertical axis (y axis). The fitted linear function should be as following:

$$y = mx + b \quad (m > 0,\ b > 0) \tag{7.5}$$

Here, m is the slope and b is the intercept. m is positive, because the

concentration of a substance is positively correlated with its peak amplitudes, and thus peak amplitude ratios. b is positive because when the concentration is lower than a certain value (a small positive number), the resulting peaks are not detectable (buried in the noise). Negative intercept make no sense physically, because when there is no a certain substance dissolved in the solution, no its resulting peak is produced.

Then, the fitted linear function are used as calibration curves to predict the detection limits through extrapolation. To demonstrate the calibration process of extrapolating detection limits from laboratory data, using the change in peak amplitude ratios with concentration, the predictions for NO_3^- using the Na^+ (23 u) and Na^+(NaOH) (63 u) peaks for references, are presented below.

1. **CDA detection limit prediction for NO_3^- using the Na^+ (23u) peak as the reference.**

   Fig. 7.8 shows the results of the CDA detection limit prediction for NO_3^-, using the Na^+ (23 u) peak as the reference. The linear TLS fitting uses the average values of the data from the three LILBID 'speed' settings. The predicted detection limit is 0.18 mM; the maximum and minimum values at a 99.7% (3σ) confidence level are 0.32 mM and 0.04 mM, respectively.

2. **CDA detection limit prediction for NO_3^- using peak Na^+(NaOH) (63 u) as the reference peak.**

   Fig. 7.9 shows the results of the CDA detection limit prediction for NO_3^-, using the Na^+(NaOH) (63 u) peak as the reference. The linear regression uses the average values of the data from the three LILBID 'speed' settings. The predicted detection limit is 0.31 mM; the maximum and minimum values at a 99.7% (3σ) confidence level are 0.53 mM and 0.11 mM, respectively.

The likelihood contours on the right panels enclose the parameter spaces of the slope and the intercept of the fitted linear functions with the likelihoods of 99.7%. This TLS linear fitting model only shows the reliability of the fit - or the calculated slope and intercept based on the uncertainties in the original data, without considering the physical reality. The values enclosed by the contours which are valid for intercepts below zero are physically unrealistic. The figures of detection limits predictions using Method 2 for all of the compounds of interest are shown in Appendix I.

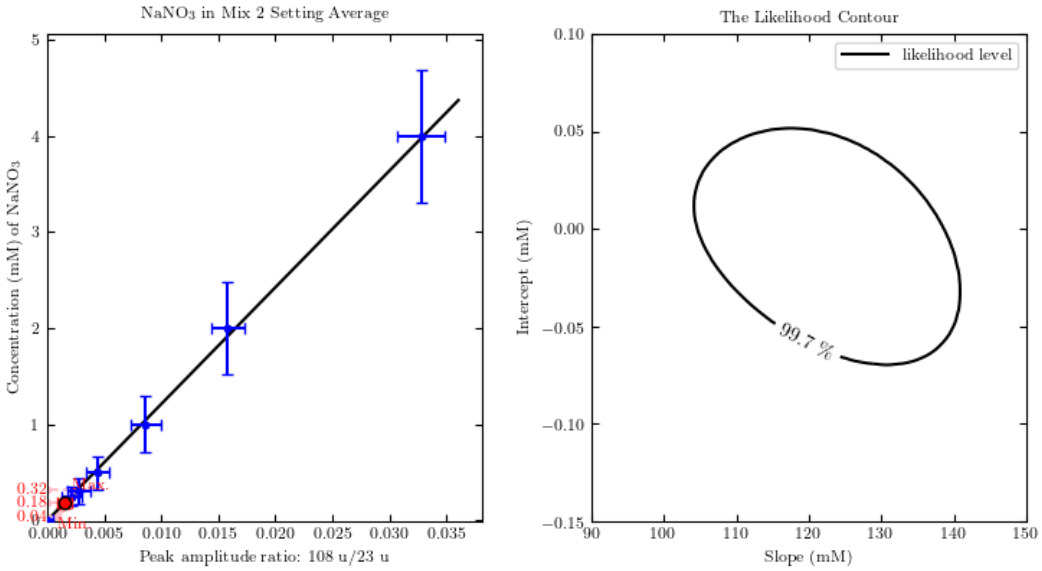

Figure 7.8: The detection limit prediction for NO_3^- in Mix 2, using peak Na^+ (23 u) as the reference peak. The left panel shows the linear TLS fit and the predicted detection limit (red text). The blue crosses indicate the measured data (peak amplitude ratios and concentrations) with error bars ; the black solid line indicates the best fit and the red dot indicates the predicted detection limit (0.18 mM). The maximum value (0.32 mM) and the minimum value (0.04 mM) of the detection limit within the 99.7% confidence range are also given. The method used to calculate the maximum values and the minimum values of the detection limits is described in Appendix I. The right panel shows the 99.7% likelihood contour of the fit parameters (slope and intercept), with which the error range of the detection limit in the left panel is calculated.

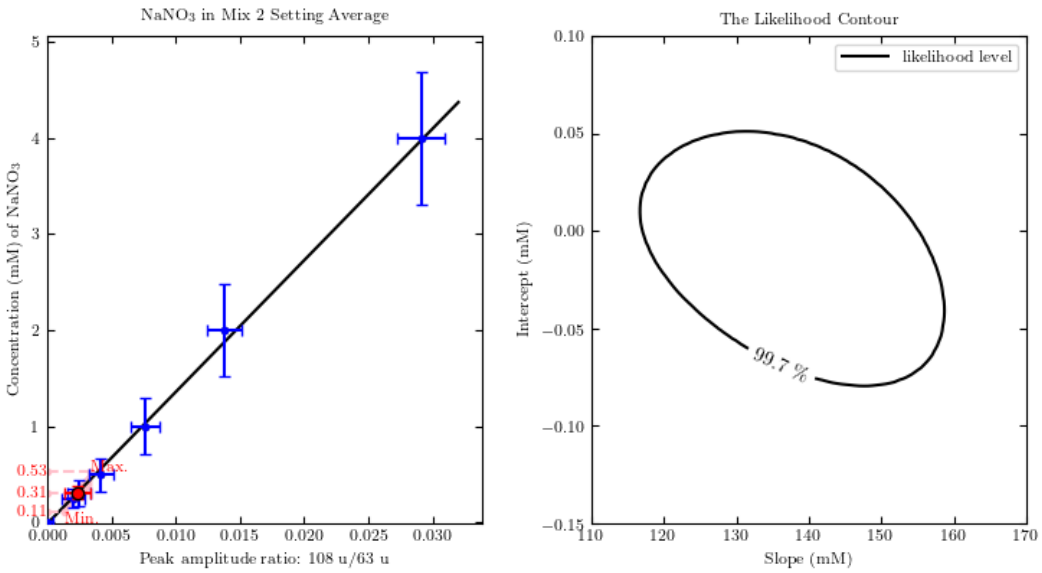

Figure 7.9: The detection limits prediction for NO_3^- in Mix 2 using peak Na^+(NaOH) (63 u) as the reference peak. The left panel shows the liner TLS fit and the predicted detection limit. The blue crosses indicate the measured data (peak amplitude ratios and concentrations) with error bars; the black solid line indicates the fitted line; and the red dot indicates the predicted detection limit (0.31 mM). The maximum value (0.53 mM) and the minimum value (0.11 mM) of the detection limit with 99.7% confidence range are also given. The method used to calculate the maximum values and the minimum values of the detection limits is described in Appendix I. The right panel shows the 99.7% likelihood contour of the fit parameters (slope and intercept), with which the error range of the detection limit in the left panel is calculated.

Detection limits determined using linear regression based on TLS fitting

The detection limits with their associated 3σ confidence levels, as evaluated with Method 2 (Section 7.2.3), are listed in Table 7.5. The unit is millimolar (mM). If too little reliable data was available for a linear fit, the chosen method does not apply (as no applicable physical model for non-linear variations of peak amplitudes with concentrations exists) and thus the table shows N.A. (Not Applicable).

Comparison of detection limits determined using the different methods

The detection limits and their 3σ (99.7%) confidence levels, determined using the two different methods defined in Section 7.2.3 are listed in Table 7.6. The unit is millimolar (mM). The values in brackets are the solubilities of the chemical in water at room temperature. If no relevant peak is detected even in a saturated solution, the solubility limits are used. If too little reliable data was available for the linear fit (as previously mentioned), Method 2 is not applicable and the detection limit is given as N.A. Values provided by Method 1 are the average resulting from the three LILBID power/delay time settings, and their uncertainties, deriving from solution preparation, were evaluated via the error propagation formulae (Eqs 7.1 and 7.2).

Taking nitrate (NO_3^-) in Mix 2 as an example, Fig. 7.10 compares the derived detection limits and their associated errors, as obtained with Method 1 (the first bar), Method 2 using Na^+(NaOH) (63 u) as the reference peak (the second bar) and Method 2 using Na^+ (23 u) as reference peak (the third bar). **Note:** The detection limit of phosphate in Mix 1 obtained from Method 1 is found using the $Na^+(Na_2HPO_4)$ (165 u) peak, whereas the detection limits in Mix 1 obtained from Method 2 uses the $Na^+(Na_3PO_4)$ (187 u) peak, which is higher than that of $Na^+(Na_2HPO_4)$ in the same spectra. This is why the detection limit of phosphate in Mix 1 obtained from Method 1 is much higher than that obtained from Method 2. The bar charts for the comparison of detection limits determined using the different methods for all the compounds of interest are shown in Appendix J.

Substance	Mix	Detection Limit (mM)	
		Method 2	
		Ref. to 23 u	Ref. to 63 u
Anions			
Sulfate (SO_4^{2-})	Mix 1	$9.5^{+12.0}_{-6.7} \times 10^{-3}$	$3.6^{+13.2}_{-1.0} \times 10^{-2}$
	Mix 2	$1.6^{+1.6}_{-0.8} \times 10^{-3}$	$3.2^{+6.8}_{-2.1} \times 10^{-3}$
Phosphate (PO_4^{3-} & HPO_4^{2-})	Mix 1	$5.6^{+31.9}_{-5.6} \times 10^{-3}$	$1.9^{+3.1}_{-1.9} \times 10^{-2}$
	Mix 2	$3.8^{+8.6}_{-1.2} \times 10^{-3}$	$6.0^{+8.1}_{-4.1} \times 10^{-3}$
Phosphite (PO_3^{3-} & HPO_3^{2-})	Mix 1	$1.5^{+2.9}_{-1.5} \times 10^{-2}$	$5.9^{+5.7}_{-5.9} \times 10^{-2}$
	Mix 2	$2.9^{+3.5}_{-2.9} \times 10^{-3}$	$6.1^{+7.4}_{-6.1} \times 10^{-3}$
Nitrate (NO_3^-)	Mix 1	$1.3^{+1.4}_{-1.3}$	$3.5^{+2.5}_{-2.2}$
	Mix 2	$0.18^{+0.14}_{-0.14}$	$0.31^{+0.22}_{-0.20}$
Fluoride (F^-)	Mix 1	$3.4^{+32.2}_{-3.4}$	21^{+93}_{-21}
	Mix 2	$1.0^{+0.3}_{-0.3}$	$2.5^{+0.7}_{-0.6}$
Bromide (Br^-)	Mix 1	$4.6^{+3.2}_{-3.9}$	18^{+13}_{-8}
	Mix 2	$1.6^{+2.9}_{-1.6}$	$2.9^{+3.6}_{-2.9}$
Sulfide (S^{2-})	Mix 1	N.A.	N.A.
	Mix 2	$1.4^{+0.6}_{-0.6}$	$3.7^{+1.1}_{-1.0}$
Cations			
Lithium (Li^+)	Mix 1	$0.77^{+0.38}_{-0.42}$	$1.9^{+0.6}_{-0.5}$
	Mix 2	$0.48^{+0.60}_{-0.42}$	$1.0^{+1.0}_{-0.6}$
Ammonium (NH_4^+)	Mix 1	56^{+13}_{-14}	71^{+13}_{-13}
	Mix 2	14^{+7}_{-7}	15^{+5}_{-5}
Calcium (Ca^{2+})	Mix 1	N.A.	N.A.
	Mix 2	N.A.	N.A.
Ferrous (Fe^{2+})	Mix 1	N.A.	N.A.
	Mix 2	N.A.	N.A.
Magnesium (Mg^{2+})	Mix 1	N.A.	N.A.
	Mix 2	N.A.	N.A.
Mineral			
Silica (SiO_2)	Mix 1	$0.19^{+0.28}_{-0.19}$	$0.56^{+0.91}_{-0.51}$
	Mix 2	$0.55^{+0.32}_{-0.33}$	$1.1^{+0.5}_{-0.4}$
Organic compounds			
Formic Acid (HCOOH)	Mix 1	$4.6^{+3.0}_{-2.9}$	23^{+8}_{-7}
	Mix 2	$0.45^{+2.46}_{-0.45}$	$1.8^{+2.3}_{-1.8}$
Formaldehyde (HCHO)	Mix 1	$1.6^{+2.2}_{-1.6} \times 10^2$	$9.2^{+4.5}_{-2.6} \times 10^2$
	Mix 2	$1.9^{+1.2}_{-1.4} \times 10^2$	$5.2^{+3.0}_{-3.7} \times 10^2$

Table 7.5: CDA detection limits evaluated via Method 2 using two different reference peaks.

Substance	**Mix**	**Detection Limit (mM)**		
		Method 1 (Average)	**Method 2**	
			Ref. to 23 u	**Ref. to 63 u**
Anions				
Carbonate (CO_3^{2-} & HCO_3^-)	Mix 2	$4.0^{+7.5}_{-4.0} \times 10^{-2}$	N.A	N.A
Chloride (Cl^-)	Mix 1	$4.0^{+7.5}_{-4.0} \times 10^{-2}$	N.A	N.A
Sulfate (SO_4^{2-})	Mix 1	$5.0^{+3.3}_{-3.3} \times 10^{-2}$	$1.2^{+1.4}_{-1.1} \times 10^{-2}$	$3.3^{+9.7}_{-2.4} \times 10^{-2}$
	Mix 2	$2.0^{+0.5}_{-0.5} \times 10^{-3}$	$1.6^{+1.6}_{-0.8} \times 10^{-3}$	$3.2^{+6.8}_{-2.1} \times 10^{-3}$
Phosphate (PO_4^{3-} & HPO_4^{2-})	Mix 1	$0.10(\pm 0.06)$	$5.6^{+31.9}_{-5.6} \times 10^{-3}$	$1.9^{+3.1}_{-1.9} \times 10^{-2}$
	Mix 2	$3.0^{+1.5}_{-1.5} \times 10^{-3}$	$3.8^{+8.6}_{-1.2} \times 10^{-3}$	$6.0^{+8.1}_{-4.1} \times 10^{-3}$
Phosphite (PO_3^{3-} & HPO_3^{2-})	Mix 1	$6.6^{+2.4}_{-2.4} \times 10^{-2}$	$1.5^{+2.9}_{-1.5} \times 10^{-2}$	$5.9^{+5.7}_{-5.9} \times 10^{-2}$
	Mix 2	$4.7^{+3.0}_{-3.0} \times 10^{-3}$	$2.9^{+3.5}_{-2.9} \times 10^{-3}$	$6.1^{+7.4}_{-6.1} \times 10^{-3}$
Nitrate (NO_3^-)	Mix 1	$1.5^{+0.74}_{-0.74}$	$1.3^{+1.4}_{-1.3}$	$3.5^{+2.5}_{-2.2}$
	Mix 2	$0.30^{+0.14}_{-0.14}$	$0.18^{+0.14}_{-0.14}$	$0.31^{+0.22}_{-0.20}$
Fluoride (F^-)	Mix 1	20^{+3}_{-3}	$3.4^{+32.2}_{-3.4}$	21^{+93}_{-21}
	Mix 2	$3.0^{+0.4}_{-0.4}$	$1.0^{+0.3}_{-0.3}$	$2.5^{+0.7}_{-0.6}$
Bromide (Br^-)	Mix 1	10^{+4}_{-4}	$4.6^{+3.2}_{-3.9}$	18^{+13}_{-8}
	Mix 2	$2.5^{+1.4}_{-1.4}$	$1.6^{+2.9}_{-1.6}$	$2.9^{+3.6}_{-2.9}$
Sulfide (S^{2-})	Mix 1	N.A.	N.A.	N.A.
	Mix 2	$2.0^{+1.0}_{-1.0}$	$1.4^{+0.6}_{-0.6}$	$3.7^{+1.1}_{-1.0}$
Cations				
Lithium (Li^+)	Mix 1	$1.0^{+0.5}_{-0.5}$	$0.77^{+0.38}_{-0.42}$	$1.9^{+0.6}_{-0.5}$
	Mix 2	$0.50^{+0.24}_{-0.24}$	$0.48^{+0.60}_{-0.42}$	$1.0^{+1.0}_{-0.6}$
Ammonium (NH_4^+)	Mix 1	70^{+17}_{-17}	56^{+13}_{-14}	71^{+13}_{-13}
	Mix 2	18^{+6}_{-6}	14^{+7}_{-7}	15^{+5}_{-5}
Calcium (Ca^{2+})	Mix 1	(8.0×10^{-1})	N.A.	N.A.
	Mix 2	4.5×10^{-1}	N.A.	N.A.
Ferrous (Fe^{2+})	Mix 1	$(2.0^{+1.0}_{-1.0} \times 10^{-1})$	N.A.	N.A.
	Mix 2	$(3.2^{+1.5}_{-1.5} \times 10^{-1})$	N.A.	N.A.
Magnesium (Mg^{2+})	Mix 1	$(4.5^{+2.0}_{-2.0})$	N.A.	N.A.
	Mix 2	$2.2^{+1.0}_{-1.0}$	N.A.	N.A.
Mineral				
Silica (SiO_2)	Mix 1	$0.34^{+0.12}_{-0.12}$	$0.19^{+0.28}_{-0.19}$	$0.56^{+0.91}_{-0.51}$
	Mix 2	$0.39^{+0.14}_{-0.14}$	$0.55^{+0.32}_{-0.33}$	$1.1^{+0.5}_{-0.4}$
Organic compounds				
Formic Acid (HCOOH)	Mix 1	10^{+4}_{-4}	$4.6^{+3.0}_{-2.9}$	23^{+8}_{-7}
	Mix 2	$4.5^{+1.9}_{-1.9}$	$0.45^{+2.46}_{-0.45}$	$1.8^{+2.3}_{-1.8}$
Formaldehyde (HCHO)	Mix 1	$7.5^{+0.8}_{-0.8} \times 10^2$	$1.6^{+2.2}_{-1.6} \times 10^2$	$9.2^{+4.5}_{-2.6} \times 10^2$
	Mix 2	$5.0^{+0.9}_{-0.9} \times 10^2$	$1.9^{+1.2}_{-1.4} \times 10^2$	$5.2^{+3.0}_{-3.7} \times 10^2$

Table 7.6: CDA detection limits derived using the Method 1 and Method 2 (with two different reference peaks, respectively), as described in the main text.

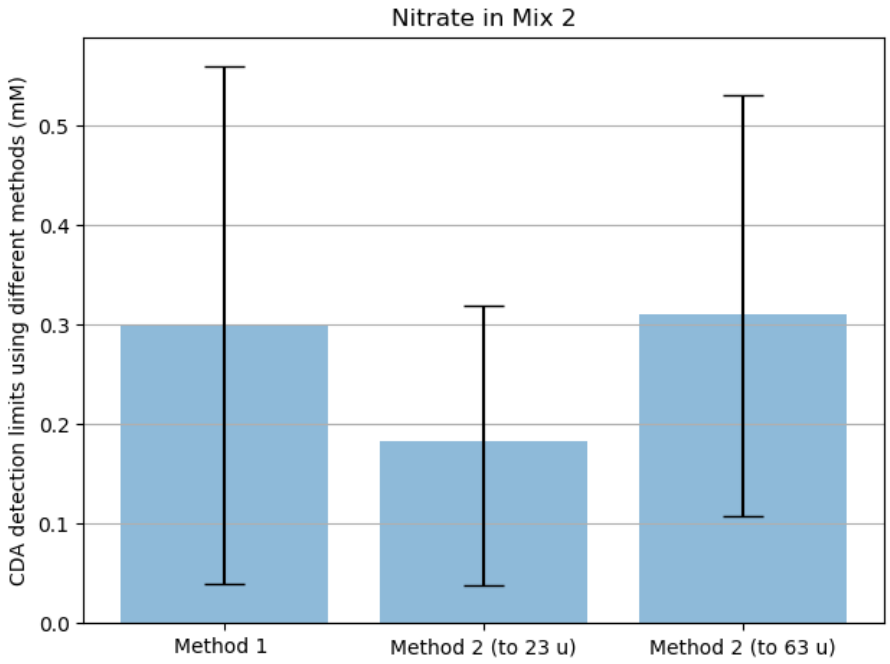

Figure 7.10: Nitrate detection limits in Mix 2 obtained with Method 1 (the first bar), Method 2 using Na^+(NaOH) (63 u) as the reference peak (the second bar) and Method 2 using Na^+ (23 u) as the reference peak (the third bar).

7.4 Discussion

7.4.1 Reaction between compounds of interest and the two analogue solutions

Some compounds of interest react with the compounds in the two analogue solutions (Mix 1 and Mix 2). As a result, the pH of the solutions is changed or/and some potentially insoluble compounds are produced. Both Mix 1 and Mix 2 are alkaline so added 'acidic' compounds, such as ammonium ions, or formic acid, react with the OH^- in the solutions, decreasing the pH of the solution. Some compounds of interest, such as magnesium and ferrous iron, react with OH^- to produce slightly soluble or insoluble hydroxides. There are often also significant concentrations of CO_3^{2-} ions (e.g. Mix 1), which some compounds of interest, such as calcium and ferrous iron, may react with CO_3^{2-} to produce slightly soluble or insoluble carbonate. Typically pH altering or precipitative effects may occur with e.g. ions of phosphite, ammonium, calcium, magnesium and ferrous iron, as well as formic acid. The

reactions for compounds of interest are shown in Appendix G.3.

7.4.2 Differences between CDA spectra and the laboratory analogue spectra

Although the similarities in appearance between the CDA spectra and laboratory spectra are high enough that the laboratory analogue spectra can be used to mimic the CDA spectra, there are still some differences.

1. A small peak at 46 u, identified as Na_2^+, which is periodically visible in CDA spectra, is never detected in the laboratory analogue spectra.
2. The relative amplitude of the Na_2O^+ (85 u) peak in laboratory analogue spectra of carbonate-rich solutions, which are designed to mimic subtype A CDA spectra, are smaller in the laboratory than those in the flight spectra.
3. There are more (higher order of) Na/K-water cluster peaks , such as $Na^+(H_2O)_n$, $K^+(H_2O)_n$ (n = 1, 2 $\cdots$), and salt-water cluster peaks, such as $Na^+(NaCl)(H_2O)_n$ (n = 1, 2 $\cdots$), present in laboratory spectra and their relative amplitudes are higher in laboratory analogue spectra than in CDA spectra.
4. There are more (higher order of) NaOH cluster peaks, such as $Na^+(NaOH)_n$ and $Na^+(Na_2CO_3)(NaOH)$ (n = 1, 2 $\cdots$), present in laboratory spectra and their relative amplitudes are higher in laboratory analogue spectra than in CDA spectra.

The above features may potentially be explained by the fact the laboratory spectra are derived from a more extended liquid water source, whereas the CDA flight spectra are generated via the melting and dispersion/ionization of micron and submicron-sized ice grains Saturn's E-ring and Enceladus plume. The water beam in the LILBID spectrometer vacuum chamber is 12 μm - 22 μm in diameter, which is much larger than the diameters of the ice particles detected by CDA in E-ring and plume. With the laser energy primarily focusing on the center of the water beam, the outer part of the water beam receives less energy, so elemental species, like Na^+ or Na_2^+, are less likely to form there. More importantly, in this large ionisation area there are much more chance and time of interaction between the initially produced species. This interaction between neutral molecules and ions which are both present, inevitably creates more and larger cluster ions. Therefore, more Na/K-water cluster

and salt-water cluster ions (and hence also OH^- related peaks) are produced while the Na_2O^+ (85 u) and Na_2^+ (46 u) ions, which survive for longer in the lower density impact plasma cloud, are suppressed.

7.4.3 Detection limits variation with different settings

Given the reasonable assumption that the three LILBID settings correspond to the impact speed ranges in Table 7.1 it is possible to test how the detection limits vary with impact speed. However, as the exact relationship between impact speed and settings is out of the scope of this work, only an qualitative link between detection limits and and impact speeds could be determined. Table H.1 demonstrates that for most compounds of interest the variations of the evaluated approximate CDA detection limits with settings are not significant, only with a few exceptions, such as Lithium, silica, Formic Acid and formaldehyde, for which the variations of the evaluated approximate CDA detection limits with settings are not significant but still limited to one order of magnitude.

7.4.4 Data used for linear regression in Method 2

For a substance, the solutions corresponding to a series of concentrations are measured and thus the peak amplitudes are obtained. As described on Section 7.3.4, if the concentration is higher than a certain value, the linearity no longer holds. Usually, it increases the slope and thus causes a negative intercept, which make no sense physically, in the plots of linear TLS fit for detection limit prediction using Method 2, such as the plots in the left panels of Figs. 7.8 and 7.9. If the concentration is so low that the amplitude of it resulting peak is comparable with the uncertainty in amplitude, using the two or more data corresponding to such low concentration could increase the uncertainty of slope and even produce negative slope (Section 7.3.4), which also make no sense physically. Therefore, the data corresponding to the highest or the lower concentrations will not be used if they depart from linearity obviously.

7.4.5 Negative intercept problem during linear regression in Method 2

As discussed in the Section 7.3.4, the negative intercept in the fitted linear function (Eq. 7.5) make no sense physically. However, sometimes negative intercept due to

the uncertainty of data used for linear regression. In this case, a data point with 0 peak amplitude ratio and a small concentration is added for a new linear regression to make the intercept equal to 0 or just above 0.

7.4.6 Detection limit differences between Mixes 1 and 2

The analogue experimental results demonstrate that:

1. For a particular concentration of a substance in Mix 1 or Mix 2, spectra obtained using the same settings, the relative amplitudes of the peaks produced by the substance are systemically lower in the Mix 1 derived spectra than in the Mix 2 derived spectra. For example, Fig. 7.11 shows this phenomenon with Ammonium as an example. The upper and lower panels show spectra of Mix 1 plus 0.1 M NH_4Cl and Mix 2 plus 0.1 M NH_4Cl, respectively. The peak ratio of NH_4^+ (18 u) to Na^+ (23 u) in the spectra of Mix 2 is approximately twice as that in spectra of Mix 1, and the highest peak in the two spectra are similar high, although the concentration of added NH_4Cl in these two solutions are the same and the salinity of these two solutions are similar.

2. If the chosen peaks related to a particular substance are similar in amplitude in spectra from the two mixes, the concentration of this substance in Mix 1 is higher than in Mix 2. Fig. G.3 in Appendix shows this phenomenon with NH_4^+ (18 u) as an example. In both spectra the NH_4^+ (18 u) peaks are similar in height, but the concentration of NH_4Cl in Mix 1 is four times that in Mix 2.

The above phenomena are observed for all of the measured substances in this thesis. This indicates that the carbonate has a stronger ability to suppress the peaks related to the measured substances than chloride, no matter whether the measured substances react with Mix 1 and/or and Mix 2 (Section 7.4.1) or not. Thus, these phenomena could be related to the fact that the relative ionization efficiency of carbonate is higher than the chloride (Section 6.3.2).

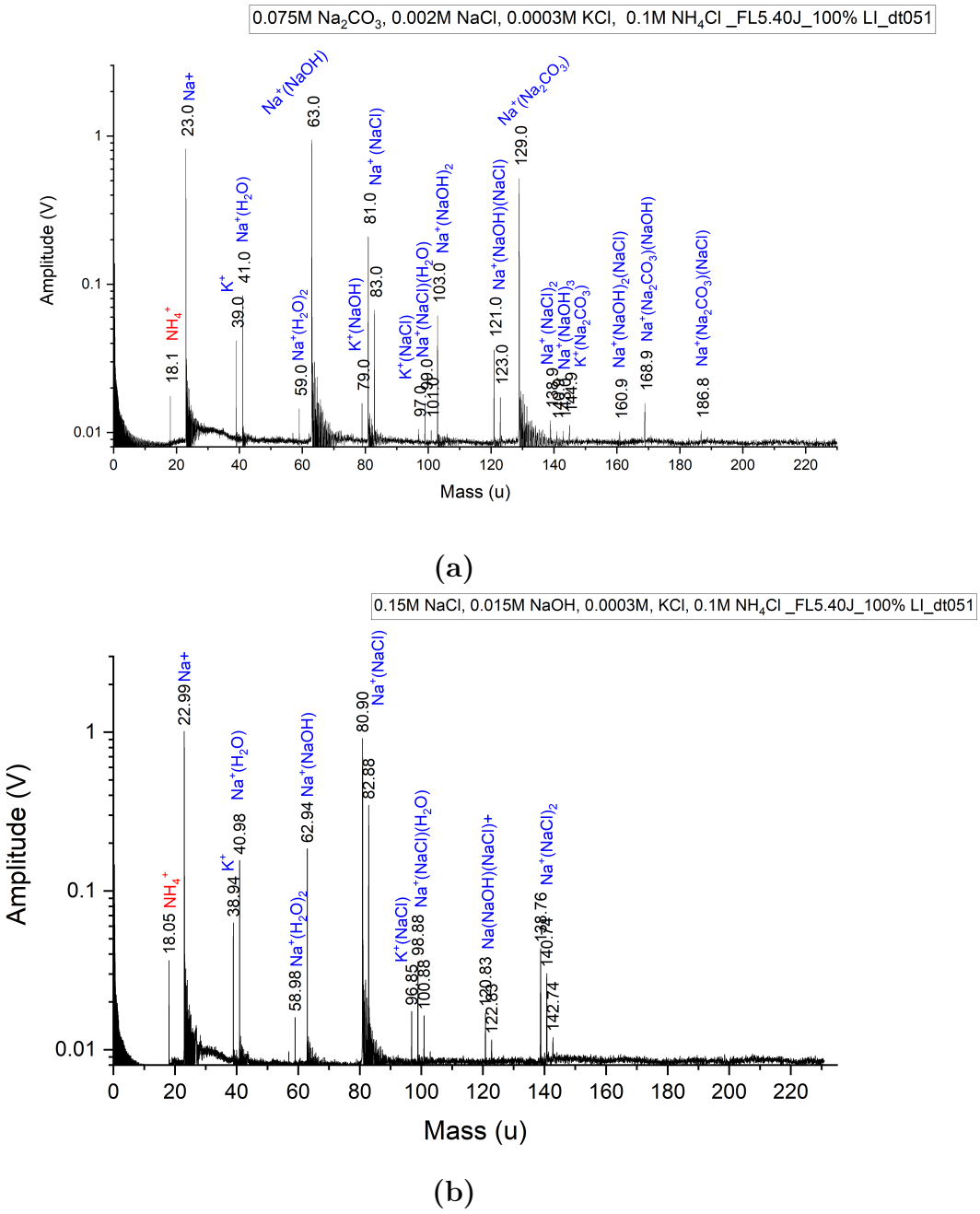

Figure 7.11: Analogue spectra of Mix 1 (Subfig. a) and Mix 2 (Subfig. b) solutions with 0.1 M NH_4Cl added, obtained using LILBID setting 1 (Table 7.1). (The chloride related peaks, such as $Na^+(NaCl)$ (81 u and 83 u) in the spectra of Mix 1 (Subfig. a) are attributed to chloride in the added NH_4Cl.)

7.4.7 Comparison of the results of CDA detection limit evaluation methods

In this chapter, two methods for evaluating approximate CDA detection limits for a variety of salts and low mass organic compounds have been presented: Method 1, peak threshold conversion based on signal to noise ratios; Method 2, function fitting based on peak amplitude ratios. Two different reference peaks have been used in Method 2 and therefore, in total, three sets of results have been obtained. The three sets of results will be compared in the following paragraphs.

- The results evaluated via Method 2 using Na^+ (23 u) and Na^+(NaOH) (63 u) as reference peaks.

  From Tables 7.5 and 7.6, it can be seen that the values obtained using Na^+(NaOH) (63 u) as the reference peak are always bigger than the values obtained when using the Na^+ (23 u) peak. The reason is that in most of the selected Type-3 CDA spectra the Na^+ (23 u) peak is higher in amplitude than the Na^+(NaOH) (63 u) peak, but the average amplitude of the Na^+ (23 u) peak in the 3 settings of analogue spectra is lower than that of the Na^+(NaOH) (63 u) peak, because the LIBID spectra used in this chapter are not to mimic impact speed ranges and the CDA spectra profiles accurately, which is discussed in Section 7.2.1. It can be seen that for some chemicals the detection limits derived with Na^+ (23 u) peak is closer to the detection limits derived using Method 1 and for other chemicals the detection limits derived with Na^+(NaOH) (63 u) peak is closer to the detection limits derived using Method 1.

- The results evaluated via Method 1.

  Table 7.6 shows that for most of the substances, the results evaluated via Method 1 lie between the two values obtained using Method 2's different reference peaks, with some exceptions such as Sulfate in Mix 1 and Fluoride in Mix 2.

- The error bars.

  For some substance/mix combinations, such as Phosphite in Mix 2, the error bars obtained from Method 2 are very large. The reason is that the ratio/concentration data produces, in these cases, poor linear fits.

  For most substances, the error bars of there three results overlap, and this provides some confidence in the suitability of the techniques applied, as well as the reliability of the predictions.

In conclusion, the results derived using both Methods 1 and 2 (both reference peaks) are reliable, although the uncertainties of the three results are still large, and there is some variability between the techniques. To improve the accuracy and precision of the detection measurements, in the future the following measures should be taken:

1. Use of improved laboratory procedures, such as using a measuring cylinder, pipette or micro-pipette to measure the volume of the liquid to reduce the sample volume uncertainties.

2. Expand the dataset to include analogue LILBID CDA spectra profiles corresponding to a variety of impact speed ranges, as performed by (Klenner et al. 2019). This may reduce the differences between the results predicted using the Na^+ (23 u) and Na^+(NaOH) (63 u) peaks.

3. In Method 2, varying the concentrations of some substances does not seem to result in linear variations in peak amplitudes, and this non-linearity should be explained and suitable fits applied in the future, to predict the detection limits more accurately.

4. In Method 2, more concentrations of target compounds will be measured to fit curves, linear or nonlinear, more accurately.

Chapter 8

Summary

This work involves two main parts: CDA mass spectral analysis (Chapters 4 and 5) and laboratory experiments (Chapters 6 and 7). These two parts are interdependent.

In Chapter 4, an in depth analysis of the properties of the mass spectra of the salt-rich ice particles (Type-3 spectra) in Saturn's E-ring was undertaken, with spectra classified according to the existence and relative amplitudes of salt peaks. Most of Type-3 CDA spectra are dominated by Na-related peaks and show only tiny or no K-related peaks. These 'Na-rich' spectra are further sub-classified. Based on this classification, the subtypes of Type-3 spectra are defined. Amongst these subtypes, 'Na-rich' subtypes A, B, C, D and L are the majorities. Subtype A spectra show no chloride peaks and high carbonated related peaks; subtype B spectra also show no chloride peak but show much lower or no carbonate related peaks; subtype C spectra show chloride peaks and no carbonate related peaks, with peak Na(NaCl) (81 u) lower than peak Na(NaOH) (63 u); subtype D spectra also show chloride peaks and no carbonate related peaks, but with peak Na(NaCl) (81 u) higher than peak Na(NaOH) (63 u); subtype L spectra show neither chloride peak nor carbonate related peak, and with only the first hydroxide related peak detected. Then, a statistical analysis of the main identified subtypes, A, B, C, D and L, was performed, and trends of salt-rich ice grain spectral features with e.g. Saturnian distance, investigated. In Chapter 5, CDA mass spectra of salt rich particles in Enceladus' plume were analyzed and the compositional distributions of E-ring and plume particle spectra compared. There is a difference between the E-ring and plume Type-3 spectra populations: for E-ring spectra the abundances of the five main spectral subtypes are comparable, but for plume spectra, subtype A dominates and subtype B is absent. This variation reflects differences in the composition of the salt-rich particles in the two different environments. Hypothetical causes of the

differences between the distributions were then postulated. In Chapter 6, four of major subtypes of spectra, A, B, C and D, were mimicked in the laboratory laser spectrometer and the salt component concentration parameter spaces explored. In Chapter 7, the detection limits of some important geochemical substances were evaluated via laboratory analogue experiments. These detection limits can provide important constraints for geochemical models (Glein et al. 2008; Matson et al. 2007; Zolotov 2007) and the habitability (Hao et al. 2020; Ray et al. 2020; Taubner et al. 2020; Glein & Waite 2020). The relative concentrations of sulfate and sulfides reflect the temperature in the core of Enceladus (Zolotov 2007). The availability of phosphorus could strongly affect the habitability of Enceladus (Hao et al. 2020) and thermodynamic and kinetic modelling based on recent results concerning the geochemistry of the ocean-seafloor system on Enceladus indicates that phosphorus dissolved in the ocean water should predominantly exist as phosphate and the total concentration of the dissolved inorganic phosphorus could reach levels of 10^{-7} to 10^{-2} mole/kg water (Hao et al. 2020). By comparison, the total concentration of dissolved inorganic phosphorus in modern terrestrial seawater is $\sim 10^{-6}$ mole/kg water (Hao et al. 2020).

Major findings:

1. The salt rich spectra exhibit significant compositional diversity. Approximately 93.5% of the E-ring salt-rich spectra are 'sodium rich but potassium poor' spectra. The 'sodium and potassium rich' spectra and the 'potassium rich but sodium poor' spectra only make up 4.3% and 2.2% of the E-ring salt-rich spectra, respectively.

2. The majority of the 'sodium rich but potassium poor' spectra also show strong compositional diversity and thus can be further classified into several subtypes. Almost all of spectra of these subtypes, with only 3 exceptions of spectra, show hydroxide related peaks indicative of high pH. The four dominant subtypes, A, B, C and D, are separated by the abundances of carbonate-related peaks and chloride related peaks. Surprisingly, carbonate and chloride are mutually exclusive in most spectra, with only very rare exceptions (Subtype H). The spectral profiles of the four subtypes show a gradual change in the relative peak amplitudes of carbonate-related and chloride-related peaks. From subtype A to subtype D, the dominance (i.e. spectral amplitudes and abundances) of carbonate-related peaks decreases and that of the chloride-related peaks increases. Subtypes A and B are the chloride poor group, with subtype A richest in carbonate; subtype H spectra (only 15) show both carbonate-related

peaks and chloride-related peaks (Fig. 4.13); subtypes C and D are the chloride rich and carbonate poor group. One further important subtype, L, consists of spectra which show neither significant carbonate nor significant chloride features, but possess significant Na^+ (23 u) and Na^+(NaOH) (63 u) peaks. Besides, there 3 spectra, showing chloride related peaks but no hydroxide related peaks and carbonate peaks, are classified into subtype E.

3. Some trends are found between subtype, relative peak amplitudes and impact speed. The relative abundance of subtype A decreases slightly with increasing impact speed, whereas that of subtype B clearly increases (Table 4.19). A possible explanation is that higher impact speeds tend to result in the destruction of carbonate ions (CO_3^{2-}) in the impact plasma and thus a lower spectral abundance of carbonate-related peaks, although more of the individual carbonate-containing particles could be melted/dispersed and ionised. The absence of the hydrogen mass line (a reliable indicator for impact speeds above $\sim$ 10 km/s) in all subtype A spectra, as well as the abundance of subtype A and absence of subtype B spectra during low-speed plume crossings also support this explanation. In contrast, impact speeds do not clearly affect the abundance of chloride-related peaks. The fractional abundances of subtypes L show clear inverse trends with impact speed (Table 4.19): it seems that lower impact speeds produce more subtype L. In addition, the ice particles which produce subtype L spectra tend to have relatively small sizes (Table 4.25). Thus, one possible explanation is that the small particles with low impact speeds produce weak spectra with smaller signal to noise. Thus, these spectra have a higher probability that chloride and carbonate peaks are not detected and thus are classified into subtype L.

4. The spatial distributions of the subtypes (Fig. 4.20) and relative peak amplitude analysis (Fig. 4.23) imply that the concentration of chloride in the ice particles is decreasing with time, assuming that the age of E-ring particles is positively correlated with the radial distance from Saturn. Figs. 4.21 and 4.21 imply carbonate is lost with the radial distance from Saturn (also with time), especially outside approximately 8 R_S.

5. The distributions of the spectral subtypes are very different for those generated by E-ring grain impacts and those generated by plume particle impacts. For E-ring spectra the fractions (relative abundances) of the five subtypes are similar, but subtype A spectra dominate in the plume. This implies that most of the extremely carbonate-rich ice particles (those which, if detected, would produce subtype A spectra) do not escape the Hill sphere of Enceladus to reach the E-ring.

6. In the laboratory, the sensitivity of the Laser Induced Liquid Beam Ion Desorption (LILBID) ion formation process (and by extension, the impact ionization process) varies significantly between different salt cations/anions. For example, carbonate can produce (cation) peaks much more efficiently than chloride and hydroxide (Table 6.2 in Section 6.3.2), which means if carbonate-related peaks and chloride-related peaks are to be similar in amplitude, the concentration of chloride in the liquid/grains is approximately 4 times that of carbonate. The exact composition parameter space, with NaOH, NaCl, and Na_2CO_3 as major salts, for subtype A, B, C, and D ice particles was explored via laboratory spectra mimicking. The result is visualised using 3D plots (Fig. 6.7 in Section 6.3.5).

7. The detection limits of important geochemical ions, including sulfate and phosphorous species, as well as silica and two organics were evaluated using two different methods. The results are listed in Table 7.6, which shows that the detection limits in carbonate-rich ice particles are higher than those in the chloride-rich ice particles for the same chemical of interest and the error bars of the results from those two different detection limit prediction methods overlap for most chemicals of interest. From the investigated species the CDA is most sensitive to sulfate, phosphate and phosphite, and least sensitive to formaldehyde. The detection limits of sulfate, phosphate and phosphite in carbonate-rich ice particles are in the range of 10^{-2} to 10^{-1} mM, and their detection limits in chloride-rich ice particles in the range 10^{-3} to 10^{-2} mM. By contrast, the detection limits of formaldehyde in carbonate-rich ice particles is within 0.1 mM and 1 mM and its detection limit in chloride-rich ice particles approximately 0.1 mM.

These results, while helping place limits on the ability of a CDA-like detector to detect dissolved compounds in ice grains, and showing the range of salt-rich ice grain compositions found in the Saturnian system, also raise new questions.

Questions for future missions:

1. How does grain compositional differentiation occur?

   Much evidence indicates there is a single, global, subsurface ocean under the ice shell of Enceladus, which means the ocean water should be - in general - compositionally uniform. However, the salt-rich ice particles which originate from this global ocean, show significant compositional diversity. One theory to explain this phenomenon is that differentiation happens as the ocean water or

ice grains move upward through the ice fractures. This differentiation remains to be understood and further modeling of the physical and chemical processes within the ice shell is required.

2. The composition of the subsurface ocean.

   The compositions of the salt-rich ice particles erupting from the Enceladean fractures may have been altered by the aforementioned unclear differentiation mechanism(s). After the differentiation mechanism(s) are fully understood, the real composition of the subsurface oceans could be well evaluated.

3. Biosignatures in the plume and the subsurface ocean.

   The resolution of CDA's mass spectrometer is believed to be too low for the unambiguous identification of biosignatures. Future missions will be equipped with higher resolution spectrometers which can distinguish biotic organics from those produced by abiotic means by measuring the relative abundances of ions (Klenner et al. 2020) and isotopes, and the fragment ions from biotic organics, such as nucleic acids, amino acids and lipids. Then, we may know if there is alien life in this icy moon.

References

Albada, G. 1947, On the Origin of the Heavy Elements., The Astrophysical Journal, 105, 393

Arnett, D., & Bazan, G. 1997, Nucleosynthesis in stars: recent developments, Science, 276, 1359

Austin, D. 2003, Impact-ionization mass spectrometry of cosmic dust, PhD thesis, California Institute of Technology

Badescu, V., & Zacny, K. 2018, Outer Solar System: Prospective Energy and Material Resources (Springer), 316

Barnett, A. 2013, Imaging Science Subsystem (ISS), https://solarsystem.nasa.gov/missions/cassini/mission/spacecraft/cassini-orbiter/imaging-science-subsystem/

Barnett, A. 2018, Enceladus: Ocean Moon, https://solarsystem.nasa.gov/missions/cassini/science/enceladus/

Barnett, A. 2019, Pioneer 9, https://solarsystem.nasa.gov/missions/pioneer-09/in-depth/

Barnett, A. 2020, Titan in depth, https://solarsystem.nasa.gov/moons/saturn-moons/titan/in-depth/

Baum, W., Kreidl, T., Westphal, J., et al. 1981, Saturn's E ring: I. CCD observations of March 1980, Icarus, 47, 84

Bellerose, J., Roth, D., Tarzi, Z., & Wagner, S. 2019, in Space Operations: Inspiring Humankind's Future (Springer), 575–588

Berg, O., & Richardson, F. 1969, The Pioneer 8 Cosmic Dust Experiment, Review of Scientific Instruments, 40, 1333

Bergh, S. 1975, Stellar Populations in Galaxies, Annual Review of Astronomy and Astrophysics, 13, 217

Birnstiel, T., Fang, M., & Johansen, A. 2016, Dust evolution and the formation of planetesimals, Space Science Reviews, 205, 41

Bordi, J. J., Antreasian, P., Jones, J., et al. 2005, Orbit Determination results and trajectory reconstruction for the Cassini/Huygens Mission, in 3rd International Planetary Probe Workshop, Attica, Greece (Pasadea, CA: Jet Propulsion Laboratory, National Aeronautics and Space . . .)

Brownlee, D. E. 1985, Cosmic dust: Collection and research, Annual Review of Earth and Planetary Sciences, 13, 147

Běhounková, M., Tobie, G., Choblet, G., & Čadek, O. 2012, Tidally-induced melting events as the origin of south-pole activity on Enceladus, Icarus, 219, 655–664

Čadek, O., Tobie, G., Van Hoolst, T., et al. 2016, Enceladus's internal ocean and ice shell constrained from Cassini gravity, shape and libration data: ENCELADUS'S INTERIOR FROM CASSINI DATA, Geophysical Research Letters, 43, doi:10.1002/2016GL068634

Cassini-Huygens-Group. 2018, Spacecraft, https://solarsystem.nasa.gov/missions/cassini/mission/spacecraft/cassini-orbiter/

Charvat, A., & Abel, B. 2007, How to make big molecules fly out of liquid water: Applications, features and physics of laser assisted liquid phase dispersion mass spectrometry, Physical chemistry chemical physics : PCCP, 9, 3335

Chen, E., & Nimmo, F. 2011, Obliquity tides do not significantly heat Enceladus, Icarus, 214, 779

Choblet, G., Tobie, G., Sotin, C., et al. 2017, Powering prolonged hydrothermal activity inside Enceladus, Nature Astronomy, 1, doi:10.1038/s41550-017-0289-8

Collins, G., & Goodman, J. 2007, Enceladus' south polar sea, Icarus, 189, 72

De Pater, I., Chau Martin, S., & Showalter, M. 2004, Keck Near-Infrared Observations of Saturn's E and G Rings during Earth's Ring Plane Crossing in August 1995, Icarus, 172, 446

De Pater, I., Showalter, M. R., Lissauer, J. J., & Graham, J. R. 1996, Keck infrared observations of Saturn's E and G rings during Earth's 1995 ring plane crossings, Icarus, 121, 195

Dietzel, H., Eichhorn, G., Fechtig, H., et al. 1973, The HEOS 2 and HELIOS micrometeoroid experiments, Journal of Physics E: Scientific Instruments, 6, 209

Dikarev, V. V. 1999, Dynamics of particles in Saturn's E ring: Effects of charge variations and the plasma drag force, Astronomy and Astrophysics, 346, 1011

Dohnanyi, J. S. 1976, 2.1.8 Sources of Interplanetary Dust: Asteroids, International Astronomical Union Colloquium, 31, 187–205

Dominik, C., Blum, J., Cuzzi, J., & Wurm, G. 2006, Growth of dust as the initial step toward planet formation, arXiv preprint astro-ph/0602617

Dong, Y., Hill, T., & Ye, S.-Y. 2015, Characteristics of ice grains in the Enceladus plume from Cassini observations, Journal of Geophysical Research: Space Physics, 120, 915

Dougherty, M., Cao, H., Khurana, K., et al. 2018, Saturn's magnetic field revealed by the Cassini Grand Finale, Science, 362, eaat5434

Feibelman, W. 1967, Concerning the "D" ring of Saturn, Nature, 214, 793

Fiege, K., Trieloff, M., Hillier, J. K., et al. 2014, Calibration of relative sensitivity factors for impact ionization detectors with high-velocity silicate microparticles, Icarus, 241, 336

Fielding, L., Hillier, J., Burchell, M., & Armes, S. 2015, Space Science Applications for Conducting Polymer Particles: Synthetic Mimics for Cosmic Dust and Micrometeorites, Chemical communications (Cambridge, England), 51, doi:10.1039/c5cc07405c

Flynn, G., Nittler, L., & Engrand, C. 2016, Composition of Cosmic Dust: Sources and Implications for the Early Solar System, Elements, 12, 177

Fortney, J., Helled, R., Nettelmann, N., et al. 2018, The Interior of Saturn (Cambridge University Press), 44–68

Fortney, J., & Nettelmann, N. 2009, The Interior Structure, Composition, and Evolution of Giant Planets, Space Science Reviews, 152, doi:10.1007/s11214-009-9582-x

Galland Kivelson, M. 2005, The Current Systems of the Jovian Magnetosphere and Ionosphere and Predictions for Saturn, Space Science Reviews - SPACE SCI REV, 116, 299

Gibson, B., Fenner, Y., Renda, A., Kawata, D., & Lee, H.-c. 2003, Galactic Chemical Evolution, Publications of the Astronomical Society of Australia, 20, doi:10.1071/AS03052

Glein, C. R., & Waite, J. H. 2020, The carbonate geochemistry of Enceladus' ocean, Geophysical Research Letters, 47, e2019GL085885

Glein, C. R., Zolotov, M. Y., & Shock, E. L. 2008, The oxidation state of hydrothermal systems on early Enceladus, Icarus, 197, 157

Goguen, J. D., Buratti, B. J., Brown, R. H., et al. 2013, The temperature and width of an active fissure on Enceladus measured with Cassini VIMS during the 14 April 2012 South Pole flyover, Icarus, 226, 1128

Gombosi, T. I., Armstrong, T. P., Arridge, C. S., et al. 2009, in Saturn from Cassini-Huygens (Springer), 203–255

Gombosi, T. I., & Ingersoll, A. P. 2010, Saturn: Atmosphere, Ionosphere, and Magnetosphere, Science, 327, 1476

Goodson, T., Gray, D., Hahn, Y., & Peralta, F. 1998, Cassini maneuver experience - Launch and early cruise, in Conference: Guidance, Navigation, and Control Conference and Exhibit

Greenberg, J. M. 2002, Cosmic dust and our origins, Surface Science, 500, 793

Grün, E., Gustafson, B., Dermott, S., & Fechtig, H. 2001, Interplanetary Dust (Springer), 310, doi:10.1007/978-3-642-56428-4

Grün, E., Krüger, H., & Srama, R. 2019, The Dawn of Dust Astronomy, Space Science Reviews, 215, doi:10.1007/s11214-019-0610-1

Grün, E., Pailer, N., Fechtig, H., & Kissel, J. 1980, Orbital and physical characteristics of micrometeoroids in the inner solar system as observed by Helios 1, Planetary and Space Science, 28, 333

Grün, E., Morfill, G. E., & Mendis, D. A. 1984, Dust-magnetosphere interactions, IN: Planetary rings, 275

Gunell, H., Mann, I., Wedlund, C. S., et al. 2015, Acceleration of ions and nano dust at a comet in the solar wind, Planetary and Space Science, 119, 13

Gurnett, D. A., Grü, E., Gallagher, D., & Kurth, W.S.and Scarf, F. 1983, Micron-Sized Particles Detected near Saturn by the Voyager Plasma Wave Instrument, Icarus, 53, 236

Hadley, K. Z. 2019, Interstellar Medium, http://www.khadley.com/courses/Astronomy/ph_206/topics/interstellarMedium/

Hamilton, D. P., & Burns, J. A. 1994, Origin of Saturn's E ring: Self-sustained, naturally, Science, 264, 550

Hansen, C., Esposito, L., Stewart, A., et al. 2008, Water vapour jets inside the plume of gas leaving Enceladus, Nature, 456, 477

Hao, J., Glein, C. R., Huang, F., et al. 2020, Abundant phosphorus for life in the Enceladus ocean, in AGU Fall Meeting 2020, AGU

Henin, B. 2018, Enceladus (Cham: Springer International Publishing), 159–188

Hillier, J., McBride, N., Green, S., Kempf, S., & Srama, R. 2006, Modelling CDA mass spectra, Planetary and Space Science, 54, 1007–1013

Hillier, J., Green, S., McBride, N., et al. 2007a, The composition of Saturn's E ring, Monthly Notices of the Royal Astronomical Society, 377, 1588

Hillier, J., Green, S., McBride, N., et al. 2007b, Interplanetary dust detected by the Cassini CDA Chemical Analyser, Icarus, 190, 643

Hillier, J. K., Sestak, S., Green, S., et al. 2009, The production of platinum-coated silicate nanoparticle aggregates for use in hypervelocity impact experiments, Planetary and Space Science, 57, 2081

Horanyi, M., Burns, J., & Hamilton, D. 1992, The dynamics of Saturn's E ring particles, Icarus, 97, 248

Horányi, M., Juhász, A., & Morfill, G. E. 2008, Large-scale structure of Saturn's E-ring, Geophysical research letters, 35

Hsu, H.-W., Postberg, F., Sekine, Y., et al. 2015, Ongoing hydrothermal activities within Enceladus, Nature, 519, 207

Huebner, W. F., Benkhoff, J., Capria, M.-T., et al. 2006, Heat and gas diffusion in comet nuclei, Vol. 133 (International Space Science Institute Bern)

Hurford, T., Bills, B., Helfenstein, P., et al. 2009, Geological implications of a physical libration on Enceladus, Icarus, 203, 541

Iess, L., Stevenson, D., Parisi, M., et al. 2014, The Gravity Field and Interior Structure of Enceladus, Science (New York, N.Y.), 344, 78

Ingersoll, A., Ewald, S., & Trumbo, S. 2019, Time variability of the Enceladus plumes: Orbital periods, decadal periods, and aperiodic change, Icarus, doi:10.1016/j.icarus.2019.06.006

Inoue, A. 2012, The origin of dust in galaxies revisited: The mechanism determining dust content, Earth, Planets, and Space, 63, doi:10.5047/eps.2011.02.013

Jacobson, R. A., Antreasian, P., Bordi, J., et al. 2006, The gravity field of the saturnian system from satellite observations and spacecraft tracking data, The Astronomical Journal, 132, 2520

Jewitt, D. 2012, The active asteroids, The Astronomical Journal, 143, 66

Jia, X., Kivelson, M. G., Khurana, K. K., & Kurth, W. S. 2018, Evidence of a plume on Europa from Galileo magnetic and plasma wave signatures, Nature Astronomy, 2, 459

Juhász, A., & Horanyi, M. 2002, Saturn's E ring: A dynamical approach, Journal of Geophysical Research, 107, doi:10.1029/2001JA000182

Juhász, A., Horanyi, M., & Morfill, G. 2007, Signatures of Enceladus in Saturn's E ring, Geophysical Research Letters - GEOPHYS RES LETT, 34, doi:10.1029/2006GL029120

Jurac, S., Johnson, R., & Richardson, J. 2001, Saturn's E ring and production of the neutral torus, Icarus, 149, 384

Kargel, J. S. 1991, Brine volcanism and the interior structures of asteroids and icy satellites, Icarus, 94, 368

Kempf, S. 2008, Interpretation of high rate dust measurements with the Cassini dust detector CDA, Planetary and Space Science - PLANET SPACE SCI, 56, 378

Kempf, S., Beckmann, U., & Schmidt, J. 2010, How the Enceladus dust plume feeds Saturn's E ring, Icarus, 206, 446

Kempf, S., Beckmann, U., Srama, R., et al. 2006, The electrostatic potential of E ring particles, Planetary and Space Science - PLANET SPACE SCI, 54, 999

Kempf, S., Horányi, M., Hsu, H.-W., et al. 2018, Saturn's diffuse E ring and its connection with Enceladus, Enceladus and the Icy Moons of Saturn, 195

Kempf, S., Beckmann, U., Moragas-Klostermeyer, G., et al. 2008, The E ring in the vicinity of Enceladus: I. Spatial distribution and properties of the ring particles, Icarus, 193, 420

Khawaja, N. 2017, Organic compounds in Saturn's E-ring and its compositional profile in the vicinity of Rhea, PhD thesis, Heidelberg University

Khawaja, N., Postberg, F., & Schmidt, J. 2017, The Compositional Profile of the Enceladian Ice Plume from the Latest Cassini Flybys, in 48th Lunar and Planetary Science Conference

Khawaja, N., Postberg, F., Hillier, J., et al. 2019, Low-mass nitrogen-, oxygen-bearing, and aromatic compounds in Enceladean ice grains, Monthly Notices of the Royal Astronomical Society, 489, doi:10.1093/mnras/stz2280

Kissel, J., Brownlee, D. E., Büchler, K., et al. 1986a, Composition of comet Halley dust particles from Giotto observations, Nature, 321, 336–337

Kissel, J., Sagdeev, R. Z., Bertaux, J. L., et al. 1986b, Composition of comet Halley dust particles from Vega observations, Nature, 321, 280

Klenner, F., Postberg, F., Hillier, J., et al. 2019, Analogue spectra for impact ionization mass spectra of water ice grains obtained at different impact speeds in space, Rapid Communications in Mass Spectrometry, doi:10.1002/rcm.8518

Klenner, F., Postberg, F., Hillier, J., et al. 2020, Discriminating abiotic and biotic fingerprints of amino acids and fatty acids in ice grains relevant to ocean worlds, Astrobiology, 20, 1168

Kurth, W., Averkamp, T., Gurnett, D., & Wang, Z. 2006, Cassini RPWS observations of dust in Saturn's E Ring, Planetary and Space Science, 54, 988

Le Gall, A., West, R. D., & Bonnefoy, L. 2019, Dust and snow cover on saturn's icy moons, Geophysical Research Letters, 46, 11747

Le Gall, A., Leyrat, C., Janssen, M., et al. 2017, Thermally anomalous features in the subsurface of Enceladus's south polar terrain, Nature Astronomy, 1, 0063

Linti, S. 2018, Compositional Analysis of Saturn's Inner E Ring and Outer F Ring as seen during Cassini's Ring-Grazing Orbits

Marouf, E., Tyler, G., A. Zebker, H., A. Simpson, R., & Eshleman, V. 1983, Particle size distributions in Saturn's rings from Voyager 1 radio occultation, Icarus, 54, doi:10.1016/0019-1035(83)90192-6

Martinez, C. 2007, Cassini Discovers Saturn's Dynamic Clouds Run Deep, https://www.nasa.gov/mission_pages/cassini/whycassini/cassini-090505-clouds.html

Matson, D. L., Castillo, J. C., Lunine, J., & Johnson, T. V. 2007, Enceladus' plume: Compositional evidence for a hot interior, Icarus, 187, 569

Maxwell, J. C. 1859, On the stability of the motion of Saturn's rings (Macmillan and Company)

McKay, C., Davila, A., Glein, C., Hand, K., & Stockton, A. 2018, Enceladus astrobiology, habitability, and the origin of life, Enceladus and the Icy Moons of Saturn; Schenk, PM, Clark, RN, Howett, CJA, Verbiscer, AJ, Waite, JH, Eds, 437

Mocker, A. 2011, Comparison of impact ionisation plasma with laser ionisation, PhD thesis, MPI for Nuclear Physics

Mocker, A., Grün, E., Sternovsky, Z., et al. 2012, On the applicability of laser ionization for simulating hypervelocity impacts, Journal of Applied Physics, 112, 3301

Morfill, G., Grün, E., Goertz, C., & Johnson, T. 1983, On the evolution of Saturn's 'Spokes' - Theory, Icarus, 53, 230

NASAwebsite. 2019a, Enceladus Flyby - April 14, 2012, https://solarsystem.nasa.gov/news/12811/enceladus-flyby-april-14-2012/

NASAwebsite. 2019b, Enceladus Flyby - March 27, 2012, https://solarsystem.nasa.gov/news/12810/enceladus-flyby-march-27-2012/

NASAwebsite. 2019c, Enceladus Flyby 21 (E-21): Deepest Dive Through the Plume, https://solarsystem.nasa.gov/news/12847/enceladus-flyby-21-e-21-deepest-dive-through-the-plume/

NASAwebsite. 2019d, Saturn by the numbers, https://solarsystem.nasa.gov/planets/saturn/by-the-numbers/

NASAwebsite. 2020, Saturn in depth, https://solarsystem.nasa.gov/planets/saturn/in-depth/

Nicholson, P. D., Showalter, M. R., Dones, L., et al. 1996, Observations of Saturn's ring-plane crossings in August and November 1995, Science, 272, 509

Nimmo, F., & Porco, C. 2014, in Encyclopedia of the Solar System (Third Edition), third edition edn., ed. T. Spohn, D. Breuer, & T. V. Johnson (Boston: Elsevier), 851 – 859

Nimmo, F., R Spencer, J., Pappalardo, R., & E Mullen, M. 2007, Shear heating as the origin of the plumes and heat flux on Enceladus, Nature, 447, 289

Nissen, S. B., Taubner, R.-S., Leitner, J. J., & Firneis, M. G. 2015, The possibility of serpentinization on enceladus, in EGU General Assembly Conference Abstracts, 13114

Nomoto, K., Kobayashi, C., & Tominaga, N. 2013, Nucleosynthesis in stars and the chemical enrichment of galaxies, Annual Review of Astronomy and Astrophysics, 51, 457

Nölle, L. 2021, Multidimensional scan of the Saturnian E-ring based on the data record of Cassini's Comic Dust Analyzer (in progress), PhD thesis, Freie Universität Berlin

Ogilvie, G. I. 2008, James Clerk Maxwell and the dynamics of astrophysical discs, Philosophical Transactions of the Royal Society A: Mathematical, Physical and Engineering Sciences, 366, 1707

Ohtsuki, K., Kawamura, H., Hirata, N., Daisaka, H., & Kimura, H. 2020, Size of the smallest particles in Saturn's rings, Icarus, 344, 113346

O'Neil, W. 1990, Project Galileo, in Space Programs and Technologies Conference

Pang, K. D., Voge, C. C., Rhoads, J. W., & Ajello, J. M. 1984, The E ring of Saturn and satellite Enceladus, Journal of Geophysical Research: Solid Earth, 89, 9459

Parkinson, C. D., Liang, M.-C., Yung, Y. L., & Kirschivnk, J. L. 2008, Habitability of Enceladus: planetary conditions for life, Origins of Life and Evolution of Biospheres, 38, 355

Patthoff, D., & Kattenhorn, S. 2011, A fracture history on Enceladus provides evidence for a global ocean, Geophysical Research Letters - GEOPHYS RES LETT, 38, doi:10.1029/2011GL048387

Porco, C., Helfenstein, P., Thomas, P., et al. 2006, Cassini Observes the Active South Pole of Enceladus, Science (New York, N.Y.), 311, 1393

Postberg, F., Clark, R., Hansen, C., et al. 2018a, Plume and Surface Composition of Enceladus (University of Arizona Press), 137

Postberg, F., Kempf, S., Hillier, J., et al. 2008, The E-ring in the vicinity of Enceladus: II. Probing the moon's interior—the composition of E-ring particles, Icarus, 193, 438

Postberg, F., Kempf, S., Rost, D., et al. 2009a, Discriminating contamination from particle components in spectra of Cassini's dust detector CDA, Planetary and Space Science, 57, 1359

Postberg, F., Kempf, S., Schmidt, J., et al. 2009b, Sodium salts in E-ring ice grains from an ocean below the surface of Enceladus, Nature, 459, 1098

Postberg, F., Kempf, S., Srama, R., et al. 2006, Composition of Jovian dust stream particles, Icarus, 183, 122

Postberg, F., Schmidt, J., Hillier, J., Kempf, S., & Srama, R. 2011, A salt-water reservoir as the source of a compositionally stratified plume on Enceladus, Nature

Postberg, F., Khawaja, N., Abel, B., et al. 2018b, Macromolecular organic compounds from the depths of Enceladus, Nature, 558, doi:10.1038/s41586-018-0246-4

Ratcliff, P. R., Burchell, M. J., Cole, M. J., Murphy, T. W., & Alladfadi, F. 1997, Experimental measurements of hypervelocity impact plasma yield and energetics, International Journal of Impact Engineering, 20, 663–674

Ray, C., Glein, C. R., Waite, J. H., et al. 2020, Oxidation processes diversify the metabolic menu on Enceladus, Icarus, 114248

Rietmeijer, F. J. 1998, Interplanetary dust particles, Planetary materials, 36, 28

Roberts, J. H. 2015, The fluffy core of Enceladus, Icarus, 258, 54

Roth, L., Saur, J., Retherford, K., et al. 2013, Transient Water Vapor at Europa's South Pole, Science (New York, N.Y.), 343, doi:10.1126/science.1247051

Schmidt, J., Brilliantov, N., Spahn, F., & Kempf, S. 2008, Slow dust in Enceladus' plume from condensation and wall collisions in tiger stripe fractures, Nature, 451, 685

Sekine, Y., Shibuya, T., & Kamata, S. 2019, in Astrobiology (Springer), 399–407

Sittler, E., André, N., Blanc, M., et al. 2008, Ion and neutral sources and sinks within Saturn's inner magnetosphere: Cassini results, Planetary and Space Science, 56, 3

Smith, E. J., Davis, L., Jones, D. E., et al. 1980, Saturn's magnetic field and magnetosphere, Science, 207, 407

Smith, E. J., Page, D. E., & Wenzel, K.-P. 1991, Ulysses: A journey above the Sun's poles, Eos, Transactions American Geophysical Union, 72, doi:10.1029/90EO00186

Spahn, F., Sachse, M., Seiß, M., et al. 2019, Circumplanetary Dust Populations, Space Science Reviews, 215, doi:10.1007/s11214-018-0577-3

Spahn, F., Schmidt, J., Albers, N., et al. 2006a, Cassini Dust Measurements at Enceladus and Implications for the Origin of the E Ring, Science (New York, N.Y.), 311, 1416

Spahn, F., Albers, N., Hörning, M., et al. 2006b, E ring dust sources: Implications from Cassini's dust measurements, Planetary and Space Science, 54, 1024

Sparks, W., Hand, K., McGrath, M., et al. 2016, Probing for Evidence of Plumes on Europa with HST/STIS, The Astrophysical Journal, 829, doi:10.3847/0004-637X/829/2/121

Sparks, W., Schmidt, B., McGrath, M., et al. 2017, Active Cryovolcanism on Europa?, Astrophysical Journal Letters, 839, doi:10.3847/2041-8213/aa67f8

Spitale, J., Hurford, T., Rhoden, A., Berkson, E., & Platts, S. 2015, Curtain eruptions from Enceladus' south-polar terrain, Nature, 521, 57

Spitale, J., & Porco, C. 2007, Association of the jets of Enceladus with the warmest regions on its south-polar fractures, Nature, 449, 695

Srama, R. 2009, Cassini-Huygens and beyond - tools for dust astronomy, PhD thesis, Universität Stuttgart

Srama, R., Ahrens, T., Altobelli, N., et al. 2004, The Cassini Cosmic Dust Analyzer, Space Science Reviews, 114, 465

Srama, R., Kempf, S., Moragas-Klostermeyer, G., et al. 2006, In situ dust measurements in the inner Saturnian system, Planetary and Space Science, 54, 967

Stanley, S. 2010, A dynamo model for axisymmetrizing Saturn's magnetic field, Geophysical Research Letters, 37, L05201

Stark, A., Hussmann, H., Oberst, J., et al. 2018, Basic geodetic and dynamical parameters of Saturn's moon Enceladus: A key target of future exploration (CRC Press), 15–30

Stone, E., & Miner, E. 1981, Voyager 1 encounter with the Saturnian system, Science, 212, 159

Stone, E., & Miner, E. 1982, Voyager 2 encounter with the Saturnian system, Science, 215, 499

Stübig, M. 2002, New insights in impact ionization and in time-of-flight mass spectroscopy with micrometeoroid detectors by improved impact simulations in the laboratory, PhD thesis, MPI for Nuclear Physics

Taubner, R.-S., Olsson-Francis, K., Vance, S. D., et al. 2020, Experimental and simulation efforts in the astrobiological exploration of exooceans, Space science reviews, 216, 1

Teolis, B., Perry, M., Hansen, C., et al. 2017, Enceladus Plume Structure and Time Variability: Comparison of Cassini Observations, Astrobiology, 17, 926

Thomas, P., Tajeddine, R., Tiscareno, M., et al. 2015, Enceladus's measured physical libration requires a global subsurface ocean, Icarus, 264, doi:10.1016/j.icarus.2015.08.037

Tjoa, J., Mueller, M., & van der Tak, F. 2020, The subsurface habitability of small, icy exomoons, Astronomy & Astrophysics, 636, A50

Tobie, G., Čadek, O., & Sotin, C. 2008, Solid tidal friction above a liquid water reservoir as the origin of the South Pole Hotspot on Enceladus, Icarus, 196, 642

Tyler, R. H. 2009, Ocean tides heat Enceladus, Geophysical Research Letters, 36, https://agupubs.onlinelibrary.wiley.com/doi/pdf/10.1029/2009GL038300

Unavane, M. 1995, Stellar populations, The Observatory, 115, 300

Verbiscer, A. J., Skrutskie, M. F., & Hamilton, D. P. 2009, Saturn's largest ring, Nature, 461, 1098

Waite, J., Magee, B., Brockwell, T., et al. 2011, Enceladus plume composition, in EPSC-DPS Joint Meeting, Vol. 61

Waite, J. H., Glein, C. R., Perryman, R. S., et al. 2017, Cassini finds molecular hydrogen in the Enceladus plume: evidence for hydrothermal processes, Science, 356, 155

Waite Jr, J. H., Lewis, W., Magee, B., et al. 2009, Liquid water on Enceladus from observations of ammonia and 40 Ar in the plume, Nature, 460, 487

Wiederschein, F., Vöhringer-Martinez, E., Beinsen, A., et al. 2015, Charge separation and isolation in strong water droplet impacts, Physical chemistry chemical physics : PCCP, 17, doi:10.1039/c4cp05618c

Zolotov, M. Y. 2007, An oceanic composition on early and today's Enceladus, Geophysical Research Letters, 34

Zolotov, M. Y., Tobie, G., Postberg, F., et al. 2011, Chemical and phase composition of Enceladus: Insights from Cassini data, EPSC Abstracts, 6

Appendix

Appendix A

Data Tables

A.1 Basic information about the original dataset of the CDA spectra used in this thesis

File	Time Duration (UTC in Year-Day)	Number of spectra	Distance from Saturn Center (R_S)	Impact Speed (km/s)
1	2004-301 to 2004-302	42	6.6 to 10.1	4.5 to 6.5
2	2005-067 to 2005-069	113	3.5 to 10.1	4.9 to 8.4
3	2005-177	49	3.6 to 5.6	6.2 to 8.7
4	2005-267 to 2005-268	90	5.2 to 16.6	6.4 to 9.2
5	2005-302 to 2005-303	139	4.6 to 7.6	4.2 to 7.2
6	2005-330	56	8.3 to 14.5	6.5 to 7.3
7	2005-358 to 2005-369	130	4.6 to 10.6	4.2 to 7.2
8	2006-016 to 2006-018	17	5.6 to 19.1	3.8 to 6.6
9	2006-056 to 2006-057	233	5.6 to 9.9	3.8 to 6.6
10	2006-080 to 2006-081	107	9.5 to 21	5.6 to 6.7
11	2006-337	39	4.9 to 6.8	10 to 12.6
12	2006-349	11	7.9 to 10.5	8.1 to 9.0
13	2007-130	39	4.6 to 4.8	10.3 to 10.3
14	2008-130 to 2008-131	42	4.3 to 4.7	14.2-14.8
15	2008-321	3	4.3 to 4.3	16.2 to 16.2
Total	2004-301 to 2008-321	1110	3.5 to 21.0	3.8 to 16.2

Table A.1: Basic information about the original dataset of the CDA spectra used in this thesis.

A.2 The subtype distribution of the spectra of salt-rich plume particles measured during flybys E17, E18, and E19

E17	**CA: 18:30:09**	
Time (UTC)	Subtype	Alternative
18:27:22	H	
18:28:10	A	H
18:29:22	A	
18:29:27	Type-2/3	
18:30:07	D	E
18:30:29	D	
18:30:31	A	
18:31:39	A	
18:31:58	A	
18:32:00	A	
18:32:02	D	
18:32:38	C	
18:32:43	A	
18:33:03	A	

E18	**CA: 14:01:38**	
Time (UTC)	Subtype	Alternative
13:58:44	A	
13:58:49	A	
13:58:50	A	
13:59:31	A	H
14:00:04	A	
14:00:46	A	
14:01:33	C	
14:03:39	A	

E21	**CA: 15:22:42**	
Time (UTC)	Subtype	Alternative
15:19:49	A	H
15:19:50	L	
15:20:06	H	A
15:21:13	A	
15:21:15	A	
15:21:43	A	
15:21:48	A	Type-2/3
15:22:05	A	
15:22:15	A	H
15:22:29	A	

Table A.2: Sampling time and assigned subtypes of salt-rich spectra from flybys E17, E18 and E21. At the top of each table, the name and closest approach times (CA) of the relevant Enceladus plume flyby are listed. The spectra sampled at the times closest to the CAs are underlined. Some ambiguous spectra may be classified as more than one subtype, so the alternatives are also listed.

Appendix B

CDA spectra

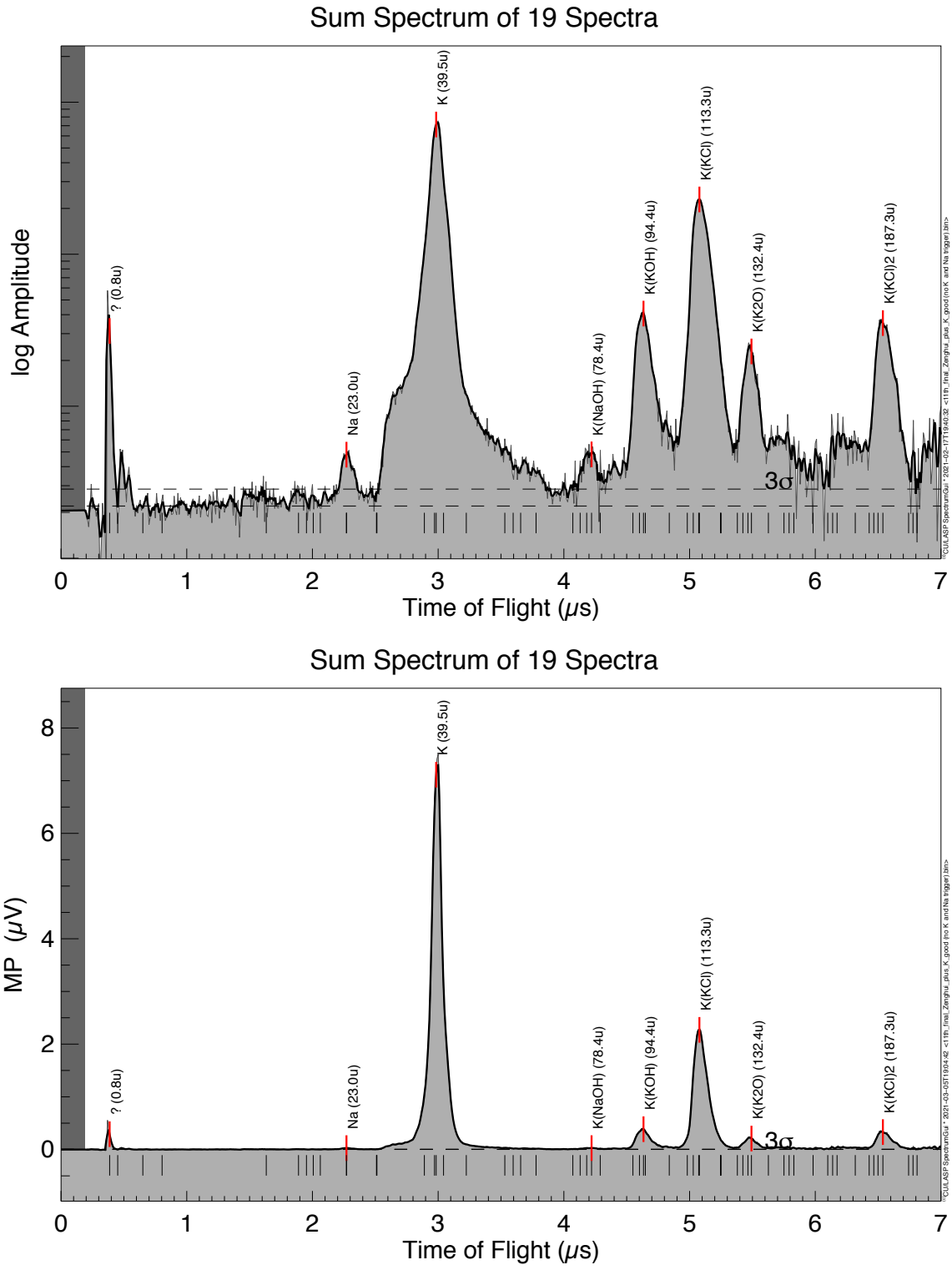

Figure B.1: The co-added subtype K spectrum (upper panel: logarithmic amplitude scale; lower panel: linear amplitude scale).

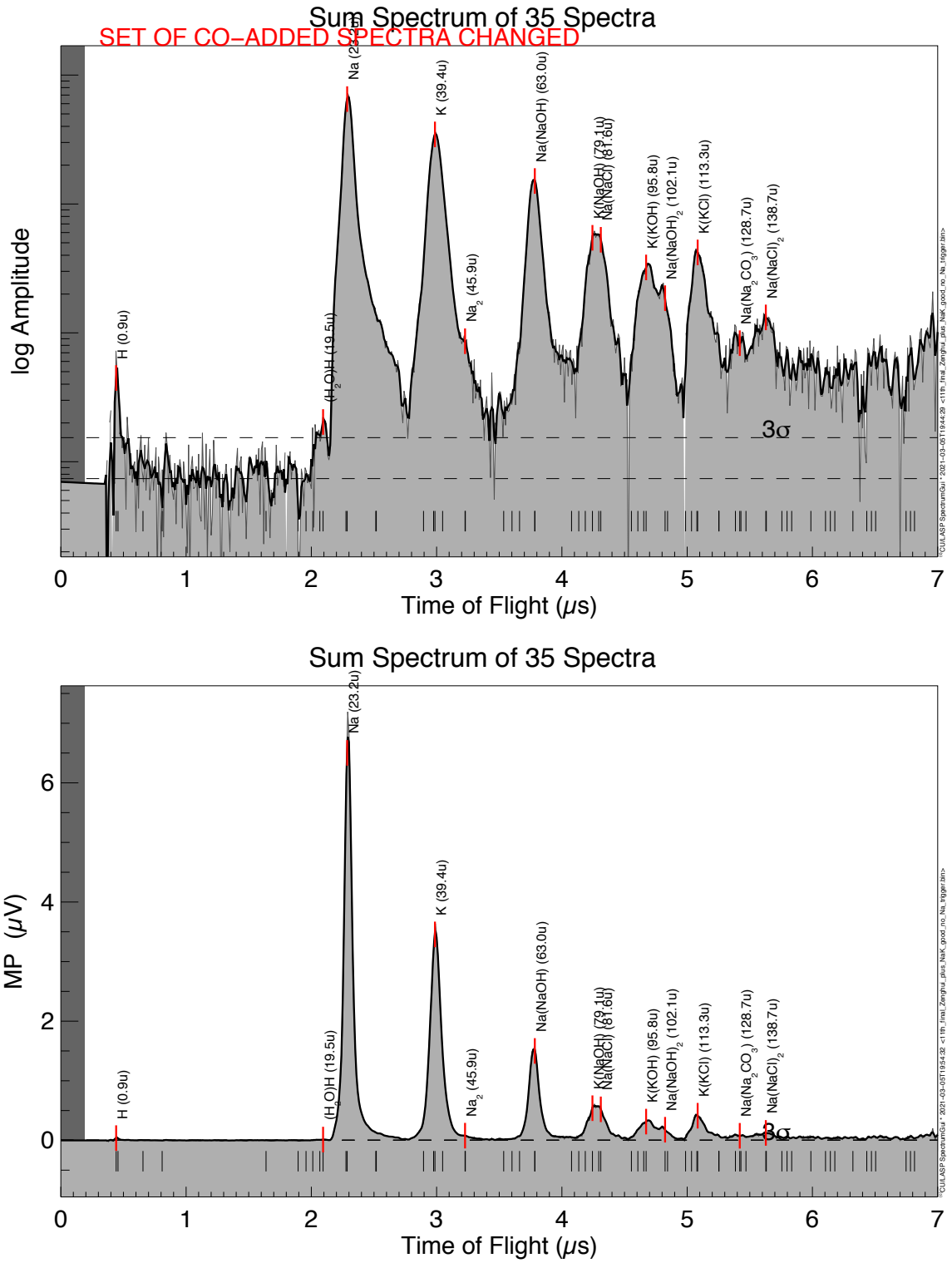

Figure B.2: The co-added subtype NaK spectrum (upper panel: logarithmic amplitude scale; lower panel: linear amplitude scale).

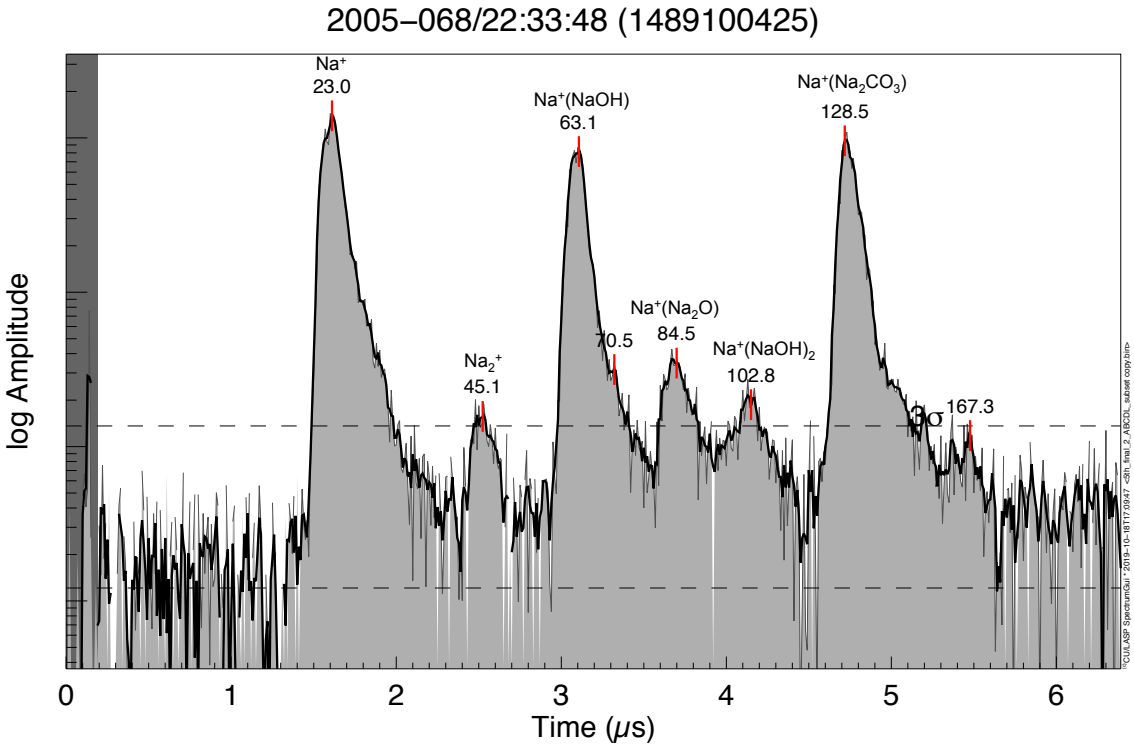

Figure B.3: A subtype A spectrum. Impact speed: 8.3 km/s. Stretch parameter a = 475 ns. Shift parameter b = -0.667 μs.

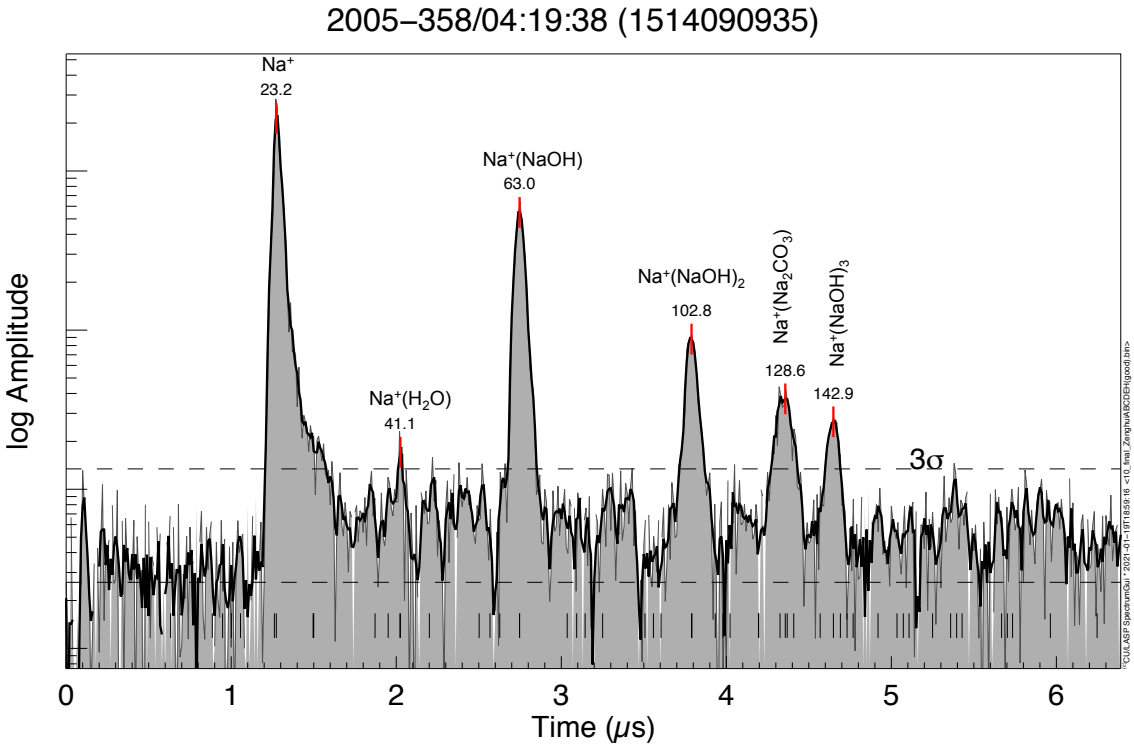

Figure B.4: A subtype B spectrum. Impact speed: 7.1 km/s. Stretch parameter a = 473 ns. Shift parameter b = -1.006 μs.

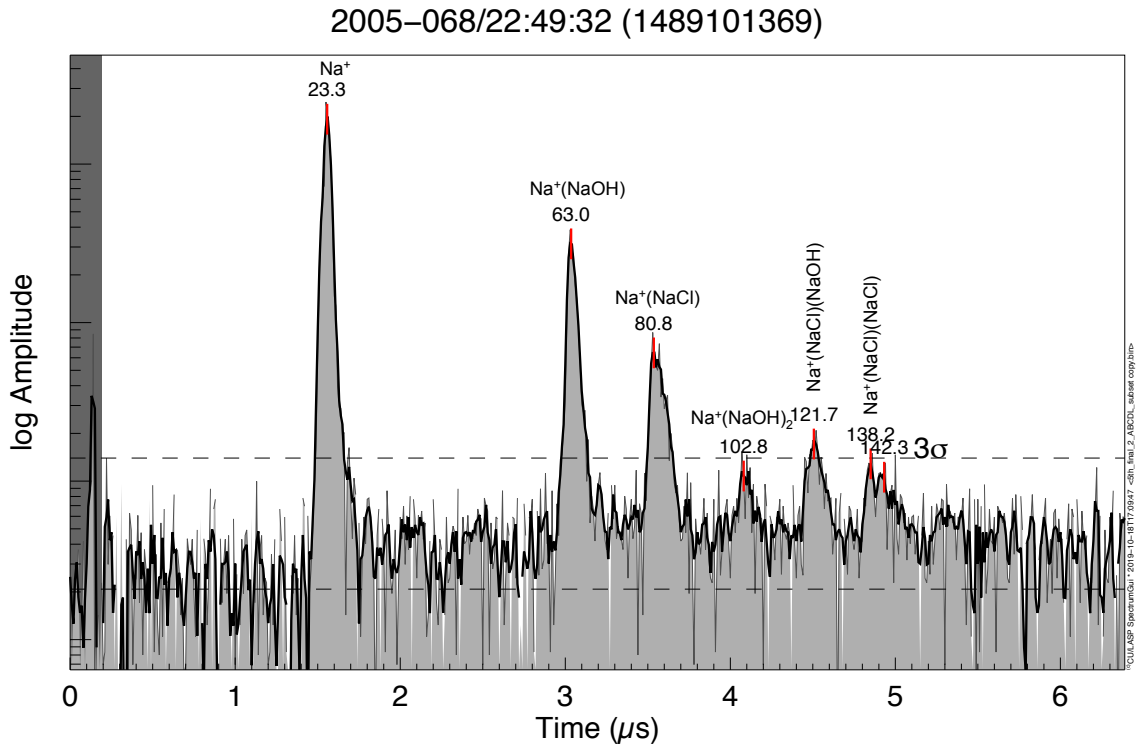

Figure B.5: A subtype C spectrum. Impact speed: 8.2 km/s. Stretch parameter a = 475 ns. Shift parameter b = -0.734 μs.

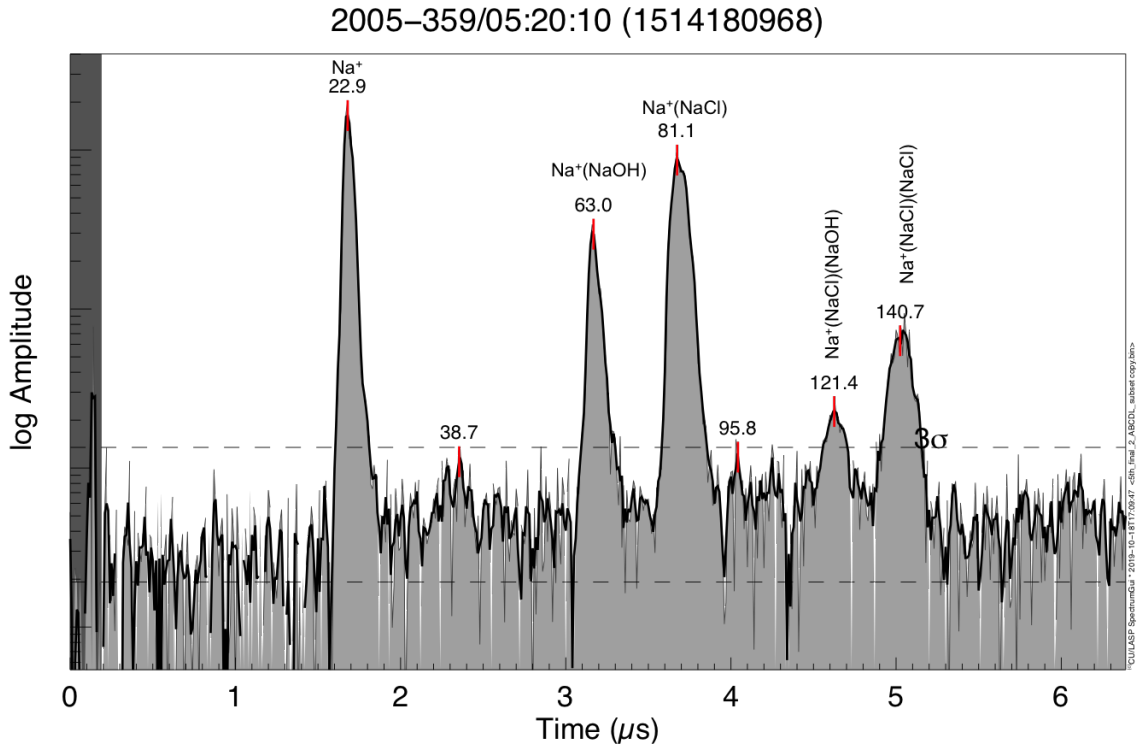

Figure B.6: A subtype D spectrum. Impact speed: 7.0 km/s. Stretch parameter a = 473 ns. Shift parameter b = -0.586 μs.

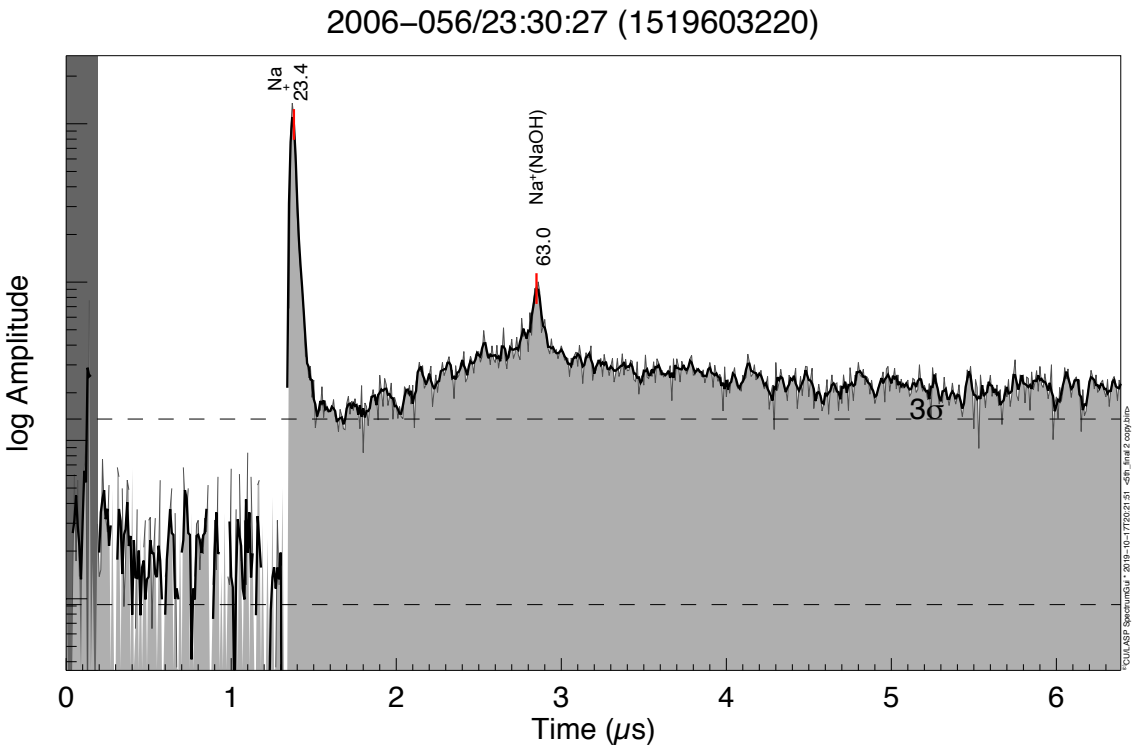

Figure B.7: A subtype L spectrum. Impact speed: 6.5 km/s. Stretch parameter a = 475 ns. Shift parameter b = -0.920 μs.

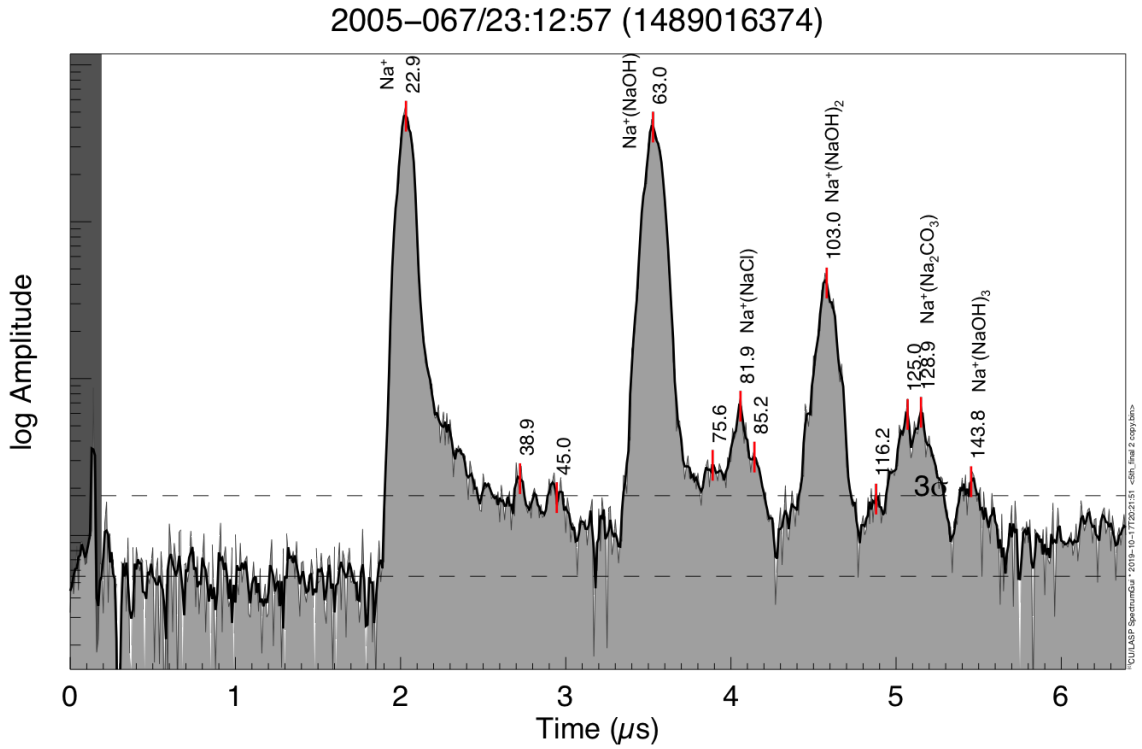

Figure B.8: A subtype H spectrum. Impact speed: 8.1 km/s. Stretch parameter a = 475 ns. Shift parameter b = -0.241 μs.

Appendix C

Determining the 129 u/63 u peak amplitude ratio boundary between Subtypes A and B

The amplitudes of carbonate-related peaks in chloride-poor Type-3 spectra vary considerably. Based on the existence of $Na^+(Na_2CO_3)$ (129 u) and $Na^+(Na_2O)$ (85 u) peaks, the chloride-poor Type-3 spectra are divided into three subgroups: (1) Both $Na^+(Na_2CO_3)$ (129 u) and $Na^+(Na_2O)$ (85 u) peaks are present (detectable); (2) Only the $Na^+(Na_2CO_3)$ (129 u) peak is present; (3) Neither the $Na^+(Na_2CO_3)$ (129 u) or $Na^+(Na_2O)$ (85 u) peaks are present. Ice particles giving rise to spectra in the first subgroup are highly rich in carbonate, and classified into Subtype A, representing highly carbonate-rich, chloride-poor, compositions. Although the third subgroup of spectra do not show a carbonate-related peak, this does not mean their parent grains do not contain carbonate, although they are not as rich in carbonate as Subtype A. The absence of the $Na^+(Na_2CO_3)$ (129 u) peak may be due to the small number of ions generated in their impacts (low QI values), resulting in lower peak amplitudes. They are classified into Subtype B, representing potentially carbonate-poor, chloride-poor, compositions. The second subgroup includes spectra which may be classified into either Subtype A or B depending on the relatively amplitudes of the $Na^+(Na_2CO_3)$ (129 u) and $Na^+(NaOH)$ (63 u) peaks. A threshold must therefore be chosen by which to classify the second subgroup spectra. There are 119 spectra in the first subgroup. The distribution of the ratios of the amplitudes of the $Na^+(Na_2CO_3)$ (129 u) and $Na^+(NaOH)$ (63 u) peaks is shown in Fig. C.1a. There are 119 spectra in the second subgroup. The distribution of peak amplitude ratios ($Na^+(Na_2CO_3)$ (129 u) to $Na^+(NaOH)$ (63 u)) is shown in Fig. C.1b. From the plot it can be seen that most spectra from the first subgroup have a 129 u/63 u

peak amplitude ratio of $>$ 0.2, and most spectra from the second subgroup have a 129 u/63 u peak amplitude ratio of $\leq$ 0.2. Therefore, 0.2 is chosen as the threshold, resulting in the classification of 84 spectra into Subtype B and the remaining 35 spectra into Subtype A.

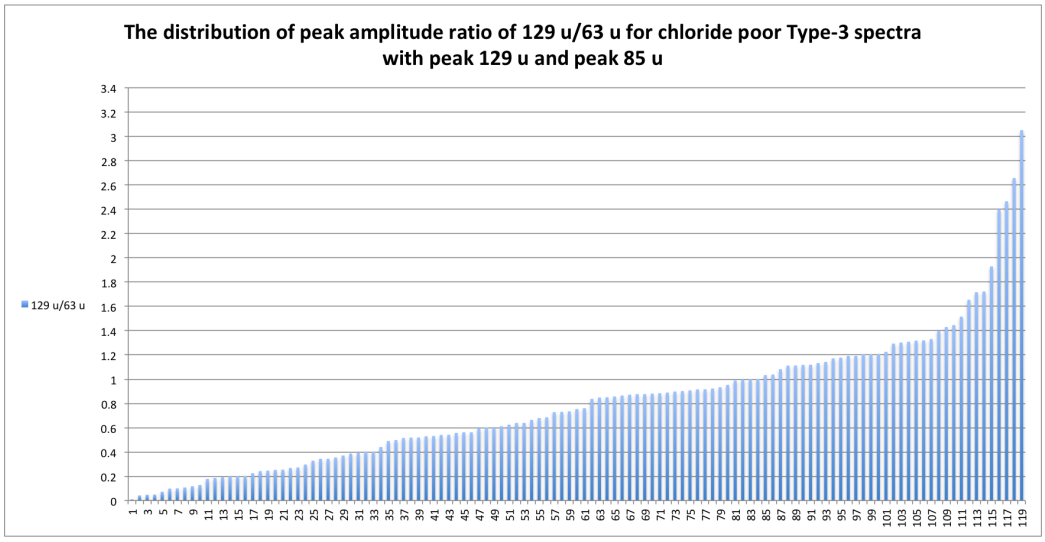

(a) The distribution of the ratios of the amplitudes of the 129 u to 63 u peaks for chloride poor Type-3 spectra (containing peaks at 129 u and 85 u).

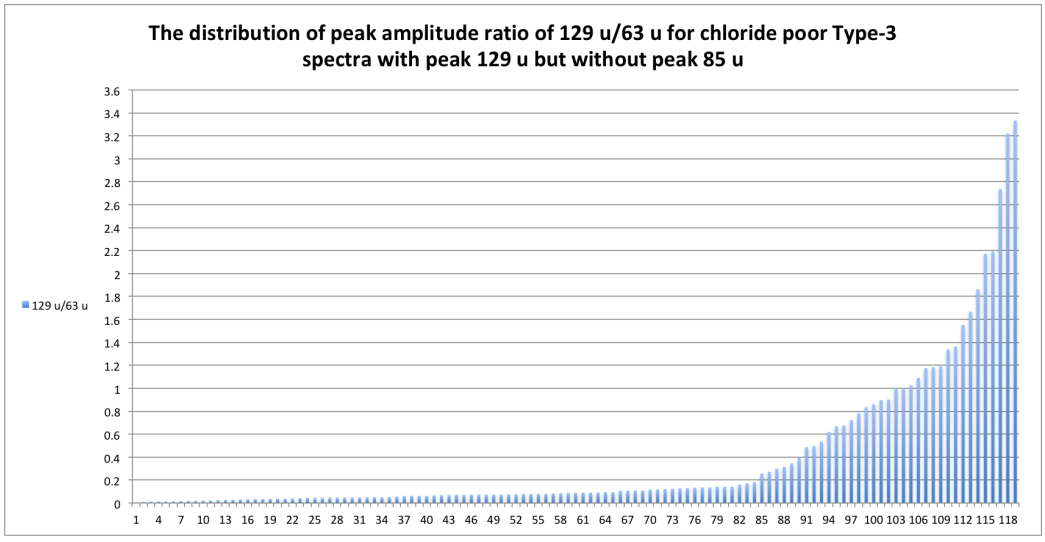

(b) The distribution of the ratios of the amplitudes of the 129 u to 63 u peaks for chloride poor Type-3 spectra (containing the 129 u peak but without the 85 u peak).

Figure C.1: The distribution of the ratios of the amplitudes of the 129 u to 63 u peaks for chloride poor Type-3 spectra containing the 129 u peak.

Appendix D

Laboratory analogue spectra

D.1 About peak at 81 u

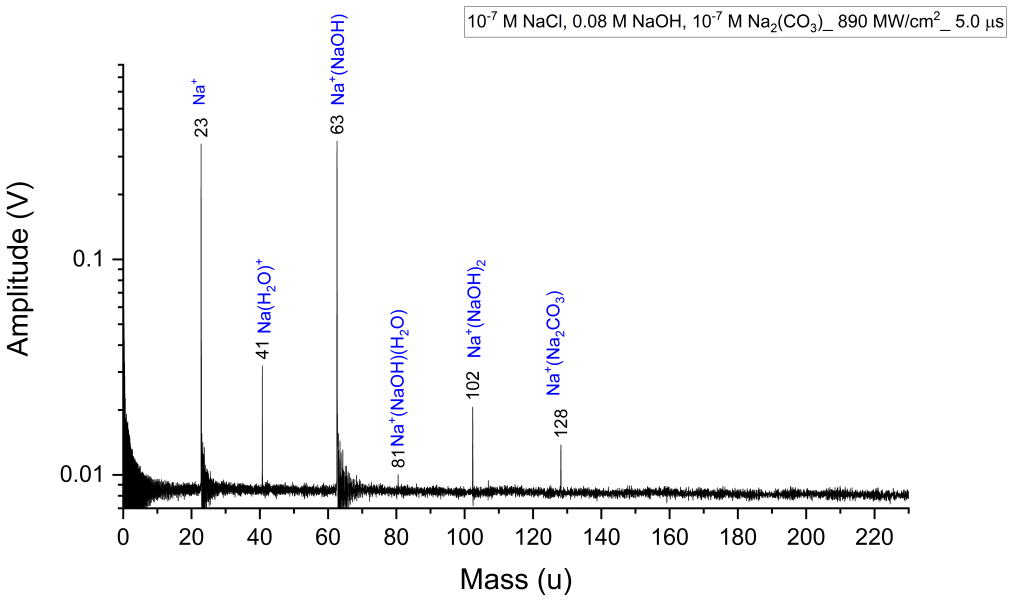

Figure D.1: A chloride poor laboratory spectrum. The Na^+ (23 u) and $Na^+(NaOH)$ (63 u) peaks are similar in amplitude, and the amplitude ratio of $Na^+(NaOH)(H_2O)$ (81 u) to $Na^+(H_2O)$ (41 u) is < 0.1 ($Na^+(NaOH)(H_2O)$ (81 u) ≈ 0.002 V and $Na^+(H_2O)$ (41 u) ≈ 0.024 V, with baseline removed).

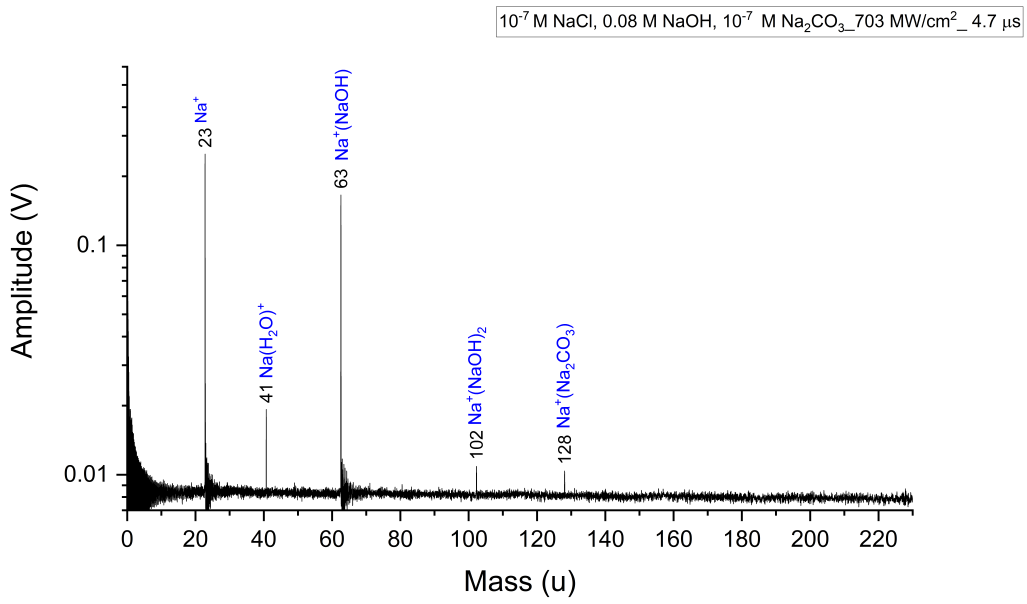

Figure D.2: A chloride poor laboratory spectrum. The amplitude ratio of the $Na^+(NaOH)$ (63 u) to Na^+ (23 u) peaks is ≈ 0.6 (Na^+ (63 u) amplitude ≈ 0.152 V and peak Na^+ (23 u) amplitude ≈ 0.242 V, with baseline removed), the peak at 81 u is below 3 σ.

D.2 A spectrum of solution of 0.1 M NaCl and 0.01 M NaOH

Fig. D.3 shows an example LILBID spectrum of a solution of 0.1 M NaCl and 0.01 M NaOH, obtained using a laser power density of $\approx 721 MW/cm^2$ and a delay time $\tau = 5.1\ \mu s$. Most water cluster peaks, such as $(H_3O)^+(H_2O)_n$ (n = 1, 2, 3...) and $Na^+(H_2O)_n$ (n = 3, 4, 5...), are not detected. The $Na^+(H_2O)$ (41 u) peak is also observed in Type-3 CDA spectra. The $Na^+(H_2O)_n$ (59 u) peak is tiny ($\sim 20\ \sigma$) compared to the highest peaks. A tiny $Na^+(H_2O)_n$ (77 u) peak is also sometimes observed. Considering the LILBID technique is extremely water-rich compared to the CDA impact ionization environment, this spectrum is acceptable.

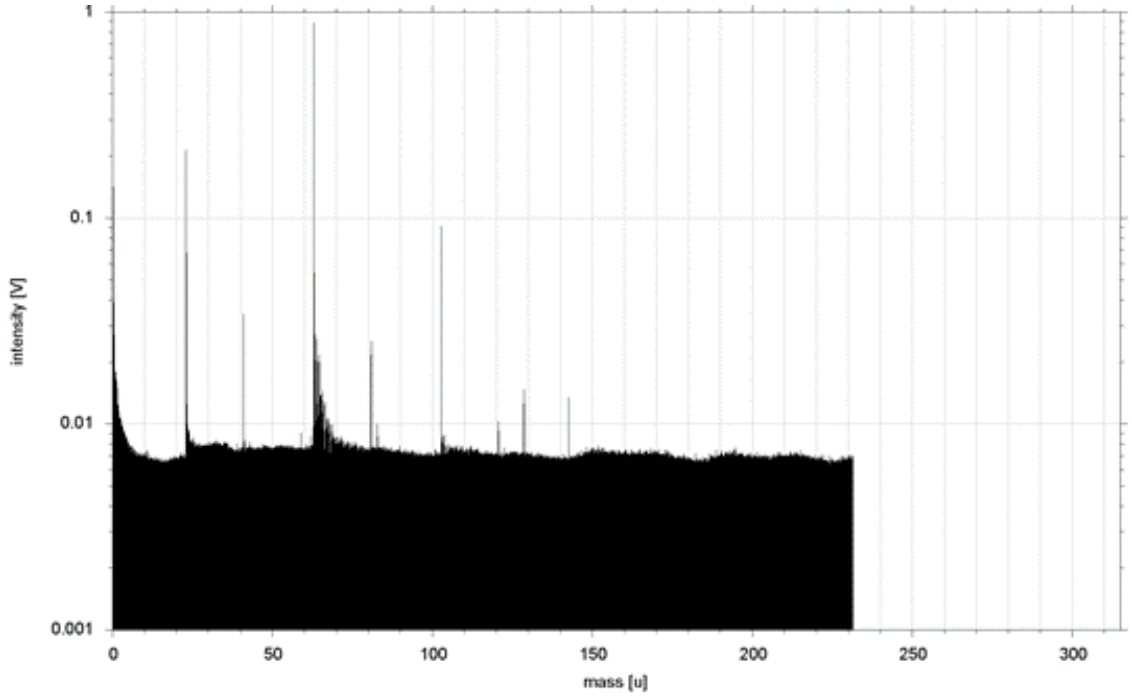

Figure D.3: A LILBID spectrum of a solution of 0.1 M NaCl and 0.01 M NaOH obtained using a power density of $\approx 721 \mathrm{MW/cm^2}$ and a delay time $\tau = 5.1\ \mu s$. Most water cluster peaks, such as $(H_3O)^+(H_2O)_n$ (n = 1, 2, 3...) and $Na^+(H_2O)_n$ (n = 3, 4, 5...), are not detected.

Appendix E

The distribution of Type-3 spectral subtypes with high certainty

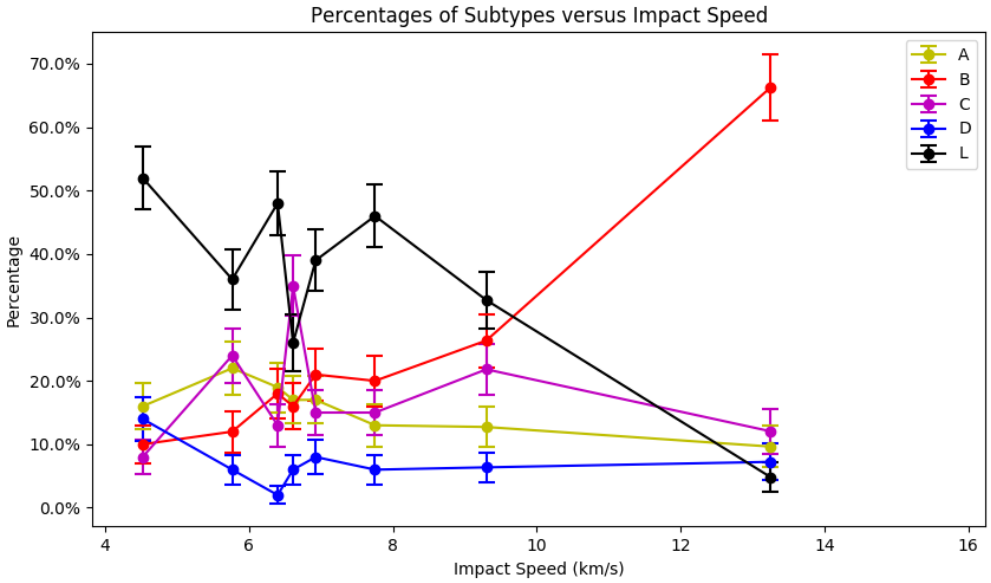

Bin	1	2	3	4	5	6	7	8	Sum
Bin Size	100	100	100	100	100	100	110	83	793
Speed (km/s)	3.8 - 5.2	5.3 - 6.3	6.3 - 6.5	6.5 - 6.7	6.7 - 7.2	7.2 - 8.3	8.3 - 10.3	10.3 - 16.2	3.8 - 16.2

Figure E.1: Speed distribution of major subtypes of spectra, excluding bad quality spectra. The data is divided into 8 bins according to their impact speeds. The horizontal axis indicates the impact speeds of the spectra. The percentage axis (vertical axis) indicates the percentages of subtypes in each bin. The error bars indicate the standard errors of the proportion of sample for each bin. The table below shows the number and the impact speed range of the spectra in each bin and the total spectra (Sum).

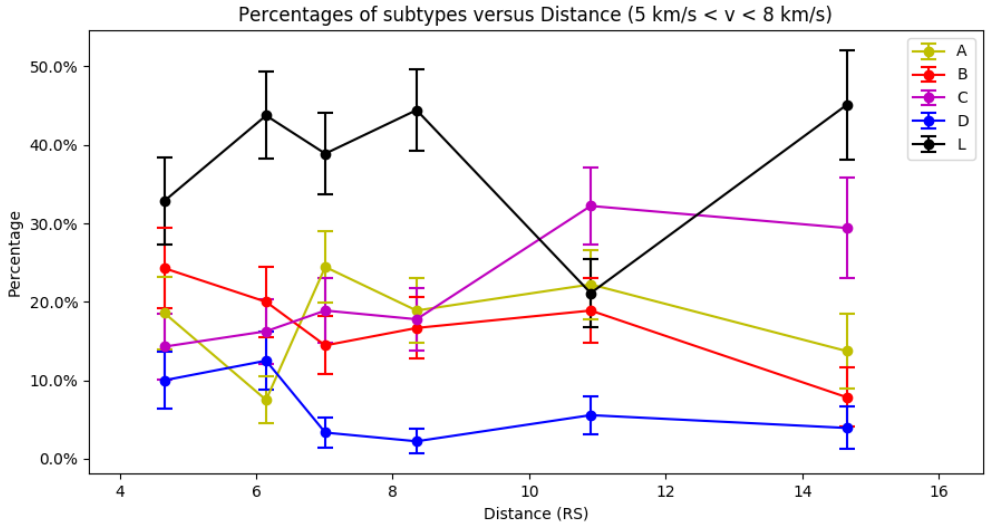

Bin	1	2	3	4	5	6	Sum
Bin Size	70	80	90	90	90	52	472
Distance (R_S)	3.6 - 5.8	5.8 - 6.5	6.5 - 7.5	7.5 - 9.2	9.2 - 12.6	12.7 - 16.6	3.6 - 16.6

Figure E.2: Distance distribution (between 5 km/s and 8 km/s) of major subtypes excluding bad quality spectra. Only spectra due to impacts at speeds between 5 - 8 km/s were considered. The data is divided into 6 bins according to the distances of the particles to the Saturn center. The horizontal axis of the plot indicates the distance of the ice grains to the Saturn center in R_S. The percentage axis (vertical axis) of the plot indicates the percentage of each bin. The error bars indicate the standard error of the proportion of sample for each bin. The table below shows that the spectra number (Bin Size) and the distance range of each bin and the total spectra (Sum).

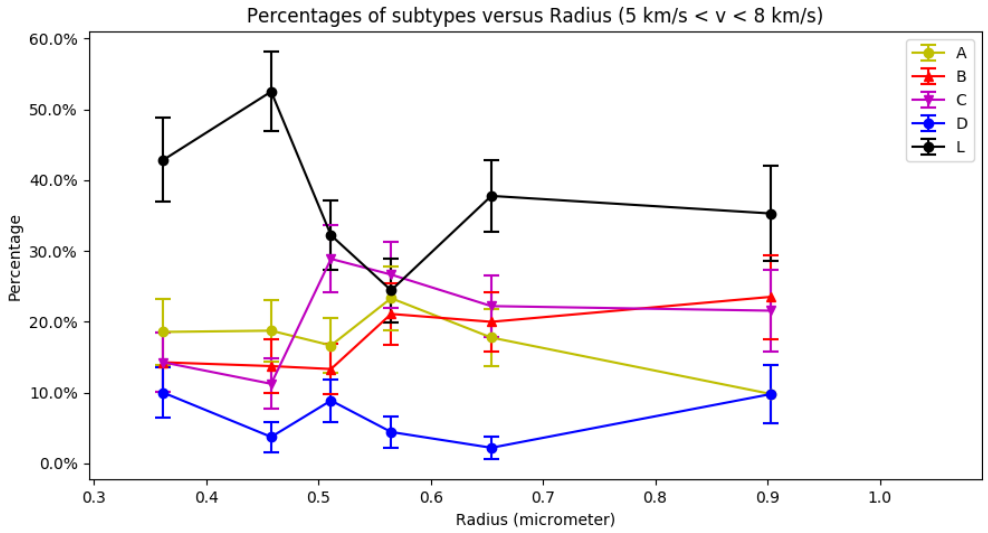

Bin	1	2	3	4	5	6	Sum
Spectra number	70	80	90	90	90	52	472
Radius (μm)	0.3 - 0.4	0.4 - 0.5	0.5 - 0.5	0.5 - 0.6	0.6 - 0.7	0.7 - 1.1	0.3 - 1.1

Figure E.3: The relative abundances of all major spectra subtypes, excluding poor quality spectra, as a function of their derived particle size. Only particles with impact speeds between 5 km/s and 8 km/s are used. The data is divided into 6 data bins according to the particle radius. The horizontal axis of the plot indicates the particle radius in μm. The percentage axis (vertical axis) of the plot indicates the percentage of each bin. The error bars indicate the standard error of the proportion of sample for each bin. The table below shows the number and the range of the particle radius of the spectra in each bin and the total spectra (Sum).

Appendix F

Analyzing the 129 u/63 u peak amplitude ratios in CDA Subtypes A and B spectra separately.

Figs. F.1 and F.2 show the 129 u/63 u peak ratio distributions as functions of saturnian distance for Subtype A and Subtype B spectra, respectively.

The ratio of the amplitudes of peaks 129u to 63u for Subtype A spectra decreases with Saturnian distance (age), particular rapidly at first. In contrast, this ratio for subtype B spectra increases with distance (age). Both trends are, however, potentially not significant, given the large error bars.

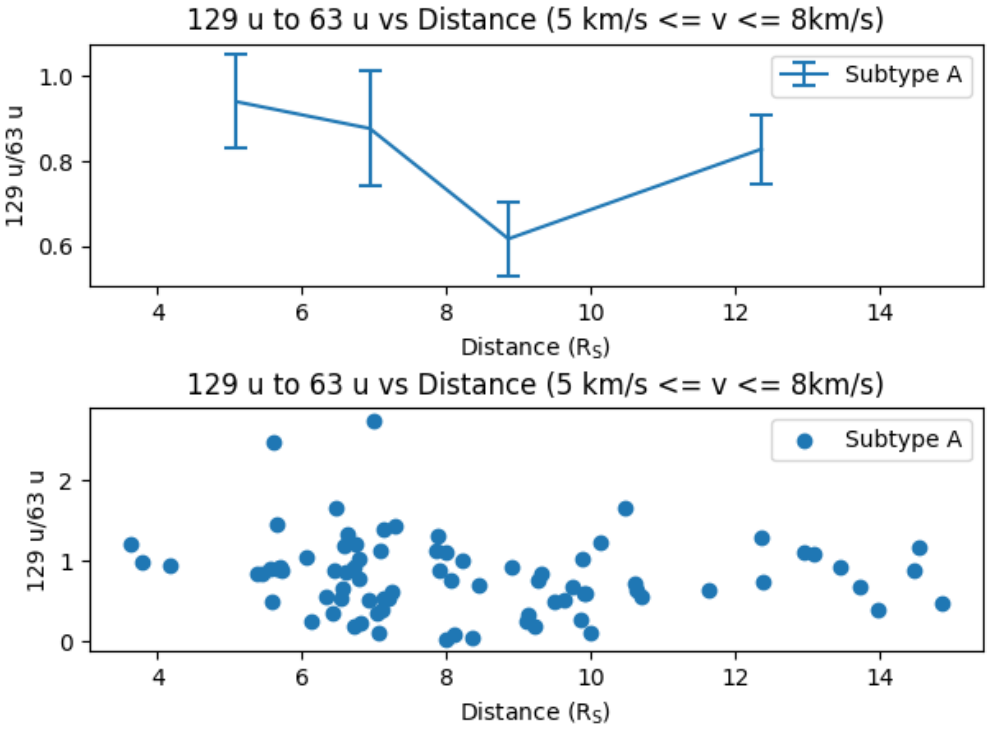

Bin	1	2	3	4	Sum
Bin Size	20	20	20	20	80
Distance (R_S)	3.6 - 6.6	6.6 - 7.3	7.9 - 9.8	9.9 - 14.8	3.6 - 14.8

Figure F.1: The 129 u/63 u peak amplitude ratios of the Subtype A (ultra carbonate-rich and chloride-poor) spectra as a function of Saturnian distance. Only spectra with impact speeds between 5 km/s and 8 km/s are used. The data is divided into 4 data bins according to the distances of the particles to the Saturn center. The upper panel of the figure shows the average values of the peak amplitude ratios in each data bin, with the error bars showing the standard error of the mean of the peak amplitude ratio of sample for each bin. The lower panel of the figure shows the peak amplitude ratios for individual spectra. The table below shows the number and the distance range of the spectra in each bin and the total spectra (Sum).

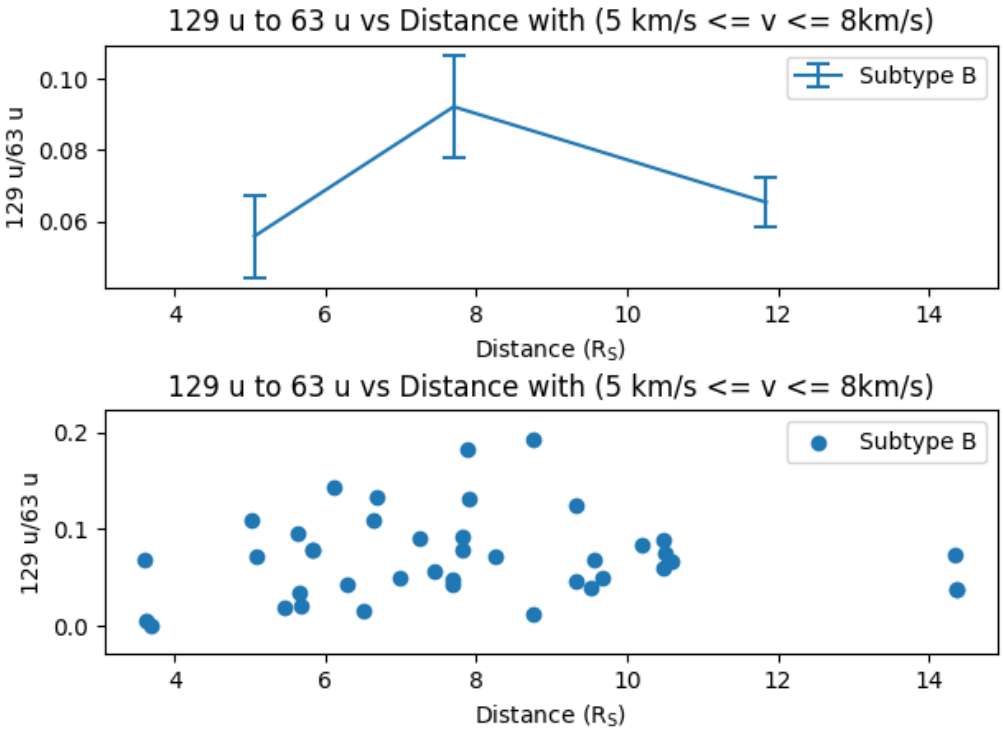

Bin	1	2	3	Sum
Bin Size	14	14	13	41
Distance (R_S)	3.6 - 6.5	6.6 - 8.8	9.3 - 14.4	3.6 - 14.4

Figure F.2: The 129 u/63 u peak amplitude ratios of Subtype B spectra with a significant peak $Na^+(Na_2CO_3)$ (129 u) as a function of Saturnian distance. Only spectra with impact speeds between 5 km/s and 8 km/s are used. The data is divided into 3 data bins according to the distances of the particles to the Saturn center. The upper panel of the figure shows the average values of the peak amplitude ratios in each data bin, , with the error bars showing the standard error of the mean of the peak amplitude ratio of sample for each bin. The lower panel of the figure shows the peak amplitude ratios for individual spectra. The table below shows the number and the distance range of the spectra in each bin and the total spectra (Sum).

APPENDIX F. ANALYZING THE 129 U/63 U PEAK AMPLITUDE RATIOS IN CDA SUBTYPES A AND B SPECTRA SEPARATELY.

Appendix G

Upper limits

G.1 Mimicked Subtype A spectrum and Subtype B spectrum

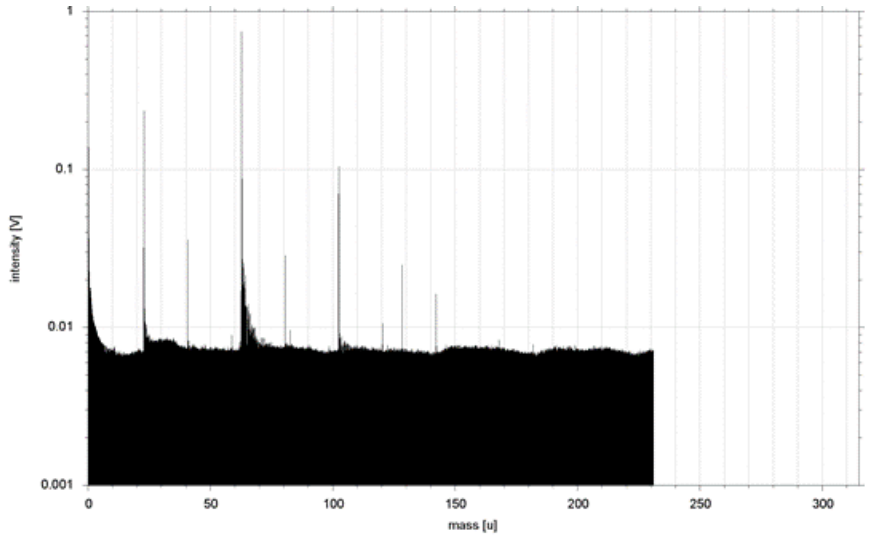

(a) A LILBID spectrum of a solution of 0.1 M NaOH, 0.0001 M Na_2CO_3 and 0.01 M NaCl obtained using a laser power density of $\approx 721 MW/cm^2$ and a delay time $\tau = 5.0\ \mu s$. This spectrum is a mimicked Subtype B spectrum. The $Na^+(Na^{37}Cl)$ (83 u) peak has an amplitude $>9\sigma$ from this concentration.

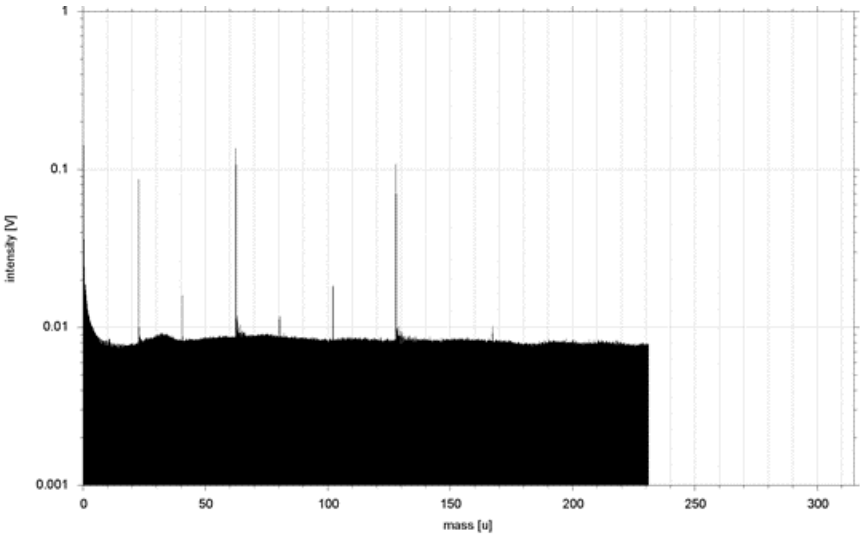

(b) A LILBID spectrum of a solution of 0.05 M Na_2CO_3 and 0.005 M NaCl obtained using a laser power density of $\approx 721 MW/cm^2$ and a delay time $\tau = 5.2\ \mu s$. This spectrum is a mimicked Subtype A spectrum. The $Na^+(Na^{37}Cl)$ (83 u) peak has an amplitude $>9\sigma$ from this concentration.

Figure G.1: The upper limit of NaCl in Subtype A and Subtype B spectra.

G.2 Criteria for spectra calibration for CDA detection limits

A 10^{-6} M NaCl solution was used for calibration. The laser flash lamp energy was fixed at 5.40 J. The spectra have to meet following criteria:

1. Low delay time (4.2 - 4.6 μs):

   The laser intensity is set to 100 %. The 19 u peak should have a higher amplitude than that at 37 u, and the 55 u peak is not observable.

2. Intermediate delay time (5.3 - 5.7 μs):

   The laser intensity is set to between 97 - 96 %. The peaks at 37 u or 55 u have highest amplitude, peak at 91 u or 109 u is the highest-mass water cluster and peak at 127 u is not observable anymore.

3. High delay time (6.6 - 7.0 μs):

   The laser intensity is set to between 94 - 92 %. The peaks at 73 u, 91 u and 109 u have the highest amplitudes and water cluster peaks are observable up to at least 217 u.

G.3 The reactions for compounds of interest

1. Phosphite

   Na_2HPO_3 was added into Mix 1 and Mix 2 solutions to measure the detection limits of phosphite, and the H^+ in the Na_2HPO_3 can react with the OH^- in both Mix 1 and Mix 2:

   $$HPO_3{}^{2-} + OH^- \longrightarrow PO_3{}^{3--} + H_2O \tag{G.1}$$

   As a result, the pH of the solutions decreases.

2. Ammonium NH_4Cl was added into Mix 1 and Mix 2 solutions to measure the detection limits of ammonium, and the NH_4^+ can react with the OH^- in both Mix 1 and Mix 2:

   $$NH_4{}^+ + OH^- \rightleftharpoons NH_3 + H_2O \tag{G.2}$$

   As a result, the pH of the solutions decreases.

3. Calcium

   $CaCl_2$ was added into Mix 1 and Mix 2 solutions to measure the detection limits of calcium ions. Ca^{2-} may react with OH^- in both Mix 1 and Mix 2 to produce slightly soluble $Ca(OH)_2$.

$$Ca^{2+} + 2OH^- \longrightarrow Ca(OH)_2 \tag{G.3}$$

   In Mix 1 Ca^{2+} reacts with CO_3^{2-} to form insoluble $CaCO_3$.

$$Ca^{2+} + {CO_3}^{2-} \longrightarrow CaCO_3\downarrow \tag{G.4}$$

   The ionization equilibrium of carbonate ions then moves to the left:

$$H_2O + {CO_3}^{2-} \rightleftharpoons {HCO_3}^- + HO^- \tag{G.5}$$

   As a result, the pH of the solutions decreases slightly. If too much $CaCl_2$ is added to solutions, especially Mix 1, precipitation may occur.

4. Magnesium

   $MgCl_2$ was added into Mix 1 and Mix 2 solutions to measure the detection limits of calcium ions. The $MgCl_2$ may react with the OH^- in both Mix 1 and Mix 2 to produce insoluble $Mg(OH)_2$.

$$Mg^{2+} + 2OH^- \longrightarrow Mg(OH)_2\downarrow \tag{G.6}$$

   In Mix 1 Mg^{2+} reacts with CO_3^{2-} to form insoluble $MgCO_3$.

$$Mg^{2+} + 2{CO_3}^{2-} \longrightarrow MgCO_3\downarrow \tag{G.7}$$

   As a result, the pH of the solutions decreases slightly. If too much $MgCl_2$ is added to solutions, especially Mix 1, precipitation may occur.

5. Ferrous iron

   $FeCl_2$ was added into Mix 1 and Mix 2 solutions to measure the detection limits of calcium ions. $FeCl_2$ may react with OH^- in both Mix 1 and Mix 2 to produce insoluble $Fe(OH)_2$.

$$Fe^{2+} + 2OH^- \longrightarrow Fe(OH)_2 \downarrow \tag{G.8}$$

In Mix 1 Fe^{2+} reacts with CO_3^{2-} to form insoluble $FeCO_3$.

$$Fe^{2+} + {CO_3}^{2-} \longrightarrow FeCO_3 \downarrow \tag{G.9}$$

As a result, the pH of the solutions decreases slightly. If too much $FeCl_2$ is added to solutions, especially Mix 1, precipitation may occur.

It is possible for Fe^{2-} to be oxidized by O_2 in air to produce Fe^{3-}, so $FeCl_2$ containing solutions were prepared to be as fresh as possible during the measurements.

6. Formic acid

As an organic acid, HCOOH consumes OH^- in both Mix 1 and Mix 2.

$$HCOOH \rightleftharpoons HCOO^- + H^+ \tag{G.10}$$
$$H^+ + OH^- \longrightarrow H_2O \tag{G.11}$$

As a result, the pH of the solutions decreases.

G.4 Spectra of pure Mix 1 solution and saturated solution of $MgCl_2$ in Mix 1 at setting 1

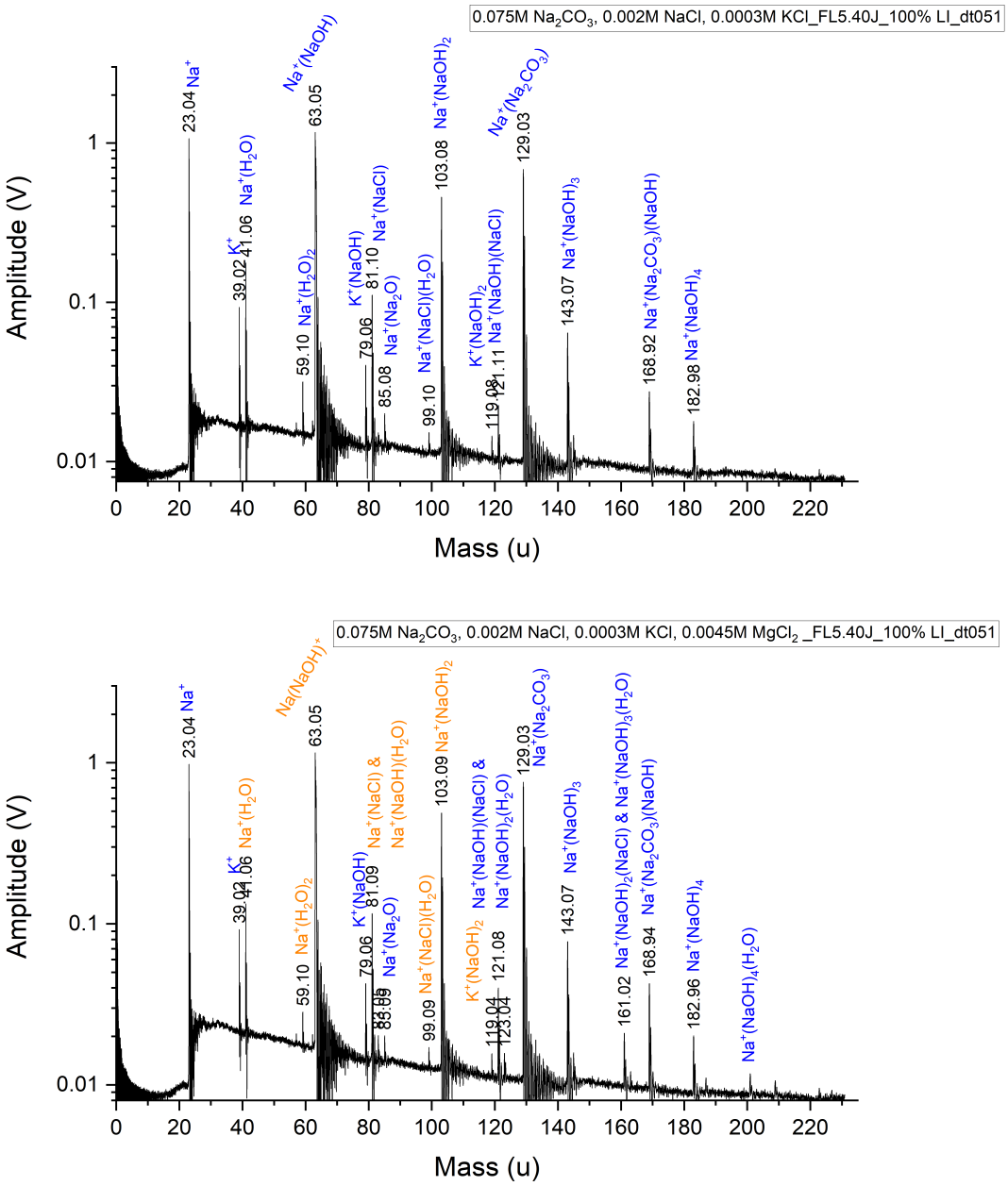

Figure G.2: **Upper panel:** A spectrum of pure Mix 1 solution obtained using setting 1; **Lower panel:** A spectrum of a 'saturated' (0.0045 M) solution of $MgCl_2$ in Mix 1 at setting 1. Some potentially magnesium-related peaks have the same masses as background salt peaks (marked in orange in the lower panel.).

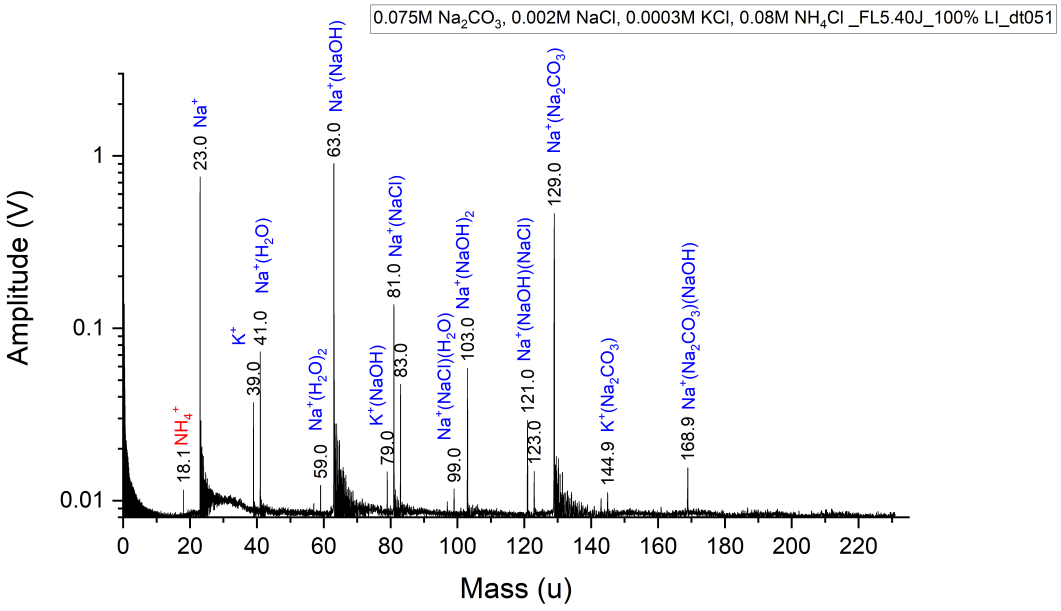

(a)

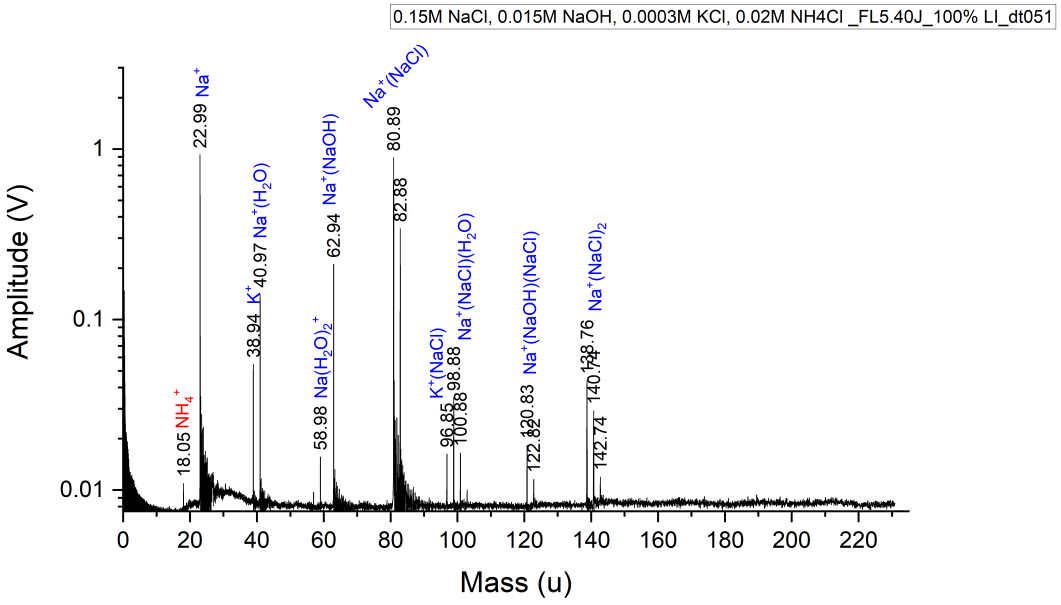

(b)

Figure G.3: (a) An analogue spectrum of Mix 1 with 0.08 M NH_4^+ ions at setting 1 (Table 7.1). (b) An analogue spectrum of Mix 2 with 0.02 M NH_4^+ ions at setting 1 (Table 7.1). (The chloride related peaks, such as Na^+NaCl (81 u and 83 u) in the spectra of Mix 1 (subfigure (a)) are attributed to chloride in NH_4Cl.)

Appendix H

Approximate detection limit predictions using Method 1

Substance	The detection limits evaluated via Method 1					
	Mix 1			Mix 2		
	Setting 1	Setting 2	Setting 3	Setting 1	Setting 2	Setting 3
Anion						
Carbonate (CO_3^{2-})	N.A.	N.A.	N.A.	$4.0^{+7.5}_{-4.0} \times 10^{-2}$ (pH $\approx$ 12.1)	$4.0^{+7.5}_{-4.0} \times 10^{-2}$ (pH $\approx$ 12.1)	$4.0^{+7.5}_{-4.0} \times 10^{-2}$ (pH $\approx$ 12.1)
Chloride (Cl^-)	10($\pm$3) (pH $\approx$ 11.5)	10($\pm$3) (pH $\approx$ 11.5)	10($\pm$3) (pH $\approx$ 11.5)	N.A.	N.A.	N.A.
Sulfate (SO_4^{2-})	$5.0(\pm3.3)\times10^{-2}$ (pH $\approx$ 11.3)	$5.0(\pm3.3)\times10^{-2}$ (pH $\approx$ 11.3)	$5.0(\pm3.3)\times10^{-2}$ (pH $\approx$ 11.3)	$2.0(\pm0.5)\times10^{-2}$ (pH $\approx$ 12.1)	$2.0(\pm0.5)\times10^{-2}$ (pH $\approx$ 12.1)	$2.0(\pm0.5)\times10^{-2}$ (pH $\approx$ 12.1)
Phosphate (PO_4^{3-} and HPO_4^{2-})	0.10($\pm$0.06) (pH $\approx$ 11.4)	0.10($\pm$0.06) (pH $\approx$ 11.4)	0.10($\pm$0.06) (pH $\approx$ 11.4)	$3.0(\pm2.7)\times10^{-3}$ (pH $\approx$ 12.0)	$2.0(\pm1.8)\times10^{-3}$ (pH $\approx$ 12.0)	$2.0(\pm1.8)\times10^{-3}$ (pH $\approx$ 12.0)
Phosphite (PO_3^{3-} and HPO_3^{2-})	0.10($\pm$0.03) (pH $\approx$ 11.3)	$5.0(\pm1.9)\times10^{-2}$ (pH $\approx$)	$5.0(\pm1.9)\times10^{-2}$ (pH $\approx$)	$1.0(\pm0.6)\times10^{-2}$ (pH $\approx$ 12.1)	$2.0(\pm1.2)\times10^{-3}$ (pH $\approx$)	$2.0(\pm1.2)\times10^{-3}$ (pH $\approx$)
Nitrate (NO_3^-)	2.5($\pm$1.3) (pH $\approx$ 11.3)	1.0($\pm$0.5) (pH $\approx$ 11.4)	1.0($\pm$0.5) (pH $\approx$ 11.4)	0.30($\pm$0.14) (pH $\approx$ 12.1)	0.30($\pm$0.14) (pH $\approx$ 12.1)	0.30($\pm$0.14) (pH $\approx$ 12.1)
Fluoride (F^-) [a]	20($\pm$3) (pH $\approx$)	20($\pm$3) (pH $\approx$)	20($\pm$3) (pH $\approx$)	3	3	3
Bromide (Br^-)	10($\pm$4) (pH $\approx$)	10($\pm$4) (pH $\approx$)	10($\pm$4) (pH $\approx$)	2.5($\pm$1.4) (pH $\approx$)	2.5($\pm$1.4) (pH $\approx$)	2.5($\pm$1.4) (pH $\approx$)
Sulfide (S^{2-})	N.A.	N.A.	N.A.	2.0($\pm$1.0) (pH $\approx$)	2.0($\pm$1.0) (pH $\approx$)	2.0($\pm$1.0) (pH $\approx$)
Cation						
Lithium (Li^+)	0.80($\pm$0.39) (pH $\approx$ 11.3)	0.80($\pm$0.39) (pH $\approx$ 11.3)	1.5($\pm$0.6) (pH $\approx$ 11.4)	0.50($\pm$0.24) (pH $\approx$ 12.1)	0.50($\pm$0.24) (pH $\approx$ 12.1)	0.50($\pm$0.24) (pH $\approx$ 12.1)
Ammonium (NH_4^+)	70($\pm$17) (pH $\approx$ 11.1)	70($\pm$17) (pH $\approx$ 11.1)	70($\pm$17) (pH $\approx$ 11.1)	18($\pm$6) (pH $\approx$ 10.0)	18($\pm$6) (pH $\approx$ 10.0)	18($\pm$6) (pH $\approx$ 10.0)
Calcium (Ca^{2+})	0.80($\pm$0.27) (pH $\approx$ 11.3)	0.80($\pm$0.27) (pH $\approx$ 11.3)	0.80($\pm$0.27) (pH $\approx$ 11.3)	2.0($\pm$0.2) (pH $\approx$ 12.1)	2.0($\pm$0.2) (pH $\approx$ 12.1)	5.0($\pm$0.3) (pH $\approx$ 12.1)
Ferrous (Fe^{2+})	$0.20^{+0.24}_{-0.20}$ (pH $\approx$ 11.2)	$0.20^{+0.24}_{-0.20}$ (pH $\approx$ 11.2)	$0.20^{+0.24}_{-0.20}$ (pH $\approx$ 11.2)	0.32($\pm$0.24) (pH $\approx$ 12.1)	0.32($\pm$0.24) (pH $\approx$ 12.1)	0.32($\pm$0.24) (pH $\approx$ 12.1)
Magnesium (Mg^{2+})	5.1($\pm$0.4) (pH $\approx$ 11.0)	5.1($\pm$0.4) (pH $\approx$ 11.0)	5.1($\pm$0.4) (pH $\approx$ 11.0)	2.2($\pm$0.1) (pH $\approx$ 11.9)	2.2($\pm$0.1) (pH $\approx$ 11.9)	2.2($\pm$0.1) (pH $\approx$ 11.9)
Mineral						
Silica (SiO_2)	0.18($\pm$0.07) (pH $\approx$ 11.4)	0.47($\pm$0.16) (pH $\approx$ 11.3)	0.36($\pm$0.12) (pH $\approx$ 11.4)	$0.17_0.17^0.50$ (pH $\approx$ 12.1)	$0.33_0.33^0.50$ (pH $\approx$ 12.1)	0.67($\pm$0.50) (pH $\approx$ 12.1)
Organic						
Formic Acid (HCOOH)	11($\pm$4) (pH $\approx$ 10.9)	11($\pm$4) (pH $\approx$ 10.9)	8.1($\pm$3) (pH $\approx$ 10.9)	5.3($\pm$2.2) (pH $\approx$ 12.0)	5.3($\pm$2.2) (pH $\approx$ 12.0)	2.7($\pm$1.2) (pH $\approx$ 12.0)
Formaldehyde (HCHO)	$1.3 \pm (0.1) \times 10^3$ (pH $\approx$ 10.8)	$4.5(0.8) \times 10^2$ (pH $\approx$ 11.0)	$4.5(0.8) \times 10^2$ (pH $\approx$ 11.0)	$6.7 \pm (1.2) \times 10^2$ (pH $\approx$ 11.3)	$3.4 \pm (0.8) \times 10^2$ (pH $\approx$ 11.6)	$2.2 \pm (0.8) \times 10^2$ (pH $\approx$ 11.7)

Table H.1: (Caption next page.)

Table H.1: (Previous page) The detection limits as evaluated using Method 1: the concentration corresponding to substance 3σ detection peak amplitudes in CDA spectra (equivalent to $9-15\sigma_{lab}$ peak amplitudes in LIBID spectra) for different compounds of interest and settings. Underlined data indicate solubility limits of certain substances, when the relevant peak cannot be detected even if the compounds are saturated in Mix 1 and/or 2 solutions. In this case, the detection limits cannot be determined via LILBID and the solubility limits are instead used as their CDA detection limits. [a]As all fluoride related peaks are too close to background salt peaks, the amplitude of the elevated flank at mass 65 u is used.

Appendix I

Approximate detection limit predictions using Method 2

Detection limit predictions for compounds in Mix 1 and Mix 2, using the Na^+ (23 u) and Na^+(NaOH) (63 u) peaks as references, are shown in the upper and lower panels respectively, of the following figures. The left panels show the linear TLS fits and the predicted detection limits. The blue crosses indicate the measured data (peak amplitude ratios and concentrations) with error bars; the black solid lines indicate the fitted lines; and the red dots indicate the predicted detection limits. The pink areas are the 99.7% confidence regions of the predicted concentration and peak amplitude ratio, calculated based on the 99.7% confidence regions of the fit parameters (slope and intercept) shown in the right subpanels. If a calculated confidence region (pink area) includes negative concentrations, the negative concentration part is truncated, since it is not physically realistic. The maximum and minimum values of the detection limit with 99.7% confidence ranges given in the left subpanels corresponds to the points with maximum concentration and minimum concentration in the 99.7% confidence regions of the predicted concentration and peak amplitude ratio, respectively. The right subpanels show the 99.7% likelihood contours of the fit parameters (slope and intercept), which enclose the corresponding confidence regions. Areas with negative intercepts are not physically realistic.

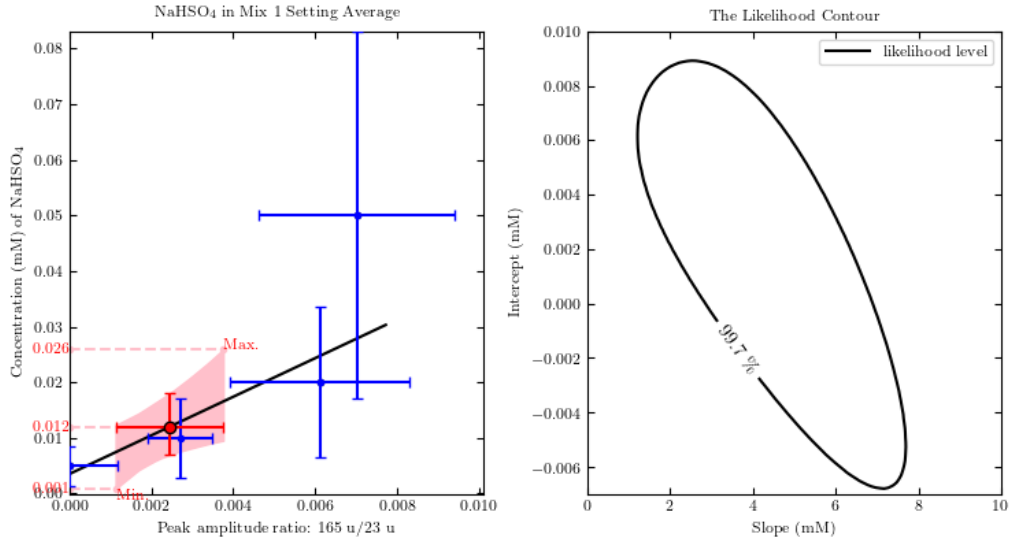

(a) The detection limit prediction for sulfate in Mix 1, using Na^+ (23 u) as the reference peak. The predicted detection limit, maximum value and minimum value are 0.012 mM, 0.026 mM and 0.0011 mM, respectively.

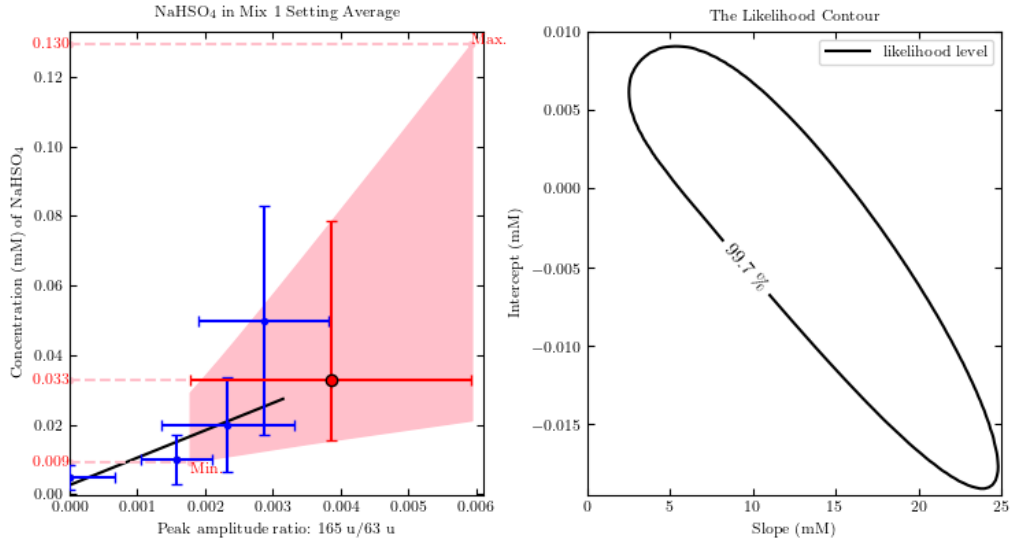

(b) The detection limits prediction for sulfate in Mix 1 using peak Na^+(NaOH) (63 u) as the reference peak. The predicted detection limit, maximum value and minimum value are 0.033 mM, 0.13 mM and 0.009 mM, respectively.

Figure I.1: The detection limit prediction for sulfate in Mix 1, using the Na^+ (23 u) (a) and Na^+(NaOH) (63 u) (b) peaks as reference peaks.

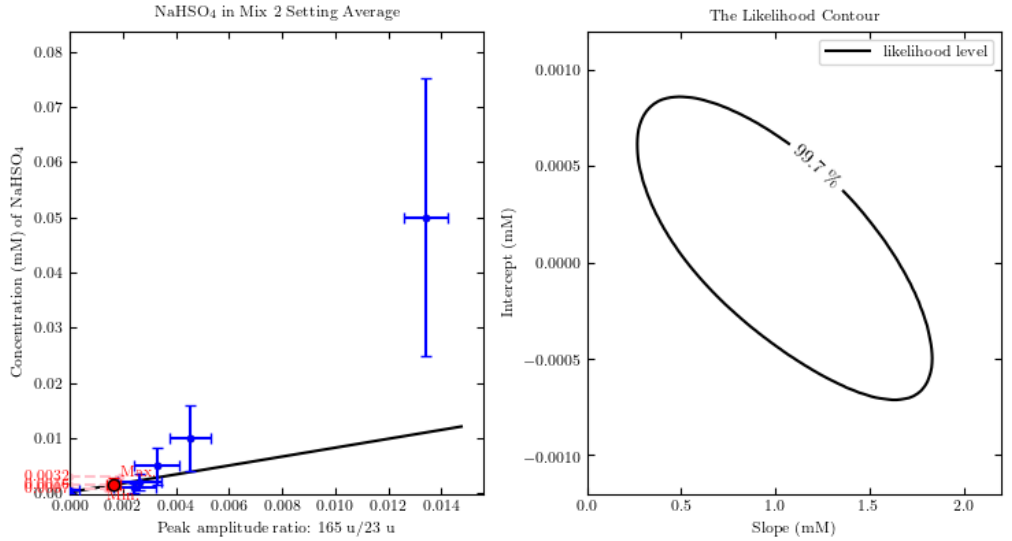

(a) The detection limit prediction for sulfate in Mix 2, using Na^+ (23 u) as the reference peak. The predicted detection limit, maximum value and minimum value are 0.0016 mM, 0.0032 mM and 0.0007 mM, respectively.

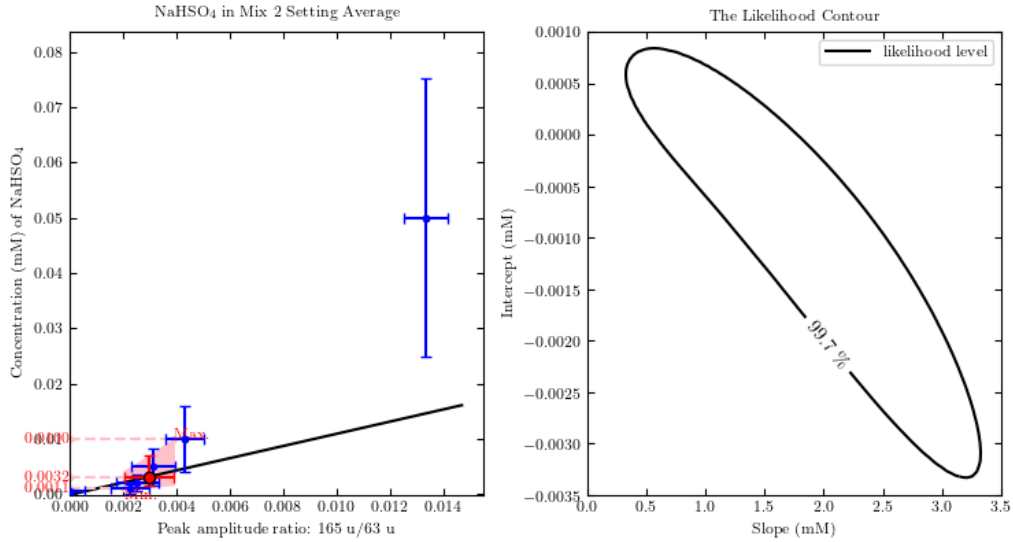

(b) The detection limits prediction for sulfate in Mix 2 using peak Na^+(NaOH) (63 u) as the reference peak. The predicted detection limit, maximum value and minimum value are 0.0032 mM, 0.010 mM and 0.0011 mM, respectively.

Figure I.2: The detection limit prediction for sulfate in Mix 2, using the Na^+ (23 u) (a) and Na^+(NaOH) (63 u) (b) peaks as reference peaks.

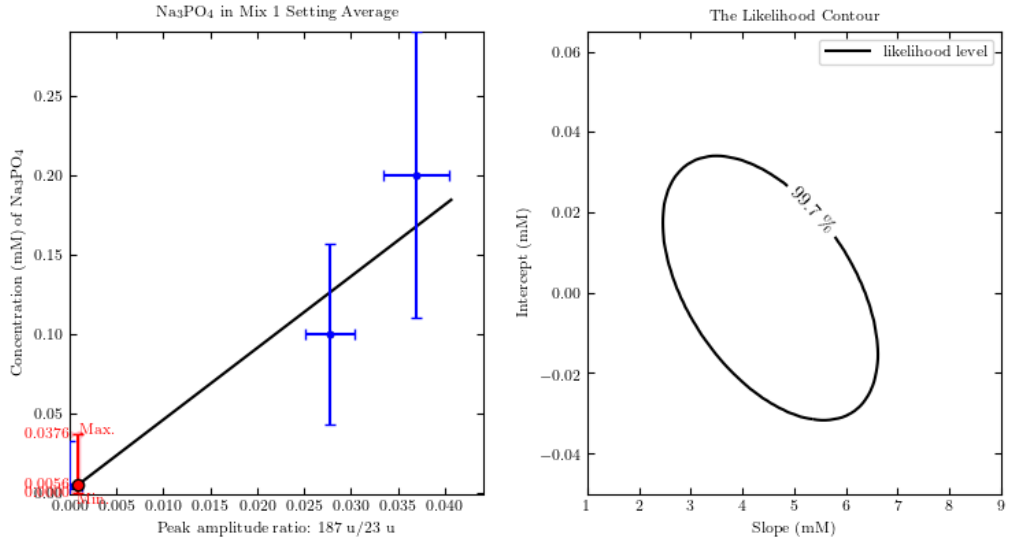

(a) The detection limit prediction for phosphate in Mix 1, using Na^+ (23 u) as the reference peak. The predicted detection limit, the maximum value and the minimum value are 0.0056 mM, 0.0376 mM and 0 mM, respectively.

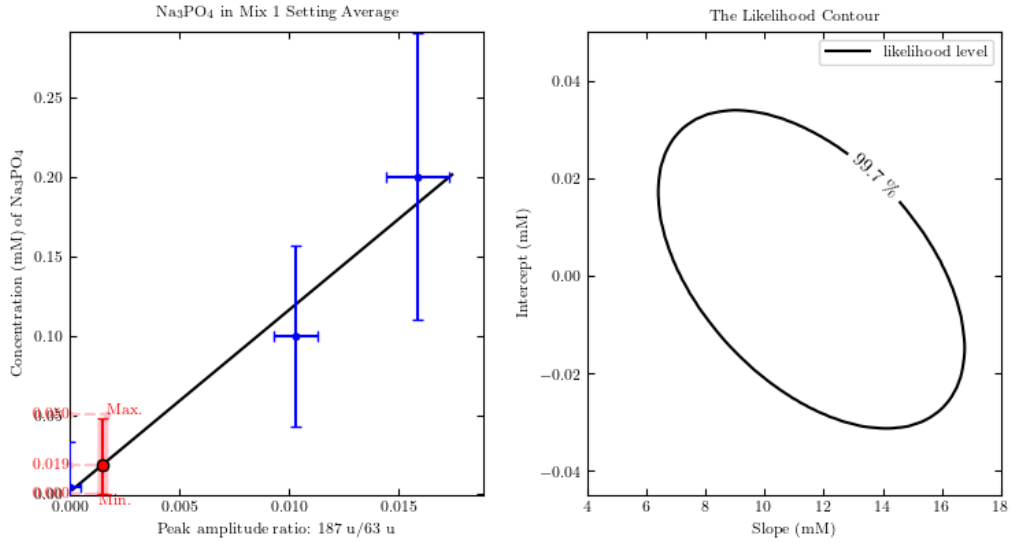

(b) The detection limits prediction for phosphate in Mix 1 using peak Na^+(NaOH) (63 u) as the reference peak. The predicted detection limit, the maximum value and the minimum value are 0.019 mM, 0.050 mM and 0 mM, respectively.

Figure I.3: The detection limit prediction for phosphate in Mix 1, using the Na^+ (23 u) (a) and peak Na^+(NaOH) (63 u) (b) peaks as reference peaks, respectively.

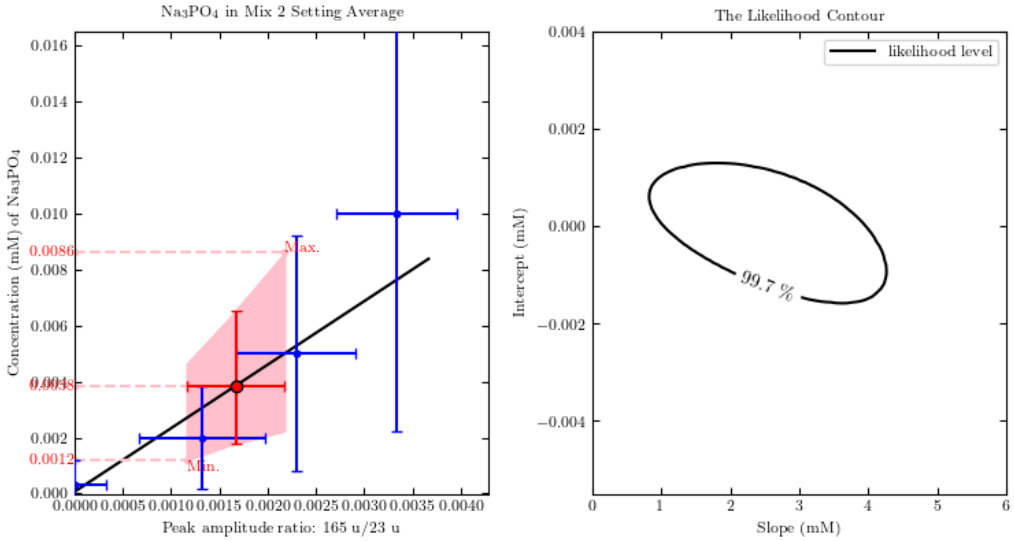

(a) The detection limit prediction for phosphate in Mix 1, using Na^+ (23 u) as the reference peak. The predicted detection limit, the maximum value and the minimum value are 0.0038 mM, 0.0086 mM and 0.0012 mM, respectively.

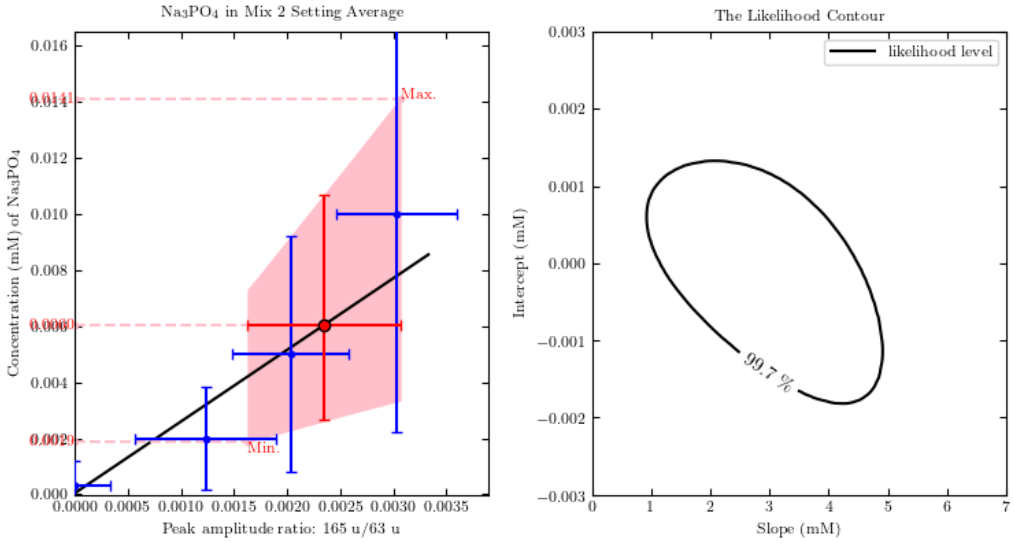

(b) The detection limits prediction for phosphate in Mix 1 using peak Na^+(NaOH) (63 u) as the reference peak. The predicted detection limit, the maximum value and the minimum value are 0.0060 mM, 0.0141 mM and 0.0019 mM, respectively.

Figure I.4: The detection limit prediction for phosphate in Mix 2, using the Na^+ (23 u) (a) and peak Na^+(NaOH) (63 u) (b) peaks as reference peaks, respectively.

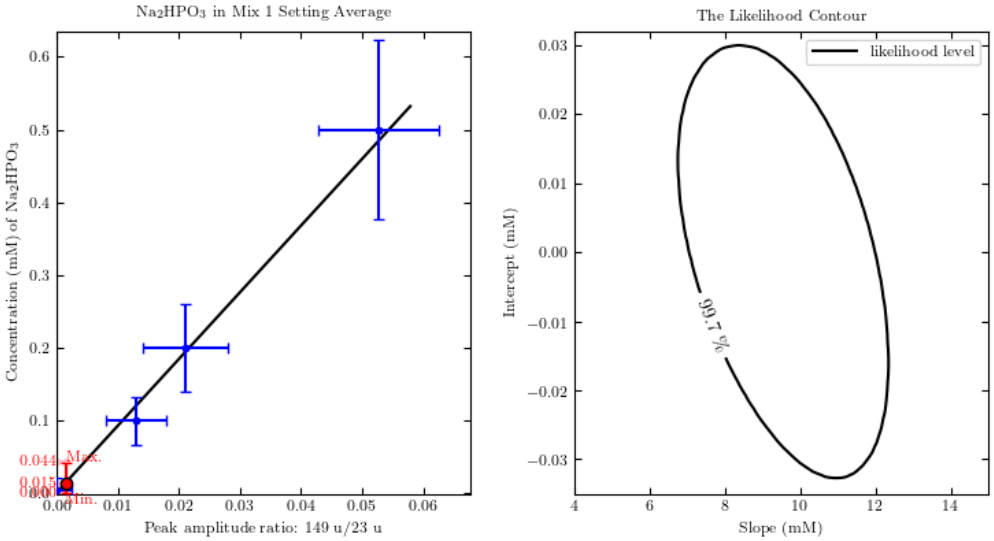

(a) The detection limit prediction for phosphite in Mix 1, using Na^+ (23 u) as the reference peak. The predicted detection limit, the maximum value and the minimum value are 0.015 mM, 0.044 mM and 0 mM, respectively.

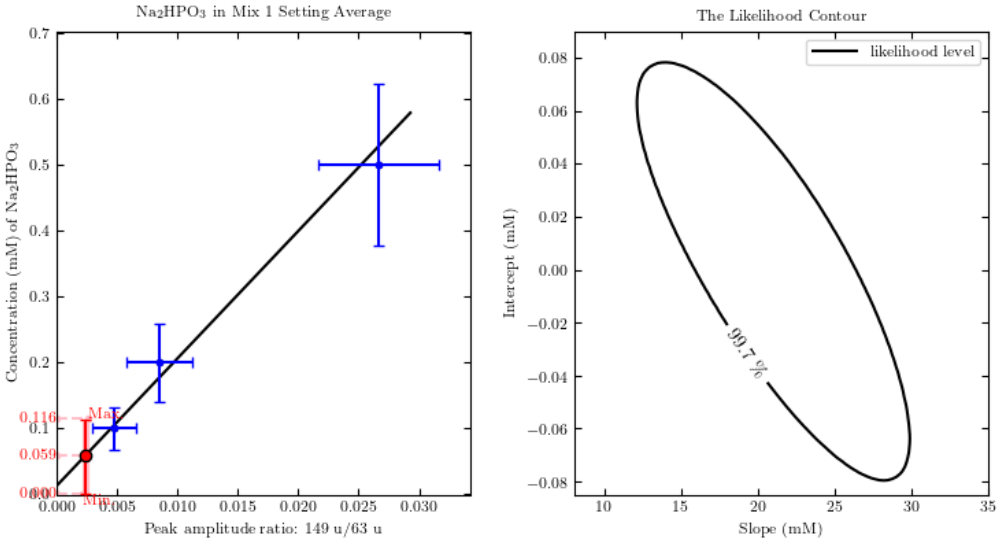

(b) The detection limits prediction for phosphite in Mix 1 using peak Na^+(NaOH) (63 u) as the reference peak. The predicted detection limit, the maximum value and the minimum value are 0.059 mM, 0.116 mM and 0 mM, respectively.

Figure I.5: The detection limit prediction for phosphite in Mix 1, using the Na^+ (23 u) (a) and Na^+(NaOH) (63 u) (b) peaks as the reference peaks, respectively.

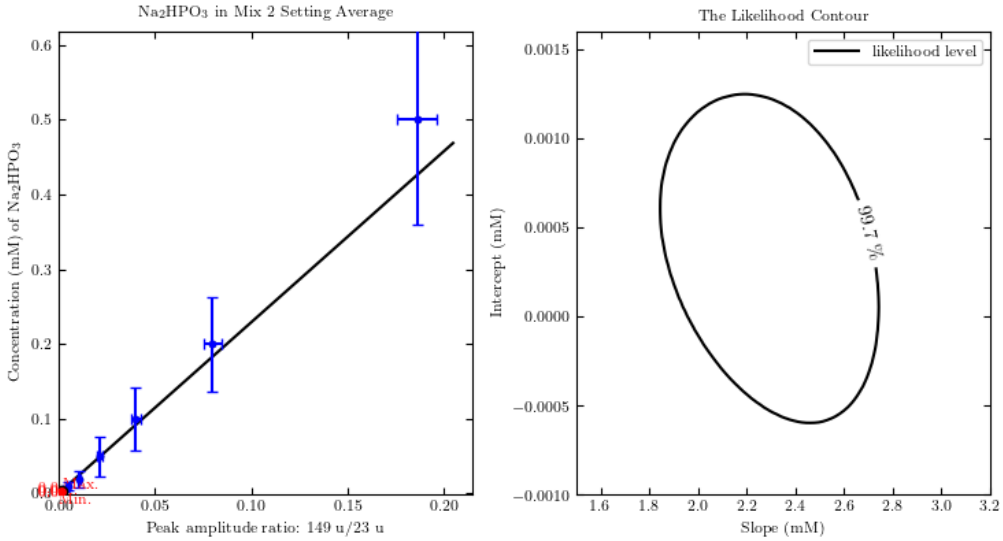

(a) The detection limit prediction for phosphite in Mix 2, using Na^+ (23 u) as the reference peak. The predicted detection limit, the maximum value and the minimum value are 0.17 mM, 0.33 mM and 0 mM, respectively.

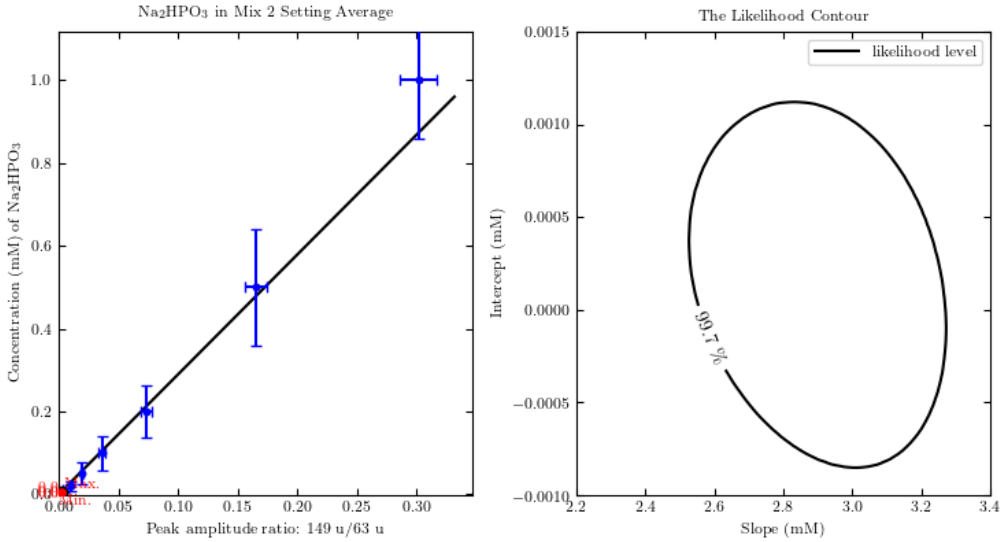

(b) The detection limits prediction for phosphite in Mix 2 using peak Na^+(NaOH) (63 u) as the reference peak. The predicted detection limit, the maximum value and the minimum value are 0.0061 mM, 0.0135 mM and 0 mM, respectively.

Figure I.6: The detection limit prediction for phosphite in Mix 2, using the Na^+ (23 u) (a) and Na^+(NaOH) (63 u) (b) peaks as the reference peaks, respectively.

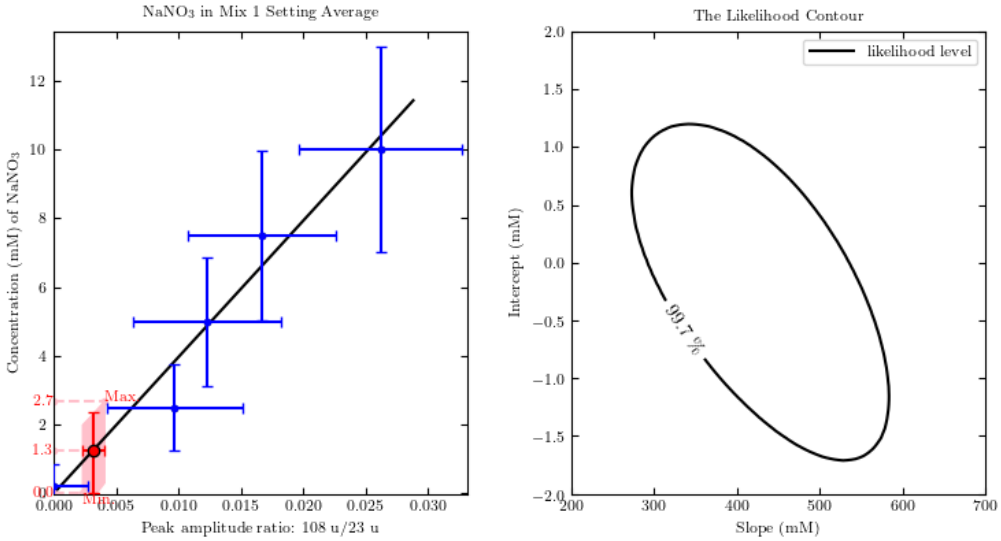

(a) The detection limit prediction for nitrate in Mix 1, using Na^+ (23 u) as the reference peak. The predicted detection limit, the maximum value and the minimum value are 1.3 mM, 2.7 mM and 0 mM, respectively.

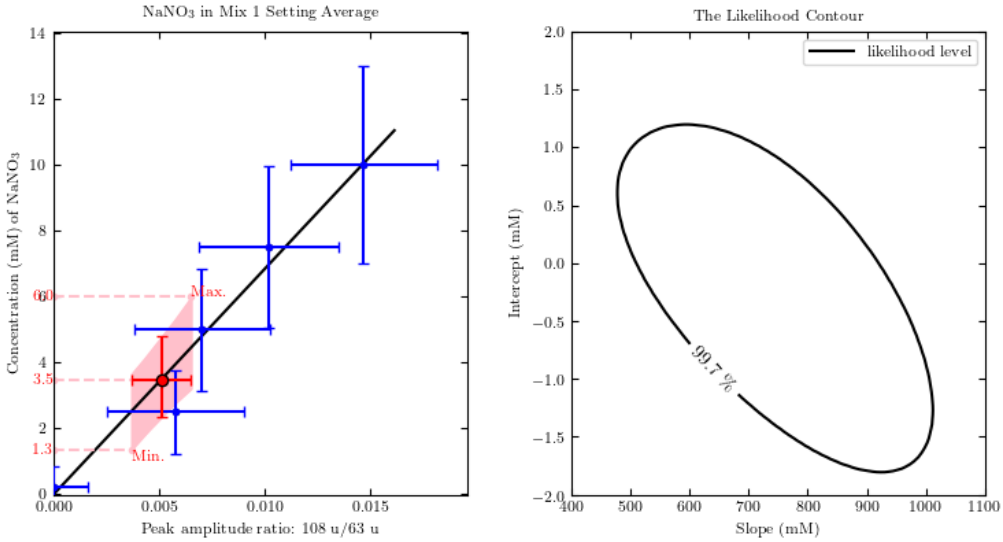

(b) The detection limits prediction for nitrate in Mix 1 using peak Na^+(NaOH) (63 u) as the reference peak. The predicted detection limit, the maximum value and the minimum value are 3.5 mM, 6.0 mM and 1.3 mM, respectively.

Figure I.7: The detection limit prediction for nitrate in Mix 1, using the Na^+ (23 u) (a) and Na^+(NaOH) (63 u) (b) peaks as reference peaks, respectively.

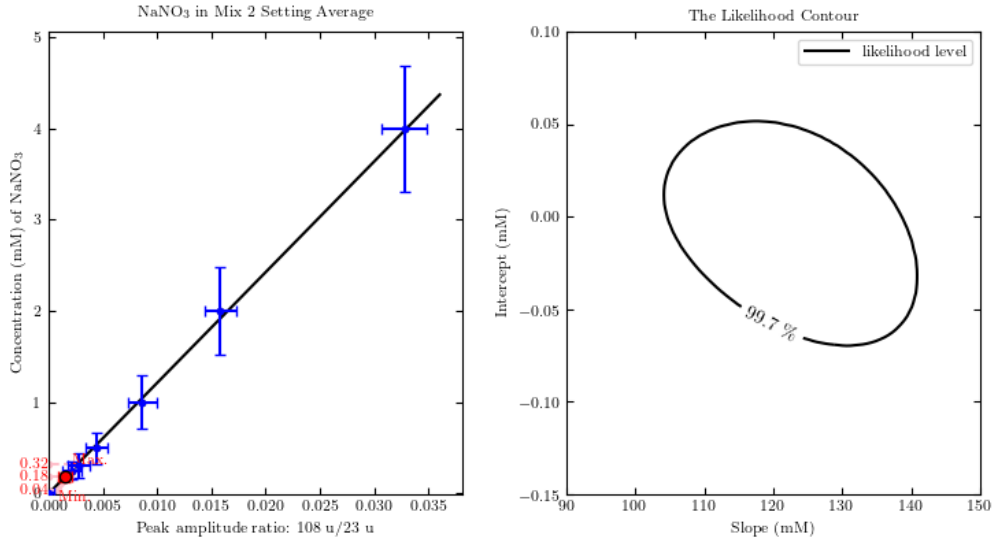

(a) The detection limit prediction for nitrate in Mix 2, using Na^+ (23 u) as the reference peak. The predicted detection limit, the maximum value and the minimum value are 0.18 mM, 0.32 mM and 0.04 mM, respectively.

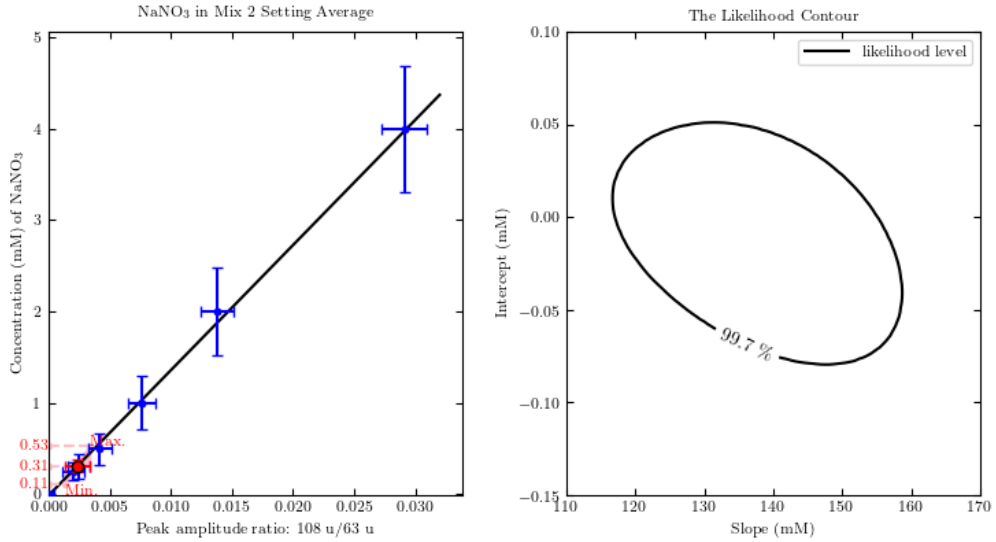

(b) The detection limits prediction for nitrate in Mix 2 using peak Na^+(NaOH) (63 u) as the reference peak. The predicted detection limit, the maximum value and the minimum value are 0.31 mM, 0.53 mM and 0.11 mM, respectively.

Figure I.8: The detection limit prediction for nitrate in Mix 2, using the Na^+ (23 u) (a) and Na^+(NaOH) (63 u) (b) peaks as reference peaks, respectively.

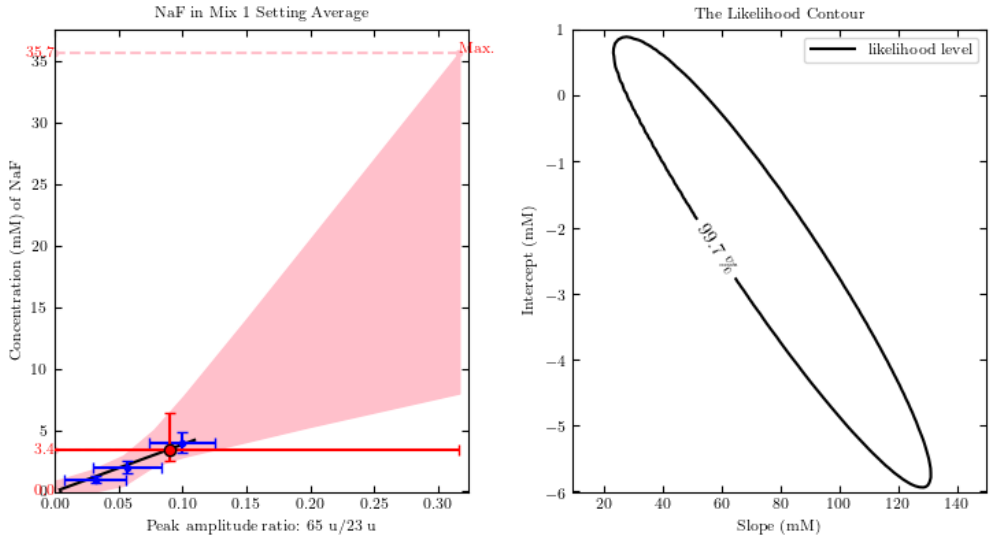

(a) The detection limit prediction for fluoride in Mix 1, using Na^+ (23 u) as the reference peak. The predicted detection limit, the maximum value and the minimum value are 3.4 mM, 35.7 mM and 0 mM, respectively.

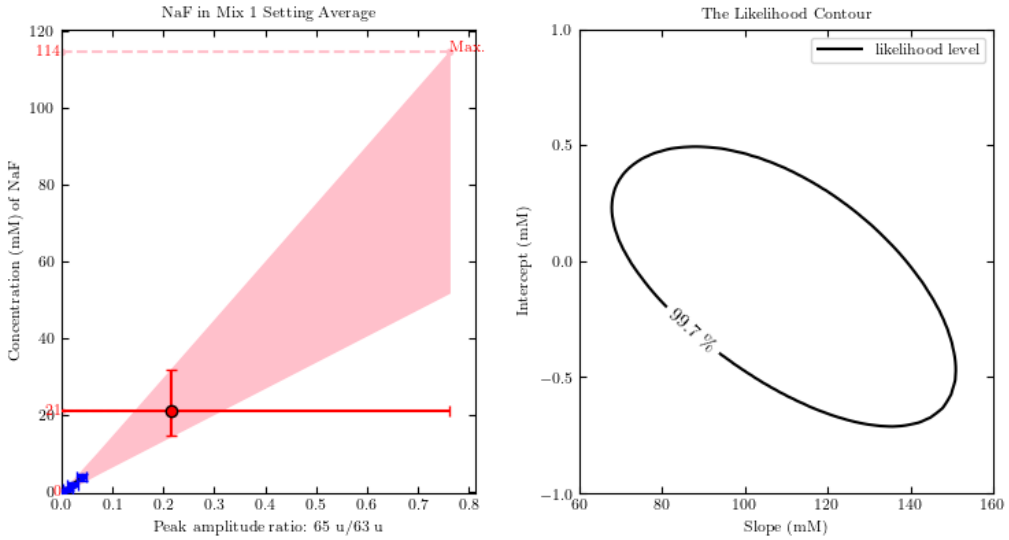

(b) The detection limits prediction for fluoride in Mix 1 using peak Na^+(NaOH) (63 u) as the reference peak. The predicted detection limit, the maximum value and the minimum value are 21 mM, 114 mM and 0 mM, respectively.

Figure I.9: The detection limit prediction for fluoride in Mix 1, using the Na^+ (23 u) (a) and Na^+(NaOH) (63 u) (b) peaks as reference peaks, respectively.

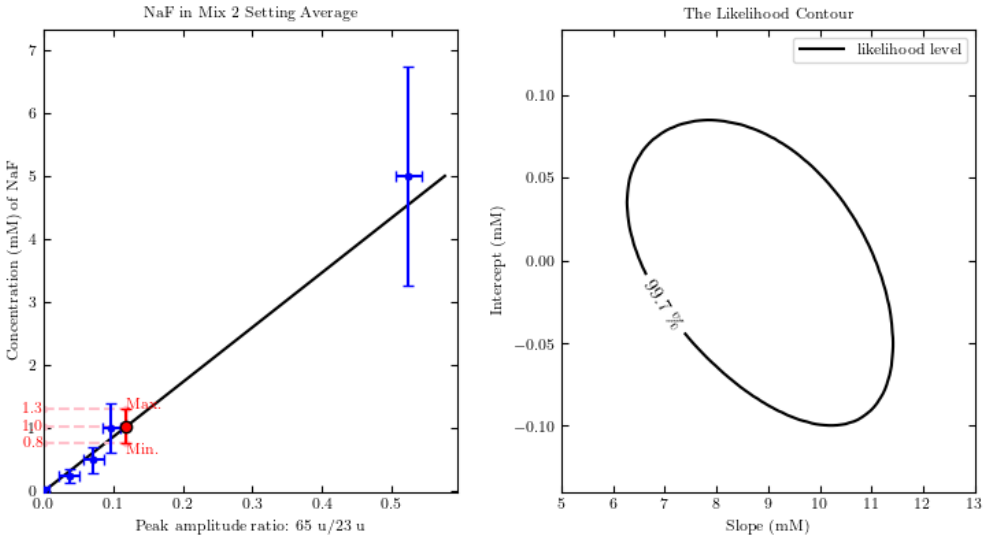

(a) The detection limit prediction for fluoride in Mix 2, using Na^+ (23 u) as the reference peak. The predicted detection limit, the maximum value and the minimum value are 1.0 mM, 1.3 mM and 0.8 mM, respectively.

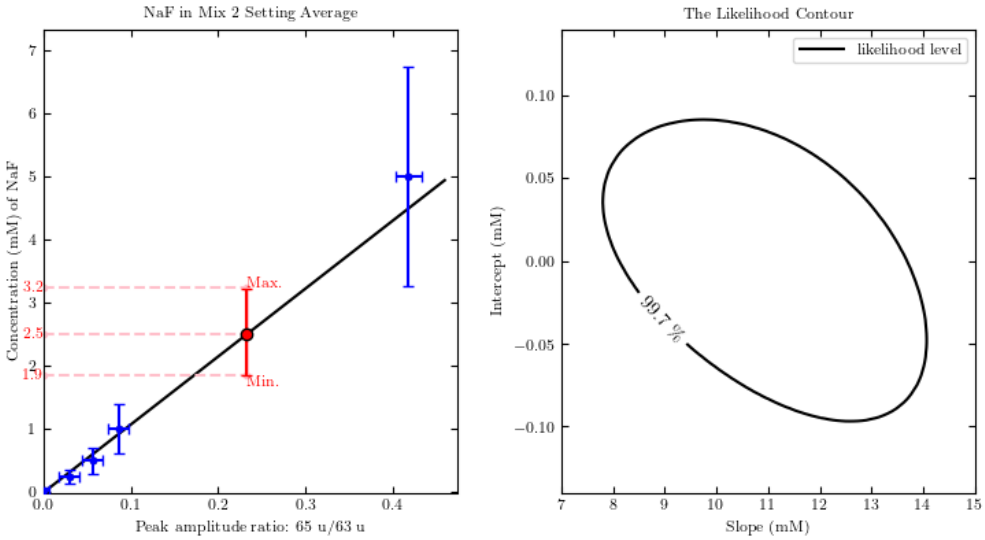

(b) The detection limits prediction for fluoride in Mix 2 using peak Na^+(NaOH) (63 u) as the reference peak. The predicted detection limit, the maximum value and the minimum value are 2.5 mM, 3.2 mM and 1.9 mM, respectively.

Figure I.10: The detection limit prediction for fluoride in Mix 2, using the Na^+ (23 u) (a) and Na^+(NaOH) (63 u) (b) peaks as reference peaks, respectively.

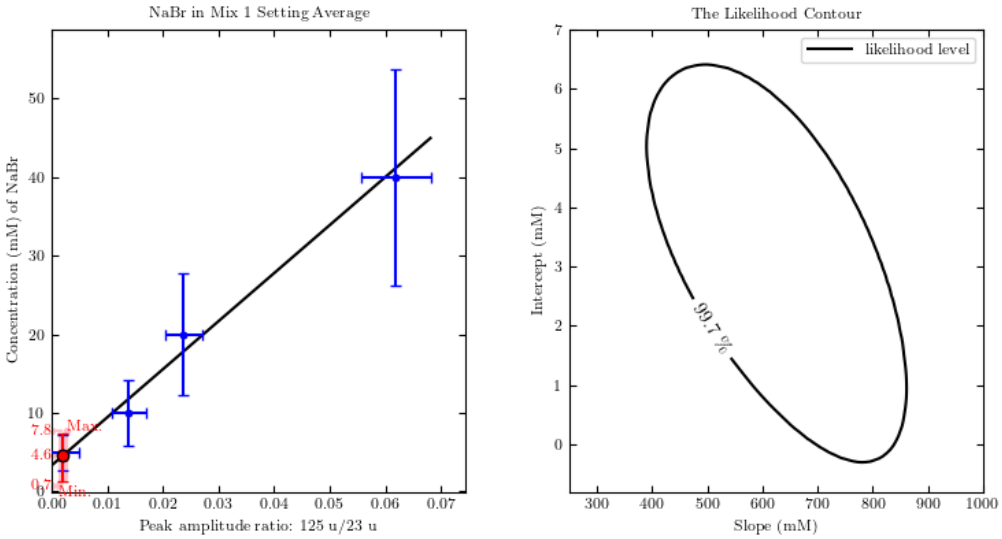

(a) The detection limit prediction for bromide in Mix 1, using Na^+ (23 u) as the reference peak. The predicted detection limit, the maximum value and the minimum value are 4.6 mM, 7.8 mM and 0.7 mM, respectively.

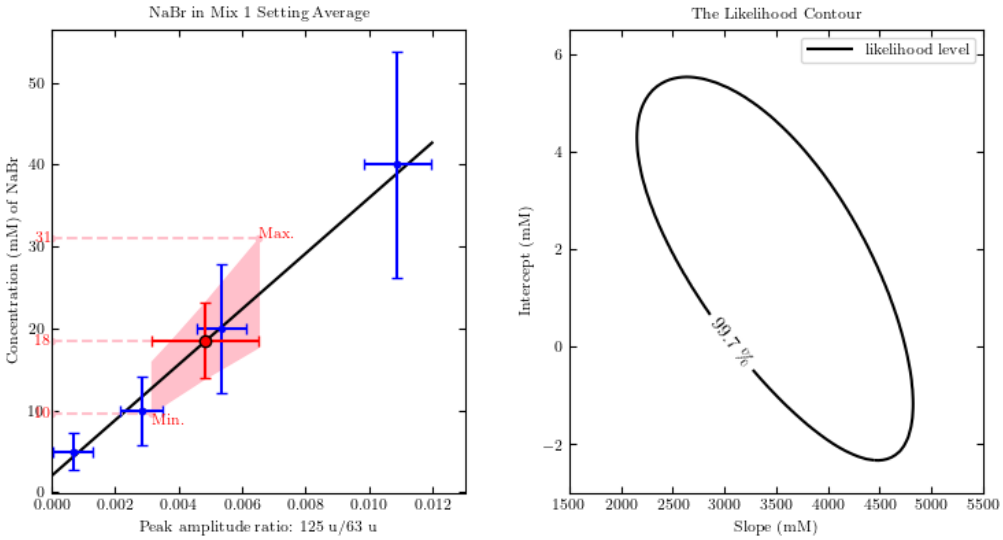

(b) The detection limits prediction for bromide in Mix 1 using peak Na^+(NaOH) (63 u) as the reference peak. The predicted detection limit, the maximum value and the minimum value are 18 mM, 31 mM and 10 mM, respectively.

Figure I.11: The detection limit prediction for bromide in Mix 1, using the Na^+ (23 u) (a) and Na^+(NaOH) (63 u) (b) peaks as reference peaks, respectively.

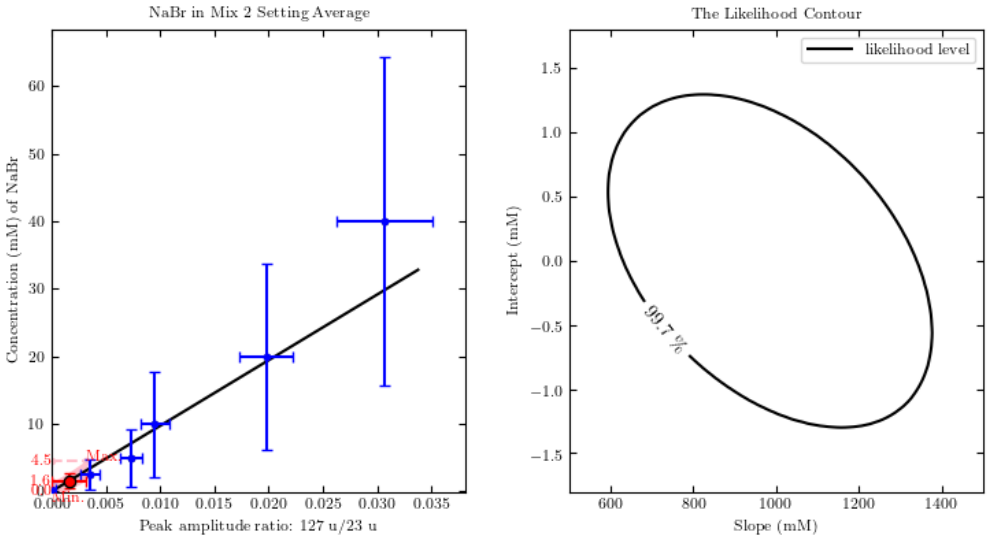

(a) The detection limit prediction for bromide in Mix 2, using Na^+ (23 u) as the reference peak. The predicted detection limit, the maximum value and the minimum value are 1.6 mM, 4.5 mM and 0 mM, respectively.

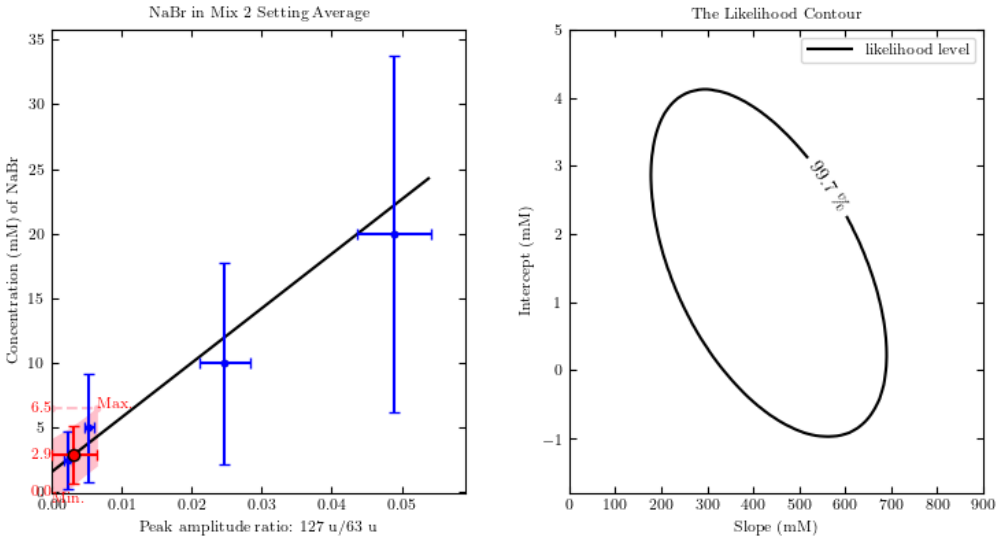

(b) The detection limits prediction for bromide in Mix 2 using peak Na^+(NaOH) (63 u) as the reference peak. The predicted detection limit, the maximum value and the minimum value are 2.9 mM, 6.5 mM and 0 mM, respectively.

Figure I.12: The detection limit prediction for bromide in Mix 2, using the Na^+ (23 u) (a) and Na^+(NaOH) (63 u) (b) peaks as reference peaks, respectively.

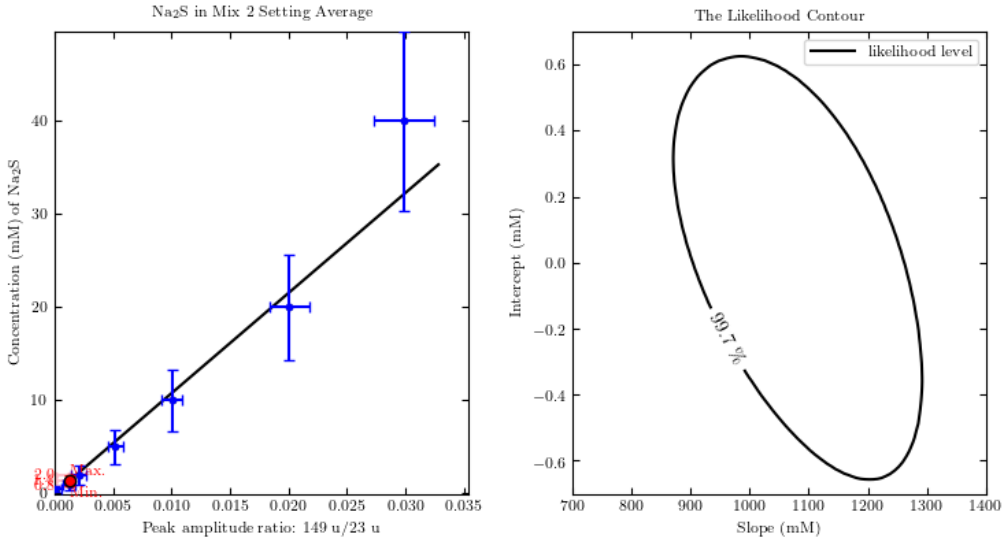

(a) The detection limit prediction for sulfide in Mix 2, using Na^+ (23 u) as the reference peak. The predicted detection limit, the maximum value and the minimum value are 1.4 mM, 2.0 mM and 0.8 mM, respectively.

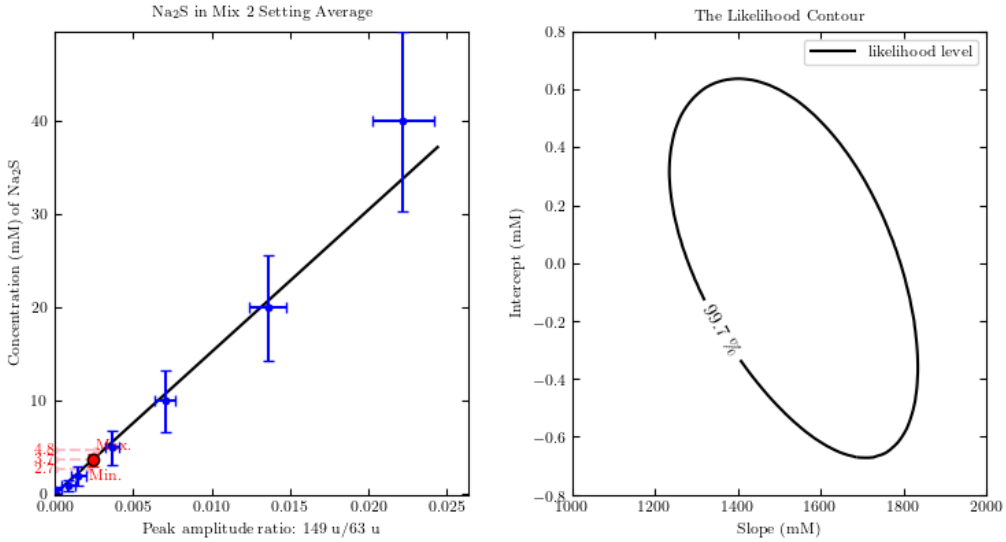

(b) The detection limits prediction for sulfide in Mix 2 using peak Na^+(NaOH) (63 u) as the reference peak. The predicted detection limit, the maximum value and the minimum value are 3.7 mM, 4.8 mM and 2.7 mM, respectively.

Figure I.13: The detection limit prediction for sulfide in Mix 2, using the Na^+ (23 u) (a) and Na^+(NaOH) (63 u) (b) peaks as reference peaks, respectively.

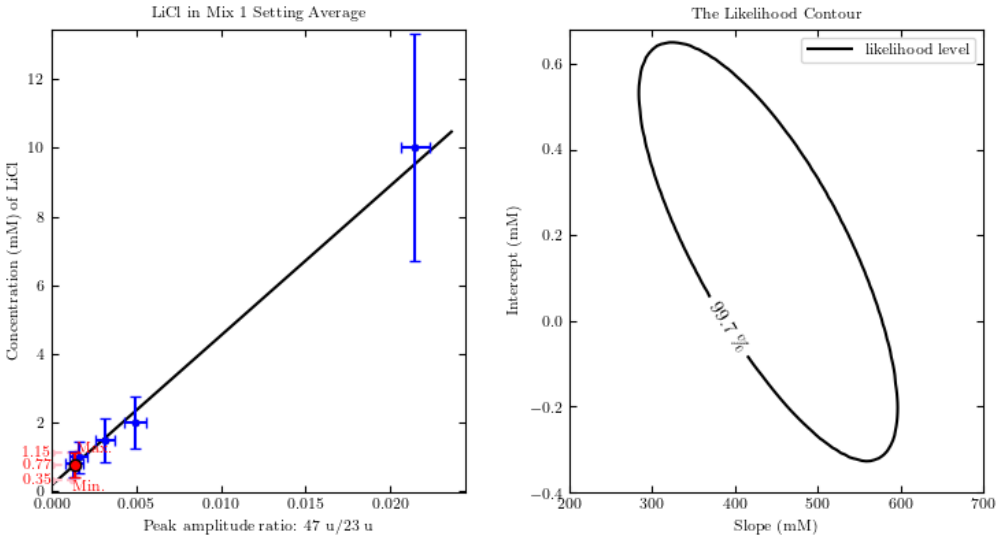

(a) The detection limit prediction for lithium in Mix1, using Na^+ (23 u) as the reference peak. The predicted detection limit, the maximum value and the minimum value are 0.77 mM, 1.15 mM and 0.35 mM, respectively.

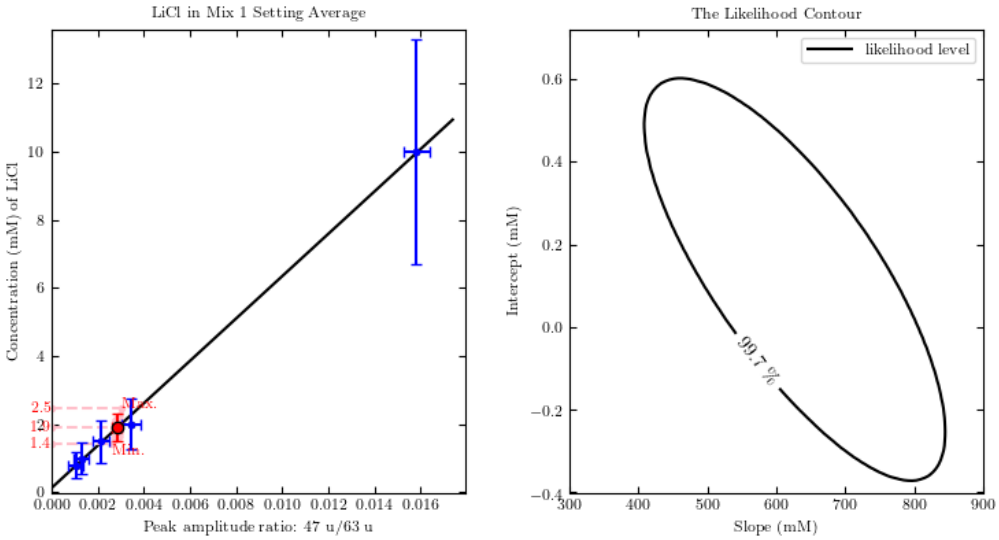

(b) The detection limits prediction for lithium in Mix 1 using peak Na^+(NaOH) (63 u) as the reference peak. The predicted detection limit, the maximum value and the minimum value are 1.9 mM, 2.5 mM and 1.4 mM, respectively.

Figure I.14: The detection limit prediction for lithium in Mix 1, using the Na^+ (23 u) (a) and Na^+(NaOH) (63 u) (b) peaks as reference peaks, respectively.

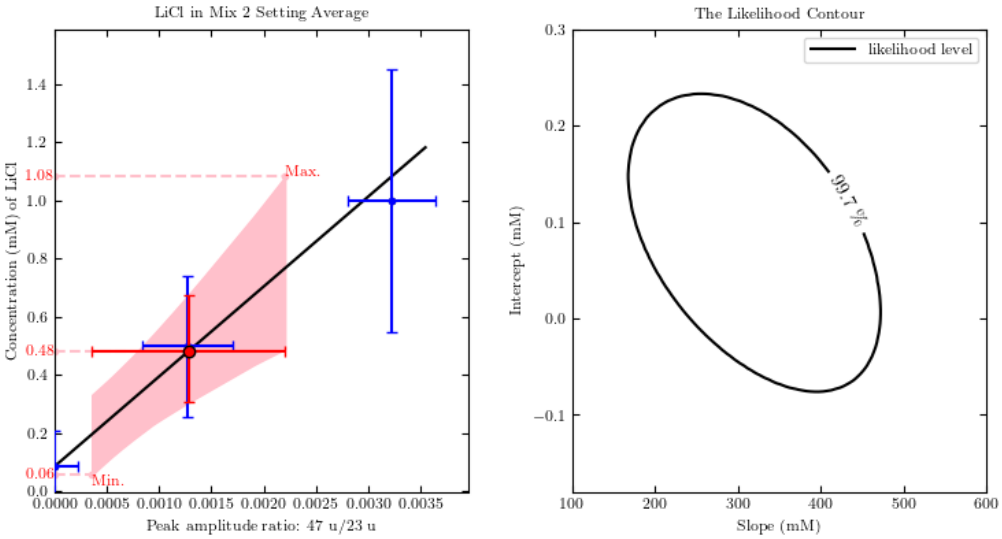

(a) The detection limit prediction for lithium in Mix 2, using Na^+ (23 u) as the reference peak. The predicted detection limit, the maximum value and the minimum value are 0.48 mM, 1.08 mM and 0.06 mM, respectively.

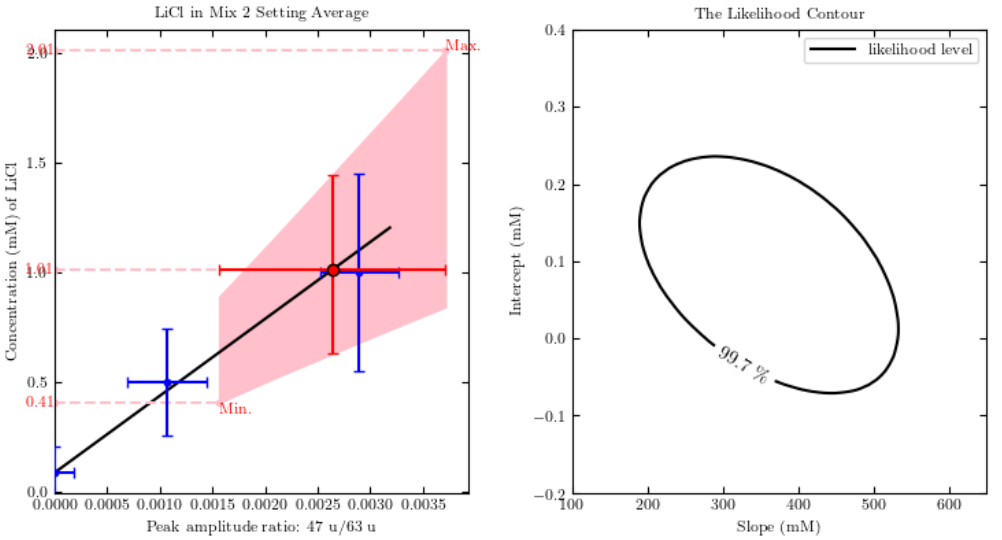

(b) The detection limits prediction for lithium in Mix 2 using peak Na^+(NaOH) (63 u) as the reference peak. The predicted detection limit, the maximum value and the minimum value are 1.0 mM, 2.0 mM and 0.4 mM, respectively.

Figure I.15: The detection limit prediction for lithium in Mix 2, using the Na^+ (23 u) (a) and Na^+(NaOH) (63 u) (b) peaks as reference peaks, respectively.

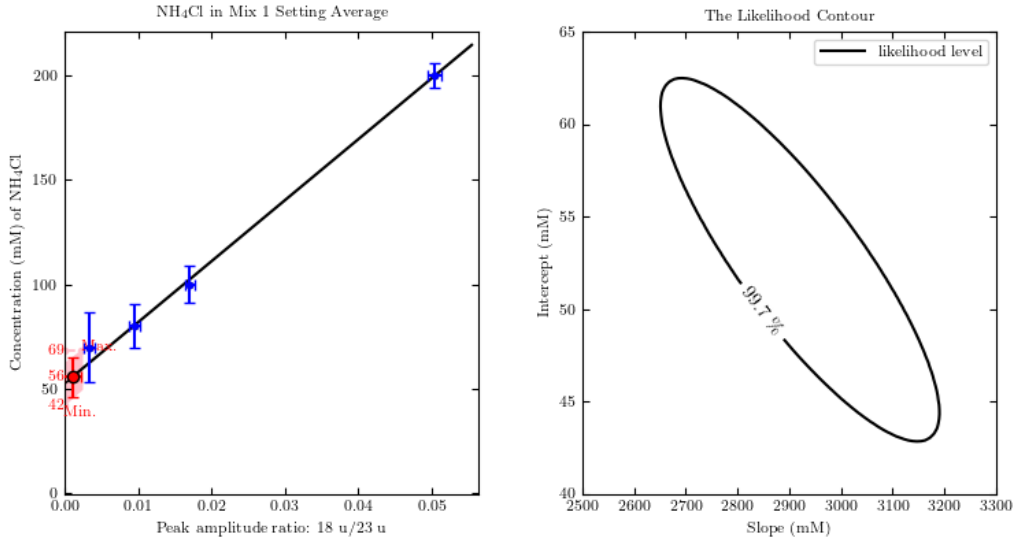

(a) The detection limit prediction for ammonium in Mix 1, using Na^+ (23 u) as the reference peak. The predicted detection limit, the maximum value and the minimum value are 56 mM, 69 mM and 42 mM, respectively.

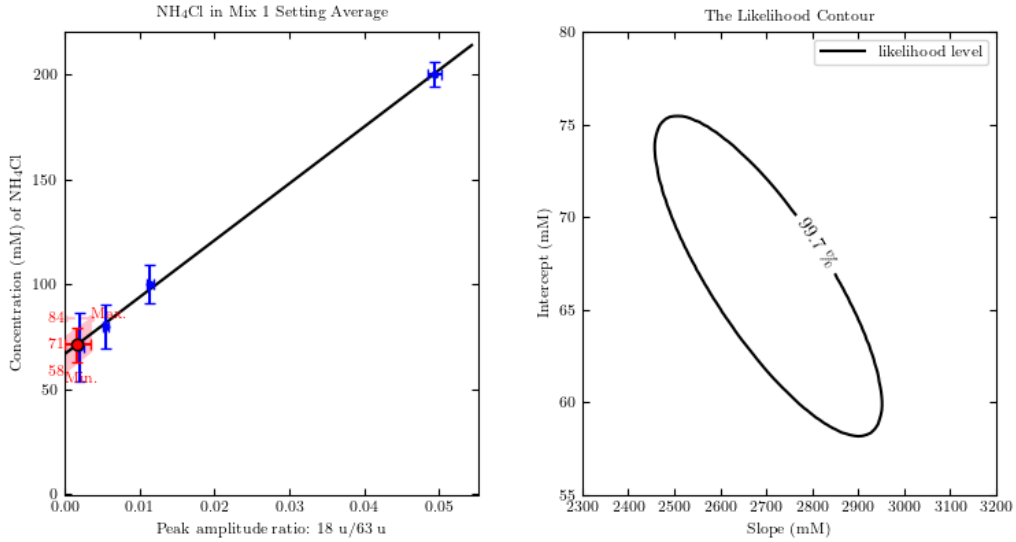

(b) The detection limits prediction for ammonium in Mix 1 using peak Na^+(NaOH) (63 u) as the reference peak. The predicted detection limit, the maximum value and the minimum value are 71 mM, 84 mM and 58 mM, respectively.

Figure I.16: The detection limit prediction for ammonium in Mix 1, using the Na^+ (23 u) (a) and Na^+(NaOH) (63 u) (b) peaks as the reference peaks, respectively.

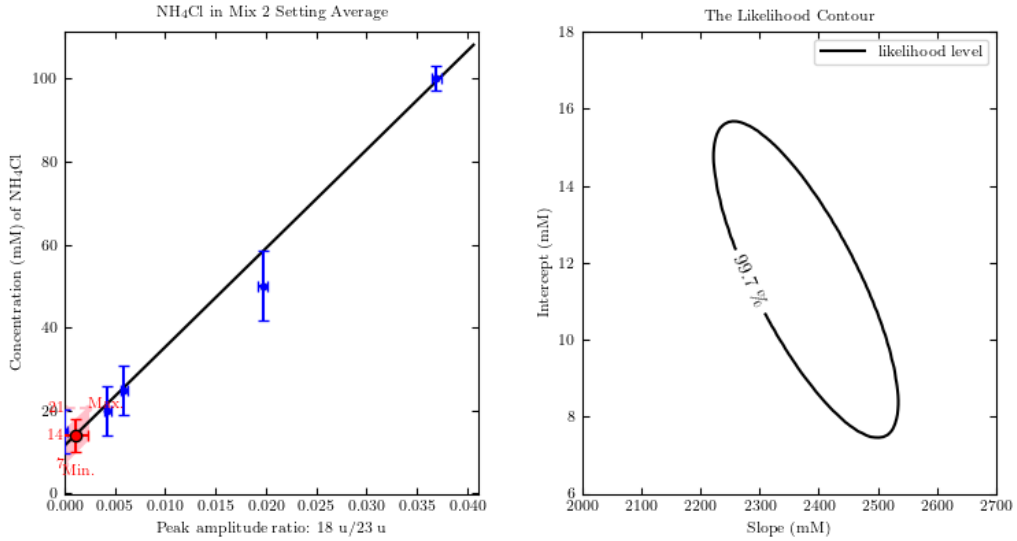

(a) The detection limit prediction for ammonium in Mix 2, using Na^+ (23 u) as the reference peak. The predicted detection limit, the maximum value and the minimum value are 14 mM, 21 mM and 7 mM, respectively.

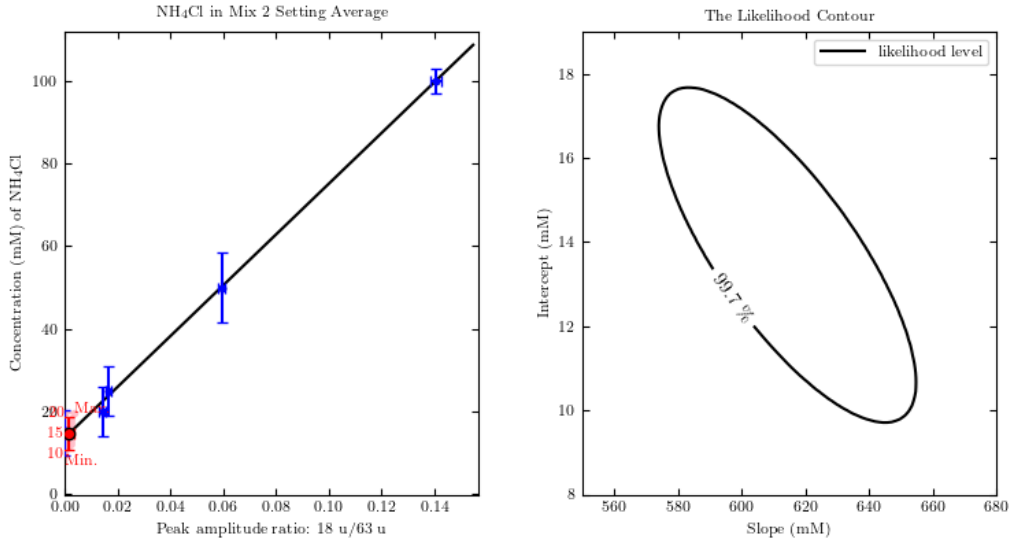

(b) The detection limits prediction for ammonium in Mix 2 using peak Na^+(NaOH) (63 u) as the reference peak. The predicted detection limit, the maximum value and the minimum value are 15 mM, 20 mM and 10 mM, respectively.

Figure I.17: The detection limit prediction for ammonium in Mix 2, using the Na^+ (23 u) (a) and Na^+(NaOH) (63 u) (b) peaks as reference peaks, respectively.

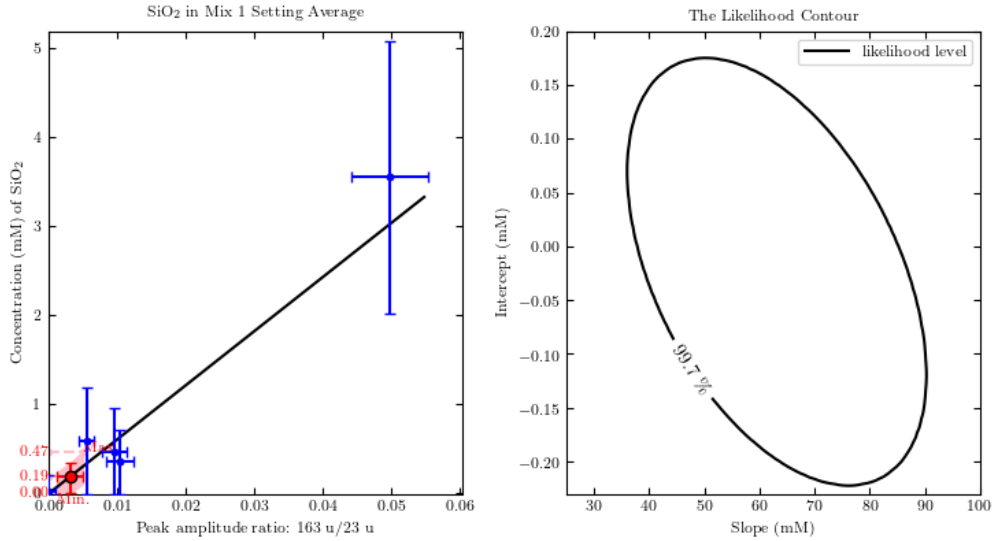

(a) The detection limit prediction for SiO_2 in Mix 1, using Na^+ (23 u) as the reference peak. The predicted detection limit, the maximum value and the minimum value are 0.19 mM, 0.47 mM and 0 mM, respectively.

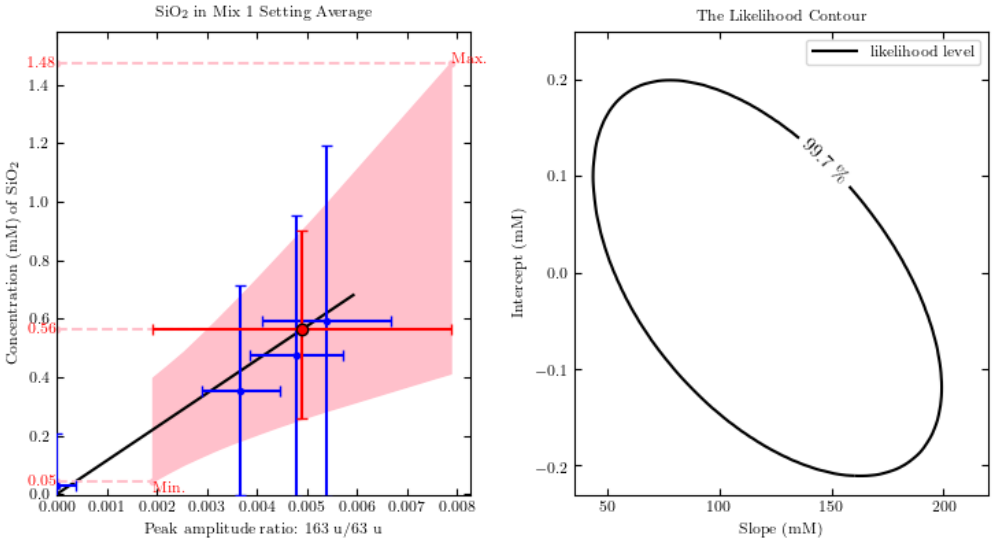

(b) The detection limits prediction for SiO_2 in Mix 1 using peak Na^+(NaOH) (63 u) as the reference peak. The predicted detection limit, the maximum value and the minimum value are 0.56 mM, 1.48 mM and 0.05 mM, respectively.

Figure I.18: The detection limit prediction for SiO_2 in Mix 1, using the Na^+ (23 u) (a) and Na^+(NaOH) (63 u) (b) peaks as reference peaks, respectively.

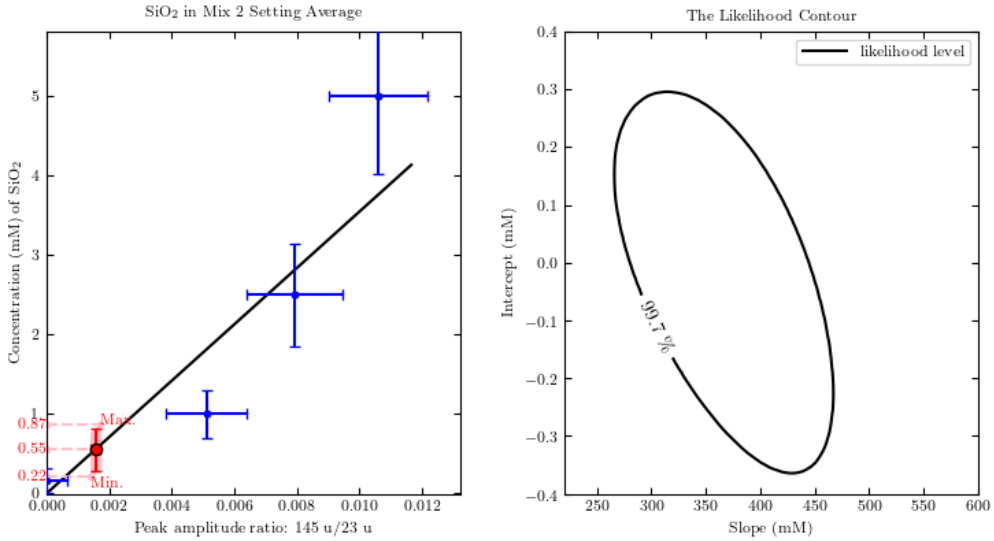

(a) The detection limit prediction for SiO_2 in Mix 2, using Na^+ (23 u) as the reference peak. The predicted detection limit, the maximum value and the minimum value are 0.55 mM, 0.87 mM and 0.22 mM, respectively.

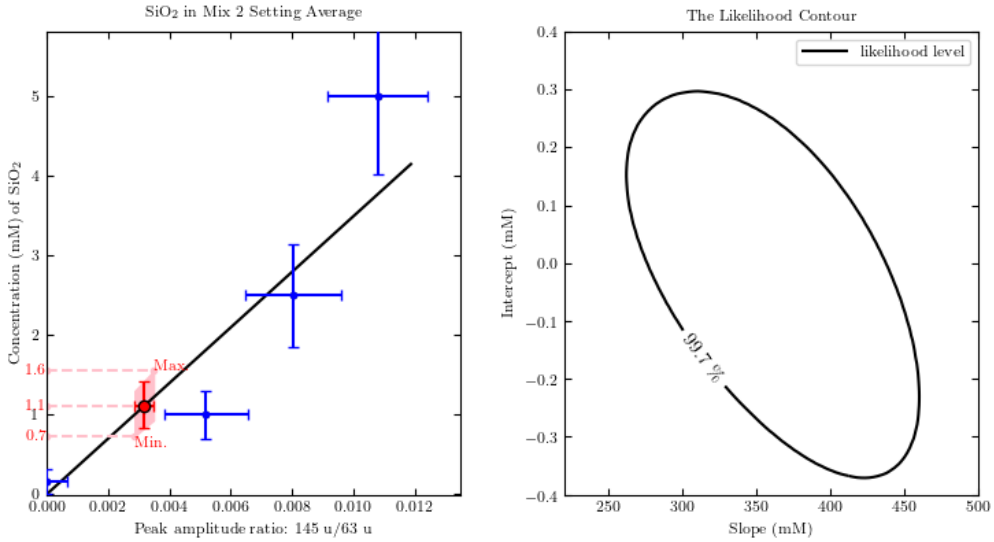

(b) The detection limits prediction for SiO_2 in Mix 2 using peak Na^+(NaOH) (63 u) as the reference peak. The predicted detection limit, the maximum value and the minimum value are 1.1 mM, 1.6 mM and 0.7 mM, respectively.

Figure I.19: The detection limit prediction for SiO_2 in Mix 2, using the Na^+ (23 u) (a) and Na^+(NaOH) (63 u) (b) peaks as reference peaks, respectively.

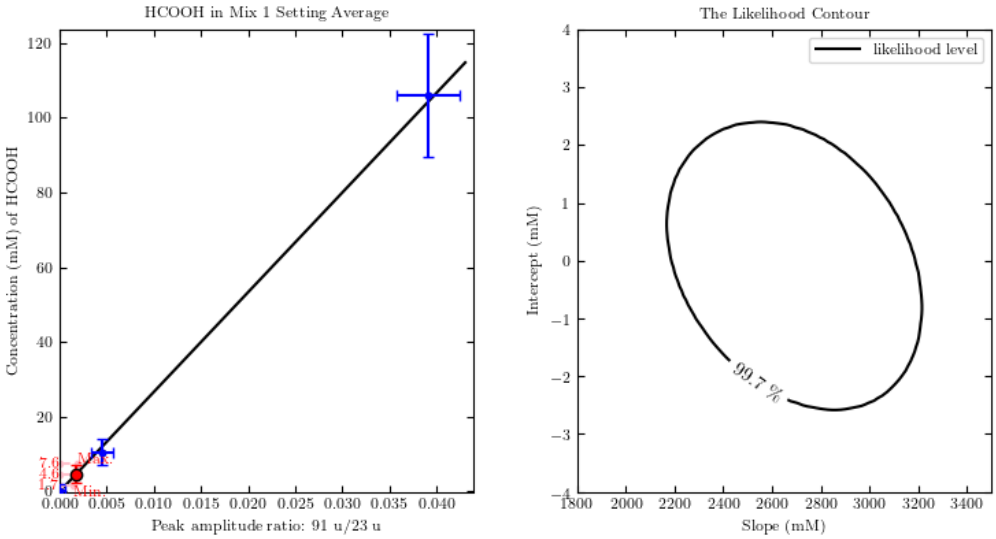

(a) The detection limit prediction for HCOOH in Mix 1, using Na^+ (23 u) as the reference peak. The predicted detection limit, the maximum value and the minimum value are 4.6 mM, 7.6 mM and 1.7 mM, respectively.

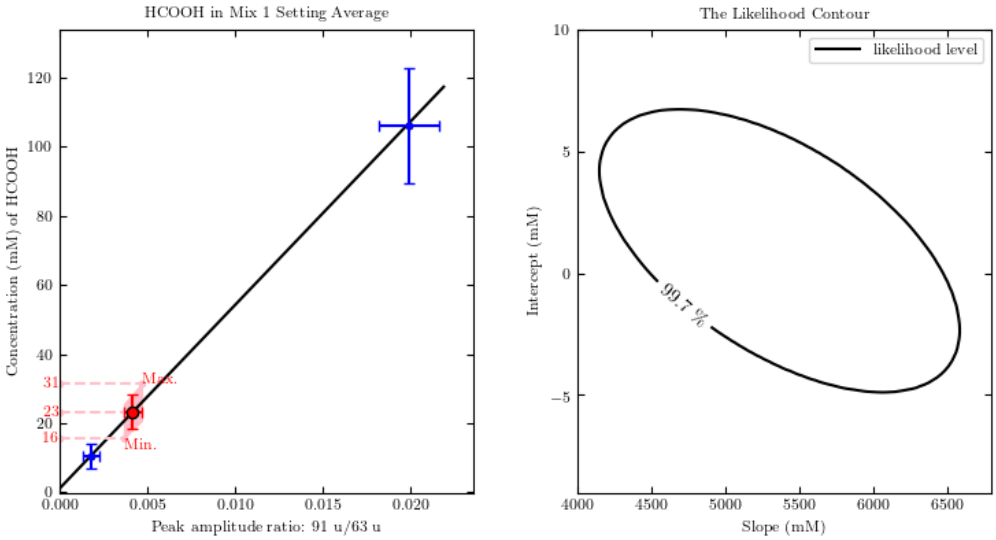

(b) The detection limits prediction for HCOOH in Mix 1 using peak Na^+(NaOH) (63 u) as the reference peak. The predicted detection limit, the maximum value and the minimum value are 23 mM, 31 mM and 16 mM, respectively.

Figure I.20: The detection limit prediction for HCOOH in Mix 1, using the Na^+ (23 u) (a) and Na^+(NaOH) (63 u) (b) peaks as the reference peaks, respectively.)

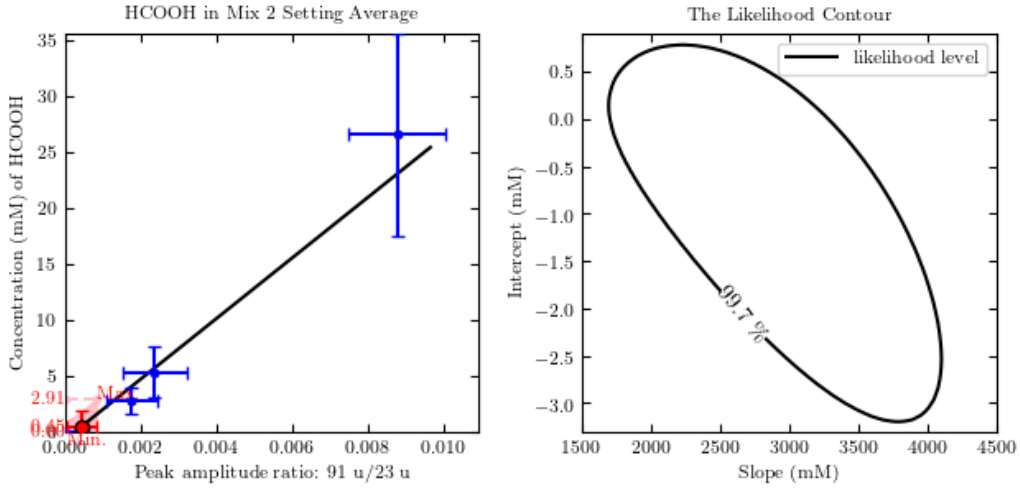

(a) The detection limit prediction for HCOOH in Mix 2, using Na^+ (23 u) as the reference peak. The predicted detection limit, the maximum value and the minimum value are 0.45 mM, 2.91 mM and 0 mM, respectively.

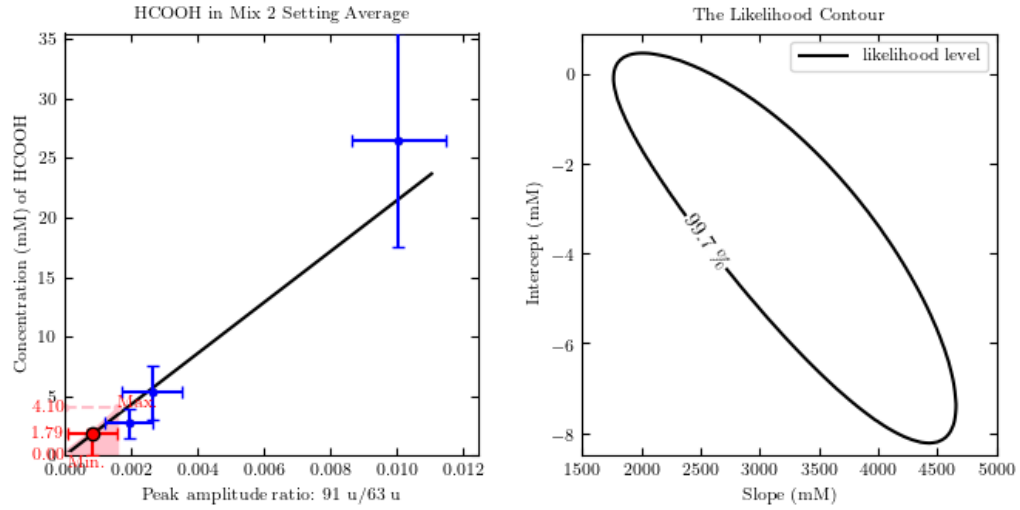

(b) The detection limits prediction for HCOOH in Mix 2 using peak Na^+(NaOH) (63 u) as the reference peak. The predicted detection limit, the maximum value and the minimum value are 1.8 mM, 4.1 mM and 0 mM, respectively.

Figure I.21: The detection limit prediction for HCOOH in Mix 2, using the Na^+ (23 u) (a) and Na^+(NaOH) (63 u) (b) peaks as reference peaks, respectively.)

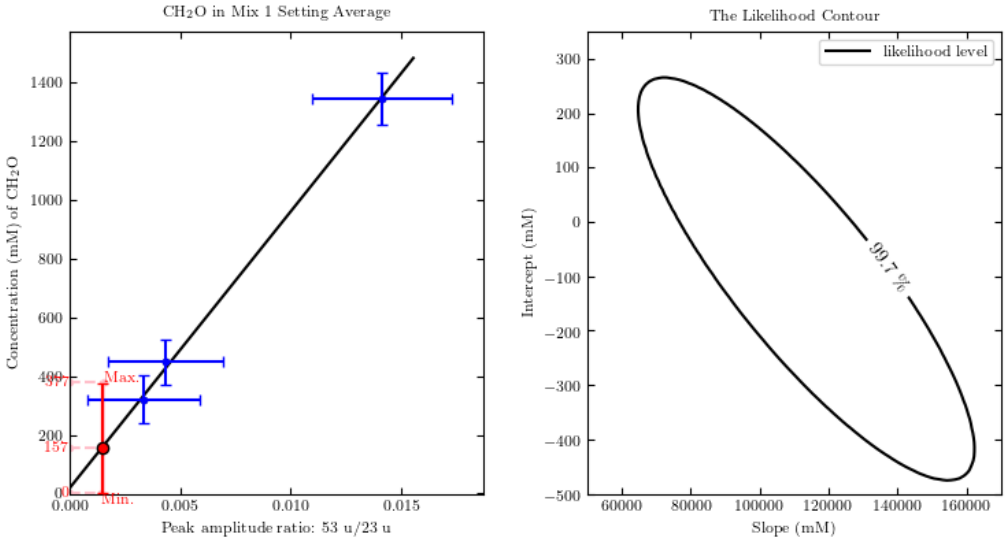

(a) The detection limit prediction for CH_2O in Mix 1, using Na^+ (23 u) as the reference peak. The predicted detection limit, the maximum value and the minimum value are 1.6×10^2 mM, 3.8×10^2 mM and 0 mM, respectively.

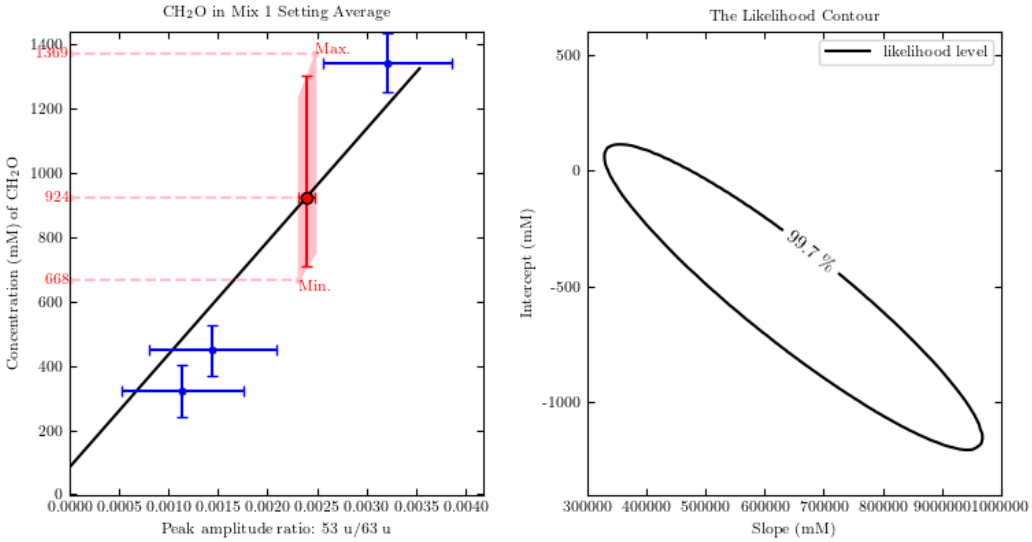

(b) The detection limits prediction for CH_2O in Mix 1 using peak CH_2O (63 u) as the reference peak. The predicted detection limit, the maximum value and the minimum value are 9.2×10^2 mM, 1.37×10^3 mM and 6.7×10^2 mM, respectively.

Figure I.22: The detection limit prediction for CH_2O in Mix 1, using the Na^+ (23 u) (a) and Na^+(NaOH) (63 u) (b) peaks as reference peaks, respectively.

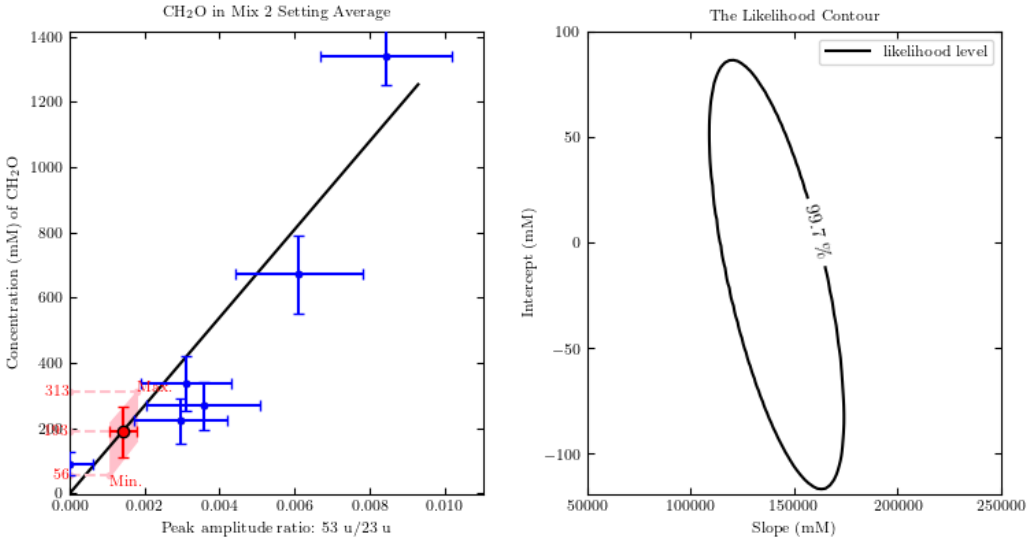

(a) The detection limit prediction for CH_2O in Mix 2, using Na^+ (23 u) as the reference peak. The predicted detection limit, the maximum value and the minimum value are 1.9×10^2 mM, 3.1×10^2 mM and 0.6×10^2mM, respectively.

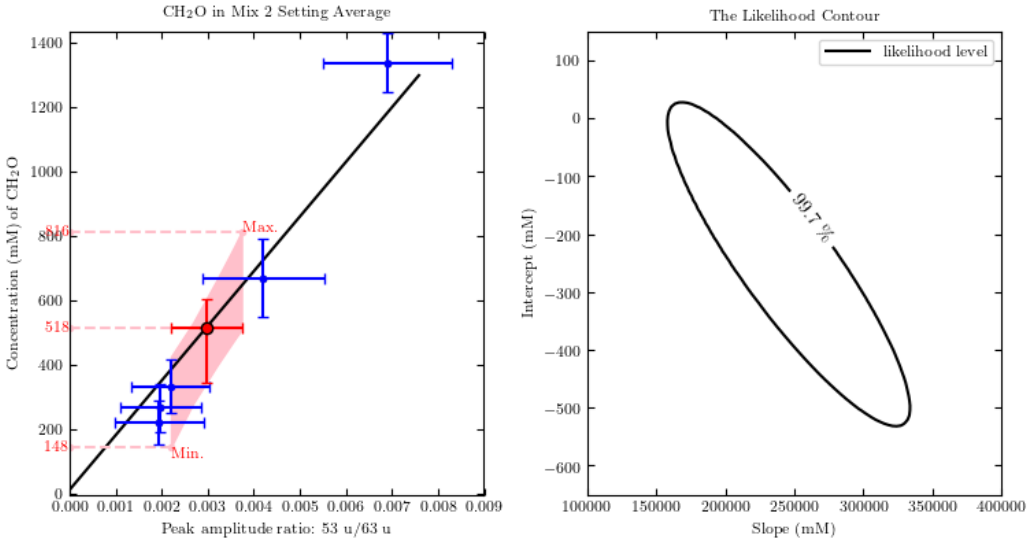

(b) The detection limits prediction for CH_2O in Mix 2 using peak CH_2O (63 u) as the reference peak. The predicted detection limit, the maximum value and the minimum value are 5.2×10^2 mM, 8.2×10^2 mM and 1.5×10^2 mM, respectively.

Figure I.23: The detection limit prediction for CH_2O in Mix 2, using the Na^+ (23 u) (a) and Na^+(NaOH) (63 u) (b) peaks as reference peaks, respectively.

Appendix J

Comparison of detection limits determined using the different methods via bar charts

APPENDIX J. COMPARISON OF DETECTION LIMITS DETERMINED USING THE DIFFERENT METHODS VIA BAR CHARTS

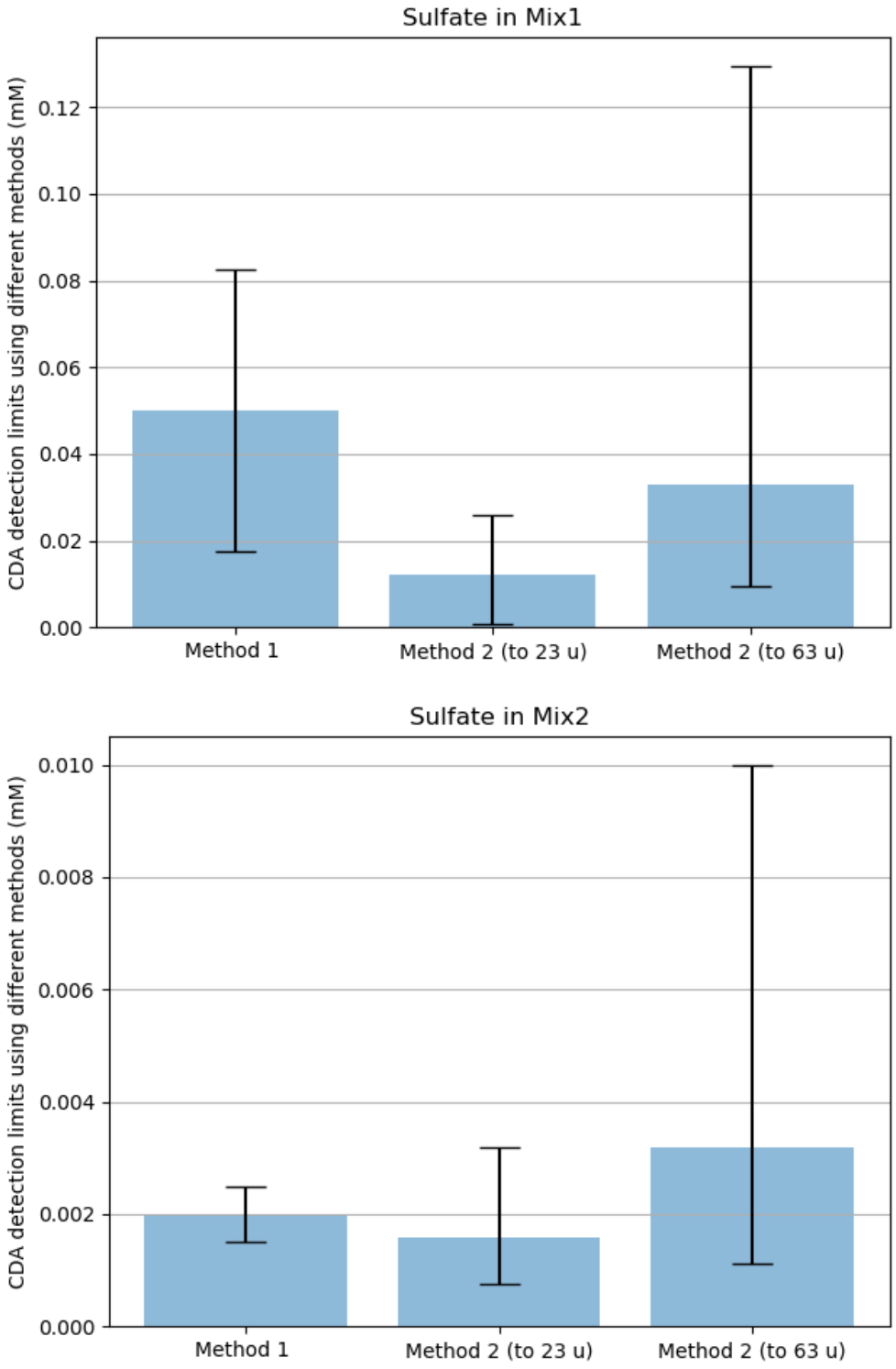

Figure J.1: The approximate CDA detection limits of sulfate in Mix 1 (upper panel) and Mix 2 (lower panel), predicted using Method 1 and Method 2 (two different reference peaks), respectively.

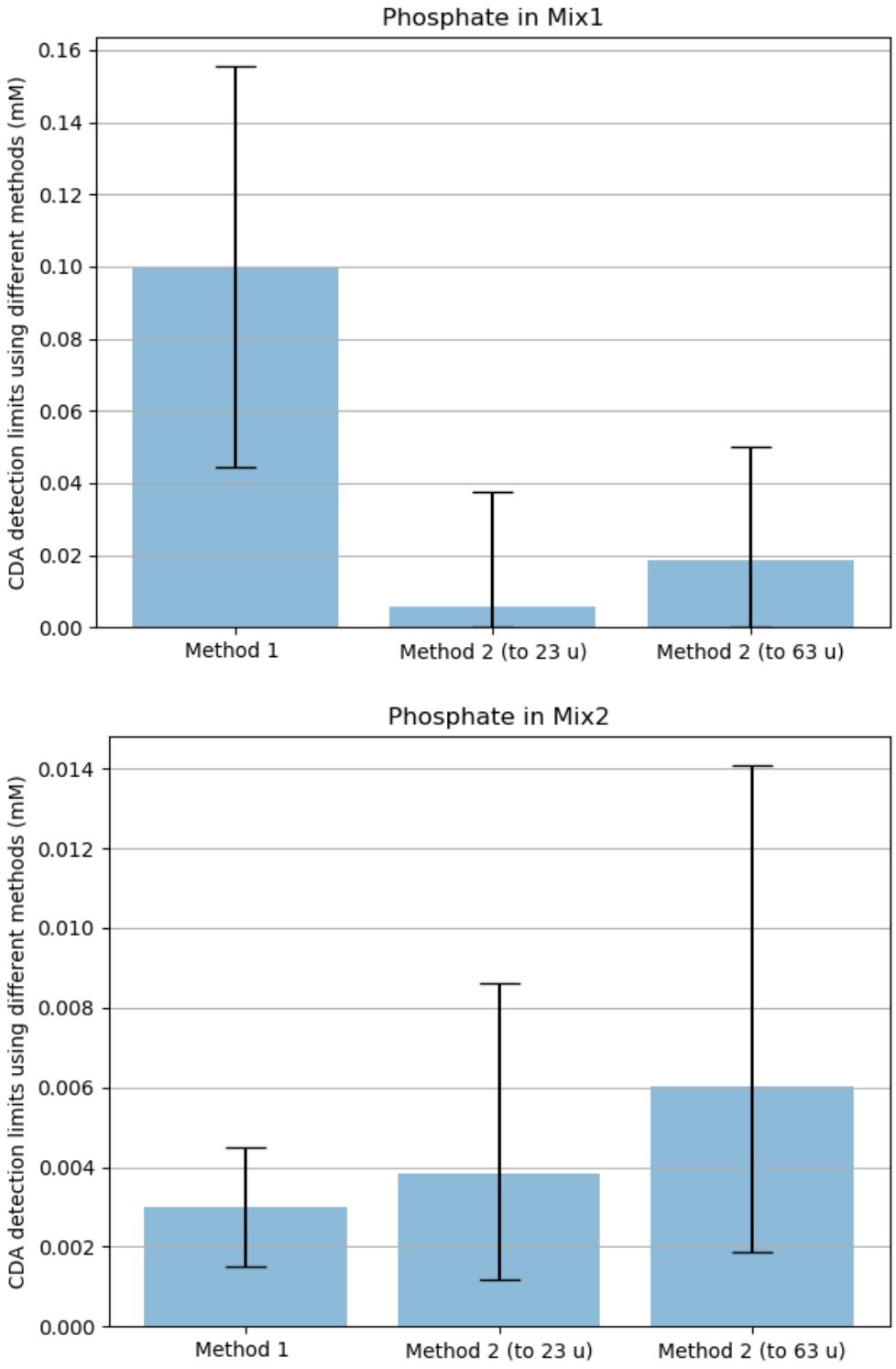

Figure J.2: The approximate CDA detection limits of phosphate in Mix 1 (upper panel) and Mix 2 (lower panel), predicted using Method 1 and Method 2 (two different reference peaks), respectively.

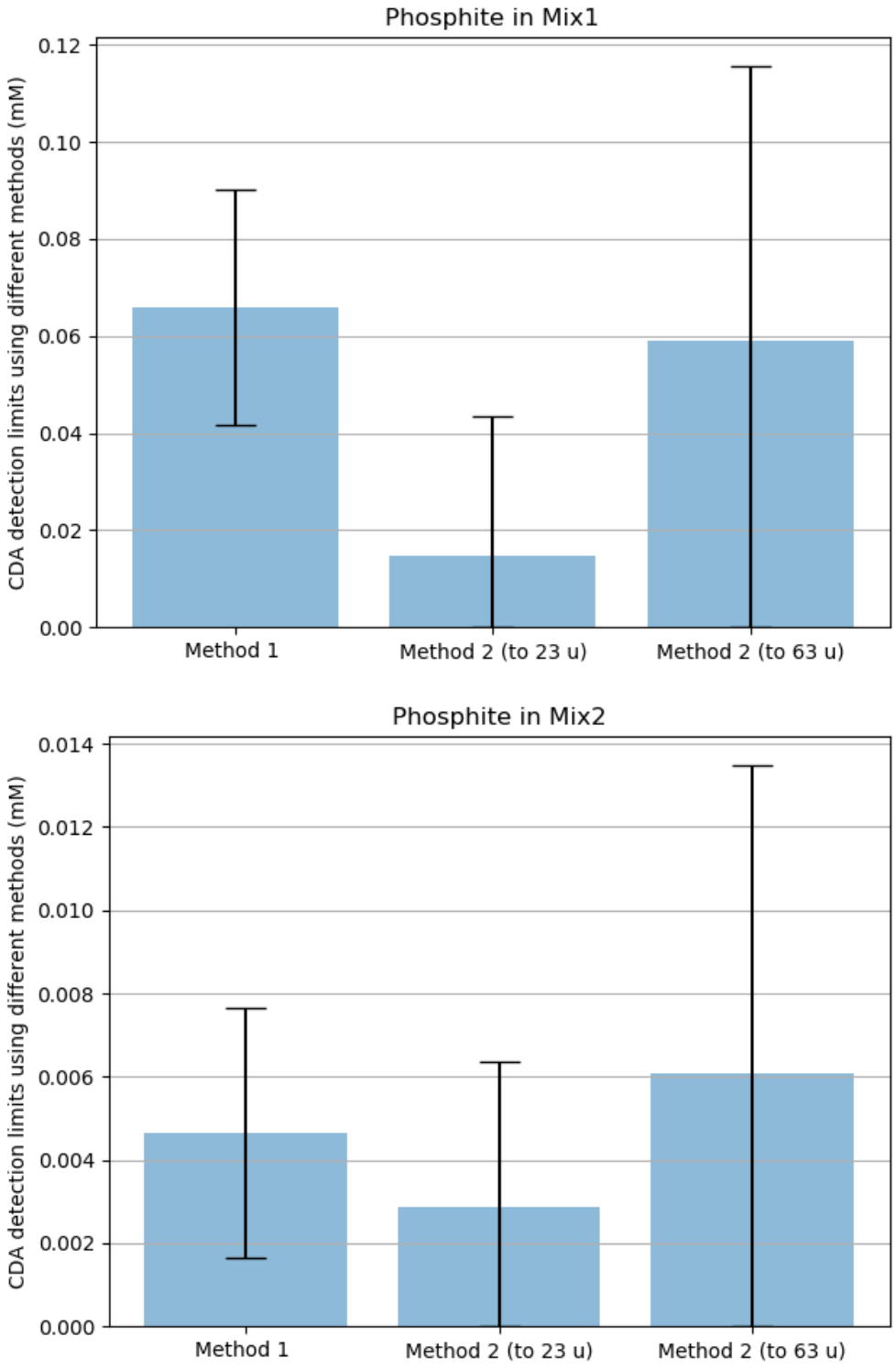

Figure J.3: The approximate CDA detection limits of phosphite in Mix 1 (upper panel) and Mix 2 (lower panel), predicted using Method 1 and Method 2 (two different reference peaks), respectively.

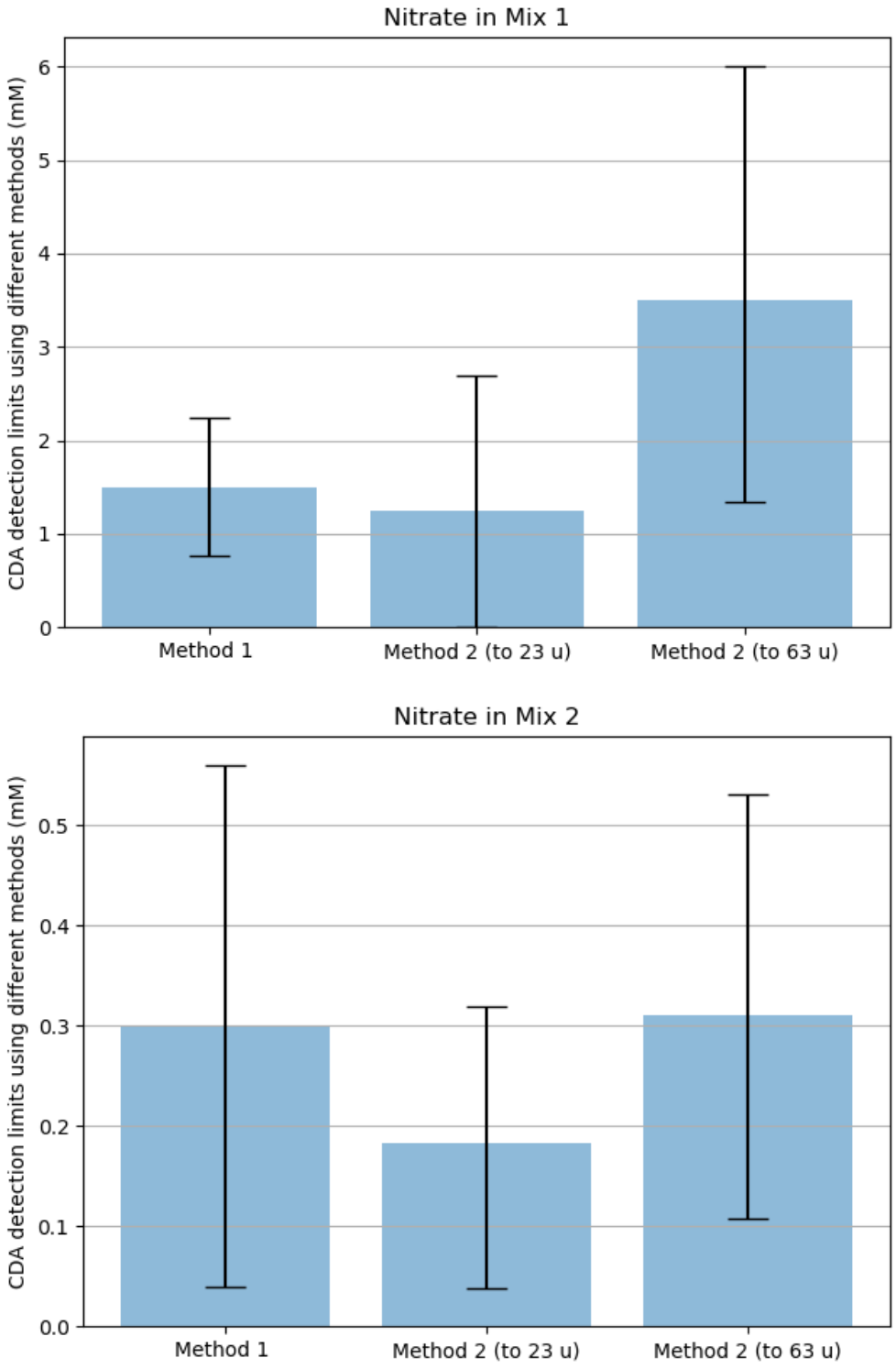

Figure J.4: The approximate CDA detection limits of nitrate in Mix 1 (upper panel) and Mix 2 (lower panel), predicted using Method 1 and Method 2 (two different reference peaks), respectively.

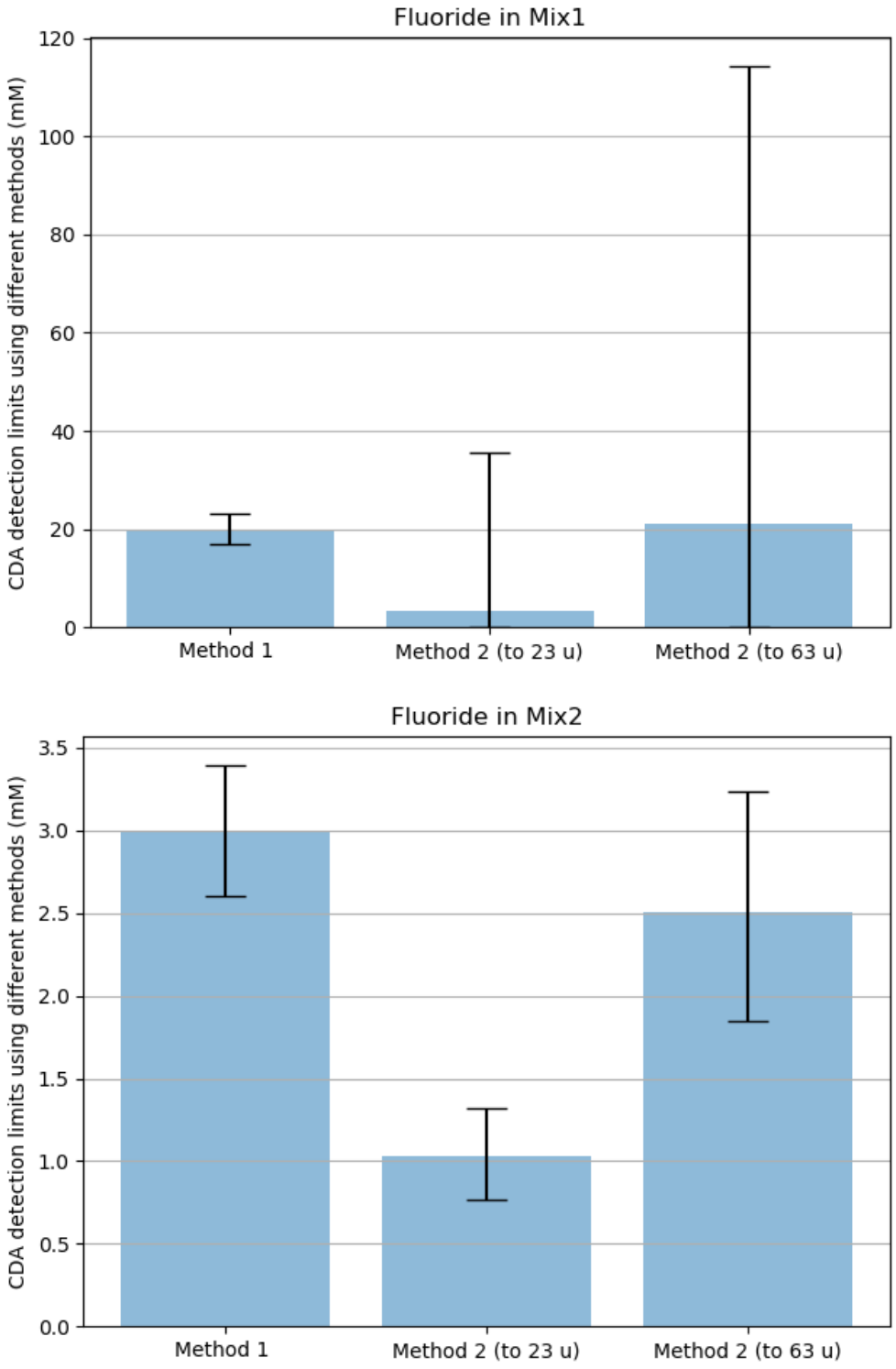

Figure J.5: The approximate CDA detection limits of fluoride in Mix 1 (upper panel) and Mix 2 (lower panel), predicted using Method 1 and Method 2 (two different reference peaks), respectively.

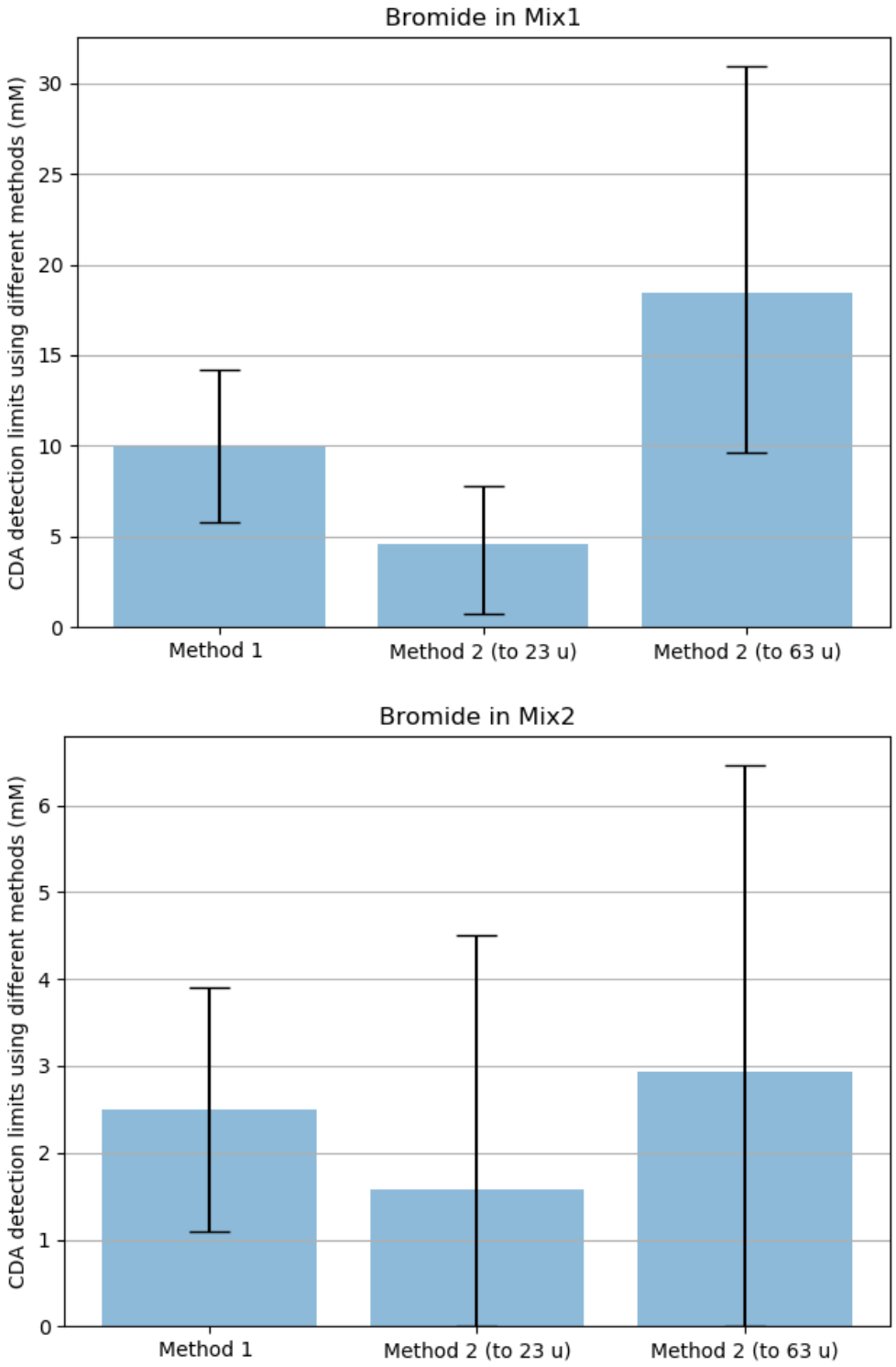

Figure J.6: The approximate CDA detection limits of bromide in Mix 1 (upper panel) and Mix 2 (lower panel), predicted using Method 1 and Method 2 (two different reference peaks), respectively.

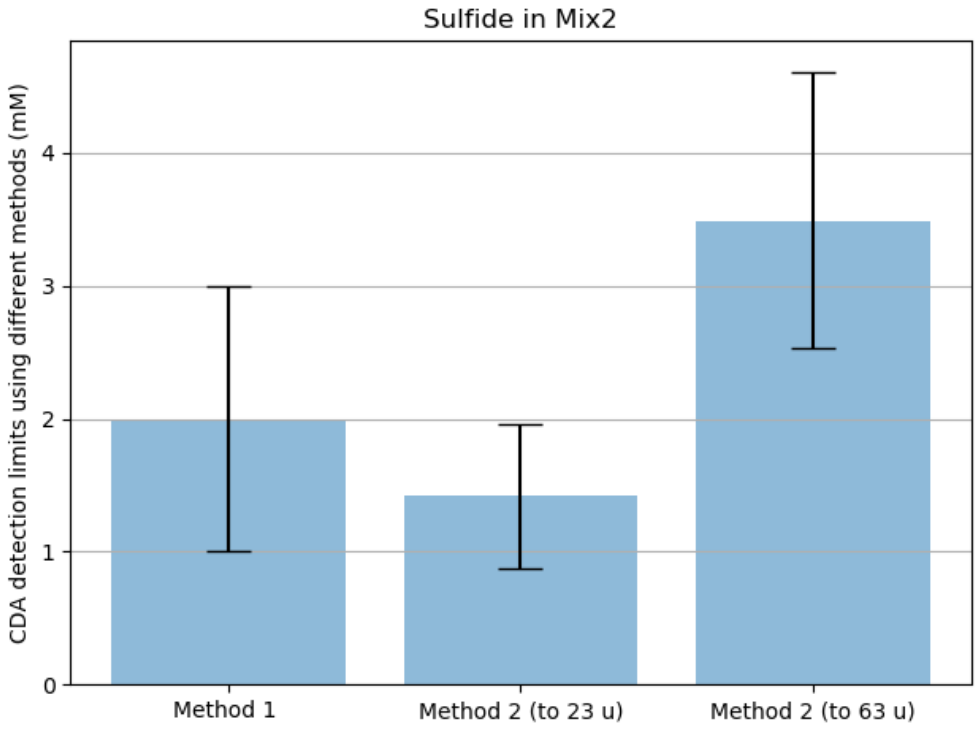

Figure J.7: The approximate CDA detection limits of sulfide in Mix 2, predicted using Method 1 and Method 2 (two different reference peaks), respectively.

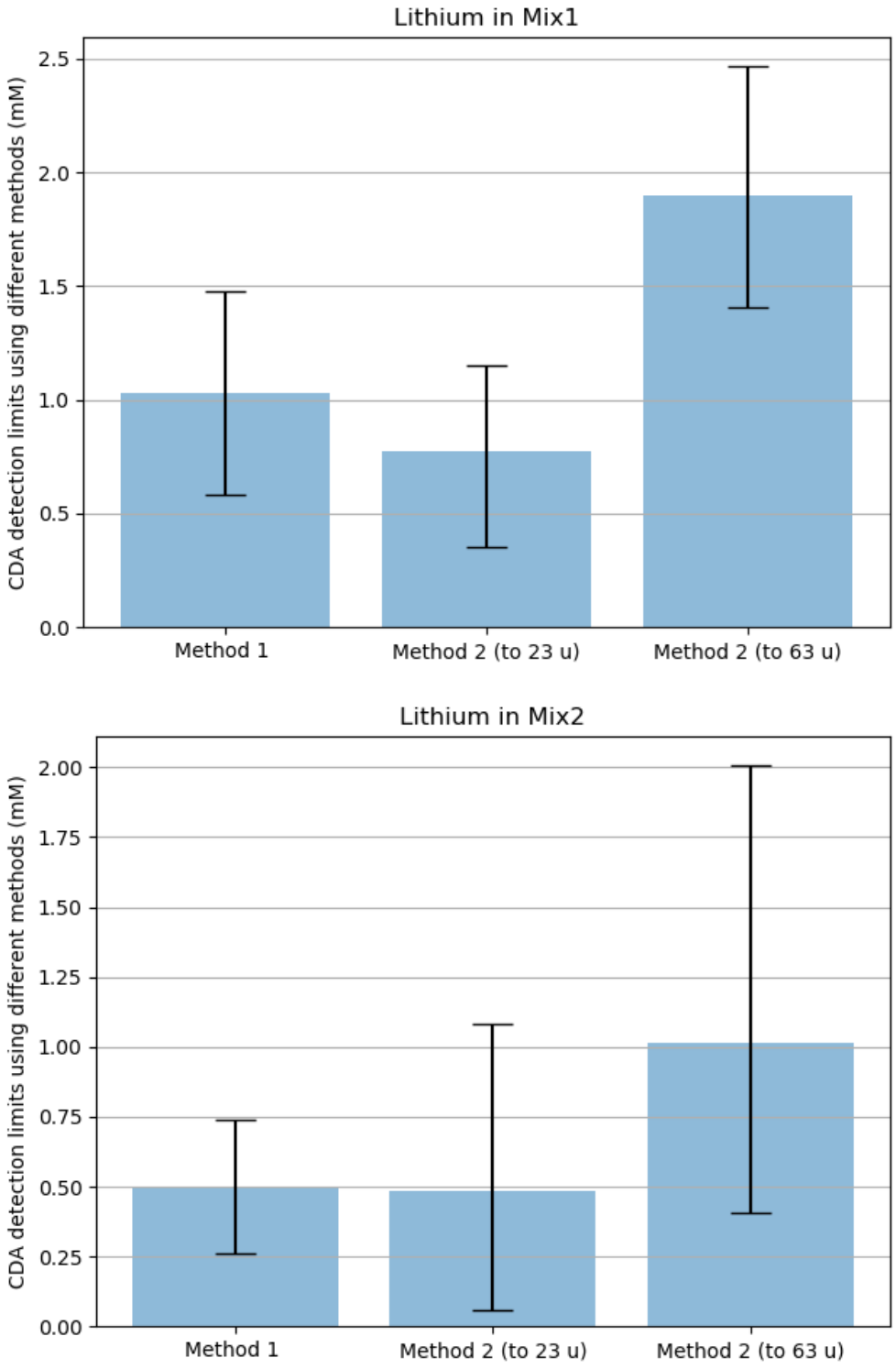

Figure J.8: The approximate CDA detection limits of lithium in Mix 1 (upper panel) and Mix 2 (lower panel), predicted using Method 1 and Method 2 (two different reference peaks), respectively.

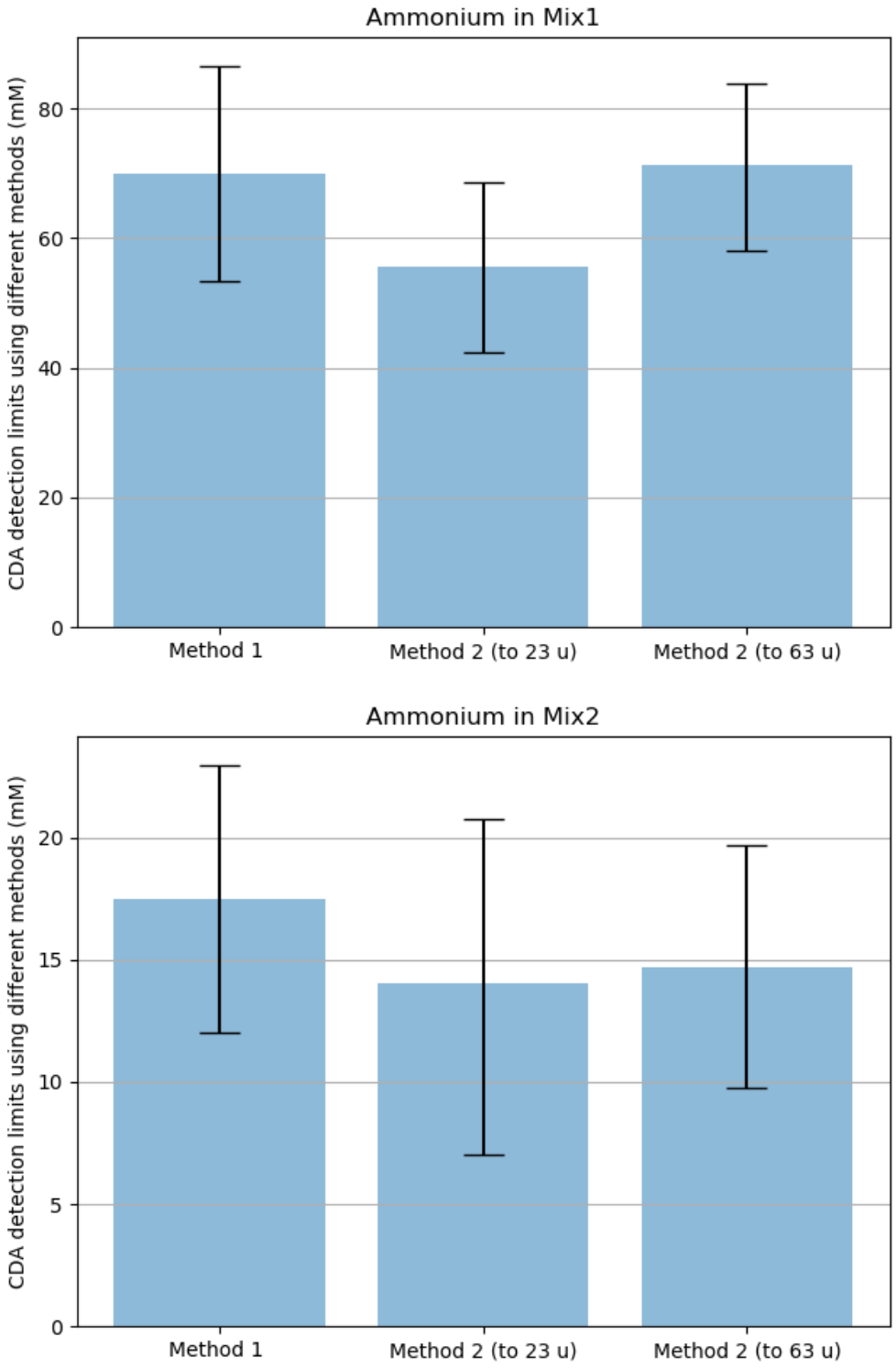

Figure J.9: The approximate CDA detection limits of ammonium in Mix 1 (upper panel) and Mix 2 (lower panel), predicted using Method 1 and Method 2 (two different reference peaks), respectively.

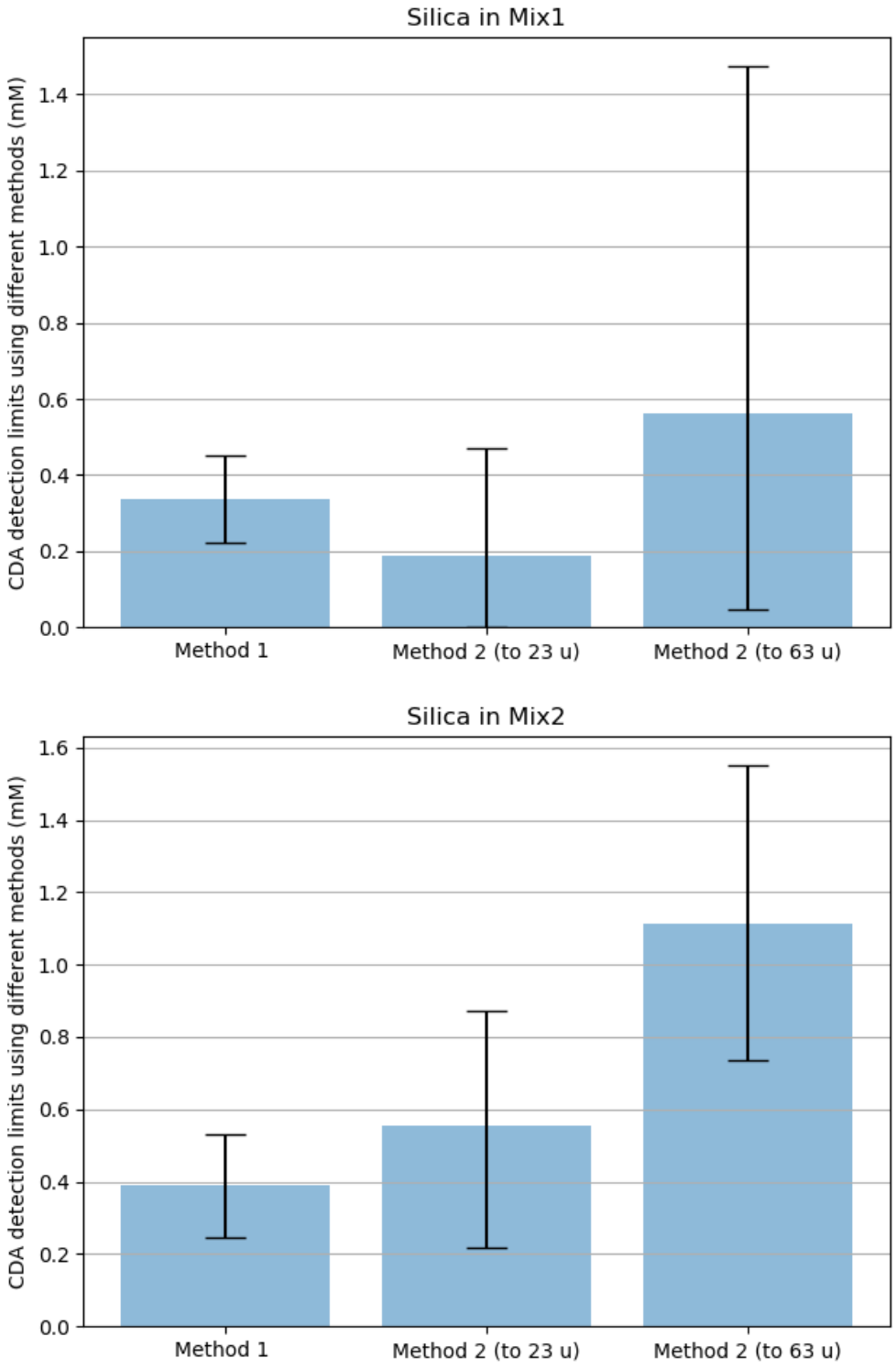

Figure J.10: The approximate CDA detection limits of SiO_2 in Mix 1 (upper panel) and Mix 2 (lower panel), predicted using Method 1 and Method 2 (two different reference peaks), respectively.

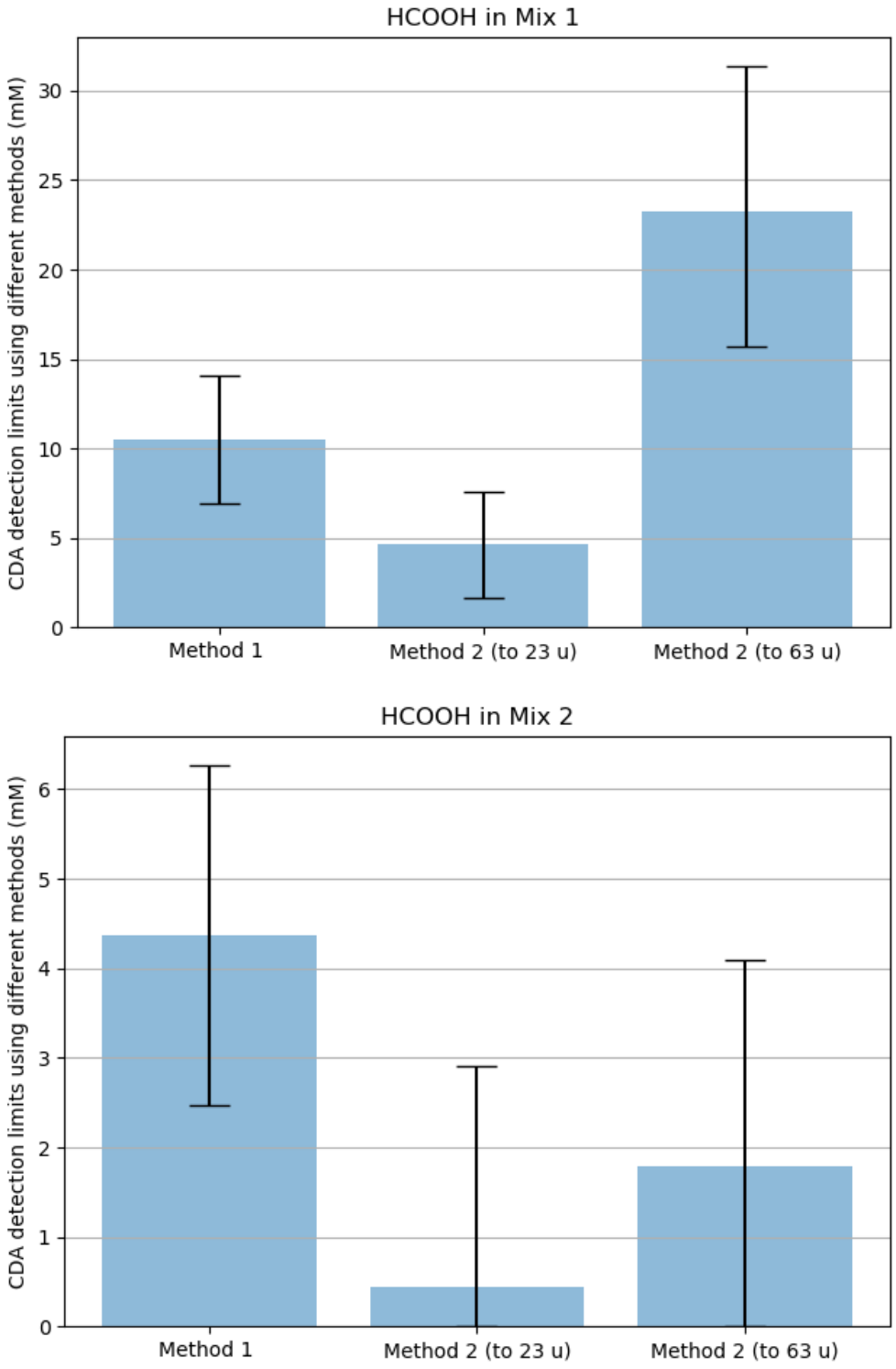

Figure J.11: The approximate CDA detection limits of HCOOH in Mix 1 (upper panel) and Mix 2 (lower panel), predicted using Method 1 and Method 2 (two different reference peaks), respectively.

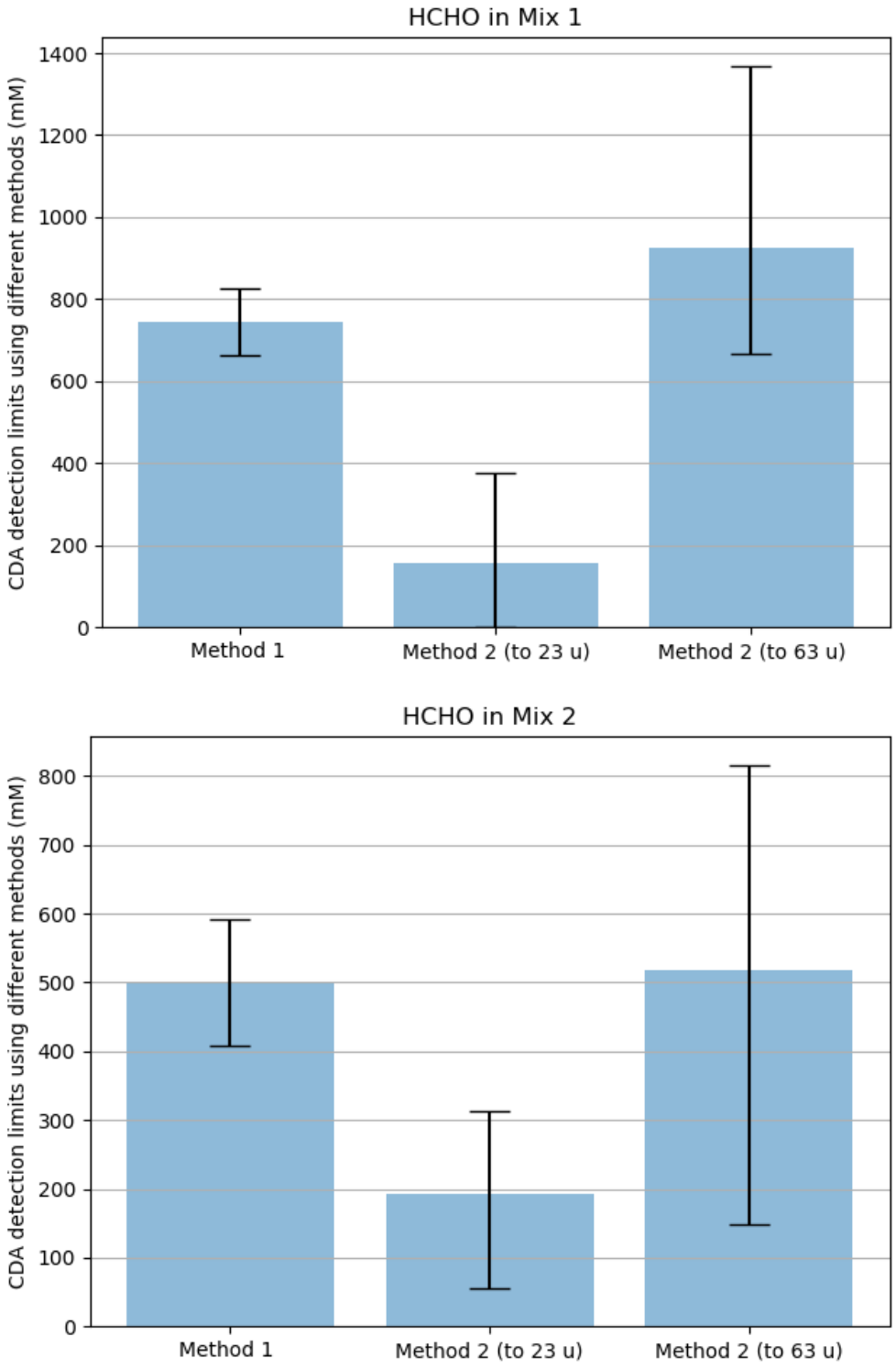

Figure J.12: The approximate CDA detection limits of HCHO in Mix 1 (upper panel) and Mix 2 (lower panel), predicted using Method 1 and Method 2 (two different reference peaks), respectively.

Eidesstattliche Erklärung

Hiermit erkläre ich, dass ich die vorliegende Dissertation mit dem Thema

The composition of salt-rich ice grains emitted by Enceladus' cryo-volcanic plume and implications for the subsurface ocean

selbstständig verfasst und angefertigt habe und keine anderen als die angegebenen Quellen und Hilfsmittel verwendet habe. Geistiges Eigentum anderer Autoren wurde als solches gekennzeichnet.

Des Weiteren versichere ich, dass ich an keiner anderen Stelle ein Prüfungsverfahren beantragt bzw. die Dissertation in dieser oder anderer Form an keiner anderen Fakultät als Dissertation vorgelegt habe.

(Zenghui Zou)

Berlin, den 11.05.2021